Secondary Ion Mass Spectrometry Analysis of Lithium-Content and Isotopic Compositions in Kerogen

by

Zebadiah Teichert

A Dissertation Presented in Partial Fulfillment
of the Requirements for the Degree
Doctor of Philosophy

Approved April 2022 by the
Graduate Supervisory Committee:

Lynda Williams, Co-Chair
Maitrayee Bose, Co-Chair
Richard Hervig
Steven Semken
Everett Shock

ARIZONA STATE UNIVERSITY

May 2022

ABSTRACT

Lithium (Li) is a trace element in kerogen, but the content and isotopic distribution (δ^7Li) in kerogen has not previously been quantified. Furthermore, kerogen has been overlooked as a potential source of Li to sedimentary porefluids and buried sediments. Thus, knowing the content and isotopic composition of Li derived from kerogen may have implications for research focused on the Li-isotopes of buried sediments (e.g., evaluating paleoclimate variations using marine carbonates).

The objective of this work is to better understand the role of kerogen in the Li geochemical cycle. The research approach consisted of 1) developing reference materials and methodologies to measure the Li-contents and δ^7Li of kerogen *in-situ* by Secondary Ion Mass Spectrometry, 2) surveying the Li-contents and δ^7Li of kerogen bearing rocks from different depositional and diagenetic environments and 3) quantifying the Li-content and δ^7Li variations in kerogen empirically in a field study and 4) experimentally through hydrous pyrolysis.

A survey of δ^7Li of coals from depositional basins across the USA showed that thermally immature coals have light δ^7Li values (–20 to – 10‰) compared to typical terrestrial materials (> –10‰) and the δ^7Li of coal increases with burial temperature suggesting that ^{6}Li is preferentially released from kerogen to porefluids during hydrocarbon generation. A field study was conducted on two Cretaceous coal seams in Colorado (USA) intruded by dikes (mafic and felsic) creating a temperature gradient from the intrusives into the country rock. Results showed that δ^7Li values of the unmetamorphosed vitrinite macerals were up to 37‰ lighter than vitrinite macerals and coke within the contact metamorphosed coal.

To understand the significance of Li derived from kerogen during burial diagenesis, hydrous pyrolysis experiments of three coals were conducted. Results showed that Li is released from kerogen during hydrocarbon generation and could increase sedimentary porefluid Li-contents up to ~100 mg/L. The δ^7Li of coals becomes heavier with increased temperature except where authigenic silicates may compete for the released Li. These results indicate that kerogen is a significant source of isotopically light Li to diagenetic fluids and is an important contributor to the global geochemical cycle.

DEDICATION

For my girls Brooke and Dorothy Sue.

ACKNOWLEDGMENTS

As a student of ASU, I acknowledge that the Tempe campus sits on the ancestral homelands of those American Indian tribes that have inhabited this place for centuries, including the Akimel O'odham (Pima) and Pee Posh (Maricopa) peoples.

My journey studying Geology began as an undergraduate at BYU-Idaho and I would like to thank the professors there for getting me excited about the science. I would like to thank Forest Gahn for his enthralling instruction, Gregory Roselle for getting me excited about Geochemistry and Dan Moore for telling me I could succeed as a graduate student.

I would like to express my gratitude to my primary advisor Lynda Williams for taking a chance on me as a researcher and giving me the opportunity to work on this mentally challenging and rewarding research project. Thank you for being patient with me as I learned SIMS, isotope geochemistry, and how to write research papers. I hope to be as proficient of a co-author as you are. I appreciate your guidance and support throughout my time here at ASU and I look forward to your continued mentorship. I want to thank Maitrayee Bose for teaching me NanoSIMS, giving me the opportunity to explore some meteorite research during my early time here and caring about my success. Thank you to Richard Hervig and Peter Williams who both taught me a great deal about SIMS, helped me work through challenging research questions and were very helpful co-authors. I would also like to thank Steve Semken and Everett Shock for agreeing to serve on my advisory committee and for their constructive criticisms and feedback during annual and technical reviews which provided valuable guidance on my research.

I would like to thank former ASU postdocs Ziliang Jin and Timothy Hahn for their friendship and guidance in NanoSIMS operation. I would like to thank Cortland Eble for determining the organic petrology of several of the coal samples studied here. I thank David Wright and Kurt Roggensack for their invaluable aid in setting up hydrous pyrolysis experiments. I appreciate the assistance of those at the METAL (Keck) lab for performing ICP-MS measurements on hydrothermal fluids. I thank Leonard Kroko for his valuable advice regarding the feasibility of the various ion implantations and the Intertek Group PLC for performing the CHN analyses of polymer samples for verification of their chemistry. I thank Shifeng Dai (Univ. Mining and Tech. Beijing, China), Neely Bostick (USGS, CO) and Salt River Project (SRP, AZ) materials division for providing the coal samples studied here. I would like to thank the reviewers of the published works that were products of this dissertation for their thoughtful questions and comments. I thank Enrique Vivoni for allowing me to work with him for my second project and taking the time to meet with me and guide me in the study of hydrology and watershed modeling. Funding for this work was provided through grants from the National Science Foundation (EAR-1811613 & EAR-1352996).

Lastly, but not least I would like to thank my family. Mom and Dad thank you for giving me all the tools necessary to succeed. To my in-laws thank you for supporting our family over these past several years. I would not have been able to complete this process without my wife Brooke, her belief in me, continued encouragement and for being the best wife and mother, I could ask for. My daughter Dorothy Sue, thank you for your hugs, kisses and the joy you bring into my life each day.

TABLE OF CONTENTS

Page

CHAPTER Page

CHAPTER Page

APPENDIX Page

LIST OF TABLES

Table Page

LIST OF FIGURES

Figure Page

Figure Page

CHAPTER 1

INTRODUCTION

Lithium in Kerogen

Kerogen is the organic matter (OM) derived from the remains of organisms found in rocks such as coal and black shale. This material is insoluble in organic solvents (Durand, 1980). Importantly, kerogen is the most abundant form of OM found on earth (Vandenbroucke and Largeau, 2007). Lithium (Li) contains two stable isotopes, ^{7}Li (92.58%) and ^{6}Li (7.42%), and the large mass difference between the isotopes (~17%) allows for significant isotope fractionation (Meija et al., 2016). Lithium isotopes are reported as the per mille (‰) deviation from the reference material NIST SRM 8545 (LSVEC, Li-carbonate) with a ^{7}Li/^{6}Li value of 12.0192 ± 0.0002 (Flesch et al., 1973).

$$\delta^{7}\text{Li}\ ‰ = \left(\frac{R_{Sample} - R_{Standard}}{R_{Standard}}\right) \times 1000 \quad (1)$$

Where R = ^{7}Li/^{6}Li

Little work has been done at the intersection of kerogen and Li and this dissertation addresses the role kerogen has in the Li-geochemical cycle as well as its potential as an economic resource.

Lithium From Organics as an Economic Resource

Lithium is a vital natural resource used chiefly today in the production of rechargeable batteries (Bibienne et al., 2020). In 2021, 71% of Li produced globally was used in the production of batteries (U.S. Geological Survey, 2021) in comparison to just 5% in 2000 (Bibienne et al., 2020). Driven by the amplified use of batteries in automobiles the demand for Li is projected to rise by a factor of 16 from 2020 to 2040

(IEA, 2021). Continental brines and pegmatite are currently the primary sources of Li (Kesler et al., 2012); however, other resources of Li including intra-caldera lacustrine clay deposits (Benson et al., 2017; Castor and Henry, 2020), oilfield brines (Li et al., 2021) and select coal/coal ash (Dai et al., 2012; Hu et al., 2018; Sun et al., 2012a) have garnered attention recently. Even though Li has been found to be associated with some oilfield brines and coal deposits at concentrations ≥500 μg/g (Collins, 1975; Dai et al., 2012), little work has been done to understand the role of OM in Li-geochemical cycles and the Li-contents of different kerogen types and maceral types and are unknown.

Implications for Paleoclimate Studies Using Li-Isotopes

Over the past 20 years understanding the flux of Li and its stable isotopes during chemical weathering of the silicate crust and fluvial transport has become a major area of research within the Li-geochemical cycle (reviews in Penniston-Dorland et al., 2017; Tomascak et al., 2016). Silicate weathering is tied to Earth's climate because the process directly sequesters atmospheric CO_2 causing a negative feedback against warming climates (Berner et al., 1983; Kump et al., 2000). Additionally, the climate at a given time controls the weathering congruency (primary silicate mineral dissolution / secondary mineral formation) (Misra and Froelich, 2012; Pogge von Strandmann et al., 2020). It has been shown that there is no significant Li-isotope fractionation for primary silicate mineral dissolution (Pistiner and Henderson, 2003; Wimpenny et al., 2010); however, during secondary mineral formation ^{6}Li is preferentially taken up by the mineral phases leaving a heavier isotopic ratio in the waters (Hindshaw et al., 2019; Millot et al., 2010; Pistiner and Henderson, 2003; Pogge von Strandmann et al., 2019; Vigier et al., 2008; Wimpenny et al., 2010). Thus, the riverine Li-isotope composition is controlled by the

climate via the weathering congruency (Pogge von Strandmann et al., 2020). During warm and wet climates weathering congruency is highest, yielding rivers with more rock-like Li-isotope compositions while during cool dry climates there is lower weathering congruency and the isotope composition of rivers becomes enriched in ^{7}Li because of the preferential uptake of ^{6}Li during secondary mineral formation (Pogge von Strandmann et al., 2020). The Li derived from weathered rocks is carried by rivers and groundwater to the ocean bearing a Li-isotope composition indicative of the climate-controlled weathering regime. Thus, the Li-isotope composition of seawater at a given time can be used to understand the global climate. Some have measured the Li-isotope compositions of various marine carbonates, which range from +5 to +40‰ and typically contain <0.2 μg/g Li, to interpret past seawater $\delta^{7}Li$ and reconstruct paleoclimates (Lechler et al., 2015; Misra and Froelich, 2012; Pogge von Strandmann et al., 2017, 2013; Ullmann et al., 2013). This method could be valid if mass-fractionation of Li-isotopes between the seawater and precipitating carbonates is known and there is no dissolution and reprecipitation of carbonates during diagenesis, which is not always the case (Dellinger et al., 2020).

Organic rich rocks are deposited within the same sedimentary basins as marine carbonates. Williams et al. (2013) proposed that during methane generation kerogen releases isotopically light Li with hydrocarbons and hydrocarbon-related fluids (Williams et al., 2013; 2015). Considering that the Li concentration of seawater is only 0.17 μg/g (Hong et al., 2018) even small concentrations of Li-released from kerogen could significantly change the Li-isotope composition of porefluids. As reservoirs for oil and gas, carbonates are as important as sandstones (Selley and Sonnenberg, 2015), thus it

reasonable to suspect that Li derived from OM could be incorporated in carbonates that precipitated/reprecipitated during burial diagenesis. Therefore, it is critical to evaluate the contribution of Li from organic matter to pore fluids and the greater Li geochemical cycle.

Tracing Hydrocarbons with Li-Isotopes

In addition to understanding how organic Li-sources may influence paleoclimate studies, interest has grown in using Li-isotopes to trace the migration of hydrocarbons. Williams and Hervig (2005) showed that clay minerals illite-smectite (I-S) take up Li at the same diagenetic conditions (T, P) that hydrocarbons are released from kerogen. Authigenic I-S in bentonites from the Wattenberg gas field in the Denver Basin (USA) showed a 30‰ shift in the δ^7Li value between the finest <0.1 μm fraction (+12‰) to the coarser 0.1 to 2.0 μm fraction (–18‰), recording a change in the fluid δ^7Li composition and temperature. The fine I-S fraction formed at ~50-80 °C from porefluids with δ^7Li value similar to seawater (+31‰), while the coarse I-S fraction of the same sample formed at higher temperatures (>150 °C) during more rapid illite growth, and in equilibrium with porefluids with lower δ^7Li (Williams et al., 2015). At temperatures >150 °C kerogen would undergo gas generation, while most oil would have been released and migrating away from the hotspot in the basin. Therefore, as Li-bearing hydrocarbons or oilfield brine fluids migrate through sedimentary basins the Li may be incorporated in authigenic illite, recording a light Li-isotope signature in illite indicative of an organic source (Williams et al., 2012, 2013). Indeed, oilfield brines tend to have lower δ^7Li than many other brines and terrestrial waters (See Chapter 2, p.35). However, data on the Li-

isotope composition and Li-content of kerogen as well as the potential fractionation of Li-isotopes upon release from kerogen are lacking.

Kerogen Background

Kerogen is composed of different macerals, which are grouped based on their physical properties under the microscope. Kerogens are also subdivided into types based on their H/C and O/C ratios (Fig. 1.1; Van Krevelen, 1950, 1961, Van Krevelen et al., 1957). Type III kerogen has a low H/C ratio compared to the Types I and II kerogen. Thus, Types I and II kerogen generate more liquid hydrocarbons than Type III kerogen, which generates primarily gaseous hydrocarbons (Vandenbroucke et al., 2007). Type I kerogen is typically derived from algal remains, has the highest H/C and is commonly found in lacustrine sediments (Taylor et al., 1998); however, cannel coals (Hutton and Hower, 1999) and some marine shales also host abundant Type I kerogen (Selley and Sonnenberg, 2015). Type II kerogen is derived from the remains of zooplankton, phytoplankton, bacteria as well as algal detritus, has lower H/C than Type 1 kerogen and forms primarily in the marine sedimentary environment (Selley and Sonnenberg, 2015; Taylor et al., 1998). Type III kerogen is derived from woody tissues, such as lignins and tannins, that are typically resistant to microbial decomposers, and accumulate in swamps and raised bogs (Orem and Finkelman, 2003; Taylor et al., 1998). Lastly, Type IV kerogen forms by processes including charring, oxidation, moldering, fungal attack or desiccation of primary organic material during deposition or early diagenesis/peatification (Taylor et al., 1998). The aquatic biomass that forms Type I and II kerogen has the highest chance of preservation when primary production is high and

benthic waters are anoxic (Selley and Sonnenberg, 2015). For Type III kerogen, however, oxic conditions are necessary during early peatification for the microbial degradation of lignins into humic substances (Chester, 2000; Taylor et al., 1998).

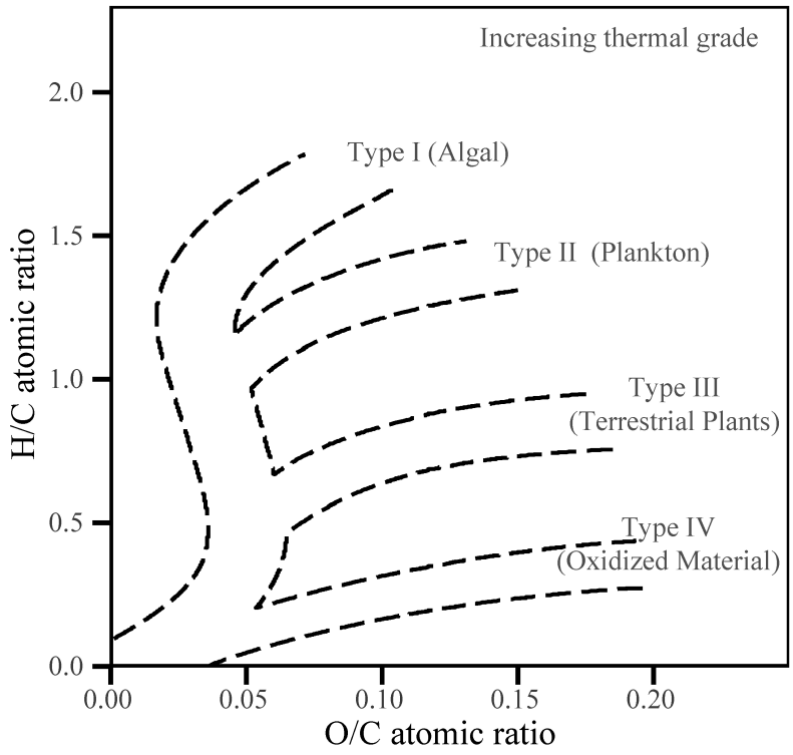

Figure. 1.1. Van Krevelen plot (Van Krevelen, 1950; modified by McCarthy et al., 2011) showing the different Types of kerogen subdivided based on H/C and O/C atomic ratios.

Primary organic material along with detrital minerals undergo burial through continued subsidence and sediment deposition, becoming lithified through compaction and cementation (McCabe, 1991). With continued burial, deposits undergo differing degrees of thermal alteration resulting in increased aromatization (Carr and Williamson, 1990) and changes to the chemical and physical structure of the kerogen. The thermal evolution of peat and coal is shown in Fig. 1.2. The onset of oil generation during natural burial can begin at temperatures as low as 60 °C; however, the most oil is produced from 100 °C – 150 °C and most gas is produced from 150 °C – 230 °C (Killops and Killops,

2004). The hydrocarbons either remain trapped in the source rock pore spaces or migrate along pathways through permeable rock into structural and stratigraphic traps, forming conventional hydrocarbon reservoirs (Russel, 1951).

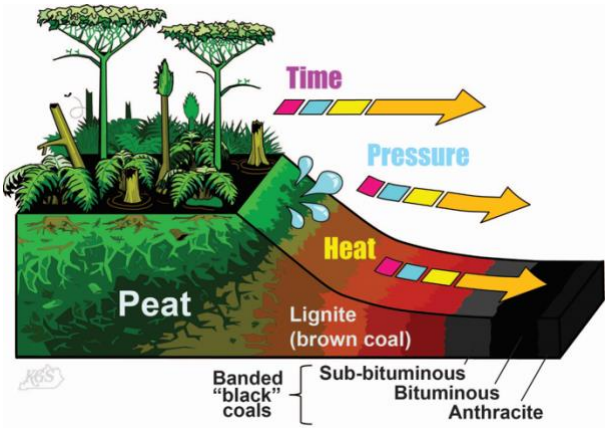

Figure 1.2. Concept sketch of coal formation processes. Art credit to Stephen Greb of the Kentucky Geological Survey.

Lithium in Organics

Few studies have examined the host phase(s) of Li in kerogen, as Li is generally thought to be primarily concentrated in the mineral matter of the coal and shales (Finkelman, 1980; Dai et al., 2012; Teng et al., 2004). However, Swaine, (1990) stated that Li was also associated with kerogen in coal and Finkelman et al. (2018) later showed that up to ~50% of Li in immature coals is associated with organic material. The Li in kerogen may be inherited directly from the organisms that accumulate to form kerogen or could be taken up by the OM during early diagenesis as kerogen is forming by chelating with carboxylic acid (COOH), and phenolic hydroxyl groups (OH) (Li et al., 2010). Among terrestrial plants, Li has a varying toxicity threshold depending on the species (Shahzad et al., 2016), yet plants contain trace amounts of Li typically ranging from 0.01 – 31 μg/g (Pendias and Kabata-Pendias, 2000). Nonetheless, leguminous plants grown in

Li-rich soils (9 – 175 μg/g) in New Zealand are reported to contain up to 143 μg/g Li (Pendias and Kabata-Pendias, 2000) which is consistent with the findings of Gough et al., (1977) that the Li-content of plants is a function of the soil Li-content. Modern soils throughout the world range from 1.2 – 98 μg/g (Pendias and Kabata-Pendias, 2000). Histosols, which are the dominant OM-rich soils in peatlands (Kolka et al., 2016), contain Li-contents ranging from 1.2 to 24 μg/g (Pendias and Kabata-Pendias, 2000; Pogge von Strandmann et al., 2021). Excluding modern anthropogenic pollution, the Li-content of soils in coal forming environments as well as benthic muds in marine and lacustrine settings is largely controlled by the geologic provenance (i.e., the sediment source and degree of sediment weathering between erosion and final deposition; Basu, 2017). Lithium is an incompatible element in igneous rocks (Best, 2002) and becomes most concentrated in granitic magmas containing Li-rich pegmatites (Bowell et al., 2020; Kesler et al., 2012). Thus, sediment derived from the erosion of Li-rich granitic and rhyolitic rocks transported to kerogen forming depositional environments with minimal weathering and loss of Li would be an ideal scenario for the concentration of Li in kerogen precursors.

Thibon et al., (2021) measured the Li-contents of several higher marine organisms including bivalves (0.42±0.14 μg/g), cephalopods (0.15±0.05 μg/g), crustaceans (0.19±0.10 μg/g) and fish (0.15±0.06 in kidneys) and found that benthic organisms which ingest sediment typically have higher Li-concentrations. In the Baffin Bay (Greenland) Copepods and Zooplankton had Li-contents of 89.6 μg/g and 79.8 μg/g, respectively (Campbell et al., 2005) while fish and seabirds from the same area contained Li-contents <0.001 μg/g, suggesting that organisms in lower trophic levels accumulate more Li than

those in higher trophic levels as was observed in Thibon et al., (2021). Indeed, some Zooplankton in the Belushya Bay (Russia) have Li-contents as high as 1622 μg/g (Lobus, 2016) and Thébault et al., (2022) found that the Li-content of scallop digestive glands increased by a factor of two or more shortly after diatomaceous blooms in from the Bay of Brest (France).

Li-Isotope Composition of Organics

Few studies have measured the δ^7Li values of organic rich rocks. Harkness et al., (2015) measured the δ^7Li values of aqueous leachates from coal fly ash and found they ranged from –7 to +12.8‰. Bulk MC-ICP-MS measurements of low rank coals from South Africa and China, with higher Li-contents (11-281 μg/g) than typical low rank coals from the USA (6 μg/g; Finkelman et al., 2018), yielded δ^7Li values ranging from +1.4 to +7.9‰ (He et al., 2019) when digested using microwave methods. Several studies measuring bulk shales by ICP-MS found δ^7Li values ranging from –3.4 to +4.3‰ (Phan et al., 2016; Romer and Meixner, 2014; Steinhoefel et al., 2021; Teng et al., 2004), although the bulk of the Li is coming from clay minerals not kerogen in shales. Considering that coal and shale are heterogeneous rocks with a variety of minerals and macerals (e.g., vitrinite, liptinite, inertinite) bulk techniques are insufficient to accurately measure the range of δ^7Li in kerogen.

Organic matter has been shown to fractionate Li-isotopes, despite claims to the contrary by investigators using Li-isotopes to study weathering (e.g., Pogge von Strandmann et al., 2021) and several examples follow. Li et al., (2020) showed that in an organic rich Hawaiian soil, the organic fraction of the soil had δ^7Li values of ~ –7‰

while the carbonates, oxides and silicates had δ^7Li values ranging from +3 to +17‰ suggesting a preference for ^{6}Li in soil OM. In a similar, but not as extreme example, the mean δ^7Li value of O (organic) soil horizons (–1.1 ± 1.1‰) was lighter than A (+3.8 ± 2.3‰), B (+6.0 ± 3.0‰) and C (3.0 ± 2.4‰) soil horizons (Pogge von Strandmann et al., 2021). Different plant tissues have displayed Li-isotope variations with grass roots being up to 3.4‰ heavier than stems and stems being up to 2.9‰ heavier than grass foliage, showing a significant ^{6}Li enrichment during biological uptake from root to leaf (Li et al., 2020). Leaf litter measured by Steinhoefel et al., (2021) had a ≥1‰ lighter δ^7Li value than the corresponding soil and bedrock. Similar results showing a light Li-isotope composition for terrestrial plants relative to soil and groundwater are detailed in Chapter 2 (p.31). Balter and Vigier (2014) found that sheep given dietary Li at +15‰ fractionated that initial ratio over a ~40‰ δ^7Li range among different organs. That is significant because the δ^7Li of geological samples spans only a slightly larger range of ~50‰.

Finally, among aquatic organisms, Dellinger et al., (2018) defined isotopic changes due to physiological vital effects of organisms as the difference between biogenic and abiogenic calcite and aragonite as follows:

$$\Delta^7\text{Li}_{\text{physio}} = \delta^7\text{Li}_{\text{biogenic carbonate}} - \delta^7\text{Li}_{\text{inorganic carbonate}} \quad (2)$$

and found vital effects among mollusks ($\Delta^7\text{Li}_{\text{physio}}$ ranging from –4‰ to +14‰), brachiopods ($\Delta^7\text{Li}_{\text{physio}}$ ranging from 0‰ to –3‰), echinoderms ($\Delta^7\text{Li}_{\text{physio}}$ ~ –3‰) and benthic foraminifera ($\Delta^7\text{Li}_{\text{physio}}$ ranging from –1‰ to –7‰; Marriott et al., 2004). In another study, aquarium coral species aragonite vs. abiotic aragonite had $\Delta^7\text{Li}_{\text{physio}}$ of –

2‰ (Bastian et al., 2018). Thus, organic molecules and organisms can fractionate Li-isotopes.

Advantages of Secondary Ion Mass Spectrometry for Measurements of Li

Bulk measurements of coal samples require the use of acids in combination with microwave digestion in order to digest all mineral and organic rock constituents (He et al., 2019). Alternatively, coal samples can be ashed in a furnace, and the ash can be measured for elemental and isotopic abundances which are then used to back-calculate the composition of inorganic elements of the bulk coal (Bullock et al., 2002). It is not known if any Li volatilizes during either of these digestion or ashing processes or if there is any Li-isotope fractionation during the volatilization.

In methods commonly used to isolate kerogen, minerals are digested using HF and HCl acids which have been shown to also react with organic functional groups (Saxby, 1976) and thus may be removing Li from the kerogen as discussed in greater detail in Chapter 4 (p.98). In this dissertation, secondary ion mass spectrometry (SIMS) was used to measure solid samples allowing *in-situ* measurements of different macerals and minerals at the micron scale.

Dissertation Outline

Two papers on the empirical trends in δ^7Li among US coals, and the calibration methods used for Li in organic matrices have been published (Chapters 2 and 3) in the journals Chemical Geology and Geostandards and Geoanalytical Research, respectively. One paper on the variations of δ^7Li among organic macerals of single coal seams transected by dikes has been accepted by the Journal Chemical Geology after revision

(Chapter 4). The last two chapters (Chapters 5 and 6) are in preparation for submission to a peer reviewed journal.

This dissertation first presents a general SIMS survey of the Li-isotope compositions of coals and shales of different thermal maturities from basins across the USA to understand what factors (e.g., thermal maturity, kerogen type) affect the bulk Li-isotope compositions of kerogen (Chapter 2). That work necessitated the development of SIMS reference materials for the determination of potential matrix effects on Li-contents and Li-isotope compositions of organic matrices (Chapter 3). Next contact metamorphosed coal samples were studied in detail to understand how the Li-contents and Li-isotope compositions of different macerals within single coal seams change through thermal alteration (Chapter 4). Preliminary SIMS investigations of a Li-rich (100's of μg/g) coal deposit from China are discussed in Chapter 5. Subsequently, hydrous pyrolysis experiments of coal samples were carried out at different temperatures to determine the amount of Li released from kerogen into water during maturation and how the Li-isotopes fractionate under those conditions (Chapter 6). I conclude by summarizing the major findings and implications of this work and discussing related future applications and research directions (Chapter 7).

CHAPTER 2

LITHIUM ISOTOPE COMPOSITIONS OF U.S. COALS AND SOURCE ROCKS: POTENTIAL TRACER OF HYDROCARBONS

Abstract

Kerogen in organic-rich rocks contains trace amounts of lithium (Li) that has been overlooked as a contributor to the global Li geochemical cycle. This study examined a variety of coals where kerogen is concentrated (> 50% organic carbon) and hydrocarbon source rocks of different ages, depositional environments and thermal maturity to determine their range of Li isotopic compositions (δ^7Li‰) and factors that influence their compositions.

Using Secondary Ion Mass Spectrometry (SIMS), we analyzed 22 coals and 4 hydrocarbon source rocks (Types I, II, III), to determine the δ^7Li of kerogen *in situ*, without chemical isolation of phases that can alter their original isotopic compositions. The δ^7Li values of the coals surveyed are distinctly isotopically light (< 0‰) compared to most natural minerals and fluids. In immature coals, with a vitrinite reflectance in oil (VR_o) of ≤0.5%, kerogen δ^7Li values average –23.4 ± 1.1‰ and become heavier with increasing thermal grade to temperatures of gas generation (VR_o ~1.3%). The linear correlation between δ^7Li and VR_o suggests that ^{6}Li may be preferentially released to pore fluid from kerogen during thermal maturation. Notably, authigenic clays forming at diagenetic temperatures substitute Li from pore fluids into silicate layers, therefore, the Li isotopic composition of the clays may record fluid isotopic compositions influenced by organic-Li sources.

NanoSIMS isotopic maps of the Lower Bakken Shale, and SIMS measurements of the Green River Shale show isotopically light Li associated with C-dominated areas, and heavier δ^7Li with Si-dominated areas of the hydrocarbon source rocks. We conclude that kerogen is a source of isotopically light Li that contributes to fluids during thermal maturation and hydrocarbon generation. Kerogen may be a significant contributor of Li to pore fluids and its distinctly light Li isotopic composition relative to other terrestrial waters and minerals could provide a tracer of organic inputs to the global geochemical cycle.

Introduction

Lithium isotopes are being increasingly utilized to aid in understanding a host of terrestrial and extraterrestrial processes. In terrestrial systems, there has been significant use of Li isotopes in low temperature crustal environments to investigate the geologic processes of weathering and fluid dynamics (Penniston-Dorland et al., 2017; Tomascak et al., 2016). However, there is limited information regarding how Li from organic compounds may play a role in these processes. If there is a significant amount of Li bound in organic compounds, it is important to know its isotopic composition and how Li from organics would contribute to the global geochemical cycle if the Li were released from the organics (e.g., with increasing burial temperature). In this study, we measured the Li isotope compositions on a suite of 22 coals from across the United States, representing different ages, depositional environments and thermal maturities. In addition, 4 hydrocarbon source rocks containing Type I, II and/or III kerogen were analyzed using Secondary Ion Mass Spectrometry (SIMS) and NanoSIMS. The goal of this study is to evaluate the range of Li isotopic compositions in organic-rich rocks

consisting of a variety of organic macerals which were exposed to a range of thermal alteration conditions.

Lithium Resources

Lithium is an important natural resource that has increased in demand due to the rising use of Li ion batteries. The primary economic sources for Li are brines, salt lakes and pegmatite deposits (Kesler et al., 2012). Seawater contains only ~0.17 mg/L Li but it is extracted economically using manganese oxide membranes to concentrate Li (Hong et al., 2018). Lithium is more concentrated in oilfield brines with concentrations up to several 100 mg/L (Collins, 1975; Eccles and Berhane, 2011; Macpherson, 2015; Millot et al., 2011; Phan et al., 2016). Interestingly, Li concentrations in bitumen (extractable organic compounds) are reported to be higher than their reservoir rocks by up to 17 mg/L, suggesting an association of Li with extractable hydrocarbons (Hosterman, 1990). In hydrocarbon source rocks, Li concentrations are highest in authigenic clay minerals (primarily illite-smectite; I-S) and some studies suggest that Li may be linked to gas generation (Williams et al., 2013, 2015). Lithium substitutes in the octahedral sites of I–S and is also adsorbed in clay interlayers (Sposito et al., 1999). Bentonite from hydrocarbon reservoirs in the Baltic Basin, contain I-S with Li contents >600 ppm after removal of interlayer-Li (Williams et al., 2013), whereas average marine shales have a reported range of 50–75 ppm Li (Horstman, 1957; Pendias and Kabata-Pendias, 2000). In Marcellus Shale source rock, Phan et al. (2016) found organics and sulfide minerals to be the second largest (up to 20%) host for Li after the silicate fraction. For coals, the worldwide average reported Li-content is lower than for clays, with ranges from 6 to 44 ppm (Finkelman et al., 2018; Ketris and Yudovich, 2009; Swanson, 1975). However,

some coals from China have been identified as containing economically viable concentrations of Li (Qin et al., 2015). Coals within the Jungar Coalfield (Mongolia) have Li concentrations exceeding 500 ppm but, in those deposits, Li is mostly concentrated in authigenic clays within the coal (Dai et al., 2012).

Geologic Background

Kerogen is the insoluble organic material found in sedimentary rocks (Durand, 1980) that is derived from the remains of organisms and is the most abundant form of organic matter on Earth (Vandenbroucke and Largeau, 2007). Kerogen is composed of a variety of organic macerals, which are grouped based on their physical properties. Just as rocks are composed of multiple minerals that each might host Li, the macerals that comprise kerogen may each host Li in different structural arrangements. Because of the complexity of organic macerals in kerogen, a simple approach to assessing major compositional changes was developed by Van Krevelen (1950) comparing their major element ratios (H/C and O/C) to classify organic Types (e.g., I, II, III) (Fig. 2.1). Coals contain primarily Type III kerogen derived from woody remains of plants that contain high O/C and low H/C (Vandenbroucke and Largeau, 2007). Coals are dominated by vitrinite (> 70% by volume; Orem and Finkelman, 2003), which is a group of organic macerals that can indicate the thermal maturity according to its reflectance in oil immersion microscopy (VR_o; Mukhopadhyay, 1994). Type III kerogen is more prone to generate gas than liquid hydrocarbons. Types I and II kerogen are primarily derived from algae and phytoplankton, containing higher H/C and lower O/C and are more prone to generate liquid hydrocarbons (Vandenbroucke and Largeau, 2007).

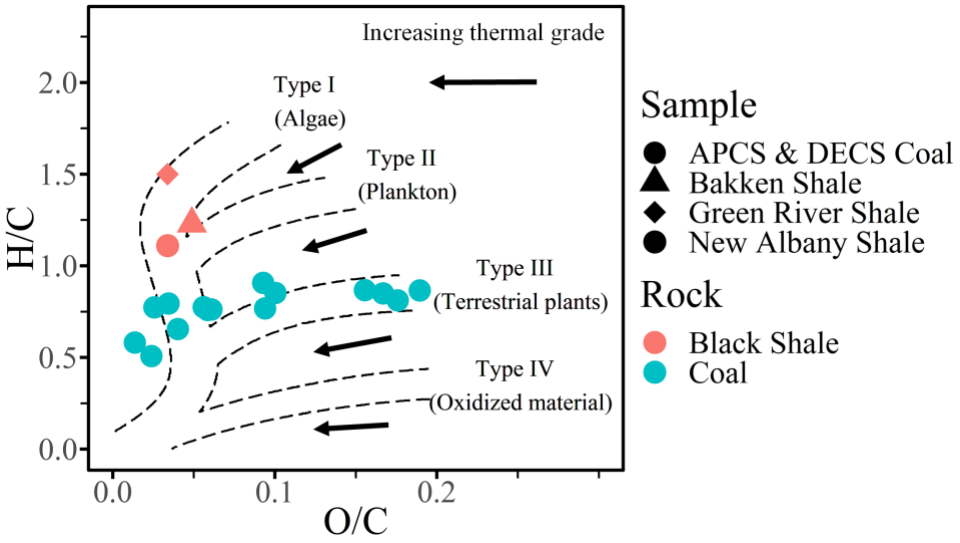

Figure 2.1. Van Krevelen plot (Van Krevelen, 1950; modified by McCarthy et al., 2011) of coal and source rock samples studied. For Bakken Shale and New Albany Shale O/C values were approximated from Oxygen Index values (Akar, 2014; Jin, 2014; Jones, 1981; Lewan and Ruble, 2002; Peters et al., 2016). This van Krevelen diagram shows the range of kerogen Types studied in this work.

Lithium Isotope Measurements of Kerogen

Lithium is a valuable tracer of fluids because of its mobility during surface weathering and under hydrothermal conditions (Millot et al., 2010; Pistiner and Henderson, 2003). Lithium isotopes are commonly used for tracing lithologic sources that contribute Li to fluids (e.g., Misra and Froelich, 2012; Williams et al., 2013, 2015; Phan et al., 2016), as different sources have a range of Li isotope ratios (Fig. 2.2).

In this study, we measured Li isotopic compositions in kerogen using solid-state secondary ion mass spectrometry (SIMS), because it has been recognized that reagents (acids) used to isolate kerogen (or insoluble organic matter (IOM); Cronin et al., 1987) from sediments also react with organic functional groups in kerogen, thus altering their composition (Saxby, 1976). To demonstrate this, Williams and Bose (2018) extracted kerogen from the Lower Bakken shale using standard 5 N HF- 1 N HCl digestion

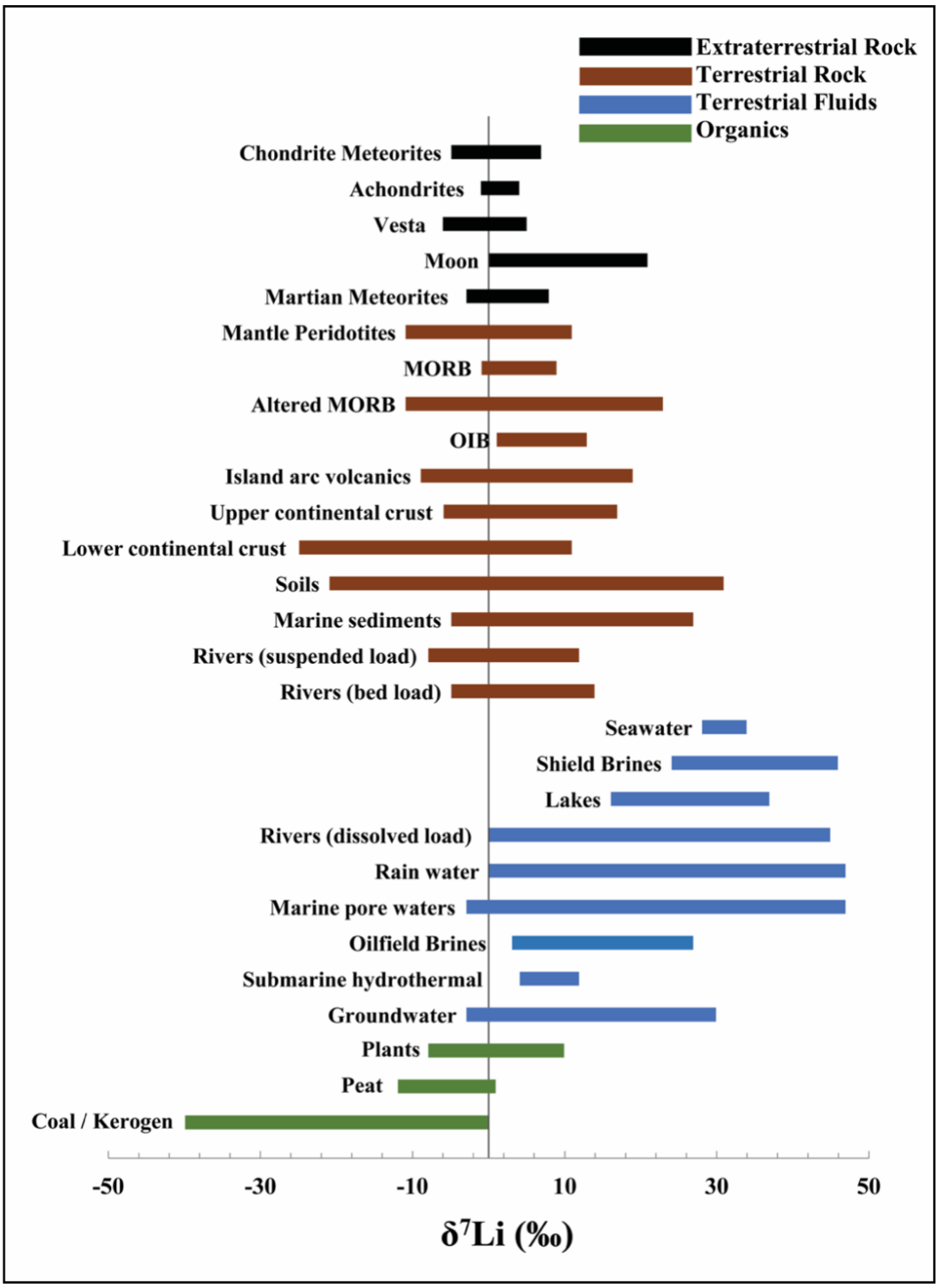

Figure 2.2. Natural variations in δ^7Li in literature (Bottomley et al., 2003, 1999; Chan et al., 2002; Clergue et al., 2015; Eccles and Berhane, 2011.; Lemarchand et al., 2010; Macpherson et al., 2014; Millot et al., 2011; Négrel et al., 2010; Penniston-Dorland et al., 2017; Phan et al., 2016; Tomascak et al., 2016). Coal/kerogenmeasurements are from this study and contain lower δ^7Li values than all other Li-reservoirs.

(Durand, 1980) and compared the $^{7}Li/^{12}C$ ratio of the acid treated IOM ($^{7}Li/^{12}C = 0.024 \pm 0.004$; n = 5) to unextracted kerogen in polished section ($^{7}Li/^{12}C = 0.244 \pm 0.020$; n = 6). This indicates an average loss of 90% Li from the acid treated kerogen. Furthermore, NanoSIMS *in situ* measurements were made (using a 300 nm spot size) of $^{7}Li/^{12}C$ on kerogen in an argon ion polished section of the same Bakken sample. This sample preparation makes it easier to avoid beam overlap with silicates, and the average $^{7}Li/^{12}C$ ratio on kerogen was even higher (0.414 ± 0.020; n = 11) confirming significant loss of organolithium in the acid treated IOM. To our knowledge, this study is the first survey of Li isotopes in kerogen that has not been isolated from silicates by acid treatments, which likely alters their Li isotopic ratios.

Methods

Samples

Powdered coal samples (< 0.25 mm) were obtained from the Pennsylvania State University (PSU) coal repository and the National Institute of Standards and Technology (NIST). The PSU samples included 8 Department of Energy Coal Samples (DECS) and 7 Argonne National Laboratory Premium Coal Samples (APCS). Additionally, 3 NIST coal samples, 4 coal samples from mines in the Rocky Mountain region of the U.S., and 4 hydrocarbon source rocks were acquired to extend the range of age, thermal grade and kerogen Types studied. The coal samples come from most of the major sedimentary basins in the U.S., range in VR_o from 0.25–5.19%, and in age from the Carboniferous to the Tertiary. Table 2.1 lists the samples studied and source rock data are shown in Table 2.2. Additional bulk coal samples were studied in thick polished sections for comparison

Table 2.1

Coal Data From the Penn. State Coal Repository and Lithium Isotope Data From This Study

			Coal Data									This Study		
Sample	State	Geologic Age	Ash dry %	V.M dmmf %	C dmmf %	H dmmf %	O dmmf %	N dmmf %	Vit %	VRo %	Li (ppm) USGS	δ7Li ‰ ± S.E.	Li/C *100	n
Argonne National Laboratory Premium Coal Samples														
1	PA	Carboniferous	13.18	30.1	88.08	4.84	4.72	1.60	71	1.16	15	–5.5 ± 2.7	2.8 ± 0.9	7
2	WY	Tertiary	8.77	48.5	76.04	5.42	16.90	1.13	89	0.32	3.9	–24.0 ± 5.0	0.8 ± 0.1	6
3	IL	Carboniferous	15.48	45.7	80.73	5.20	10.11	1.43	85	0.46	7.7	–25.9 ± 5.3	2.3 ± 0.5	9
4	PA	Carboniferous	9.25	40.8	84.95	5.43	6.90	1.68	85	0.81	8.9	–17.2 ± 4.3	4.2 ± 1.0	4
5	VA	Carboniferous	4.77	19.0	91.81	4.48	1.66	1.34	89	1.68	5.5	–21.9 ± 2.7	1.7 ± 0.6	3
6	UT	Cretaceous	4.71	47.8	81.32	5.81	10.88	1.59	86	0.57	5.5	–16.5 ± 2.1	4.3 ± 0.8	2
7	WV	Carboniferous	19.84	36.2	85.47	5.44	6.68	1.61	73	0.89	27	–14.0 ± 1.4	5.3 ± 1.2	6
8	ND	Tertiary	9.72	49.2	74.05	4.90	19.13	1.17	nr	0.25	2.7	nr	2.5 ± 1.0	
Department of Energy Coal Samples														
1	TX	Tertiary	15.81	55.5	76.13	5.54	15.78	1.50	78	0.36	nr	–15.7 ± 2.4	2.4 ± 0.6	13
3	CO	Cretaceous	5.37	28.2	87.78	5.85	4.03	1.76	94	1.28	nr	–4.6 ± 0.15	0.4 ± 0.1	4
6	UT	Cretaceous	5.84	46.9	81.72	6.22	10.10	1.56	69	0.66	nr	–16.5 ± 2.8	3.3 ± 0.3	4
21	PA	Carboniferous	11.15	3.9	91.87	3.91	2.92	0.81	87	5.19	nr	–39.4 ± 3.9	13.6 ± 1.5	10
22	PA	Carboniferous	23.27	37.8	88.64	5.75	3.03	1.86	30	0.77	nr	–12.5 ± 2.9	4.0 ± 0.6	4
25	MT	Tertiary	11.85	46.9	75.64	5.15	17.72	1.09	74	0.23	nr	–24.3 ± 4.5	1.7 ± 0.8	5
34	PA	Carboniferous	7.35	40.4	85.41	5.55	6.38	1.72	83	0.83	nr	–12.4 ± 6.3	2.3 ± 0.7	3
39	WY	Tertiary	8.03	64.6	74.75	5.43	18.87	1.01	84	0.3	nr	–25.9 ± 3.0	2.3 ± 1.2	5
National Institute of Standards and Technology Samples														
1632c *unrinsed*	PA	Carboniferous	7.16	nr	77.45	5.11	nr	1.50	nr	0.81	nr	–32.5 ± 7.7	2.0 ± 0.4	2
2682b	WY	Tertiary	6.32	48.5	68.43	4.88	16.24	nr	89	0.32	nr	–42.0 ± 7.0	0.4 ± 0.1	3
2684b	IL	Carboniferous	10.85	36.4	69.25	4.59	nr	1.45	nr	0.75	nr	–12.1 ± 4.6	2.8 ± 1.0	3
Additional coal samples					This Study									
San Juan	NM	Cretaceous	16.77	40.05*	69.90*	nr.	nr.	nr.	67.6	0.51	nr	–27.1 ± 5.6	2.0 ± 0.9	7
Four Corners	NM	Cretaceous	15.78	38.12*	70.30*	nr.	nr.	nr.	75.2	0.5	nr	–27.4 ± 0.1	1.9 ± 1.1	33
Savage	MT	Tertiary	4.89	47.26*	71.20*	nr.	nr.	nr.	32.8	0.27	nr	–27.6 ± 2.2	nr	2
Black thunder	WY	Tertiary	4.92	41.90*	72.71*	nr.	nr.	nr.	24.4	0.39	nr	–27.3 ± 1.7	0.2 ± 0.1	21

Chemical data (wt. %) is calculated moisture free; dmmf – Dry mineral matter free; S.E. – 1σ standard errors; nr - not reported; VRo- vitrinite reflectance; VM- volatile material; * indicates VM dry basis; Vit- Vitrinite % (Palmer, 1997; Vorres, 1990)

Table 2.2

Lithium Isotope Results for U.S Source Rocks of Different Organic Types

Sample	State	Age	VRo %	δ7Li ‰ ± S.E.	n	Organic Type
Hydrocarbon source rocks						
[1]Wilcox Fm. Lignite	TX	Lower Eocene	0.45	–19.8 ± 2.4	4	III
[2]Bakken Fm. Lower Bakken Mbr	ND	Mississippian	0.50	–8.8 ± 1.9	8	I/II
[3]Green River Fm.	WY	Eocene	0.65	–15.0 ± 3.6	4	I
[4]New Albany Fm. Blocher Mbr.	IL	Mississippian	0.95	–0.9 ± 2.2	8	II

Lithium isotope compositions determined by IMS-6f, where n= number of analyses on each sample; S.E. – 1s standard error; nr – not reported; VRo - vitrinite reflectance values %; VRo values for Wilcox, Green River and New Albany shales are estimated from: [1] Mukhopadhyay, 1994; [2] Canter et al., 2016; [3] Pawlewicz and Finn, 2002; [4] East et al., 2012; [4] Lewan et al., 1995; [4] Nuccio and Hatch, 1996.

to the powdered samples. These samples came from the Williston Basin (Montana), Powder River Basin (Wyoming) and San Juan Basin (New Mexico).

Two of the whole rock samples are from the Fruitland Fm. of the San Juan Basin and were selected specifically because of their high (up to 39 ppm) Li content (Bregg et al., 1998), relative to average sub-bituminous coals (6–7 ppm). Coal from the Powder River Basin was selected because of its low ash content, while the coal from Williston Basin was obtained to determine the reproducibility of Li isotope compositions of samples taken from separate locations within the same deposit (DECS-25 and the Savage Lignite).

Source rock shales (Table 2.2) were acquired from the US Geological Survey (Denver, CO) and were previously studied for B isotope compositions (Williams and Hervig, 2004). These rocks were selected to determine whether the Li isotopic composition varied with organic Type; Type I (Green River Fm.), Type II (New Albany Fm.), Type I/II (Bakken Fm. Lower Bakken) and Type III (Wilcox Fm.). The Green River Fm. (Type 1) is the type locality for lacustrine deposition (Bradley, 1931). The kerogen found in these deposits comes primarily from algal sources, with total organic carbon (TOC) up to 15.8% (Vandenbroucke and Largeau, 2007). The Type II New Albany Fm. Blocher member from the Eastern Interior Basin contains TOC up to 9.4% (Lewan et al., 1995) and represents a typical Type II kerogen marine shale, where planktonic organisms are the primary input (Vandenbroucke and Largeau, 2007). The Lower Bakken Fm. (Type I/II) from the Williston Basin has a variable TOC up to 35% (Jin and Sonnenberg, 2012) and contains inputs of both terrestrial and planktonic origin where it was deposited in an offshore ramp depositional environment (Albert, 2014). Wilcox Fm. (Type III) from the Gulf of Mexico Sedimentary Basin has a primary input

of higher plants and was deposited in a wide range of depositional environments (lagoonal, fluvial, and deltaic) (Nichols and Traverse, 1971). The Wilcox sample we analyzed is a lignite with >50% TOC.

Sample Preparation

To remove surface adsorbed Li on minerals and organic macerals, all samples were rinsed in 1.82% mannitol solution which was shown to complex with B(OH)3 (Hingston, 1964; Tonarini et al., 1997) for removal of surface adsorbed B. Mannitol also complexes with surface adsorbed Li(OH) and was shown to significantly reduce Li contents of clay separates (Williams et al., 2015). After sonication and soaking in mannitol 24 h., the samples were rinsed in triplicate using Nanopure water (18.5 MΩ-cm resistivity), centrifuged to settle, and dried at 60 ºC. Powdered samples were then pressed into round flat pellets using a Carver die press at 9000 psi for ~5 min. DECS-21 powder, with the highest VR_o (5.19%), was too brittle to press into a pellet and was instead pressed into indium for analysis. Source rocks and additional coal samples were made into polished thick sections. Samples were heated to 60 ºC overnight to remove surface volatiles for better vacuum in the SIMS instruments. To alleviate sample charging a thin conductive gold coat (20–50 nm) was applied to sample surfaces using a gold coater (Hummer 6.2 by Anatech Inc.).

Lithium Isotopes

The stable isotopes of Li include ^{7}Li that makes up 92.58% and ^{6}Li that makes up 7.42% of the natural abundance of Li (Meija et al., 2016). Stable isotope values are reported in per mille (‰) notation of the deviation from an accepted standard reference

material, which for Li isotopes is NIST SRM 8545 (LSVEC, Li-carbonate) with an accepted $^{7}Li/^{6}Li$ value of 12.0192 0.0002 (Flesch et al., 1973).

$$\delta^{7}\text{Li}\ ‰ = \left(\frac{R_{Sample} - R_{Standard}}{R_{Standard}}\right) \times 1000 \quad (1)$$

Where R = $^{7}Li/^{6}Li$

Secondary Ion Mass Spectrometry

Two different SIMS instruments, the Cameca Ametek Ion Mass Spectrometer (IMS-6f) and NanoSIMS 50 L (NanoSIMS) were used to obtain *in situ* Li isotopic ratios of samples. Both instruments have duoplasmatron sources which generate a plasma beam of O− ions. The primary beam is focused to a spot on the sample surface. This high energy ion bombardment sputters the sample surface ejecting ions, atoms, and electrons (Hervig, 1996). Positive secondary ions, such as $^{7}Li^{+}$ and $^{6}Li^{+}$, are transmitted through a series of lenses and apertures in the secondary column and separated by energy in an electrostatic analyzer. Ions are differentiated by their mass (m) to charge (z) ratio in the mass spectrometer and are detected using either an electron multiplier or faraday cup. For our analyses, all ions were detected using electron multipliers, calibrated using internal reference standards. Mass interferences must be eliminated by using energy filtering (for molecular interferences) or by adjusting the entrance and exit slits (or apertures) to the mass spectrometer to increase the mass resolving power (MRP = mass/Δmass). Primary interferences were $^{24}Mg^{2+}$ and $^{11}BH^{+}$ interfering with $^{12}C^{+}$. The $^{14}N^{2+}$ signal was easily resolved from ^{7}Li, and sufficient MRP was used on both instruments to resolve m/z interferences.

To determine the instrumental mass fractionation (IMF) we used several standard reference materials (NIST SRM 610, NIST SRM 612), and illite from the Clay Minerals

Society Source Clay Repository (IMt-1; www.clays.org). Each of these standards verified consistent values of IMF (mean daily S.E. ± 1.0‰, 1σ) and standard bracketing of unknowns, with one or more of these internal reference materials, was used to monitor instrumental drift during each analytical session (See Appendix A Fig. A.1).

SIMS measurements are subject to matrix effects, where ions sputter at different rates (cps) from different matrices (Burnett et al., 2015; Hauri et al., 2006; Seah and Shard, 2018). We acknowledge that compositional differences between standards and unknowns (e.g., silicates vs. organics) may lead to matrix effects on the ionization process, which could shift the isotopic ratios measured (Hauri et al., 2006). For example, Bell et al. (2009) found that changes in Mg-content of olivine affected the δ^7Li values by 1.3‰ per mole Mg substituted. There is not yet a kerogen standard with known Li isotopic composition verified by alternative analytical techniques. However, we suggest that δ^7Li values within a kerogen Type class (I, II or III) will be comparable as their major element compositions are similar (e.g., Ishida et al., 2018). Furthermore, we found no correlation between δ^7Li and the C-H-O contents of measured Type III kerogen in coals (Appendix A; Figs. A.6-A.8). There is also no standard for calibration of Li contents in kerogen matrices but the ^{7}Li/^{12}C intensity ratio can be used to compare relative abundances among similar phases (e.g., Type III kerogen).

IMS-6f analytical protocol. The primary beam current and ion optics determine the beam diameter and therefore the analysis spot size. For the IMS-6f, the duoplasmatron source generates a primary beam of O^- ions at −12.5 kV and the sample is held at +9.0 kV for a total impact energy of 21.5 kV. The spot size can be as small as a few microns (~5 μm) in diameter, but in samples with low Li content, higher currents

were necessary to provide enough Li^+ secondary ions counts for statistical significance. Generally, a 5–20 nA primary current yielding a beam diameter of<50 μm was used for spot analyses on all samples measured by IMS-6 f. Ions with an energy range 20 eV were allowed into the secondary magnet where the magnetic field can be adjusted to select the m/z of interest. For the IMS-6f analyses, each sample was analyzed on multiple spots as indicated in Tables 2.1 and 2.2 (n = 2 to 33). The IMF measured before and after analysis of unknowns was used to correct the raw isotope ratios.

NanoSIMS analytical protocol. A duoplasmatron source was also used for NanoSIMS measurements, generating a plasma beam of O^- ions at −8 kV. The sample is held at +8 kV for a total impact energy of 16 kV. The NanoSIMS design uses a smaller primary beam of tens to hundreds pA of O^-, to achieve greater spatial resolution than the IMS-6 f. The advantage of NanoSIMS is the ability to make ion images of the distribution of isotopes over a small area (typically 5–25 μm^2) and at a greater spatial resolution. This allows spatial separation of measurements in the kerogen matrix avoiding silicate minerals (e.g., clays) in the kerogen matrix.

For the NanoSIMS analyses, ion maps were made in the imaging mode by rastering the beam over 25 μm^2 areas to measure the distribution of $^7Li^+$, $^{12}C^+$ and $^{30}Si^+$ (cps). Images were taken at two different pixel resolutions (256 × 256 and 512 × 512) and varying spatial resolutions with beam diameter ranging from ~300 nm to 2 μm (3 pA – 500 pA primary current). All images were taken with a counting time of 1000 μs/pixel. NanoSIMS real time imaging was used in conjunction with the ion maps to pinpoint regions of interest (ROI) within the rastered area where the $^{12}C^+$ or $^{30}Si^+$ signals were high. Maps of $^{14}N^+$, $^{24}Mg^+$, $^{39}K^+$, and $^{40}Ca^+$ ions were also made to help identify the

matrix being measured, e.g., determining if a spot with relatively high $^{12}C^{+}$ counts was kerogen or a carbonate mineral, differentiating K-bearing clays vs. quartz, and to confirm that the $^{24}Mg^{2+}$ m/z was not interfering with the $^{12}C^{+}$ m/z measurements. Using a primary beam current of 100–500 pA with a beam diameter of 1–3 μm we measured Li isotopic ratios in areas of high-$^{12}C^{+}$ versus high-$^{30}Si^{+}$ (cps). Using this protocol, we were able to separate analyses of kerogen and silicate phases and acquire their Li isotopic compositions at high spatial resolution.

Results

A histogram of all measurements of δ^{7}Li by IMS-6f and NanoSIMS instruments for coals and source rocks is shown in Fig. 2.3. Multiple SIMS measurements on each sample were averaged and are summarized in Tables 2.1 and 2.2. The individual analyses and statistical evaluation can be found in Table A.1. The δ^{7}Li values measured are mostly <0‰, except where analyses possibly overlapped silicates. We also characterized spot measurements according to their $^{12}C/^{30}Si$ ratios and defined Si-rich areas where $^{12}C/^{30}Si$ < 1.0, while C-rich areas ranged from $^{12}C/^{30}Si$ = 1 to 12,000. For Si-rich areas (n = 28) the average δ^{7}Li is −7.3 ± 1.7‰, and for C-rich areas (n = 130) the average δ^{7}Li is −23.6 ± 1.1‰ (Fig. A.9). Each coal sample (Table 2.1) was measured in multiple spots (n = 2–33) and the mean and standard error of the mean for all analyses on each sample is plotted in Fig. 2.4. The variability in measurements from spot to spot within a single sample may be due to heterogeneity of the various organic macerals, beam overlapping multiple phases (kerogen and silicates), sample charging, or surface roughness of pressed powders. Nonetheless, the average analytical error on each spot analysis was 1.1‰ (1σ) which is far less than the observed range of values (Appendix A; Table A.1).

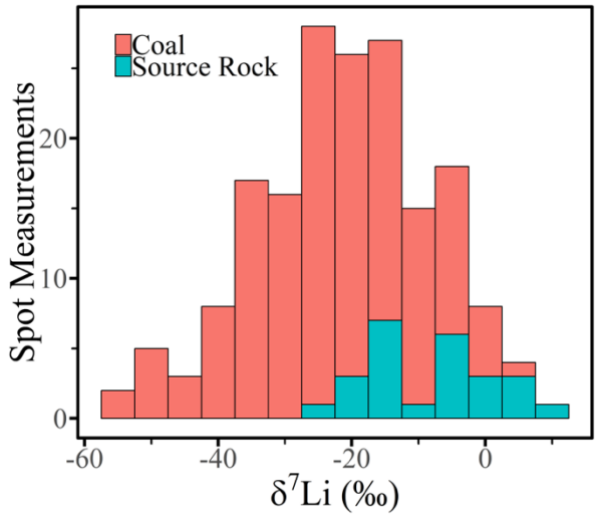

Figure 2.3. Histogram of all IMS-6f and NanoSIMS spot measurements taken on coal and source rock samples. Coal samples generally had lower δ^7Li than source rocks which may be because of beam overlap of kerogen and silicates during source rock measurements.

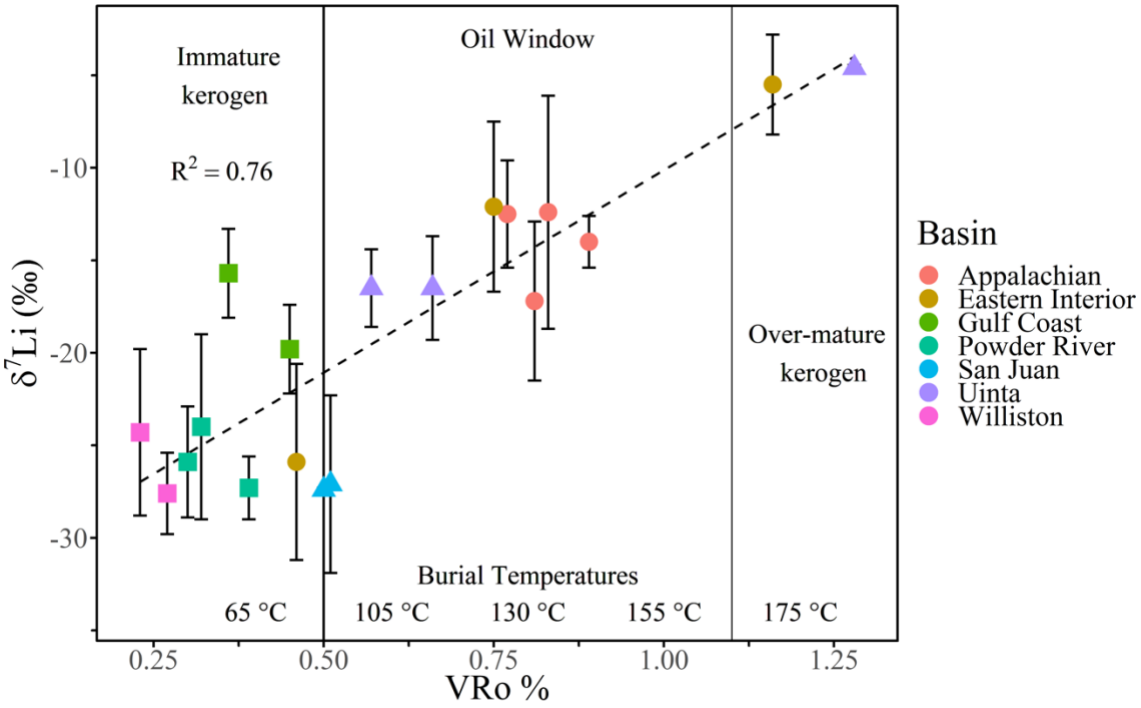

Figure 2.4. Vitrinite reflectance in oil (VR_o %) is plotted against the Li isotope ratios of coal samples. Each point represents the mean value for multiple (n) measurements of a single sample. Error bars indicate 1σ standard error of n analyses (see Table 2.1; all data shown in Table A.1). Two samples have error bars smaller than the point. Burial temperatures were estimated based on VR_o % (Barker and Goldstein, 1990; Bostick, 1979; Burnham and Sweeney, 1989). Symbols indicate age; Tertiary (squares), Cretaceous (triangles) and Carboniferous (circles). There is a positive correlation between δ^7Li and VR_o % of measured coals.

The source rock samples from the Green River Fm., New Albany Fm. and Wilcox Fm were measured by IMS-6f and the Lower Bakken shale sample was measured by both IMS-6f and NanoSIMS. Given the range of VR_o values reported for these source rocks (Table 3.2), the more thermally mature New Albany shale has the highest δ^7Li values, while the less mature source rocks have lower δ^7Li values on average. Spot analyses in the Green River Fm. (Type I) showed a correlation ($R^2 = 0.93$) between $^7Li/^{30}Si$ ratios and $^{12}C/^{30}Si$ ratios (Fig. 2.5) with isotopically lighter values observed in C-rich spots.

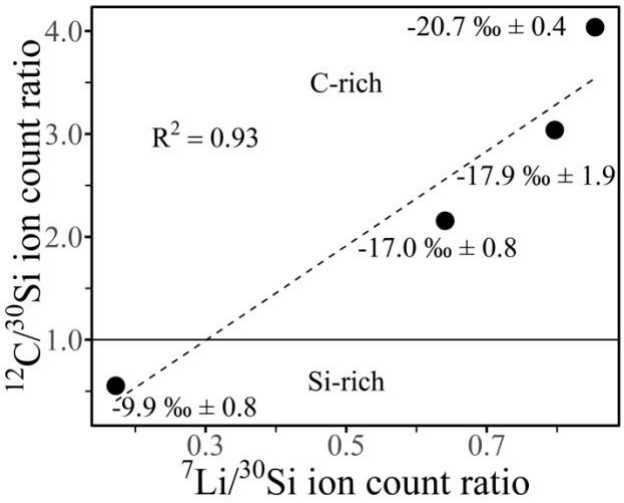

Figure 2.5. Measurements on Green River Shale sample using IMS-6f. The δ^7Li values are indicated beside each analysis. C-rich spots are isotopically lighter than Si-rich spots. Standard errors are smaller than the symbols.

NanoSIMS Imaging of Bakken Shale

NanoSIMS ion maps and nanometric spot measurements of $^6Li^+$, $^7Li^+$, $^{12}C^+$, $^{30}Si^+$, were made on immature (VR_o 0.5%) samples of the Mississippian Lower Bakken Shale to discriminate isotopic differences between kerogen and mineral matrices (Fig. 2.6). Regions of interest (ROI) circled in white had high C counts and ROI circled in red had high Si counts, relative to other regions in that image, and were selected for precise spot

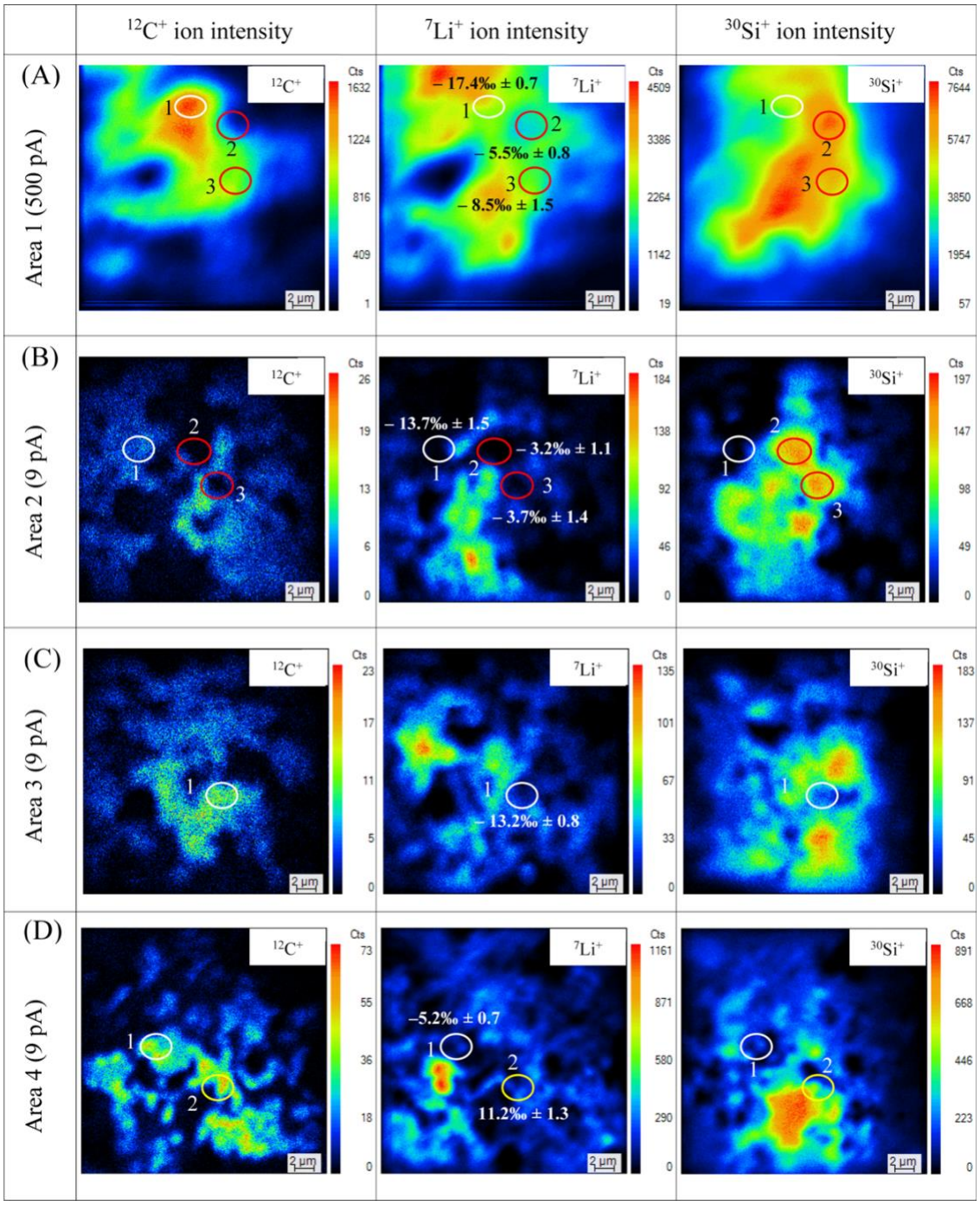

Figure 2.6. Ion maps of $^{12}C^+$, $^{7}Li^+$, and $^{30}Si^+$ on 25µm^2 areas of the immature (VR_o 0.5 %) Lower Bakken shale. Area 1 used a 500 pA primary beam, Areas 2-4 used a 9 pA beam to increase spatial resolution, at the expense of secondary ion counts. One scan was taken for all images apart from Area 4 (Fig. 2.6D) which is an accumulation of 20 scans which were corrected for drift and summed. Circled areas show high ^{12}C (white), high ^{30}Si (red) or mixed ^{12}C and ^{30}Si (yellow) spots where δ^7Li measurements were made; values shown on the ^{7}Li-map. ROI with high ^{12}C have lower δ^7Li values than high ^{30}Si ROI.

analyses of Li isotopes. The δ^7Li values are labeled next to each ROI on the $^7Li^+$ ion maps. Regions dominated by ^{12}C, generally showed lower δ^7Li values than regions with higher $^{30}Si^+$ counts. One isotopic measurement (Fig. 2.6D; spot 2) had a positive value (+11.2‰) and notably the $^7Li^+$ in this region was spatially correlated with $^{39}K^+$ ions. This suggests that the isotopically heavy Li was from a K-bearing mineral (e.g., feldspar or clay).

Discussion

Coal Survey of δ^7LI

Few studies have examined the organic vs. mineral hosts of Li in coal, although some bulk measurements of Li in coals have reported that Li is hosted by the silicates or "ash" portion (Finkelman, 1980; Dai et al., 2012). Our *in-situ* study of Li in coals shows no correlation between δ^7Li and the contents of elements commonly associated with ash (Si, Al, K) for measured APCS and DECS coals (Appendix A; Figs. A.3-A.5). Swaine (1990) stated that Li is partly associated with organic matter, and Finkelman et al. (2018) later reported up to ~50% of Li in immature coals may be associated with organic material. Terrestrial plant matter that is the primary component of coals is one possible source of organolithium compounds. Gough et al. (1977) found the Li content of plants to be positively correlated with the Li content of the soils in which they grew. Li has a varying toxicity threshold among plants depending on the species, yet plants contain trace amounts of Li (0.01–31 ppm) on average (Pendias and Kabata-Pendias, 2000). Leguminous plants grown in Li rich soils (9–175 ppm) in New Zealand are reported to contain up to 143 ppm Li (Pendias and Kabata-Pendias, 2000). Beets can take up even higher amounts of Li (up to 5500 ppm) from Li-rich soils and have been proposed for

agro-mining (Kavanagh et al., 2018). Even though Li is present in small concentrations in most plants, it can become concentrated during the formation of kerogen due to the breakdown of biomolecules and consolidation of plant material during burial and lithification. Littke and Leythaeuser (1993) found that a 1-m thick layer of peat generates ~20 cm of bituminous coal, therefore 3 ppm Li in peat can produce a coal with 15 ppm Li.

The range of Li isotopes published for various terrestrial and extraterrestrial samples is summarized in Fig. 2.2 (Clergue et al., 2015; Lemarchand et al., 2010; Négrel et al., 2010; Penniston-Dorland et al., 2017; Tomascak et al., 2016). The coals measured in this study represent the lowest δ^7Li values measured, typically<0‰ for the most organic-rich samples. This range of δ^7Li values is similar to the range of δ^{11}B values measured on these same coal samples (Williams and Hervig, 2004). The low δ^7Li values in low rank coals suggest that immature organic macerals in the coal are enriched in ^{6}Li compared to most rocks, minerals and waters evaluated in the global geochemical cycle (Fig. 2.2).

Consistent with our Li isotope results for kerogens, other studies of Li isotopes in organic materials have reported isotopically light δ^7Li values. Lemarchand et al. (2010) found forest soil solutions as well as fir tree needles, branches and roots to δ^7Li values lower (−5 to −17‰) than the parent granite (+0.3‰), soil (+0.7 to +3.3‰) and stream waters (+5 to +20‰) in a forested granitic catchment in France. Another study on peat from the Massif Central in France (Négrel et al., 2010) reported δ^7Li values of −11 to 0‰.

Only two studies have reported δ^7Li of coal constituents. Harkness et al. (2015) measured δ^7Li values from −7 to +12.8‰ for aqueous leachates of the inorganic constituents of coals from the Powder River, Appalachian and Eastern Interior basins. He et al. (2019) used microwave digested coal samples from the high Li, (> 500 ppm) Guanbanwusu mine (China) and reported δ^7Li values from +6 to +8‰ on residues measured by ICP-MS. The anomalously high Li contents of this coal have been shown to be positively correlated with the ash content suggesting secondary Li enrichment from a hydrothermal source (Sun et al., 2012b). Therefore, the somewhat heavier lithium isotope compositions reported for this Guanbanwusu coal are likely controlled by the silicate hosted minerals.

Our results show a clear positive correlation ($R^2 = 0.76$) between δ^7Li of coals and thermal maturity as indicated by VR_o (Fig. 2.4). Low rank coals ($VR_o < 0.5\%$) have the lowest δ^7Li values (average − 23.4 ± 1.1‰) and the Li isotope composition becomes heavier (up to −5‰) with increasing rank up to VR_o ~1.3% (bituminous), irrespective of age and depositional environment (Table 2.1). The observation that δ^7Li values of kerogen in coals become higher as thermal maturity increases may be interpreted as either a preferential release of ^{6}Li to pore fluids as temperature increases, or an uptake of ^{7}Li from hydrothermal fluid during thermal maturation. However, no clear correlation was observed between Li/C and either VR_o or δ^7Li (Fig. A.2). Given that these samples each come from many different sedimentary basins of varying geological ages, they each have their own initial Li contents and diagenetic histories that would affect the Li/C ratios. Kerogen from different ages spanning 300 Myr may come from plants with varying Li contents. Considering that a positive trend is shown among all coals studied, it

is most likely that the trend reflects a preferential loss of ^{6}Li rather than incorporation of exogenous ^{7}Li. While hydrothermal Li certainly influences some basins (e.g., Dai et al., 2012), if this were the case ubiquitously, we would expect higher Li/C ratios in hydrothermally influenced (more mature) samples, which is not observed.

The trend of increasing $\delta^{7}Li$ with thermal maturity is consistent with a previous study showing ^{6}Li enrichment in authigenic clays associated with the migration of gas into the Wattenberg gas field, Denver Basin (Williams et al., 2015). That study proposed that ^{6}Li preferentially leaves organolithium compounds during gas generation from kerogen (VR_o > 1.5%). Different kerogen Types generate hydrocarbons (oil and gas) over a range of burial temperatures. The 'oil window' spans a VR_o range from 0.50 to 1.35% (Hunt, 1996; Mukhopadhyay, 1994; Peters and Cassa, 2007; Pittion and Gouadain, 1985; Taylor et al., 1998; Tissot et al., 1987; Tissot and Welte, 1984). On the other hand, Type III kerogen (coals) have an effective 'oil window' at VR_o values of 0.65–2.0% with gas generation dominant above VR_o 1.5% (Petersen, 2006). The trend in $\delta^{7}Li$ values of coals (Fig. 2.4) clearly coincides with the temperatures of hydrocarbon generation from kerogen, supporting a preferential release of ^{6}Li to hydrocarbon-related fluids.

Interestingly, we measured two over mature samples APCS-6 from UT (VR_o 1.68%) and DECS-21 from PA (VR_o 5.19%) that fell off the trendline demonstrated by other coals. These samples show very low $\delta^{7}Li$ values (-22 ± 0.8 and -39 ± 4.0‰, respectively; Table 2.1). Clearly at very high temperatures, the coal remaining is largely residual C and ash. It is possible that at very high thermal maturity, most of the organolithium compounds have been degraded (released) during hydrocarbon generation, and that any remaining Li is hosted by silicates, or residual C.

Hydrocarbon Source Rocks

Oil and gas are generated from source rocks at temperatures between ~60–150 ºC, generally at burial depths from 1 to >4 km. The hydrocarbons can be expelled from source rocks and migrate along pathways through permeable rock into structural and stratigraphic traps, forming conventional hydrocarbon reservoirs. Black shale source rocks can also host oil and gas forming unconventional reservoirs. Therefore, a distinctly light Li isotopic composition of pore fluids, suggesting influx of hydrocarbon-sourced Li, may be useful in identifying productive intervals of a shale. We studied several well-known hydrocarbon source rocks to compare the Li isotopic compositions of their different kerogen Types.

It was recognized while measuring source rocks with the IMS-6f instrument, that the large (up to 50 μm) primary ion beam diameter on the IMS-6f and the predominance of silicates over kerogen in source rocks influenced analyses where kerogen and silicate analyses overlapped. This resulted in slightly more positive δ^7Li values in the shale source rocks than coals (Fig. 2.3), which are dominated by carbonaceous material (ASTM Committee, 2019), thus decreasing overlap on minerals. Primary beam overlap on silicates was avoided using the NanoSIMS on the Bakken shale sample, so that Li isotope measurements could be compared between kerogen and mineral phases (Section 3.1). The Mississippian Lower Bakken shale was studied in detail because it is a Type I/II source rock with high total organic carbon (up to 35 wt%; Jin and Sonnenberg, 2012). NanoSIMS maps of the Bakken shale (Fig. 2.6) and IMS-6f measurements of Green River Fm. (Fig. 2.5) showed that the C-rich areas have isotopically lower δ^7Li values than Si-rich areas of the source rocks. Like the coal measurements, immature kerogen in

source rocks contains isotopically light Li (Table 2). The general trend for source rock kerogen similarly shows δ^7Li values increasing with thermal maturity over the temperature range of oil and gas generation.

Implications for Li Geochemical Cycles

The results presented here support the idea that Li derived from kerogen can be used to trace organic-related fluids because the Li isotopic composition of pore waters from kerogen should be lighter than most other natural waters (Fig. 2.2). Oilfield brines generally range from δ^7Li +4 to +16‰ (Eccles and Berhane, 2011; Macpherson et al., 2014; Millot et al., 2011; Phan et al., 2016), except where evaporative processes enrich the brines in ^{7}Li (Chan et al., 2002) (Table A2). These brines are lighter than seawater (δ^7Li ~ +31‰) (Chan and Edmond, 1988; Misra and Froelich, 2012), rivers (mean = +23‰), and lakes (+17 to +36). Hydrocarbon-related fluids contain elevated contents of many organically derived trace elements (e.g., Li, B, N) and many of these elements are substituted into authigenic clays that form under diagenetic conditions affecting coals and hydrocarbon sources (Williams et al., 2012, 2013, 2015). Given that up to 50% of Li in immature coals may be associated with kerogen (Finkelman et al., 2018) and the observation that more mature bituminous coal contains Li associated with the silicates (ash) (Finkelman et al., 2018), we hypothesize that the Li is released from dispersed organic matter and becomes concentrated in authigenic clays. Among coals surveyed by Finkelman et al. (2018), 6 immature coals contained on average only ~6 ppm Li while 14 bituminous (mature) coals contain on average 44 ppm Li. If Li accumulates in porefluids during burial, then the porefluids become enriched in the Li released from organolithium complexes in the source kerogen (Fig. 2.7).

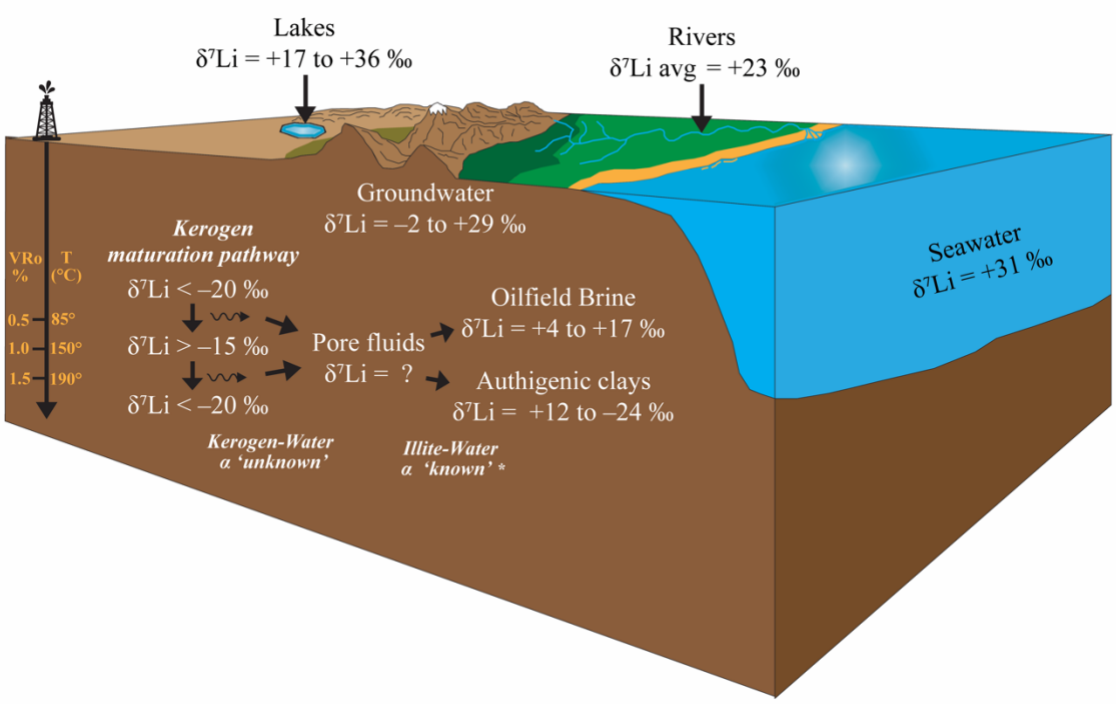

Figure 2.7. Schematic diagram summarizing δ^7Li‰ values measured in this study* compared to other fluid reservoirs. The temperature scale (left) indicates the 'oil window' (VR_o from 0.5 to 1.5%) where heavier δ^7Li‰ values may include exogenous Li in nanopores. In general, Li released from kerogen is enriched in ^{6}Li, as reflected by isotopically light oilfield brines. The distinctly light isotopic compositions derived from kerogen can be incorporated into authigenic clays to trace organic inputs to fluids. (Sources: this study; Macpherson et al., 2014; Penniston-Dorland et al., 2017; Tomascak et al., 2016; Williams and Hervig, 2005*).

The isotopic fractionation as Li is released from organic compounds in kerogen to pore fluid is unknown, but the isotopic fractionation of Li between water and authigenic clays (smectite-illite) is well-known (Wunder et al., 2007; Vigier et al., 2008; Williams et al., 2012). Therefore, where temperatures can be constrained, assuming equilibrium conditions, the Li isotopic composition of the fluid can be calculated. For example, the δ^7Li of the high Si area in the Bakken shale (Fig. 2.6; Area 1; ROI-2) gave a value of −5.5‰. High ^{39}K in this area suggests that this may be illite (or possibly a detrital

feldspar). Using the isotopic fractionation equation determined for illite-water fractionation:

$$1000 \ln \alpha = 6.15 - 0.07(1000/T\ (K)) \quad (2)$$

(Williams et al., 2012) and estimating a temperature ~ 80 °C based on the vitrinite reflectance of the Bakken immature kerogen, one can calculate a pore fluid δ^7Li value of +14.5‰, which is in the range of other natural ground waters (Fig. 2.2). Realistically, the measured δ^7Li measured (Fig. 2.6; Area 1; ROI-2) includes interlayer Li in addition to structurally bound Li in the clay, so this value may be slightly heavier than the water that equilibrated with the authigenic clay (Williams et al., 2015). Evaluating the isotopic fractionation of Li between kerogen and water will be useful in refining the potential use of Li isotopes for tracing hydrocarbon migration paths through organic-rich shales.

Another important implication for this work is its impact on interpretations of continental weathering based on δ^7Li values. For example, the Li isotopic composition of seawater over the Cenozoic era has been interpreted to have been lighter in the past due to high rates of continental weathering based on the δ^7Li of foraminifera (Misra and Froelich, 2012) and other biogenic carbonate (Sun et al., 2018). While the trend of decreasing δ^7Li in foraminifera over the Cenozoic era is robust, the effects of diagenesis on the re-equilibration of carbonate δ^7Li with diagenetically altered fluids, might warrant reconsideration in light of our data showing distinctly light Li isotopic compositions of kerogen. It is possible that increased nutrient supplies to the ocean, associated with high erosion rates, caused eutrophication and hypoxia, and these conditions led to preservation of sedimentary organic matter (Gallois, 1976; Liu and Wang, 2013; Loftus and Greensmith, 1988). Therefore, the low δ^7Li values recorded by deeply buried forams,

where diagenesis is likely, may be reflecting the isotopic composition of organic-derived Li on paleofluid compositions. Understanding the exchange of Li between organic matter, fluids and minerals in sedimentary basins contributes not only to our understanding of hydrocarbon generation and migration, but also to the evaluation of Li sources important to the global Li geochemical cycle.

Conclusions

Our survey of Li isotopic compositions in organic rich rocks of varying depositional environment, age, and thermal maturity leads to the following insights:

1. Immature kerogen measured in this study has a lighter Li isotopic composition than any other crustal material (mineral or fluid) yet reported.
2. With increasing thermal maturity, from immature to mature (up to VR_o 1.3%), the δ^7Li values of kerogen increase. We conclude that ^6Li is preferentially released from the organic matrix to pore fluids during thermal maturation.
3. The organic matrix in hydrocarbon source rocks has a lighter Li isotopic composition than the silicate matrix.
4. If Li released from kerogen is isotopically light relative to most pore fluids, then the uptake of Li from these fluids by authigenic clays will record the isotopically light Li related to hydrocarbon generation.
5. The recognition of isotopically light Li derived from organic sources could impact interpretations of continental weathering and should be further investigated for its significance in the global geochemical cycle.

CHAPTER 3

SECONDARY ION MASS SPECTROMETRY REFERENCE MATERIALS FOR LITHIUM IN CARBONACEOUS MATRICES

Abstract

Secondary Ion Mass Spectrometry techniques are used to study trace elements in organic samples where matrix compositions vary spatially. This study was conducted to develop calibrations for Li-content and Li-isotope measurements in kerogen. Known concentrations of Li ions (^{6}Li and ^{7}Li) were implanted into organic polymers, with a range of H/C and O/C ratios similar to kerogen, along with glassy carbon (SPI Glas-22) and silicate glass (NIST SRM 612). Results show that Li-content calibration factors (K*) are similar for carbonaceous samples when analyzed using a 5 kV secondary ion accelerating voltage. Using a 9 kV secondary ion accelerating voltage, K* factors are negatively correlated with the sample O-content, changing ~30% between 0 and 15 oxygen atomic %. Thus, to avoid the matrix effect related to O-content, using a 5 kV secondary ion accelerating voltage is best for quantification of Li-contents based on $^{7}Li^{+}/^{12}C^{+}$ ratios. Under these analytical conditions Li ppm (atomic) = (132 (±8) * $^{7}Li^{+}/^{12}C^{+}$) * ^{12}C atom fraction of the sample measured. Lithium isotope ratio measurements of SPI Glas-22 and NIST SRM 612 are within error; however, the organic polymer samples as a group show a 10‰ higher δ^{7}Li than NIST SRM 612.

Introduction

Lithium matrix effects, defined as the variable instrumental sensitivity due to differences in matrix chemistry, have been identified in several secondary ion mass spectrometry (SIMS) studies of silicate mineral and glass matrices (e.g., Wilson and Long, 1982, Hervig et al. 2004, Kasemann et al. 2005, Jeffcoate et al. 2007, Bell et al. 2009); however no previous SIMS studies have attempted to quantify Li-content and Li-isotopic ratios in carbonaceous matrices. Lithium derived from organic sources has been largely overlooked in the Li geochemical cycle until recently (Lemarchand et al. 2010, Williams et al. 2013, 2015). Teichert et al. (2020) reported that Li-isotopic ratios ($^{7}Li^{+}/^{6}Li^{+}$) in kerogen from coal increased linearly with thermal maturity. That study prompted this research to develop appropriate SIMS reference materials for the determination of Li-content in organic matrices and to evaluate potential matrix effects on Li-isotope ratio measurements.

Isolating kerogen from mineral matter in coal and other hydrocarbon source rocks using acids alters the Li-content and isotopic composition (Williams and Bose, 2018). Therefore, we used dynamic SIMS for an *in-situ* study of Li in kerogen. SIMS generally requires matrix matched reference materials for interpreting ion ratios. Consequently, the objective of this study was to quantitatively implant Li into a suite of organic polymers with different C-H-O contents, allowing their use as SIMS reference materials for Li-content and Li-isotopic composition in organic matrices.

SIMS Matrix Effects and Ion-Implant Reference Materials

In SIMS analyses, secondary ions undergo instrumental mass fractionation (IMF) during sputtering, ionization, and transmission through the instrument (Wilson et al.

1989). Sputtering and ionization are the only sample dependent fractionation processes and measuring different matrices can result in a deviation of ion yields by more than two orders of magnitude in synthetic materials (Andersen and Hinthorne, 1972, Deline et al. 1978a, Williams, 1979a). While the physics of sputtering and ionization processes has been evaluated (e.g., Williams, 1979b), an all-encompassing sputtering/ionization theory that can correct for matrix effects is unavailable. Therefore, to quantify elemental abundances of materials via SIMS, matrix-matched reference materials are best. Similarly, for isotopic analysis, matrix matched reference materials should be used to avoid misinterpretation of measured ion ratios (e.g., Isa et al., 2017).

Because of the difficulty of preparing homogeneous solid-phase samples the use of quantitative ion implantation into a matrix similar to the unknown was developed as a means of preparing reference materials in the 1970's. Researchers studying solar wind implantation used artificial ion implantation to quantify surface concentrations of solar wind implanted elements in a lunar sample (Zinner and Walker 1975, Zinner et al. 1976). Deline et al. (1978a) investigated the ion yields of five materials (C, Si, Ge, GaAs, Sn) implanted with B, C, O, F, P, As and Sb. They found the ion yields of a given species changed by up to three orders of magnitude depending on the substrate into which the ions were implanted, demonstrating the need for matrix-matched reference materials for quantification of SIMS measurements. For geological samples, implant reference materials have been used to quantify hydrogen, carbon and oxygen in trapped glass inclusions in volcanic rocks (Hervig et al. 2003, Regier et al. 2016); hydrogen in terrestrial diamonds (Kaminsky et al. 2020); nitrogen in upper mantle minerals (Li et al. 2013); and chromium in carbonates (Steele et al. 2017). Burnett et al. (2015) recently

reviewed the key parameters for preparation of implant reference materials and methods for implant calibration of geological samples. They demonstrated how to quantify the trace Li-content in melilite samples by implanting the minor isotope ^{6}Li directly into the mineral at a known concentration and then measuring both ^{7}Li and ^{6}Li. The terrestrial abundance ratio of ^{7}Li /^{6}Li then allowed calculation of the ^{7}Li abundance from the known ^{6}Li implant fluence. Williams et al. (1983) first demonstrated this technique by implanting deuterium into hydrogenated amorphous silicon films to determine their H-content. Franzreb et al. (2004) later demonstrated the use of ^{18}O implants to quantify major levels of oxygen in silicon sputtered by $^{16}O^{-}$ primary ions while backfilling the analysis chamber with various amounts of O_2.

The creation of an implant reference material is achieved by using an ion implanter to generate a high energy (10 – 200 keV) ion beam (0.3 to 0.6 cm beam diameter) of an isotope of interest and rastering that beam over the surface of the sample to implant a user-defined and uniform areal density (atoms/cm^2) and depth of the implant species. The implant results in an approximately Gaussian, subsurface distribution, which allows it to be clearly distinguished from any intrinsic (uniform) level of the same species. Following ion implantation, the depth profiling capabilities of SIMS instruments allow the shape of the implant profile to be determined. The implant profile, together with a measurement of the analysis crater depth using a profilometer, is used to determine the concentration (atoms/cm^3) integrated over the implant depth. This procedure will only work well if the sample being implanted is relatively homogeneous. The atomic density of the implanted species can be related to the ion intensity by calculating a content

calibration factor (section 2.2.1), which can be used to quantify the concentrations of elements in an unknown sample.

The use of ion implantation to create an isotopic calibration to detect isotope matrix effects is much less mature. Williams et al. (1983) used ion implantation to create an isotopic reference material by implanting a silicon wafer with HD^+ ions to produce identical doses of H and D (^2H) to determine the isotope fractionation between H^- and D^- secondary ions. Results showed that the fractionation factor for low energy H^-/D^- secondary ions was 1.32 ± .01; for high-energy H^-/D^- and for $^{30}SiH^-/^{30}SiD^-$ the fractionation was much smaller: undetectable for H^-/D^- and 0.95 for SiH^-/SiD^-, both with an uncertainty of 3%. More recently, Burnett et al. (2015) separately implanted two isotopes of the same element, ^{25}Mg and ^{26}Mg in order to quantify isotopic compositions.

Matrix Effects Due to the Presence of H and O

Perhaps the most important analytical advancement for the study of biological and other organic materials by SIMS techniques was the development of the NanoSIMS 50L (Cameca-Ametek) which has been used widely in the measurement of biomaterials and other organics (Nuñez et al. 2017). The NanoSIMS is particularly suited to the measurement of biological samples at the cellular level due to its small primary beam size (down to ~50 nm), its multi-collector detection, and chemical imaging capabilities. Despite the growing body of literature containing SIMS data from organic materials, absolute quantification of chemical abundances and the determination of matrix effects related to variable concentrations of H or O in carbonaceous materials remain scarce in comparison with studies of inorganic materials. Researchers studying Archaean and Proterozoic organic matter with a primary focus on identifying bio-signatures using

carbon isotopes have led the way in quantifying matrix effects in organic matter. SIMS reference materials of graphite (Mojzsis et al. 1996, Farquhar et al. 1999), diamond (Kaufman and Xiao, 2003) and pyrobitumen (Fletcher et al. 2008) have been used in these studies. For carbon isotopes, House et al. (2000) suspected a matrix effect in an algal coal that showed a 10 ‰ different $\delta^{13}C$ IMF than graphite compared to bulk measurements. Orphan et al. (2001) found more than a +10 ‰ $\delta^{13}C$ matrix effect between microbial cell biomass and graphite. House et al. (2000) reported a <1 ‰ variation in $\delta^{13}C$ among kerogen matrices with a range of H/C atomic ratios (0.12 to 0.79) while Sangély et al. (2005) detected up to a 5 ‰ matrix effect associated with a larger H/C range (0.04 and 1.74), with higher H contents resulting in lower $\delta^{13}C$ values.

The presence of H and O in inorganic materials has also been found to cause matrix effects, e.g., Hauri et al. (2002, 2006) discovered that as the H_2O content of high-silica glasses increased, the D^-/H^- ion ratio decreased (after correction for absolute D/H content). The same effect was reproduced recently (Befus et al. 2020), confirming the non-linear influence of increasing H_2O on the D^-/H^- ion ratio. In another study (Othmane et al. 2015) variable H_2O content of turquoise minerals was shown to be partially responsible for a variation of up to 20 ‰ in δD and 7 ‰ in $\delta^{65}Cu$. These effects are important because H and O are abundant in most carbonaceous compounds and their contents vary widely. Our goal in this study is to evaluate how the presence of H and O atoms present in organic matrices affect the sputtering and ionization of Li.

Experimental

Ion Implantation

Figure 3.1 shows a Van Krevelen plot for organic source rock Types (Van Krevelen, 1950, 1961) indicating the range of H/C and O/C compositions of the organic polymers studied relative to the range of different kerogen types and macerals (Van Krevelen, 1950, 1961, Van Krevelen et al. 1957).

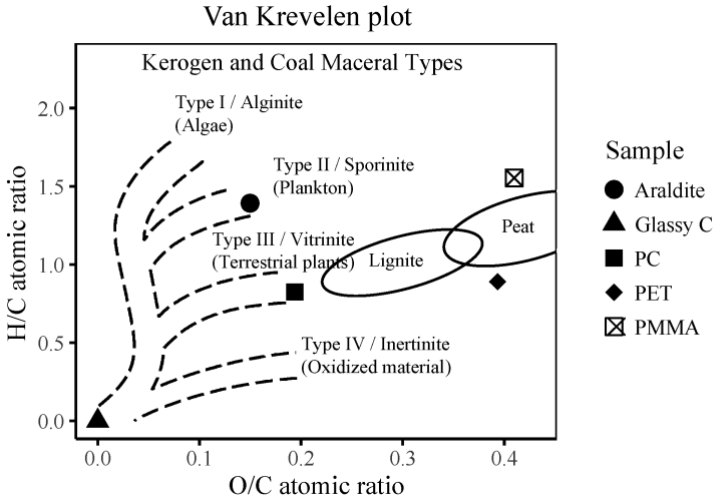

Figure 3.1. H/C and O/C ratios for polymer and glassy carbon samples used in this study are plotted relative to types of kerogen and kerogen macerals commonly found in coal (Van Krevelen 1950, Van Krevelen and Schuyer 1957). Modified from Van Krevelen (1961) and McCarthy et al. (2011).

A variety of chemically homogeneous organic polymers were obtained from industrial suppliers (Table 3.1) for comparison to a pure glassy carbon (SPI Glas-22) and a silicate glass reference material (NIST SRM 612). The elemental abundances of C and H in the polymers were verified using a Perkin Elmer 2400 Series 2 CHNS/O analyzer at the Intertek Group PLC (https://www.intertek.com/). The O-content was calculated by difference as it was assumed to be the remaining major element in each polymer apart from Araldite which also has ~ 0.06 g/g Cl (https://www.tedpella.com).

Table 3.1

Implant Reference Materials H-C-O Content and Density

Standard Name	Chemical Formula	H (g/g)	C (g/g)	O (g/g)	Density (g/cm3)	Supplier
Araldite 502 epoxy**	Proprietary	0.0834	0.714	0.1416	1.1	(Luft, 1961)
Lexan Polycarbonate (PC)	(C16H14O3)n	0.0521	0.753	0.1944	1.2	Sabic Innovative Plastics US LLC
Polyethylene terephthalate (PET)	(C10H8O4)n	0.0467	0.626	0.3278	1.44	Professional Plastics, Inc.
Polymethyl methacrylate (PMMA)	(C5H8O2)n	0.0776	0.595	0.3249	1.18	SourceOne Displays LLC
SPI-GLASTM 22	NA	<0.0001	~1	<0.0001	1.5	Structure Probe, Inc.
NIST SRM 612*	NA	NA	NA	0.464	2.3	National Institute of Standards and Technology

[a] Araldite contains 0.06 g g-1 Cl, in addition to C, H and O.

[b] The reported O content for NIST SRM 612 glass is from Hollocher and Ruiz (1995).

The materials (Table 3.1) were implanted with Li, (among other elements of interest) by Leonard Kroko Inc. (Tustin, CA; krokoimplants.com) in two separate sessions. The first implant session was designed to generate reference materials for the determination of the Li-content in kerogen (Section 2.2), while the second session was intended to produce Li-isotope implant reference materials for kerogen (Section 2.3). Only ^{7}Li was implanted for the content calibration while both ^{7}Li and ^{6}Li isotopes were implanted for Li-isotope calibration. Separate samples of the same materials implanted for Li-content calibration (Table 3.1) were implanted for Li-isotope calibration, in addition to NIST SRM 612. In both sessions all materials were implanted simultaneously. Implant fluences can be inaccurate by more than 10% (Heber et al., 2014) and as such must be absolutely calibrated by implanting a sample that has a known concentration. We used the NIST SRM 612 glass to calibrate the implant fluence of the isotope implant sample batch and used an intercalibration technique (Burnett et al. 2015) to determine the

fluence of the content calibration implant. The uncertainty in the implantation fluences were within 1.0% of the nominal fluences (i.e., fluences specified to the implanter) (see Appendix B for details on fluence calibration). The Li concentrations of the un-implanted carbonaceous matrices were near the limits of detection for the SIMS measurement settings described below. A software package for calculating the transport of ions in matter (TRIM; Ziegler et al. 2010) was used to determine the implant energy (Table 3.2) required for the peak concentration at a specified depth.

Table 3.2

Implant Session 1

Ion	Fluence (atoms/cm2)	Implant energy (keV)
^{7}Li	1.56×10^{15}	17
^{11}B	1.28×10^{15}	40
^{14}N	1.31×10^{15}	52
^{32}S	1.31×10^{15}	110

List of ion implants into araldite, PC, PET, PMMA and glassy carbon (SF Glas-22) used for this study. NIST SRM 612 was not included in Session

Each implant species was implanted to generate peak signals near 200 nm depth for polymer samples, such that the entire implant profile could be captured by SIMS depth profiling. Assuming a Gaussian implant profile, which is reasonable for low energy ion implants (tens of keV) (Hofker, 1975), the implant fluence can be used to estimate the concentration of the implant species at the peak following Leta and Morrison (1980) as shown in Eq.1.

$$C_p = \frac{0.4\phi}{\Delta R_p} \quad (1)$$

where;

C_p = The peak concentration of the implant species (atoms/cm^3)

ϕ = Fluence of implant species (atoms/cm^2)

ΔR_p = Longitudinal straggle or reference material deviation of the gaussian implant profile width (cm)

TRIM can be used to calculate the ΔR_p, which is the standard deviation of the Gaussian implant profile width, for each material to obtain a desirable implant fluence (±0.5%) with a known peak concentration. We selected a concentration of 1000 µg/g Li, (~1.3 x 10^{20} atoms/cm^3) at the implant peak, which corresponds to a fluence of 1.56 x 10^{15} atoms/cm^2 in these materials.

The secondary ion yield is affected by sample flatness (Deng and Williams, 1989), so it is essential that the analyzed area has a height variation < 1µm. Thus, prior to implantation, PET, Araldite and NIST SRM 612 samples were polished with a final grit size of <1 µm colloidal silica, while PC, PMMA and glassy carbon samples were delivered with mirror finishes. All samples (cut to 2.54 or 1 cm diameters) were sonified in 1.82% mannitol (a polyhydric alcohol; Tonarini et al. 1997) to remove surface adsorbed Li (Williams et al. 2012).

Content Calibration

The polymer samples (Table 3.1) along with glassy carbon (SPI Glas-22) were implanted with the major isotope ^{7}Li (92.4%) for Li-content calibration. Additional ions were implanted for other investigations (Table 3.2), but their low abundance is inconsequential to the ^{7}Li sputter yield. SIMS depth profiles were obtained with the Cameca (Ametek) secondary ion mass spectrometer (IMS-6f) using three different

analytical Setups including different primary ion beams (O_2^- and O^-), impact energies and secondary ion accelerating voltages (Table 3.3).

Table 3.3

Setup Conditions Used for Depth Profiles

Analytical Setup	Primary Ion	Secondary ion accelerating voltage	Impact energy per primary atom
1	O^-	9 kV	21.6 kV
2	O_2^-	9 kV	10.8 kV
3	O_2^-	5 kV	8.8 kV

The same primary ion accelerating voltage (-12.6 ±0.01 kV) was used for all Analytical Setups. To avoid repetition, further discussion will refer to the Analytical Setup by number (1-3). The change in impact energy and accelerating voltage causes differences in sputter yields and useful secondary ion yields (mass selected ions of a given species detected per atom of that species sputtered; Hervig et al. 2006) that are evaluated below (see Appendix B for calculations of sputter yield and useful secondary ion yields).

For each Analytical Setup, a focused primary beam with a diameter of 10-30 μm was rastered across a 125 × 125 μm^2 area using primary ion currents of 30 nA of O_2^- or 60 nA of O^-. A field aperture was used to ensure that only ions coming from a circular area 30 μm in diameter in the middle of the rastered area were counted, eliminating ions from the crater walls. Depth profiling measurements of $^7Li^+$ and $^{12}C^+$ were performed at a mass resolving power (MRP = mass/Δmass) of ~1000 which is sufficient to resolve $^{11}BH^+$ (~12 amu) from interfering with the $^{12}C^+$ peak. Energy filtering (Shimizu, 1979) of secondary ions was applied by reducing the sample voltage by 75 V so that only ions

with excess energies of 75 ± 20 eV could be detected, which can reduce molecular interferences. We used energy filtering because it is important for the ion energies detected to be the same for the reference material and unknowns. Energy filtering also reduces the secondary ion signal allowing all ions to be detected using the electron multiplier detector. Sample charging was controlled at each cycle of the analyses using a routine which scans the sample voltage while monitoring the $^{7}Li^{+}$ ion signal and returns the voltage to the value that gives the maximum $^{7}Li^{+}$ signal before applying the offset voltage. The efficiency of the electron multiplier detector was maximized for each analytical session using a reference material of known isotopic composition and adjusting the EM gain to get the same ratio (within error) obtained for each analytical session.

Crater depths were determined by taking an average of 3 to 4 measurements of rastered craters in the x, y and diagonal directions using a KLA Tencor™ Alpha-Step® 200 stylus profilometer. The crater depth measurements had a $\pm 2\sigma_{\bar{x}}$ precision <5%.

Content calibration data reduction. The SIMS relative sensitivity factor (RSF) (Wilson et al., 1989) is frequently used for determining the content of elements in matrix-matched materials. However, because the C concentrations in the carbonaceous implant reference materials measured here, and kerogen unknowns vary widely, we define a content calibration factor that takes variations in matrix composition into account.

Dividing the integrated $^{7}Li^{+}$ counts in an implant depth profile by the total measurement time spent on $^{7}Li^{+}$ (not the total time for the profile) gives an average count rate for $^{7}Li^{+}$ (c/s). Dividing the ^{7}Li implant dose (^{7}Li atoms/cm^{2}) by the total crater depth (in cm) gives an average Li atomic concentration over that profile (^{7}Li atoms/cm^{3}). A factor that converts count rates to concentration can then be defined as follows.

$$K = (^{7}Li\ atoms/cm^{3})/(^{7}Li^{+}\ c/s) \quad (2)$$

This K value is specific to the particular matrix and to the analytical conditions used, i.e., primary ion current, both primary and secondary ion accelerating voltages, primary ion species, mass resolving power, secondary ion energy bandpass. To be able to apply a conversion factor to other samples of the same matrix possibly analyzed using a different primary ion current value, the $^{7}Li^{+}$ count rate in the implant reference material and ^{7}Li concentration must be normalized to the count rate and concentration for a matrix signal from the target, and ^{12}C was chosen. Because the carbon content varies among different polymers, the ^{12}C concentration must be defined in units of atoms/cm^3 which can be calculated as follows.

$$N_C = \left(\frac{(wf_m\ \rho)}{u_m\ NA}\right) \times a_m \quad (3)$$

where;

N_C = Atom density of reference isotope (C atoms/cm^3)

wf_m = Weight fraction of reference matrix atom in the implant reference material (grams/grams; Table 3.1)

ρ = Material density (grams/cm^3; Table 3.1)

u_m = Average molar mass of reference matrix atom (grams/mole; 12.011 g/mol for all C)

NA = Avogadro's number (6.023E23 atoms/mole)

a_m = Isotopic abundance fraction of reference matrix isotope (0.9893 for ^{12}C)

Using the ^{12}C count rate and concentration we define a normalized calibration factor K*:

$$K^* = (\text{atoms/cm}^3)^*/(\text{c/s})^* \quad (4)$$

where now both the ^{7}Li concentration and count rate are normalized to the corresponding values for ^{12}C in the implant sample. The ^{7}Li concentrations in other samples may then be calculated as a fraction of the concentration of ^{12}C by multiplying the $^{7}Li^{+}/^{12}C^{+}$ count rate ratio in the unknown sample by the factor K*. It is possible that K* may be affected by some or all of the analytical conditions listed above, as discussed below. Lower K* values indicate higher sensitivity of the implant ion ($^{7}Li^{+}$) relative to the reference ion ($^{12}C^{+}$).

Isotope Calibration

In a previous study of Li in kerogen (Teichert et al. 2020) NIST SRM 612 was used as a reference material for $\delta^{7}Li$ measurements in coal because there were no known reference materials for Li in a carbonaceous matrix. Therefore, in addition to comparing carbonaceous samples with varying H/C and O/C ratios, another goal of this calibration study was to determine the magnitude of possible matrix effects on Li-isotopes among silicate glass and carbon matrices. The materials listed in Table 3.1 were implanted with both ^{7}Li and ^{6}Li ions at fluences of 1.0×10^{15} and 1.0×10^{14} atoms/cm^2, respectively. The implant energy used was calculated based on the highest density material to be implanted, which was the NIST SRM glass reference material (SRM 612; 2.3 g/cm^3; Hervig et al. 2006), therefore a 21 keV implant energy was used for all materials.

SIMS depth profiles of ^{7}Li and ^{6}Li were obtained using the same primary beam types, primary and secondary ion accelerating voltages, raster size and field aperture settings as those described above (Section 2.2), except that depth profile measurements for the O_2^- primary beam coupled with a 9 kV secondary ion accelerating voltage (Setup

2; Table 3.3) were not performed. Additionally, no energy filtering was used for isotope ratio measurements, therefore, to avoid oversaturating the electron multiplier detector, entrance and exit slit widths were adjusted to a MRP of ~1800 and lower primary beam currents were used (5nA for Setup 3, 10 nA for Setup 1). Spot measurements were made on an un-implanted NIST SRM 612 reference material using standard-unknown measurement bracketing to monitor the instrumental mass fractionation (IMF) during the analytical sessions.

Isotope Calibration Data Reduction. The integrated signals for ^{7}Li and ^{6}Li were used to obtain δ^{7}Li values as follows.

$$\delta^{7}Li\ ‰ = \left(\frac{R_{Sample}}{R_{Standard}} - 1\right) \times 1000 \quad (5)$$

where;

R_{Sample} = ^{7}Li/^{6}Li signal ratio

$R_{Standard}$ = 12.0192 ± 0.0002 (Flesch et al. 1973)

For the NIST SRM 612 glass, the background Li count rate was subtracted from the integrated Li profile. For polymer and glassy carbon samples there was no significant Li background (<100 cps). The δ^{7}Li‰ deviations of each implanted carbonaceous sample from the NIST SRM 612 Li-isotope implant reference material ($\delta^{7}Li_{612}$) were determined with the following expression.

$$\delta^{7}Li_{612} = \delta^{7}Li_{612\ \text{implant reference material}} - \delta^{7}Li_{i\ \text{implant reference material}} \quad (6)$$

where;

$\delta^{7}Li_{612\ \text{implant std}}$ = The δ^{7}Li value for the NIST SRM 612 implant reference material

$\delta^{7}Li_{i\ \text{implant std}}$ = The δ^{7}Li for each of the carbonaceous implant reference materials

A minor correction for differences in backscattering between the NIST SRM 612 glass and the carbonaceous samples was also applied. According to TRIM simulations, during the ion implant process the NIST SRM 612 glass backscattered approximately 1.4% of the $^{7}Li^{+}$ ions and 1.6% of the $^{6}Li^{+}$ ions. The carbonaceous materials backscattered less <0.2% of both Li implant species. Accordingly, we calculated that the implant ratio of the NIST SRM 612 is 1.5‰ larger than for the carbonaceous samples and applied this correction.

Potential problems related to the instantaneous count rate loss when using a secondary ion aperture over a rastered beam (Simons et al. 2005) may be approximated by multiplying the average count rate by the ratio of the rastered area to the apertured area, but this method will overestimate the instantaneous count rate if the beam diameter is larger than the analyzed diameter. Another method to calculate the instantaneous count rate loss is to use the dynamic transfer operating system (DTOS) and to calculate the intensity ratio of Li ions at 100% DTOS (where all counts from the raster are focused to a spot) and the 0% DTOS (no electronic gating) as the factor by which to multiply the average count rate. It is necessary that the diameter of the 100% DTOS beam be roughly equal to the diameter of the primary beam for this correction to be accurate. The second procedure was applied by measuring $^{7}Li^{+}$ on the un-implanted NIST SRM 612 reference material using both 100% DTOS and 0% DTOS to calculate the factor needed to obtain the instantaneous count rate loss. Once the instantaneous count rate was calculated for each cycle in a given measurement, a correction was made for both Li isotopes by adding count losses to those integrated signals. The count loss correction changed the $\delta^{7}Li_{612}$ by

a range of +1 to +18‰ and was applied to all the Li isotope implant reference material measurements but was not necessary for the content calibration because the instantaneous count rate correction was not significant (<1.5%). Ideally, both isotopes are implanted with the same fluence so that the instantaneous count losses are the same and correction is not necessary.

Results and Discussion

Lithium Content Calibration

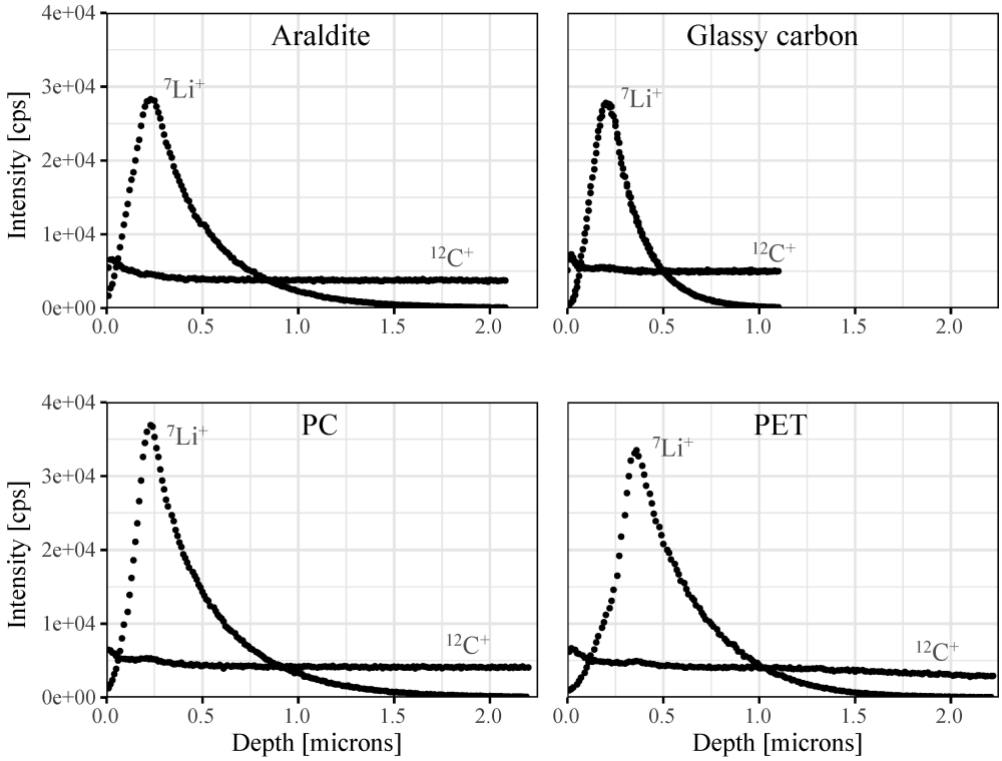

Figure 3.2. Depth profile measurements into (a) araldite, (b) glassy carbon, (c) PC and (d) PET materials, showing the implant ion ($^{7}Li^{+}$) and reference ion ($^{12}C^{+}$) intensities using Setup 2 (O_2^-, 9 kV secondary ion accelerating voltage). Note that $^{12}C^{+}$ signals were subjected to transient effects near the surface and therefore the first several cycles were not used to determine the mean $^{12}C^{+}$ count rate. In some materials, $^{12}C+$ signals would continue to decrease throughout the profile and were the main source of uncertainty in the K* factor calculations. For consistency, the $^{12}C^{+}$ signal was averaged from where transient effects ended where the $^{7}Li^{+}$ signal reached 5% of its peak value for all depth profiles.

The secondary ion intensities of $^{7}Li^{+}$ and $^{12}C^{+}$ are plotted against depth in Fig. 3.2 for several depth profile measurements into ion implant reference materials. The K* calibration factors (Eq. 4) for each material are plotted against the atomic abundances of H and O for the different Analytical Setup conditions (Fig. 3.3). Multiple depth profiles were taken for each material. Table 3.4 shows the mean K* factors, sputter yields (atoms sputtered per impinging atom) and $^{7}Li^{+}$ and $^{12}C^{+}$ useful secondary ion yields for each material.

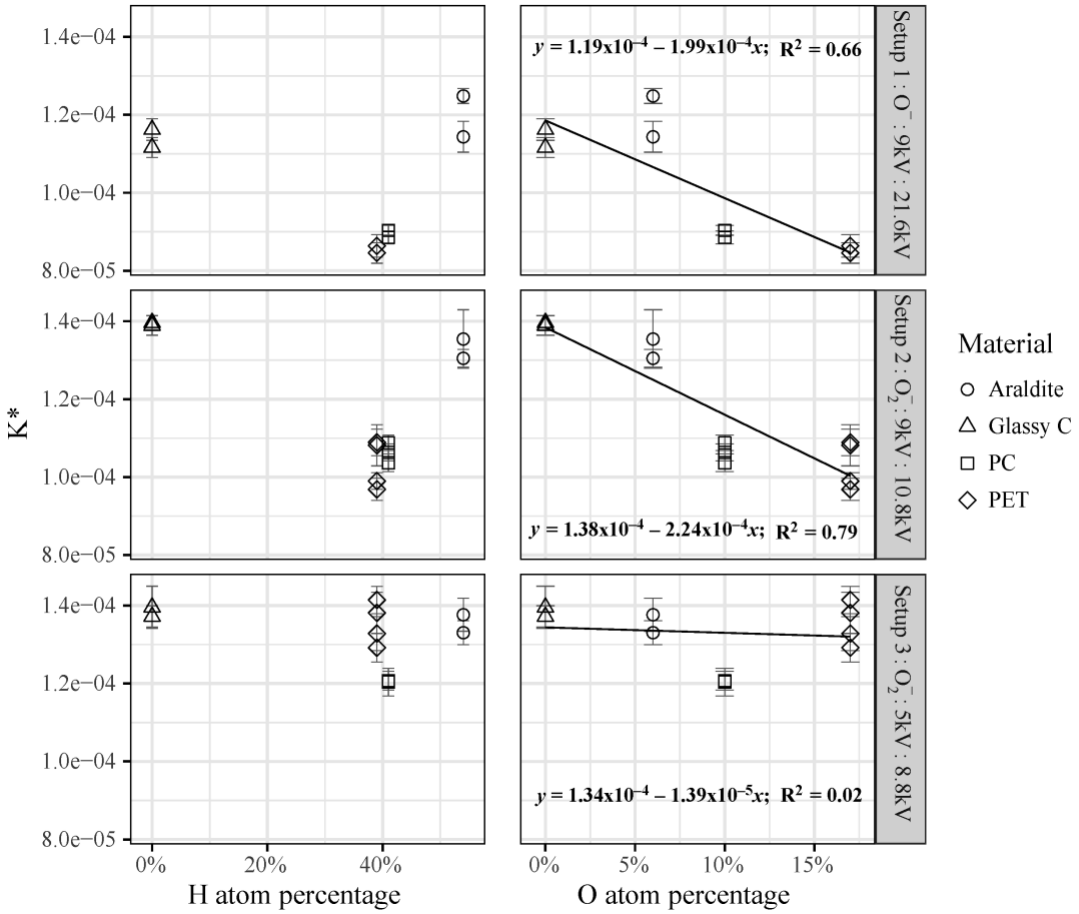

Figure 3.3. Scatter plots of K* factors are plotted against the atomic abundances of H and O present in polymer and glassy C samples for different instrument setups (primary ion/secondary accelerating voltage/impact energy). See section Content calibration for additional setup parameters. $\pm 2\sigma_x$ of individual analyses is plotted and is the result of uncertainty in the $^{12}C^{+}$ count rate and profilometer depth measurements.

The polymethyl methacrylate (PMMA; or plexiglass), which has the lowest melting point (160°C) showed evidence of melting (Fig. 3.4) during ion bombardment resulting in unstable secondary ion signals and therefore the results from those analyses are not included or discussed further.

Table 3.4

Mean Calculated Data and Associated Uncertainties

Setup 1 O^- / 9 kV / 21.6 kV	Sputter yield	$\pm 2\sigma x$	$^{7}Li^{+}$ useful secondary ion yield	$\pm 2\sigma x$	$^{12}C^{+}$ useful secondary ion yield	$\pm 2\sigma x$	K*	$\pm 2\sigma x$	n
Araldite	3.78	0.28	1.21×10^{-3}	3.6×10^{-5}	1.43×10^{-7}	1.7×10^{-8}	1.20×10^{-4}	1.1×10^{-5}	2
Glassy C	2.03	0.01	1.25×10^{-3}	2.4×10^{-5}	1.40×10^{-7}	8×10^{-9}	1.14×10^{-4}	5×10^{-6}	2
PET	6.61	0.06	1.02×10^{-3}	1.2×10^{-5}	8.6×10^{-8}	2×10^{-9}	8.6×10^{-5}	2×10^{-6}	2
PC	4.66	0.11	1.23×10^{-3}	3.3×10^{-5}	1.08×10^{-7}	7×10^{-10}	9.0×10^{-5}	2×10^{-6}	2
Setup 2 O_2^- / 9 kV / 10.8 kV									
Araldite	4.02	0.2	8.8×10^{-4}	3×10^{-6}	1.14×10^{-7}	4×10^{-9}	1.33×10^{-4}	5×10^{-6}	2
Glassy C	2.05	0.01	1.05×10^{-3}	2×10^{-6}	1.44×10^{-7}	1×10^{-9}	1.39×10^{-4}	8×10^{-7}	2
PET	6.64	0.08	8.2×10^{-4}	6.8×10^{-5}	8.3×10^{-8}	2×10^{-9}	1.03×10^{-4}	6×10^{-6}	4
PC	4.95	0.11	9.9×10^{-4}	3.1×10^{-5}	1.03×10^{-7}	8×10^{-10}	1.06×10^{-4}	3×10^{-6}	3
Setup 3 O_2^- / 5 kV / 8.8 kV									
Araldite	4.68	0.05	6.0×10^{-4}	3×10^{-6}	7.9×10^{-8}	3×10^{-9}	1.35×10^{-4}	5×10^{-6}	2
Glassy C	2.2	0.05	7.6×10^{-4}	7×10^{-6}	1.03×10^{-7}	3×10^{-9}	1.38×10^{-4}	2×10^{-6}	2
PET	7.06	0.08	5.6×10^{-4}	4.1×10^{-5}	7.4×10^{-8}	4×10^{-9}	1.35×10^{-4}	6×10^{-6}	4
PC	5.37	0.05	7.0×10^{-4}	1×10^{-6}	8.3×10^{-8}	1×10^{-10}	1.21×10^{-4}	4×10^{-7}	2

The mean values of sputter yields, useful secondary ion yields and K* factors grouped by material and analytical setup.
The uncertainties are 2sx determined from the mean values of the number of analyses (n).

For Analytical Setups 1 and 2, using the 9 kV secondary ion accelerating voltage, the Araldite and Glassy C have higher K* factors than PC and PET resulting in a negative trend between K* factors and the atomic abundance of O (Fig. 3.3). Despite having a similar trend for the materials, the K* factors are shifted higher in Setup 2 compared to Setup 1. Even though the same primary and secondary ion accelerating voltages were used in both Setup 1 and 2, the impact energies of the impinging atoms are different because O_2^- ions break into two O atoms when they strike the sample surface which

halves the impact energy of each O atom. The lower impact energy of Setup 2 (10.8 keV) compared to Setup 1 (21.6 keV) decreases the depth range of the primary ions and thus

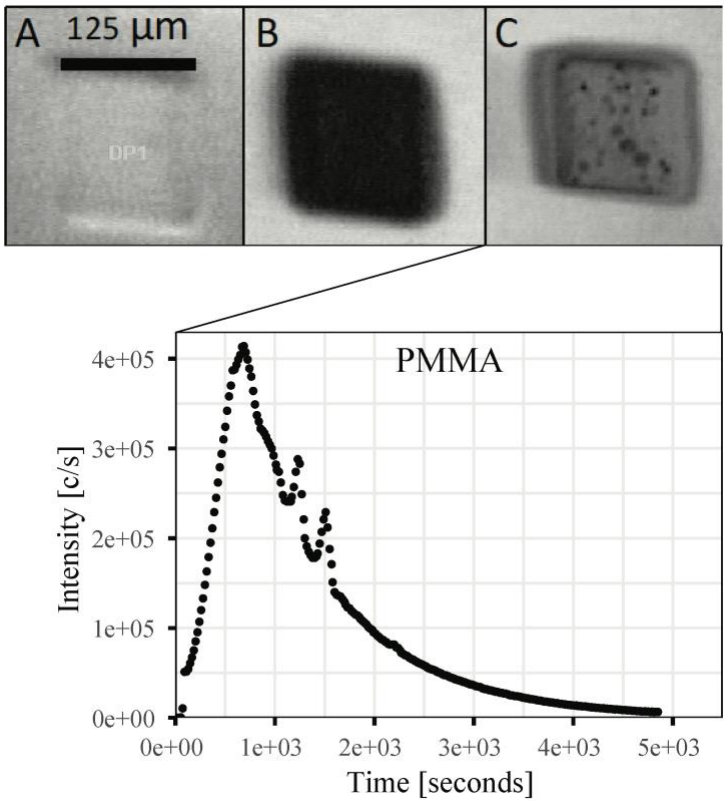

Figure 3.4. Comparison of analytical craters in different matrices; (a) NIST SRM 612 glass, (b) polycarbonate (PC), (c) polymethacrylate (PMMA). The spots shown in C appear to be bubbles related to melting. The effect of this melting on the $^{7}Li^{+}$ implant profile is shown in the PMMA depth profile.

sets more surface atoms in motion, resulting in higher sputter yields (Fig. 3.5; Table 3.4; Sigmund, 1969). Conversely, the lower impact energies decrease the surface concentration of the primary ion species (oxygen) implanted into the sample which is approximately equivalent to the reciprocal of the sputter yield (Liebl, 1975, Deline et al. 1978b, Williams, 1979a). Williams (1979a) found that secondary ion yields are negatively correlated with the sputter yield as demonstrated in this study (Fig. 3.5)

because primary oxygen accumulates in the craters, enhancing ionization due to its high electronegativity.

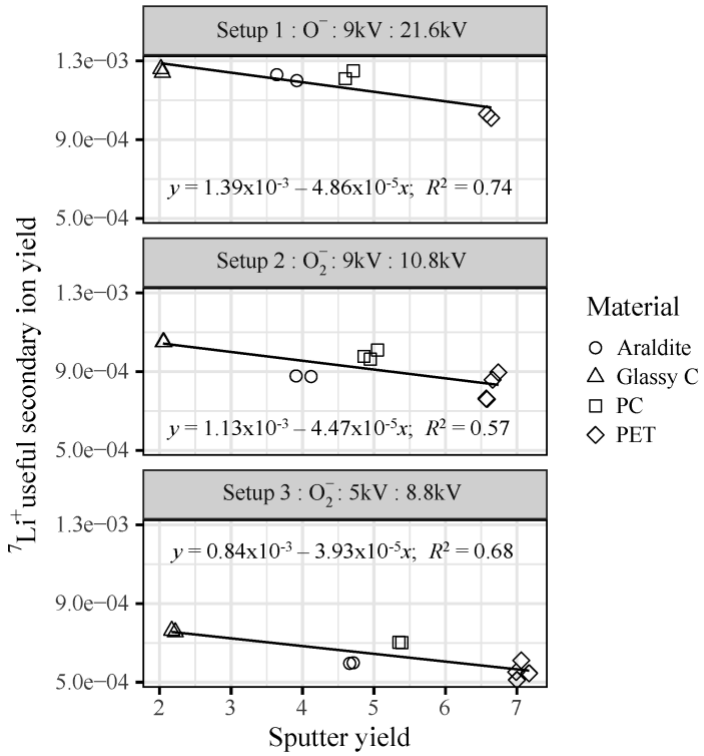

Figure 3.5. $^{7}Li^{+}$ useful secondary ion yields are plotted against the sputter yields for each material and for each analytical setup. See section Content calibration for additional setup parameters. Uncertainties ($2\sigma_x$) for individual useful secondary ion yields are < 5%.

The K* calibration factor can also be expressed as the implant ion useful secondary ion yield ($^{7}Li^{+}$) relative to the reference ion useful secondary ion yield ($^{12}C^{+}$).

$$K^{*} = \left(\frac{Useful\ ^{12}C\ ion\ yield}{Useful\ ^{7}Li\ ion\ yield}\right); see\ Section\ 2.2.1) \quad (7)$$

Therefore, increasing the surface concentration of O by primary beam implantation evidently enhances the $^{7}Li^{+}$ ion yields by a greater factor than the $^{12}C^{+}$ ion yields and this can be seen in Fig. 3.6 and Table 3.4 by comparing how $^{7}Li^{+}$ and $^{12}C^{+}$ secondary ion useful yields change from Setup 2 to Setup 1 for each material. The trends

in Fig. 3.6 suggest that samples with higher O-content will have lower K* factors (i.e., greater sensitivity to $^{7}Li^{+}$ relative to $^{12}C^{+}$) as is observed in Fig. 3.3 for Setups 1 and 2.

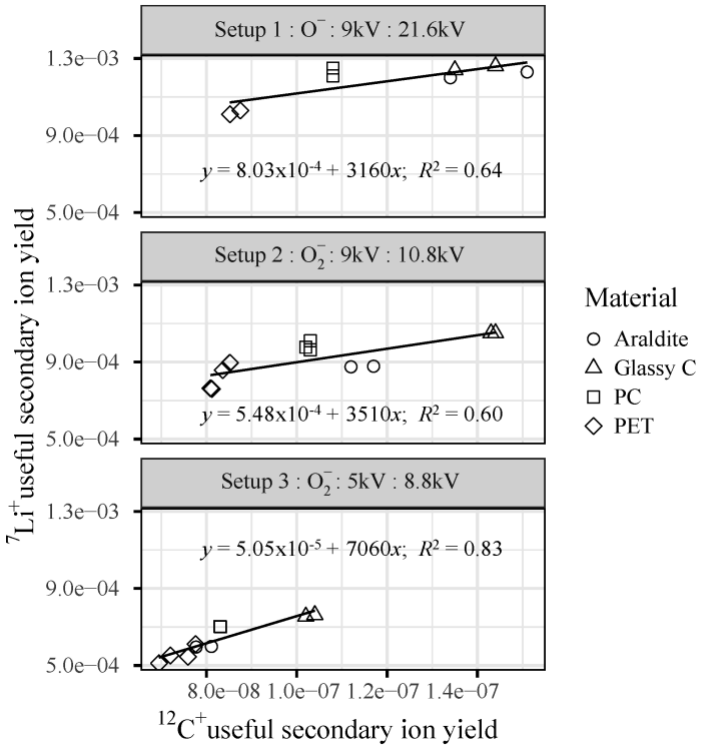

Figure 3.6. $^{7}Li^{+}$ useful secondary ion yields are plotted against the $^{12}C^{+}$ useful secondary ion yields for each material and analytical setup. See section Content calibration for additional setup parameters. Uncertainties ($\pm 2\sigma_x$) for individual useful secondary ion yields are < 5%.

Using Setup 3, the mean values for the K* factors of each material, apart from PC, are within statistical error. The PC K* factor is 13% lower than Glassy C with Setup 3, 24% lower with Setup 2 and 21% lower with Setup 1. Therefore, by measuring the carbonaceous samples using a 5 kV secondary ion accelerating voltage one can effectively eliminate matrix effects related to the O-contents.

Hervig et al. (2006) observed that useful secondary ion yields increased proportionally with secondary ion accelerating voltage in NIST SRM 610 glass. In addition to the lower secondary ion accelerating voltage, Setup 3 also has a lower impact

energy (8.8 keV) than the other Setups which also decreases ion yields. Fig. 3.7 shows the percent change in the useful secondary ion yields as the secondary voltage is

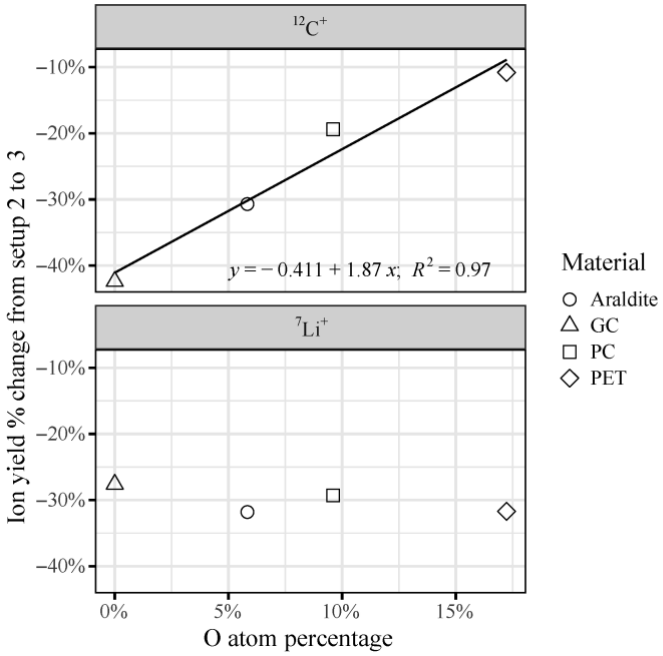

Figure 3.7. Scatter plots showing the percent change in the useful secondary ion yields of $^{7}Li^{+}$ and $^{12}C^{+}$ between analysis using a 9 kV (Setup 2) and a 5 kV (Setup 3) secondary ion accelerating voltage. The trend line for $^{12}C^{+}$ shows how the ^{12}C useful ion yields decreased as a function of sample O content going from setup 2 to setup 3.

increased from 9 kV to 5 kV secondary ion accelerating voltage. The useful secondary ion yields of $^{7}Li^{+}$ decrease by ~30% for all samples. The $^{12}C^{+}$ useful secondary ion yields however, decrease as a function of the O-content of the sample, with the samples with higher O-content having a smaller decrease when changing from Setup 2 to Setup 3. At a 9 kV secondary ion accelerating voltage (Setups 1 and 2) it was observed that the materials with higher O-contents had lower K* factors (i.e., $\left(\frac{Useful\ ^{12}C\ ion\ yield}{Useful\ ^{7}Li\ ion\ yield}\right)$). That is not observed at a 5 kV secondary ion accelerating voltage (Setup 3) because the useful secondary ion yields of $^{12}C^{+}$ decrease the least in the materials with high O-contents (Fig. 3.7), thus equalizing the $\left(\frac{Useful\ ^{12}C\ ion\ yield}{Useful\ ^{7}Li\ ion\ yield}\right)$ (i.e., K* factors) for all materials. It is

unclear why the secondary ion accelerating voltage affects the useful ion yields of $^{12}C^{+}$ so significantly and this question requires further study.

Electron Multiplier effects on the Li-content calibration factor (K*). Several instrumental parameters including the primary ion current (5 - 50 nA), sample height (±15µm) and immersion lens voltage were tested to determine how each might affect the K* factors, and those parameters were determined to have a negligible effect. The electron multiplier gain has a considerable influence on the K* factors because of the higher detection efficiency of $^{12}C^{+}$ relative to $^{7}Li^{+}$ secondary ions (Zinner et al. 1986). It is common for the electron multiplier gain to be adjusted with aging of the detector because the sensitivity of ion conversion to electrons degrades with use (Frank *et al*. 1969), therefore it is important to maximize the EM response. Fig. 3.8a demonstrates the magnitude of the effect of EM gain on K* factors, showing a systematic decrease as the EM gain is increased. The K* factor changes because $^{7}Li^{+}$ counts increase relative to $^{12}C^{+}$ as the detector sensitivity is increased. The K* factor is linearly correlated with the average $^{12}C^{+}$ / $^{7}Li^{+}$ peak intensity (Fig. 3.8b), thus maximizing the ratio can be used to set the EM Gain.

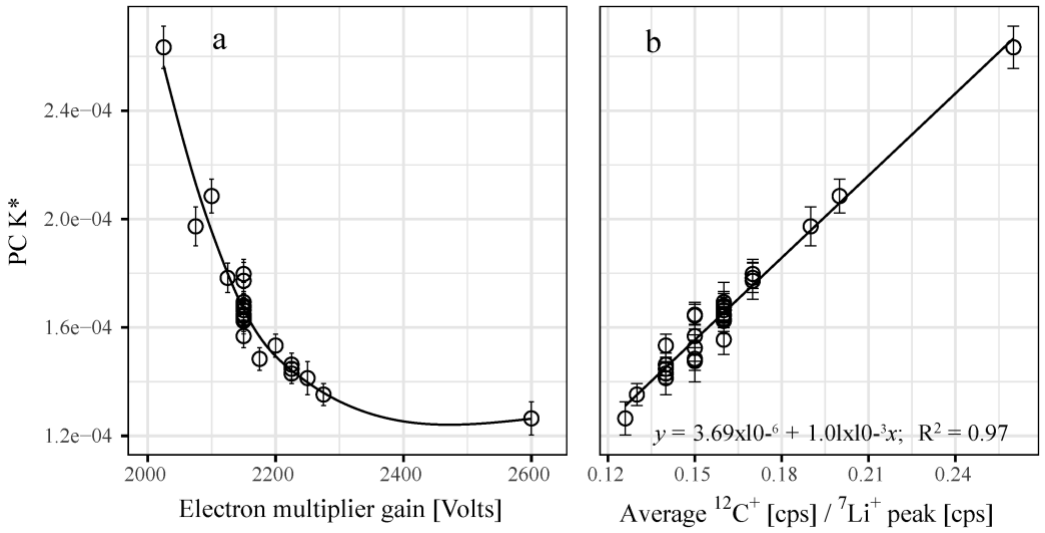

Figure 3.8. Plot showing the (a) EM gain vs. K* factors on PC and (b) the mean $^{12}C^{+}/^{7}Li^{+}$ peak correlation with K* factors using Setup 3 (5 kV secondary ion accelerating voltage). Range bars shown are $2\sigma_x$.

Application of content calibration. Figure 3.9 shows calibration curves for the conversion of $^{7}Li^{+}/^{12}C^{+}$ count ratios to the ^{7}Li atom/^{12}C atom fraction in organic matrices for each of the Analytical Setups described here. Because Li is typically a trace element in organic materials the atom fraction ratio is multiplied by $1*10^{6}$ to express the ^{7}Li concentration, in ppm atomic (ppma), in terms of the ^{12}C concentration. Once this value (y-axis) is obtained from a given $^{7}Li^{+}/^{12}C^{+}$ count ratio it can be multiplied by the ^{12}C atom fraction of the unknown to convert to ^{7}Li ppma for the entire sample which can then be converted to μg/g convenient to geochemical studies.

For Setup 1 and 2 the calibration is a function of sample O-content (atom fraction; O_{af}) as well as the $^{7}Li^{+}/^{12}C^{+}$ intensity ratios whereas the calibration for Setup 3 (using a 5 kV secondary ion accelerating voltage) is a single curve independent of sample O-content. It is key to note that these trendlines are accurate only if the electron multiplier detection efficiency is maximized, the MRP is approximately 1000 and ions with 75±20

eV initial kinetic energy are detected. Content calibrations determined here with an IMS-6f may not be directly transferable to different instruments (e.g., NanoSIMS) where secondary ion optics and detection systems differ significantly. Ideally calibration curves should be determined for different types of SIMS instruments.

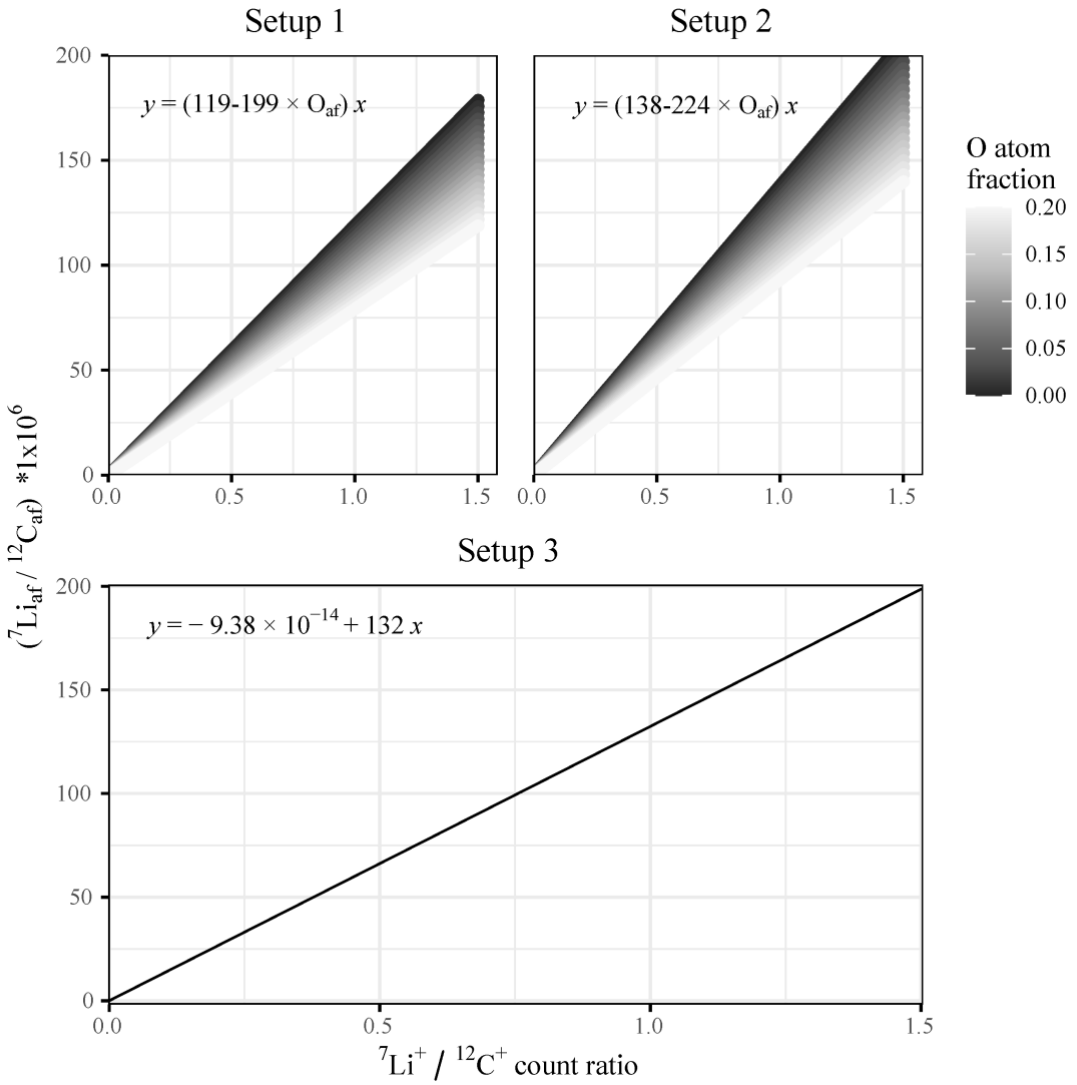

Figure 3.9. Calibration lines are plotted for each of the three analytical setups used (Table 3.3). The x-axis is the $^7Li^+/^{12}C^+$ count rate on the unknown sample and the y-axis is the ^7Li atom fraction (af) normalized to the ^{12}Caf expressed in ppma. For Setups 1 and 2, the calibration is a function of the oxygen atom fraction (O_{af}), calculated from the trend lines shown in Fig 3.3. The single calibration curve for Setup 3 is derived from the mean of the K* factors for all carbonaceous materials. Multiplication of the y-axis value by the $^{12}C_{af}$ of the sample measured gives Li content in ppma.

Li-Isotopic Calibration

The δ^7Li‰ deviations of each implanted carbonaceous sample from the NIST SRM 612 Li-isotope implant reference material (δ^7Li_{612}) are plotted against their atomic abundances of H and O (Fig. 3.10) for Analytical Setups 1 and 3. Using either Analytical

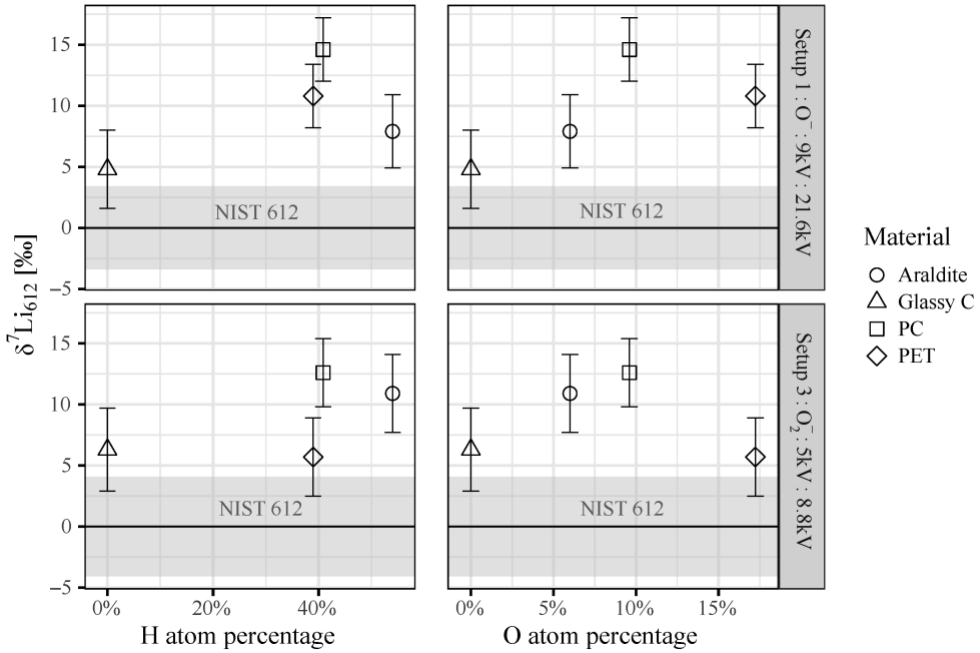

Figure 3.10. NIST SRM 612 implant reference materials' mean isotope ratio is plotted as the origin of the y-axis with the grey region indicating the analytical uncertainty in the measurement. The isotopic deviations from the NIST SRM 612 implant reference materials' isotope ratio (δ^7Li_{612}) are plotted for each sample against H and O atom percent for instrument Setups 1 and 3. The range bars shown are the sum of $2\sigma_x$ uncertainty in the IMF and the Poisson Error (P.E.) of the individual analyses of the implant reference materials plotted.

Setup, the Li-isotope calibration in glassy carbon (SPI Glas-22) is within error of the NIST SRM 612 glass. The carbonaceous matrices are on average +10‰ higher than the NIST SRM 612 silicate glass reference material using both Analytical Setups. In each case PC has the largest deviation from the NIST SRM 612 glass reference material. There is no apparent relationship between sample H and O-contents and the measured Li-isotope ratio.

Conclusions

Organic polymer samples were implanted with Li ions to serve as reference materials for SIMS measurements of Li-content and isotope ratios in kerogen. SIMS depth profile measurements through Li-ion implants were used to calculate a Li-content calibration factor (K*). The results show no matrix effects related to variable H and O-contents of the carbonaceous materials using an O_2^- primary ion beam and 5 kV secondary ion accelerating voltage. However, a matrix effect related to sample O-content was observed when using an O^- or O_2^- primary beam with a 9 kV secondary ion accelerating voltage. Therefore, at a MRP of ~1000 we recommend the use of a 5 kV secondary ion accelerating voltage when measuring Li in organic matrices, to avoid a matrix effect related to sample O-content and to improve depth resolution.

For Li isotope calibration reference materials, there is a matrix effect with organic polymer samples having a +10‰ greater δ^7Li‰ than silicate glass (NIST SRM 612) on average; however glassy C (SPI-Glas-22) is within error of NIST SRM 612 glass. Preparation of implant reference materials as described in this study can provide matrix matched calibrations for both Li-content and Li-isotopes in similar organic matrices.

CHAPTER 4

EFFECTS OF CONTACT METAMORPHISM ON THE LITHIUM CONTENT AND ISOTOPIC COMPOSITION OF KEROGEN IN COAL

Abstract

Lithium isotopes (δ^7Li) in coals have been shown to increase with thermal maturity, suggesting preferential release of ^{6}Li from kerogen to porefluids. This has important implications for paleoclimate studies based on δ^7Li of buried marine carbonates, which may incorporate Li from porefluids during recrystallization. Here, the Li content and isotopic composition of macerals from two coal seams intruded by dikes, were studied as a function of temperature across a thermal gradient into the unmetamorphosed coal. Samples were collected in Colorado (USA) from a Vermejo Fm. coal seam intruded by a mafic-lamprophyre dike and compared to a Dutch Creek No.2 coal seam intruded by felsic-porphyry dike; a potential source of Li-rich fluids.

The Li-content and Li-isotope compositions of coal macerals were measured *in situ* by Secondary Ion Mass Spectrometry (SIMS). The macerals of the Vermejo coal samples, buried to VR_o 0.68%, contained <1.5 μg/g Li with an average vitrinite δ^7Li of –28.4±1.6‰, while liptinite and inertinite were heavier, averaging –15.4±3.6‰ and –10.5±3.7‰, respectively. The contact metamorphosed vitrinite/coke showed the greatest change with temperature with δ^7Li 18 to 37‰ heavier than the unmetamorphosed vitrinite.

The Dutch Creek coal, buried to VRo 1.15%, prior to dike emplacement, may have released Li during burial, as less isotopic change was observed between contact metamorphosed and unmetamorphosed macerals. Overall, Li contents were <1μg/g, and

the vitrinite in metamorphosed coal had δ^7Li 8 to 21‰ heavier than the unmetamorphosed coal. SIMS measurements on macerals near the dike did not show any change in Li-content indicative of Li derived from dike fluids, however previous bulk measurements showed slightly higher (2-3µg/g) Li-contents near the dike, suggesting possible Li incorporation from dike fluid into metamorphic silicates. A negative correlation was observed between Li-content and $^{12}C^+/^{30}Si^+$ count ratios, indicating that at metamorphic temperatures Li becomes concentrated in silicates.

Introduction

Kerogen is the most abundant form of organic matter on earth and kerogen bearing rocks, such as coal, are in some cases potential sources of lithium (Li) (Qin et al., 2015) but have been largely overlooked in studies of Li geochemical cycles (Teichert et al., 2020). Lithium and its stable isotopes (^{7}Li and ^{6}Li) are used to trace many dynamic earth processes because the relatively large mass difference between the isotopes (~17%) results in a terrestrial fractionation of up to ~70‰ (Penniston-Dorland et al., 2017; Tomascak et al., 2016). Lithium isotopes have been utilized in >50 studies related to continental weathering over the past two decades, in part because the Li-isotope system traces the chemical weathering of silicates which consume atmospheric CO_2 (Berner et al., 1983; Kump et al., 2000). During primary silicate dissolution there is limited Li-isotope fractionation, however secondary minerals which form during weathering preferentially incorporate ^{6}Li (Pogge von Strandmann et al., 2020). The ratio of primary silicate dissolution to secondary mineral formation, coined ‘the weathering congruency’, is controlled by the climate at a given time (Pogge von Strandmann et al., 2020). Lithium from silicate weathering accumulates in the dissolved load of rivers and groundwater

with a Li-isotope composition determined by the weathering congruency and accounts for ~50% of the Li input into seawater (Hathorne and James, 2006). Thus, the Li-isotopic composition of seawater at a given time, contains information about global weathering and therefore climate, which is a major driver of continental weathering (Kennedy and Wagner, 2011; Pogge von Strandmann et al., 2020). The Li-isotope composition of seawater can be recorded by inorganic or biogenic carbonates forming in the marine environment and have been used to reconstruct paleoclimate (Lechler et al., 2015; Misra and Froelich, 2012; Pogge von Strandmann et al., 2017, 2013; Ullmann et al., 2013), which may be valid if there is no overprinting of the carbonate Li-isotope signature during diagenesis (Dellinger et al., 2020).

Kerogen has been identified as a potential source of isotopically light Li and it has been proposed that Li is released from kerogen into porefluids during diagenesis at the temperatures of oil and gas generation and can be useful in tracing hydrocarbons (Williams et al., 2012; 2013; 2015). Accordingly, formation waters tend to have lighter isotope ratios (δ^7Li + 4 to +16‰; Collins, 1975; Eccles and Berhane, 2011; Macpherson, 2014; Millot et al., 2011; Phan et al., 2016) than lakes (+17 to +36‰; Chan and Edmond, 1988; Tomascak et al., 2003; Witherow et al., 2010), rivers (mean +23‰; Penniston-Dorland et al., 2017; Tomascak et al., 2016) and seawater (δ^7Li ~ +31‰; Chan and Edmond, 1988; You and Chan, 1996). In a survey of coals from basins across the United States, Teichert et al., (2020) found that low-rank coals are isotopically lighter (–10‰ to –20‰) than most thermally mature coals (–5‰ to +5‰) irrespective of age or sedimentary basin (Fig. 4.1) suggesting that ^{6}Li is preferentially released from kerogen into porefluids during thermal maturation and hydrocarbon generation. This is consistent

with the finding that up to 50% of the Li in low rank coals can be associated with organic matter (OM) whereas Li is almost entirely associated with silicates in high rank coals (bituminous to anthracite) (Dai et al., 2021; Finkelman et al., 2018). Low-rank coals contain 10 μg/g Li on average (Ketris and Yudovich, 2009) and it has been hypothesized that many inorganic elements, such as Li, bond to carboxylic acid (COOH), and phenolic hydroxyl groups (OH) to form chelates during peatification; a precursor to coal formation (Swaine, 1990). With increasing coal rank (thermal maturity) volatiles are lost and OM releases various hydrocarbons. The C – C and C – H bonds in the OM are strengthened causing the weakly bound inorganic heteroatoms to be expelled via demetallation and decarboxylation reactions and aromatization (Filby and van Berkel, 1987; Li et al., 2010).

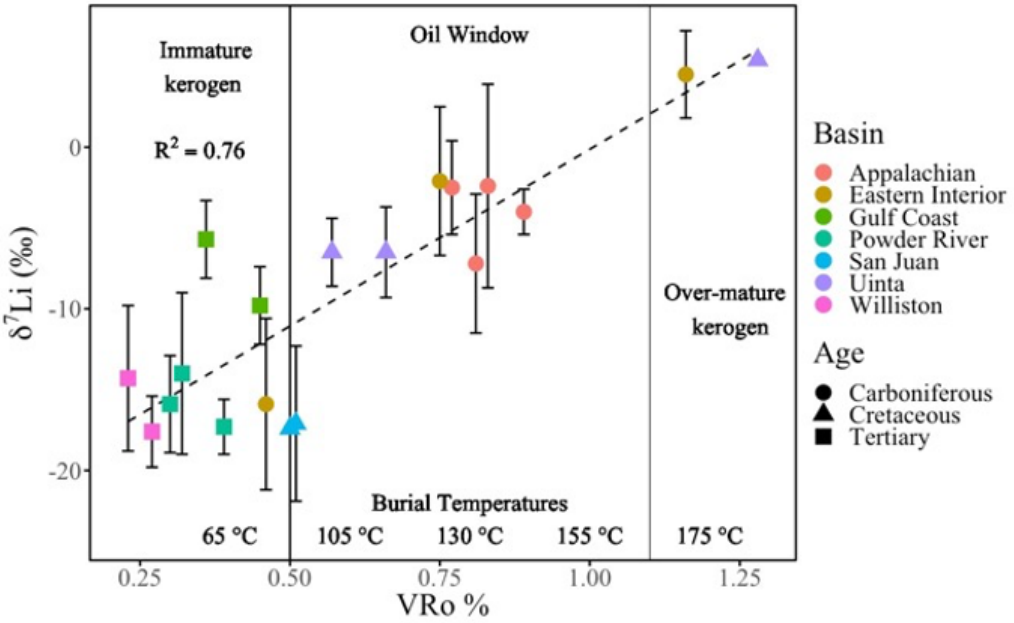

Figure 4.1. Scatter plot showing a correlation between vitrinite reflectance (VR_o ‰) and δ^7Li measurements of coal samples from different sedimentary basins (color) and of different ages (shape) from across the United States (Teichert et al., 2020). The δ^7Li values shown here have been corrected by +10‰ based on an analytical matrix effect described in Teichert et al., (2022).

In this study we examined the effect of thermal maturity on the Li-contents and isotopic compositions across two coal seams from Colorado (USA), which have been altered by contact metamorphism. Varying temperatures of contact metamorphism across a single coal seam allows comparison to the unmetamorphosed coal which experienced only burial diagenetic temperatures (<150˚C). The Li-contents and isotopic changes across the contact metamorphosed coal seams are used as an analog for increasing coal rank while it is recognized that the metamorphic heating is rapid compared to burial so that reaction mechanisms will differ. The aim of this study was to evaluate the range of δ^7Li in coal macerals and their change during thermal alteration. The importance of this work is that Li released from kerogen into sedimentary porefluids can affect the δ^7Li of other authigenic minerals incorporating organic sources of Li. This should be recognized particularly in studies of buried marine sediments used to interpret paleoclimate.

Materials and Methods

Samples and Geologic Settings

The Morley Dike is a mafic lamprophyre dike which is exposed in outcrop where it cuts across sedimentary rocks of the Upper Cretaceous Vermejo Fm. in the Raton Basin of South-Central Colorado, USA (Cooper et al., 2007; Johnson, 1969) (Fig. 4.2a). Samples were collected from a high volatile bituminous B coal seam in contact with the dike (Fig. 4.2b). The Morley Dike has a thickness of 1.6 m, a strike of 114° and is locally vertical where it contacts sedimentary layers which have a local strike of 14° and a dip of 16°. The coal seam, sampled on the north side of the Morley Dike, has an average exposed thickness of 1.1 m and is exposed laterally for approximately 16 m. The coal seam was sampled within a ~4 m thick sedimentary unit with alternating layers

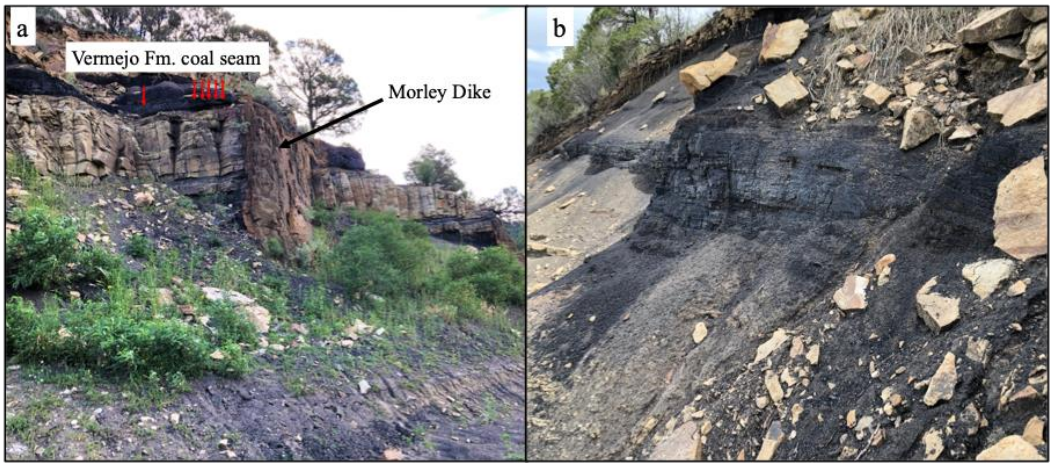

Figure 4.2. Photographs of the (a) outcrop and (b) coal seam where contact metamorphosed Vermejo Fm. coals were collected adjacent to the mafic lamprophyre 'Morley' dike.

of coal benches and shaley coal forming talus slopes. The coal rich unit is bounded by sandstone units above and beneath as displayed in the stratigraphic column (Fig. 4.3). Coal and coke samples were collected from the middle ~0.3 m of the 1.1 m coal seam. Five samples were collected within the contact aureole zone of the coal seam and one coal sample was collected far from the dike (3.26 m) to determine the baseline composition of the coal prior to contact metamorphism. This sample is unmetamorphosed, having experienced temperatures <200˚C, and pressures <300MPa (Coombs, 1961). At each sampling location, samples were recovered at least 10 cm into the exposed surface to avoid highly weathered samples. Presumably the coal macerals that were contact metamorphosed had a similar composition to the unmetamorphosed coal seam prior to being altered by the intrusion.

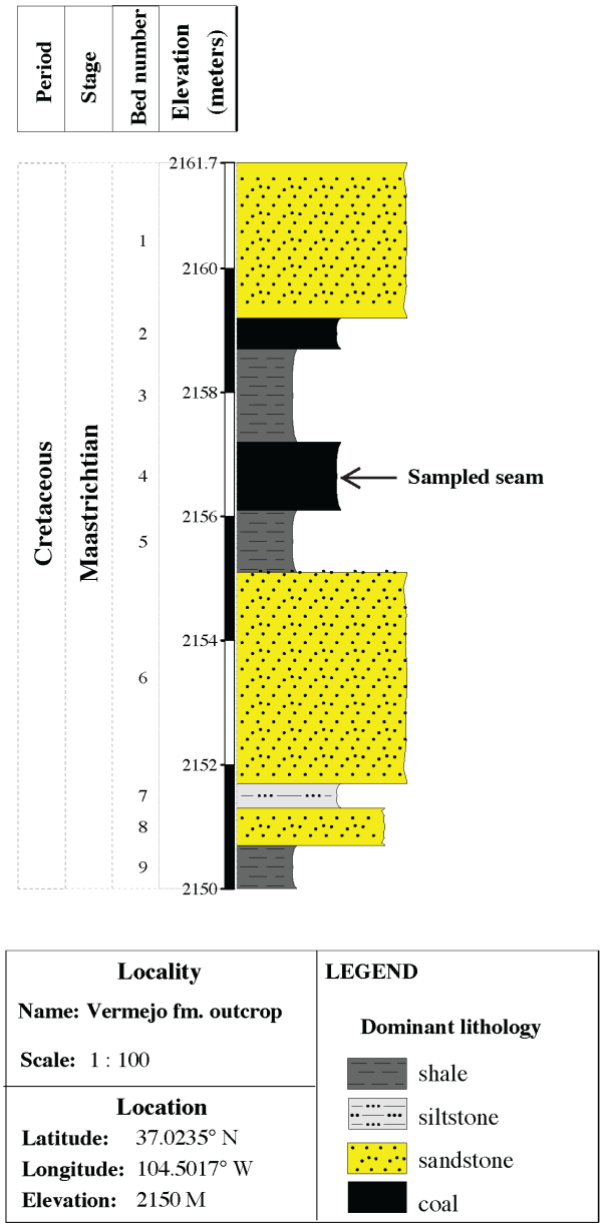

Figure 4.3. Stratigraphic column of Vermejo Fm. outcrop adjacent to the Morley Dike.

Additionally, four samples were obtained from the Dutch Creek No. 2 mine in the Piceance Basin (west-central Colorado), a medium volatile bituminous coal seam adjacent to a 1.5 m thick felsic porphyry dike, which intruded the coal seam at a 60° angle from bedding (Bostick and Collins, 1987). These samples were chosen to evaluate the potential addition of Li from fluids associated with a felsic dike compared to the

mafic Morley Dike. These Upper Cretaceous coal samples were collected (and donated for this study) by Bostick and Collins (1987), who determined the coal/coke sample compositions and VR_o (% vitrinite reflectance using an oil immersion objective). The Dutch Creek No. 2 mine coal is found in the Bowie Shale Mbr. of the Williams Fork Fm. (Hettinger et al., 2000). The chemical content of 66 elements in this sample suite (including Li) were reported by Finkelman et al., (1998) who found that 45 lithophile elements (including Li) had maximum contents at the heated coal and low volatile coke transition zone (31 cm from the dike (0.21 X/D)) where silicates such as illite and kaolinite were abundant (25 wt.% of mineral matter).

Analytical Methods

Vermejo coal samples were prepared according to procedures described by the American Society for Testing and Materials (ASTM) D2013/D2013M-18 (ASTM, 2018a) by first crushing them to -8 mesh (2.36 mm screen openings) using a hammermill crusher. The samples were then halved using a sample riffler with one half being re-bagged for storage. The other half was further reduced in size to -20 mesh (850 micrometer screen openings) using a plate-grinding mill and split again. One split of -20 mesh coal was used for the construction of coal petrographic pellets. The other split was further reduced in size to -60 mesh (250 micrometer screen openings), using a pulverizer, for proximate and total carbon/sulfur analyses. The equipment used was blown out with compressed air and wiped down with disposable towels and isopropyl alcohol between each successive sample.

Geochemistry. Proximate analyses were performed according to ASTM D7582-15 using a Leco TGA 701 analyzer (ASTM, 2015). Total carbon/sulfur analyses were performed according to ASTM D4239-18e1 using a Leco SC-432 carbon/sulfur analyzer (ASTM, 2018b). All values, except for moisture content, are reported on a weight percent, dry basis unless noted otherwise. Mineral matter was calculated from ash and sulfur data using the Parr formula (Parr, 1922, 1928), where:

$$\text{Mineral Matter (wt.\%, dry basis)} = (\text{Ash} \times 1.08) + (\text{Sulfur} \times 0.55). \quad (1)$$

Petrology. Coal petrographic pellets were constructed from the -20-mesh material by mixing 5 g of coal with epoxy resin in 3.2 cm diameter phenolic ring molds and allowed to cure. Upon hardening, samples were polished with a final grit size 0.04 micrometer with colloidal silica. Samples were point counted using a Zeiss Universal reflecting, and transmitting, light microscope equipped with both white and fluorescent (UV) light sources. Maceral percentages are based on 500-point counts of organic material for each sample, in accordance with ASTM D2799-13 (ASTM, 2013) and are reported on a volume percent, mineral matter free (vol.%, mmf) basis. Whole coal maceral percentages were calculated by including the amount of mineral matter in each sample, converted from weight to volume percent based on ASTM D2799-13 (ASTM, 2013), where:

$$\text{Mineral Matter}_{\text{vol.\%}} = [100 \times (\text{MM}_{\text{wt.\%}} / 2.8)] / [((100 - \text{MM}_{\text{wt.\%}}) / 1.2) + (\text{MM}_{\text{wt.\%}} / 2.8)] \quad (2)$$

Vitrinite reflectance analyses were performed according to ASTM D2798-11a (ASTM, 2011) by first calibrating a Hamamatsu 928A photomultiplier with glass standards of known reflectance. The Schott glass standards used for calibration were

SF13-714-276 (0.496 %), LaSF9-850-322 (1.009 %), and LaSF6-961-349 (1.662 %). Following this, 50 random reflectance measurements were collected for each sample using an oil immersion objective ($R_{o\ random}$). Maximum reflectance ($R_{o\ maximum}$) values were calculated from the average $R_{o\ random}$ values using the conversion formula cited in ASTM D2798-11a (ASTM, 2011), where:

$$\text{calculated } R_{o\ maximum} = (R_{o\ random} \times 1.09) - 0.034. \quad (3)$$

Mineral identification was performed on Vermejo coal and coke samples and the Morley Lamprophyre dike rock using a Malvern PANalytical Aeris powder X-Ray Diffractometer with Cu kα radiation. Samples were crushed to <40 μm using a BICO Ring and Puck mill. The OM in the two coal samples with the lowest rank was digested in 35% H_2O_2 at ~85 °C for 3-6 days prior to XRD measurements, following Ward, (1974), while the heavily coked samples were measured without organic oxidation. During H_2O_2 digestion carbonates can also be removed by organic acids that form during the OM digestion process (Ward, 1974). Proximate and ultimate analyses, vitrinite reflectance, mineralogy, and inorganic element determinations for Dutch Creek coal samples were determined previously (Bostick and Collins, 1987; Finkelman et al., 1998).

Contact metamorphism heat flow and vitrinite reflectance modeling. The maximum temperatures (T_{max}) and vitrinite reflectance values reached by coal within the contact aureoles were modeled using the MATLAB® program SILLi 1.0 which was developed by Iyer et al., (2018). This program uses an energy diffusion equation building off of earlier work on the thermal modeling of dikes (Jaeger, 1959, 1957; Lovering, 1935) and calculates the T_{max} at each pre-defined time step along a 1-dimensional path adjacent to the intrusion. The input parameters used here are listed in Table C1 along

with references. Additionally, the measured mean VR_o % was used to predict T_{max} within the contact aureole using the empirical relationship between experimental pressure bomb temperatures and VR_o % (Bostick and Pawlewicz, 1984). Burial T_{max} values, for the samples outside of the contact aureole, were also determined using measured VR_o % (Barker and Pawlewicz, 1994). Predicted VR_o % values were calculated for comparison to measured VR_o % values using the SILLi 1.0 tool which applies the EASY%Ro method (Sweeney and Burnham, 1990) that uses an Arrhenius reaction model to calculate the maturation of vitrinite with respect to time and temperature.

SIMS analyses. Samples of coal and coke were prepared as <2 mm grains embedded in epoxy and then polished with final grit size of <1 μm colloidal silica. Samples were rinsed in 0.1 M mannitol solution to remove surface adsorbed Li (Teichert et al., 2020) followed by rinsing in de-ionized water that was filtered through AmberSep™ G26 H (www.dupont.com) to remove trace Li. Conductive gold coats were deposited on the sample surfaces to compensate for sample charging during SIMS analyses.

Li-content and isotopes were measured at Arizona State University *in-situ* by Secondary Ion Mass Spectrometry (SIMS) using a Cameca (Ametek Inc.) IMS-6f instrument to evaluate the Li-content and isotopic composition of different coal components including macerals and coke. Sample maps were made with a reflected light petrographic microscope, and effort was made to measure macerals while avoiding silicate minerals. An O_2^- primary ion beam was accelerated toward the sample surfaces at –12.6 keV and defocused to a ~30 to 50 μm diameter spot on the sample which was held at +5 kV for a total impact energy of +8.8 keV per primary atom impact. Impacting primary ions sputter off secondary atoms, electrons and ions from the sample surface

(Sigmund, 1969). Positive secondary ions were detected using an electron multiplier detector after being separated by energy and mass/charge, using an electron multiplier detector. Mass interferences were eliminated by adjusting the entrance and exit slits to the mass spectrometer to increase the mass resolving power (MRP = mass/Δmass) to ~1000. This MRP was sufficient to resolve isobaric mass interferences which were $^{24}Mg^{2+}$ and $^{11}BH^{+}$ interfering with $^{12}C^{+}$, $^{14}N^{2+}$ interfering with $^{7}Li^{+}$ and $^{12}C^{2+}$ interfering with $^{6}Li^{+}$.

For Li-content measurements, high energy $^{7}Li^{+}$, $^{12}C^{+}$ and $^{30}Si^{+}$ ions were monitored using a sample voltage offset of –75 V to count only high energy ions thus removing molecular interferences (Hervig et al., 2006) and to reduce counts enough for all species to be measured on the electron multiplier detector. Using all the settings described above has been shown to simplify the determination of Li-contents, based on measured $^{7}Li^{+}/^{12}C^{+}$ ratios, by eliminating matrix effects caused by variations sample O-contents (Teichert et al., 2022). The measured $^{7}Li^{+}/^{12}C^{+}$ ratios of each spot measurement were used to determine the Li-contents using the Li-ion implanted polycarbonate standard described in Teichert et al., (2022), which has H-C-O abundances similar to kerogen. The homogenous polycarbonate Li-implant standard was measured prior to analyses of coal samples to determine the Li-content calibration factor (k* =142) used to determine Li content with the following expression.

$$Li\ ppm\ atomic = (^{7}Li^{+}/^{12}C^{+} \times k^{*}) \times C_{af} \times 1.0832 \qquad (4)$$

where;

C_{af} = Carbon atom fraction of the sample being measured

1.0832 = (^{6}Li + ^{7}Li)/(^{7}Li) to account for ^{6}Li

After determining the Li ppm atomic, contents were converted to wt. ppm (μg/g) using the stoichiometry of each sample.

Note that the Li-content standard (polycarbonate) lacks any significant contribution of inorganic elements commonly present in kerogen that might alter the secondary ion yields of both $^{7}Li^{+}$ and $^{12}C^{+}$. For SIMS spot analyses where inorganic elements have concentrations >1% trace element calibrations become more approximate (Williams, 1985).

Lithium isotope ratios are reported as the per mille deviation from the LSVEC standard (Flesch et al., 1973) with the following expression.

$$\delta^{7}\text{Li}\ ‰ = \left(\frac{R_{Sample} - R_{Standard}}{R_{Standard}}\right) \times 1000 \quad (5)$$

where R = $^{7}Li/^{6}Li$ and the standard is NIST SRM 612 (R=12.0192)

For isotope measurements, $^{7}Li^{+}$ and $^{6}Li^{+}$ were both monitored with no energy offset. To determine the instrumental mass fractionation (IMF), measurements of the NIST SRM 612 silica-based glass with a certified Li content of 40 μg/g (SRM 612 certificate, 2012) and δ^{7}Li values of +32‰ (Bluztajn et al., 2004) were taken before and after measurements of unknown samples. NIST SRM 612 standard measurements produced consistent values of the IMF ($2\sigma_x$ ±1.4‰) during each analytical session. Isotope ratios measured on coal macerals were corrected by +10‰ because of a matrix effect between the NIST SRM 612 glass and organic materials (Teichert et al., 2022).

Results

The sample distances from the igneous dikes, proximate analysis and average random vitrinite reflectance (VR_o %) values are summarized in Table 4.1. For the Vermejo and Dutch Creek coals the volatile matter decreased while the ash yield, mineral matter and the average VR_o increased with increasing proximity to the dike. Table 4.2 shows the wt. % of coke and major maceral groups of the coals studied (detailed organic petrology shown in Supplementary Information, Table C.2), the minerals present in each sample (in order of abundance) and the mineral matter vol. %. Notably, the coke content of the coal increases closer to the dike as the volatile matter is lost from vitrinite and liptinite macerals. Representative reflected light microscope images showing analytical craters in different macerals and coke in select Vermejo and Dutch Creek coals are shown in Figs. 4.4 and 4.5. The macerals type/coke, δ^7Li values, Li-contents and $^{12}C^+/^{30}Si^+$ ratios for spot analyses are tabulated below each figure (Tables 4.3 and 4.4). All individual spot analyses measured in this study can be found in Table C.3. Crater sizes vary based on the primary beam current used. For macerals with very low Li-contents it was necessary to use higher primary beam currents to obtain enough counts for statistically significant Li-isotope ratios. Table 4.5 summarizes Li-contents determined by bulk techniques (Finkelman et al., 1998) as well as mean Li-contents and δ^7Li values of multiple spot analyses made on different organic maceral types in this SIMS study. The large 2σ values (Table 4.5) show the Li heterogeneity of the samples among the various coal components.

Table 4.1

Some Values from Proximate Analyses of Coal and Coke Samples

Sample	Distance from Dike (cm)	Residual Moisture (wt.%, ar)	Volatile Matter (wt.%, dry)	Ash yield (wt.%, dry)	Mineral Matter (wt.%, dry)	Total carbon (wt.%, dry)	Total sulfur (wt.%, dry)	Avg. VR_o random (%)
Vermejo Samples								
V-A	4	1.0	6.0	35.8	38.8	60.9	0.20	4.09
V-B	34	1.9	9.3	25.4	27.7	68.4	0.45	3.92
V-C	84	2.1	10.5	19.8	21.7	72.9	0.55	3.14
V-D	123	2.1	11.3	16.2	17.9	76.6	0.59	3.03
V-E	143	4.0	29.8	12.3	13.6	70.9	0.62	1.02
V-UM	330	5.6	37.9	5.7	6.5	73.7	0.64	0.68
Dutch Creek Samples (Bostick and Collins, 1987; Finkelman et al., 1998)								
DC-B	9	1.3	13.0	19.1	20.9	70.9	0.54	4.86
DC-D	24	1.4	10.6	9.2	10.4	83.0	0.89	3.91
DC-F	42	0.7	13.6	7.2	8.1	83.1	0.58	2.03
DC-K	106	0.7	28.0	4.8	5.4	83.7	0.45	1.15

VR_o- vitrinite reflectance in oil; ar stands for "as recieved". The Dutch Creek samples use the same naming scheme used in Finkelman et al., (1998).

Table 4.2

Major Maceral Groups and Mineralogy of Coal and Coke Samples

Sample	Distance from Dike (cm)	Vitrinite (wt.%, dmmf)	Inertinite (wt.%, dmmf)	Liptinite (wt.%, dmmf)	Coke (wt.%, dmmf)	Minerals present	Mineral Matter (vol.%, dry)
Vermejo Samples							
V-A	4	0.0	24.8	0.0	75.2	qtz	23.4
V-B	34	0.0	23.2	0.0	76.8	qtz, kao	15.6
V-C	84	0.0	23.2	0.0	76.8	qtz, kao	11.8
V-D	123	0.0	17.6	0.0	82.4	qtz, kao	9.5
V-E	143	48.0	13.2	1.6	37.2	qtz, dck, vrm, aer kao	7.1
V-UM	330	67.2	29.2	3.6	0.0	qtz, kao, dck, vrm, ame, aer	3.2
Morley Dike	NA	NA	NA	NA	NA	bar, crn, chl, dck, kao, bt, cal, aug	NA
Dutch Creek Samples (Bostick and Collins, 1987; Finkelman et al., 1998)							
DC-B	9	nm	nm	nm	nm	cal, ank, qtz, fs, sd, py, hm	*10.5
DC-D	24	nm	nm	nm	nm	ank, qtz, cal, py, hm, sd, fs	*5.2
DC-F	42	nm	nm	nm	nm	qtz, ank, kao, sd, ill, py, cal, fs	*4.0
DC-K	106	nm	nm	nm	nm	ank, kao, sd, fs, ill, py, hm, qtz	*2.7

*Mineral matter vol.% approximated from mineral matter wt.% for some samples by dividing by 2 following Matjie et al., (2016). dmmf indicates " dry mineral matter free"; nm = not measured; NA = not applicable.

Qtz = Quartz; Kao = Kaolinite; Dck = Dickite; Vrm = Vermiculite; Aer = Aerinite; Ame = Amesite; Bar = Barite; Crn = Corundum; Chl = Chlorite; Bt = Biotite; Cal = Calcite; Aug = Augite; Ank = Ankerite; Sd = Siderite; Ill = Illite; Fsp = Feldspar group; Py = Pyrite; Hm = Hematite

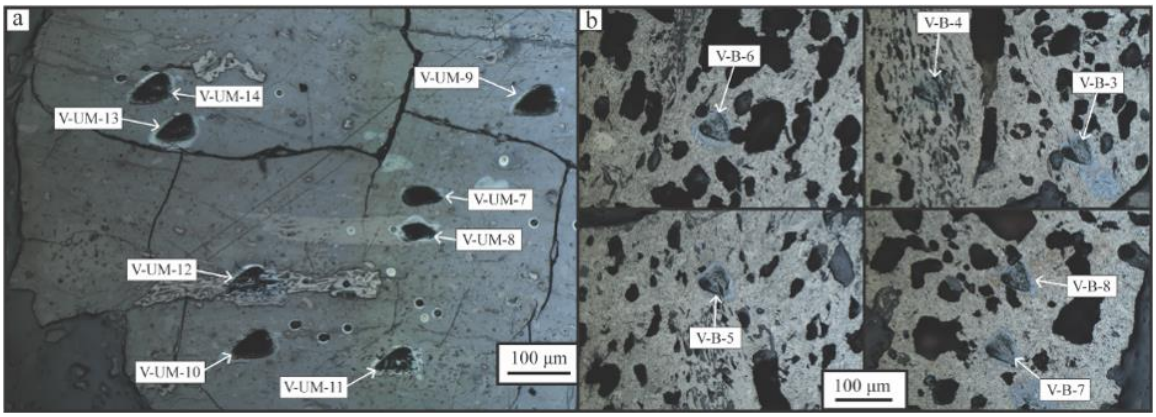

Figure 4.4. Reflected light microscope images of Vermejo coal samples (a) V-UM and (b) V-B with analytical craters labeled.

Table 4.3

SIMS Results for Selected Vermejo Coal Spot Measurements

Measurement	Primary maceral or coke	δ^7Li (‰)	S.E. (‰)	P.E. (‰)	Li (µg/g)	$^{12}C^+/^{30}Si^+$
V-UM-7	Vitrinite	-37.8	1.9	2.2	0.23	9.37
V-UM-8	Inertinite	-22.9	2.2	2	0.14	147.70
V-UM-9	Vitrinite	-30.0	1.9	2.1	0.20	31.97
V-UM-10	Vitrinite	-21.0	2.3	2.4	0.21	23.55
V-UM-11	Inertinite	-14.0	1.1	1	0.78	1.42
V-UM-12	Inertinite	-7.1	0.7	0.8	1.67	0.92
V-UM-13	Vitrinite	-26.8	1.9	2.1	0.33	7.26
V-UM-14	Liptinite	-19.2	2	2.4	0.26	16.90
V-B-3	Coke	2.8	1.4	1.3	0.37	4.22
V-B-4	Inertinite	-0.3	1.2	1	0.41	12.73
V-B-5	Coke	9.0	0.9	0.9	0.55	2.96
V-B-6	Coke	11.8	1	1	0.82	2.02
V-B-7	Coke	10.3	0.9	1	0.46	2.16
V-B-8	Coke	7.3	0.7	0.8	1.05	1.40

Standard error (S.E.) and Poisson error (P.E.) are 1σ. V-UM is the distal coal sample and V-B is 34 cm from the dike.

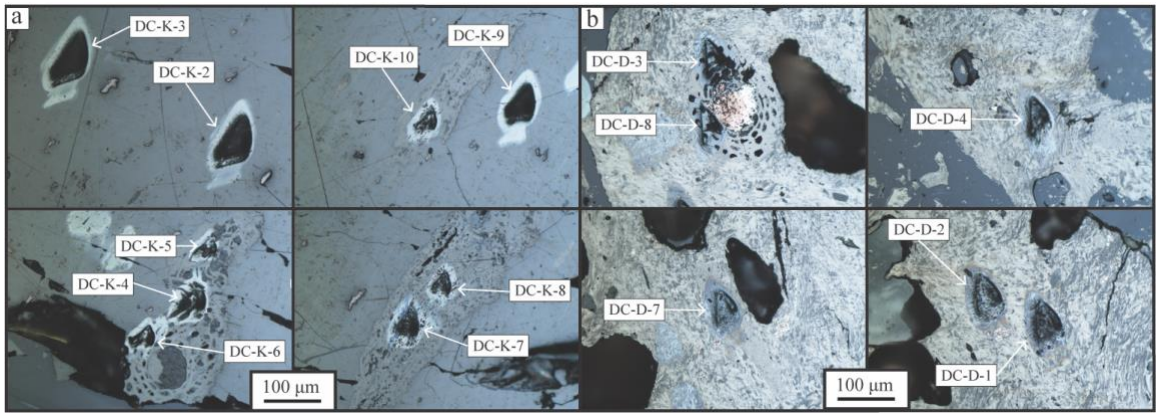

Figure 4.5. Reflected light microscope images of Dutch Creek coal samples (a) DC-K and (b) DC-D with analytical craters labeled. Analytical craters vary in size according to the primary current used.

Table 4.4

SIMS Results for Selected Dutch Creek Coal Spot Measurements

Measurement	Primary maceral or coke	δ^7Li (‰)	S.E. (‰)	P.E. (‰)	Li (µg/g)	$^{12}C^+/^{30}Si^+$
DC-K-2	Vitrinite	-1.5	1.6	1.6	0.04	831.03
DC-K-3	Vitrinite	-0.4	1.5	1.3	0.31	115.03
DC-K-4	Inertinite	9.5	0.4	0.5	9.82	1.35
DC-K-5	Inertinite	4.0	0.5	0.5	12.46	1.17
DC-K-6	Inertinite	-4.8	1	1.1	1.39	10.00
DC-K-7	Inertinite	1.8	0.5	0.4	7.22	2.62
DC-K-8	Inertinite	3.7	0.4	0.4	6.86	3.04
DC-K-9	Vitrinite	-6.8	1.6	1.3	0.04	727.96
DC-K-10	Inertinite	5.8	0.6	0.4	5.74	3.96
DC-D-1	Coke	8.8	1.1	1.1	0.34	45.87
DC-D-2	Coke	11.8	1	1	0.46	27.58
DC-D-3	Inertinite	-3.8	1	0.6	0.63	1.54
DC-D-4	Coke	12.5	0.7	0.6	0.63	33.04
DC-D-7	Vitrinite	4.9	0.8	0.9	0.76	19.22
DC-D-8	Inertinite	2.1	1.3	1.3	0.25	4.18

DC-K is the country rock sample and DC-D is 24 cm from the dike.

Table 4.5

Average Li Contents and Isotope Ratios of Coal Macerals and Coke

Sample	Distance from Dike (cm)	Bulk Li contents (μg/g)	Avg. Li contents from SIMS (μg/g)	S.E.	δ^7Li (‰)	S.E. (‰)	n
Vermejo Samples							
V-A	**4**	**nm**					
Coke			0.9	0.2	-5.0	4.0	5
V-B	**34**	**nm**					
Coke			0.6	0.1	9.4	1.4	7
Inertinite			0.4	NA	-0.3	NA	1
V-C	**84**	**nm**					
Coke			0.7	0.04	3.0	0.8	4
Inertinite			0.5	NA	-3.0	NA	1
V-D	**123**	**nm**					
Coke			0.6	0.1	4.8	1.5	3
Inertinite			1.5	1.1	11.6	6.1	2
V-E	**143**	**nm**					
Vitrinite			0.9	0.3	-9.5	2.2	5
Coke			0.8	0.2	-10.8	1.5	2
Liptinite			0.9	NA	-8.3	NA	1
V-UM	**330**	**nm**					
Vitrinite			0.3	0.04	-28.4	1.6	11
Inertinite			0.7	0.3	-10.5	3.6	5
Liptinite			0.2	0.1	-15.4	3.7	2
Sample	Distance from Dike (cm)	Bulk Li contents (μg/g)	Avg. Li contents from SIMS (μg/g)	S.E.	δ^7Li (‰)	S.E. (‰)	n
Dutch Creek Samples							
DC-B	**9**	**7.1**					
Coke			0.5	0.1	7.1	2.5	4
Inertinite			0.1	NA	-1.4	NA	1
Vitrinite			0.1	NA	14.0	NA	1
DC-D	**24**	**7.1**					
Coke			0.4	0.1	12.8	1.5	5
Inertinite			0.4	0.2	-0.8	2.9	2
Vitrinite			0.8	NA	4.9	NA	1
DC-F	**42**	**8.1**					
Coke			0.2	0.03	9.0	0.8	3
Inertinite			2.3	0.5	-0.9	3.2	2
Vitrinite			0.3	NA	17.6	NA	1
DC-K	**106**	**4.8**					
Vitrinite			0.1	0.1	-3.3	0.1	4
Inertinite			7.2	0.1	3.3	0.1	6

S.E. values are $2\sigma_x$. Bulk Li contents from Finkelman et al., (1998) for Dutch Creek samples.

nm = not measured.

Heat-Flow Modeling of Contact Aureoles

T_{max} and VR_o % values for each sample were plotted against distance from the dike (X) divided by the width of the dike (D) for the Vermejo and Dutch Creek coal samples (Fig. 4.6). It has been observed that contact aureoles are typically one dike thickness (X/D = 1; Bostick, 1973) or two dike thicknesses (X/D = 2; Dow,1977), thus plotting the distance from the dike as X/D or a percentage of the dike thickness makes it simple to compare contact aureoles of different dike widths (Barker et al., 1998). T_{max} values predicted from heat-flow modeling (Iyer et al., 2018) are compared to T_{max} values derived from a logarithmic relationship between VR_o % and T_{max} (Bostick and Pawlewicz, 1984), and show a better fit for Dutch Creek coal (Fig. 4.6c) than for Vermejo Coal sample (Fig. 4.6a). The burial T_{max} values for samples farthest from the igneous dikes (V-UM = 104 °C; D-K = 147 °C) are indicated by triangles and are significantly lower than T_{max} values derived from heat-flow modeling for both contact aureoles. Additionally measured values for VR_o % are compared to the EASY%Ro modeled VR_o % values (Figs. 4.6b & 4.7d). As with T_{max}, Dutch Creek coal VR_o % values (Fig. 4.6d) match SILLi 1.0 modeling results better than the higher temperature Vermejo coal samples (Fig. 4.6b). Using VR_o % to determine the width of the contact aureoles, it is observed that the contact aureole is ~1.5 dike widths for the Vermejo coal seam and only ~0.5 dike widths for the Dutch Creek coal seam.

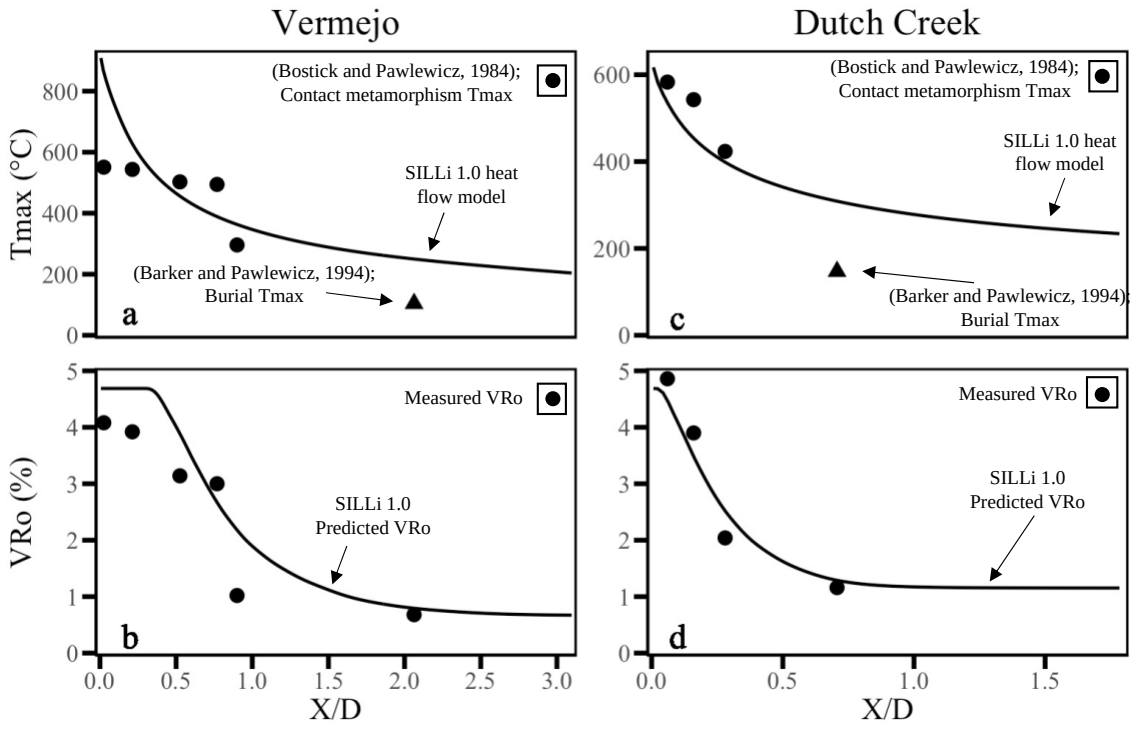

Figure 4.6. Vermejo and Dutch Creek contact aureoles T_{max} and VR_o % plotted against X (distance from the dike) divided by D (dike width). In 6a and 6c, heat flow modeling T_{max} values (lines) are compared to T_{max} values derived from an empirical relationship between T_{max} and VR_o (points). Measured VR_o values (points) are compared to predicted VR_o values from the EASY%Ro method (lines) in 6b and 6d. The modeled and empirically derived T_{max} values as well as measured and modeled VR_o values coincide more closely for the Dutch Creek contact aureole than for the Vermejo contact aureole.

SIMS Measurements of Li-Contents and Li-Isotopes for Dike Cut Coal Samples

Finkelman et al., (1998) noted that: 1) removal of elements through volatilization, 2) concentration of refractory phase elements and 3) the loss or addition of elements from fluids (magmatic or hydrothermal) are the three mechanisms by which an igneous intrusion could change the chemical composition of a coal. Although many trace elements remain in refractory phases (e.g., quartz, meta-kaolin), up to 50% of the coal mass can be lost through the release volatile matter and moisture from organics during the thermal maturation. Therefore, an increase in concentration of a given trace element does not necessarily equate to an addition of that element but may be resulting from a

loss of mass and residual concentration. Understanding the loss of mass is complicated in contact metamorphic settings where there is likely the addition of mass to the country rock from dike-related fluids precipitating authigenic minerals as chemically active fluids migrate away from the dike.

For the Vermejo coal samples the loss of mass was estimated at ~30% in the heavily coked zone (Sample V-A through V-D) and a 10% for sample V-E based on changes in volatile matter (Table 4.1). This mass change was used to correct for elemental compositions of macerals and coke within the contact aureole for comparison to macerals in the unmetamorphosed coal. Finkelman et al., 1998 estimated a total mass loss of 20% for Dutch Creek coal samples within the coked zone and this same estimation was used to correct for Li-contents measured here. Mass loss corrected Li-contents are shown for the Vermejo (Fig. 4.7) and Dutch Creek (Fig. 4.8) macerals plotted against X/D.

The Li-contents of the Vermejo macerals and coke overlap among all samples, with mean Li-contents ≤1.5 μg/g and no clear trends. For the Dutch Creek coal, several high Li (5-13 μg/g) inertinite grains were measured on the unmetamorphosed coal samples while the measured vitrinite spots were <0.5 μg/g for the same sample (Fig. 4.8). Aside from some high Li inertinite spot analyses in samples DC-K and DC-F the Li-contents of all other macerals are <1 μg/g (Fig. 4.8) with no clear trends related to changes in Li-contents among samples.

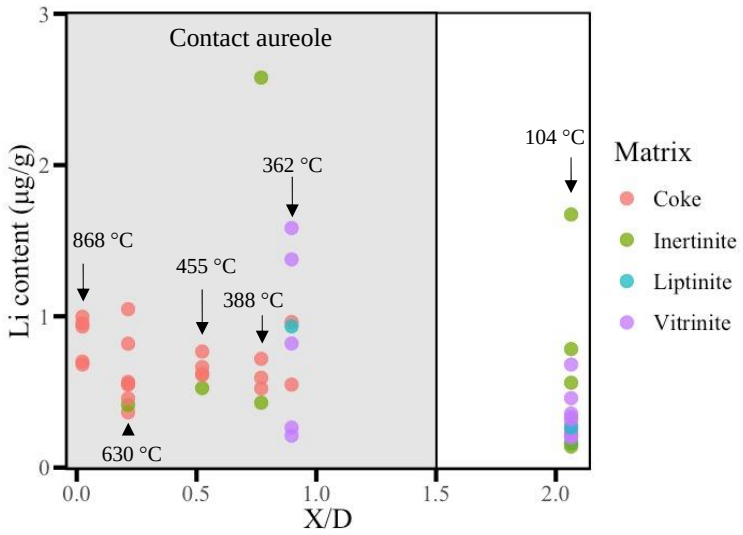

Figure 4.7. Plot of Li-content measurements corrected for mass loss against X/D for Vermejo coal samples. Points colors indicate maceral type or coke. The contact aureole is shown in gray. T_{max} values from SILLi 1.0 heat flow modeling are labeled for each sample in the contact aureole. The burial T_{max} is shown for the V-UM coal sample outside of the contact aureole. There is significant overlap among the Li-contents of spot measurements from each sample with no clear trend of increasing or decreasing Li-content.

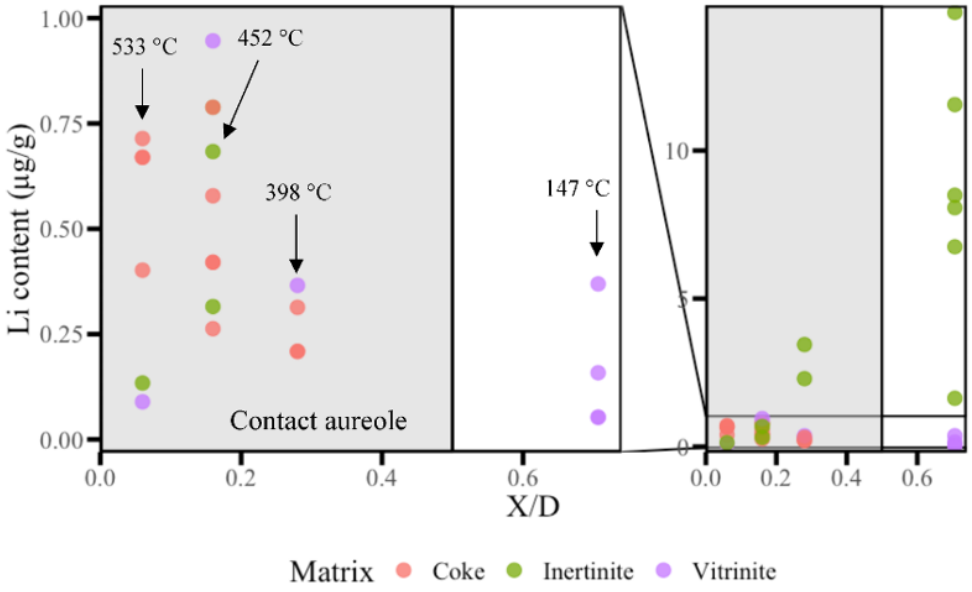

Figure 4.8. Plot of Li-content measurements corrected for mass loss against X/D for Dutch Creek coal samples. Point colors indicate maceral type or coke. The plot on the left is expanded to show the lower Li-contents <1 µg/g. The UM sample (DC-K) has several spot measurements in inertinite grains with significantly higher Li-contents than spots measured in other samples, likely due to the silicate pore filling in the inertinite macerals.

The δ^7Li values of each measurement are plotted against X/D for the Vermejo coal seam (Fig. 4.9) and the Dutch Creek coal seam (Fig. 4.10). Analytical errors of individual measurements are not shown but the mean $2\sigma_x$ value for a given Li-isotope measurement was ±2.4‰. Large variability in δ^7Li was observed, with samples having ranges ≥8‰ among different organic maceral types and minerals. Vitrinite macerals were particularly light in the unmetamorhposed coal (–28‰ for Vermejo coal and –3‰ for Dutch Creek coal) compared to the average inertinite and liptinite in those samples (Figs. 4.9 & 4.10). The mean δ^7Li of the Vermejo unmetamorphosed coal vitrinite was 18 to 37‰ lighter than vitrinite macerals and coke measured within the contact aureole. Likewise, the δ^7Li of the Dutch Creek unmetamorphosed coal vitrinite was 8 to 21‰ lighter than coke and vitrinite within the contact aureole (Table 4.5). For the Dutch Creek coal samples, the inertinite macerals are isotopically lighter (by 6 to 19‰) than coke and vitrinite within the contact aureole (Fig. 4.10), but in the unmetamorphosed coal the average inertinite samples are 7‰ heavier than the average vitrinite.

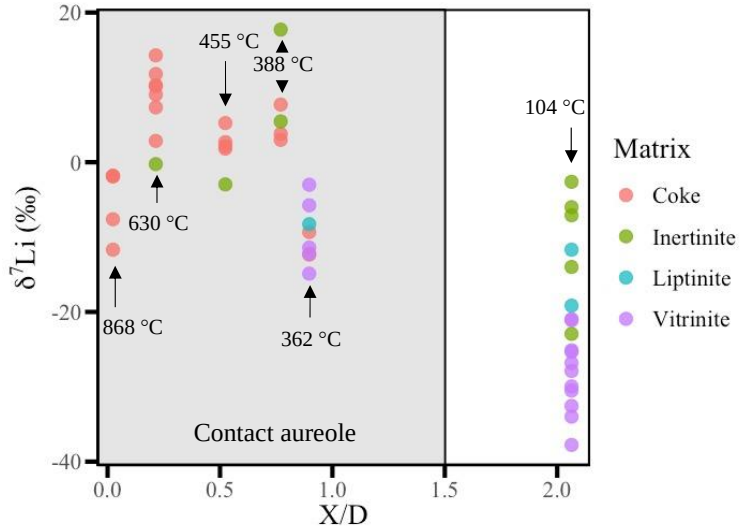

Figure 4.9. Plot of δ^7Li measurements against X/D for Vermejo coal samples. The unmetamorphosed coal sample (V-UM) has significantly lower δ^7Li values than samples within the contact aureole with particularly lower δ^7Li among vitrinite macerals.

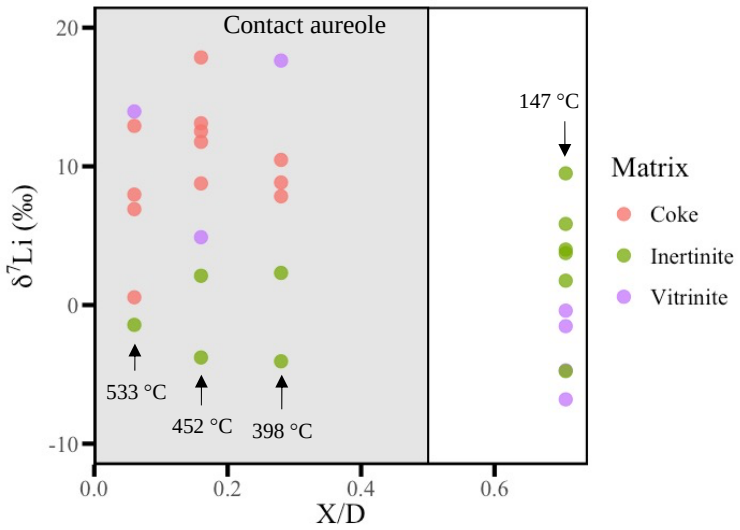

Figure 4.10. Plot of δ^7Li measurements against X/D for Dutch Creek coal samples. All samples have mean δ^7Li values within error although there is some variation among different maceral groups and coke.

The Li-contents and δ^7Li of spot measurements are plotted against the $^{12}C^+/^{30}Si^+$ count ratio for the Vermejo and Dutch Creek coal samples (Figs. 4.11 & 4.12). The $^{12}C^+$ counts per second (cps) from spot to spot vary up to a factor of 10 although the mean $2\sigma_x$ in the $^{12}C^+$ cps among all carbonaceous spots is only ± 8%. The $^{30}Si^+$ cps, however, commonly range over 4 orders of magnitude from spot to spot, thus the change in the $^{12}C^+/^{30}Si^+$ is typically more indicative of changes in the $^{30}Si^+$cps than $^{12}C^+$ cps (Fig. C.1). For the Vermejo coal samples there is a weak negative correlation between both the Li-contents (R^2 = 0.48; Fig. 4.11a) and δ^7Li (R^2 = 0.55; Fig. 4.11b) with the $^{12}C^+/^{30}Si^+$ count ratios. For the Dutch Creek coal there is a stronger negative correlation between Li-contents and $^{12}C^+/^{30}Si^+$ (R^2 = 0.74; Fig. 4.12a) but no correlation between δ^7Li and $^{12}C^+/^{30}Si^+$ (Fig. 4.12b). The $^{12}C^+/^{30}Si^+$ ratios on vitrinite macerals in both the mafic and felsic intrusive contact aureoles are higher than the liptinite and inertinite macerals, and coke.

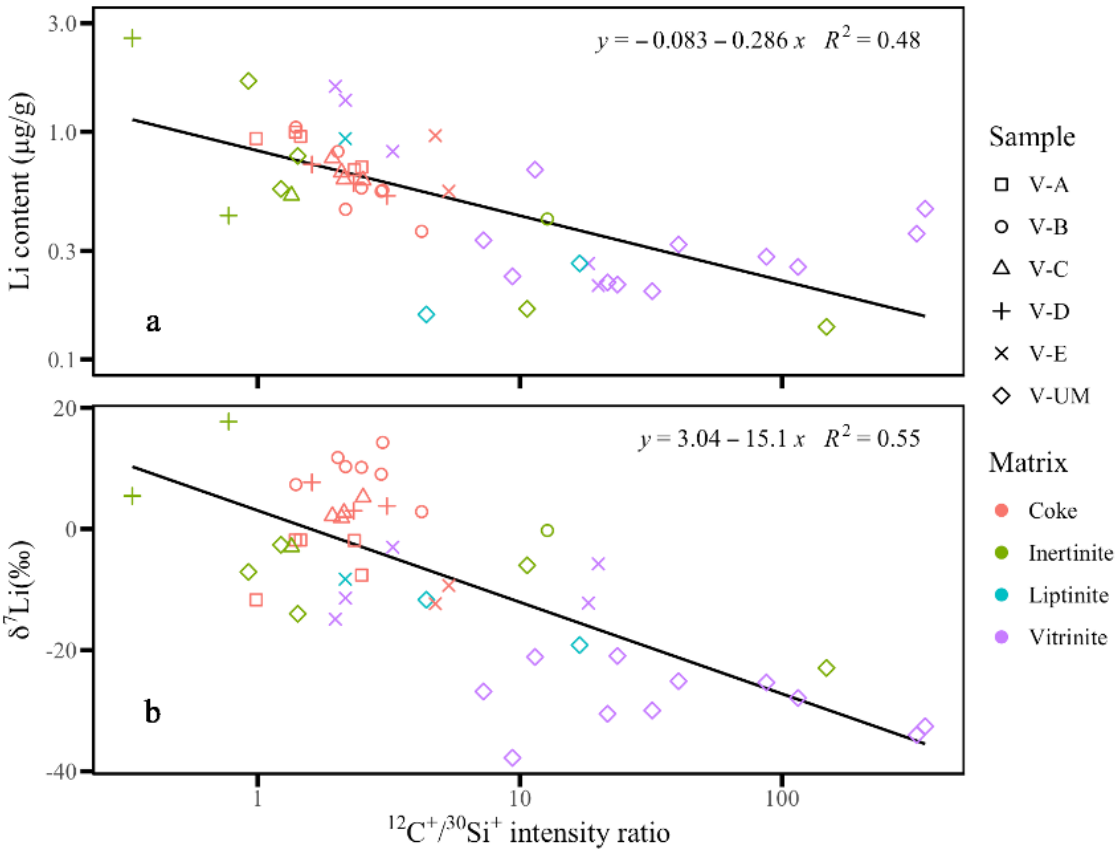

Figure 4.11. Scatter plot of Vermejo coal (a) Li-contents and (b) δ^7Li against $^{12}C^+/^{30}Si^+$ count ratio with the point shape indicating the sample and color indicating organic petrology. Linear regression trendlines, equations and R^2 values are shown. There are weak negative correlations between both Li-content and $^{12}C^+/^{30}Si$ (R^2 = 0.48) as well as δ^7Li and $^{12}C^+/^{30}Si^+$ (R^2 = 0.55).

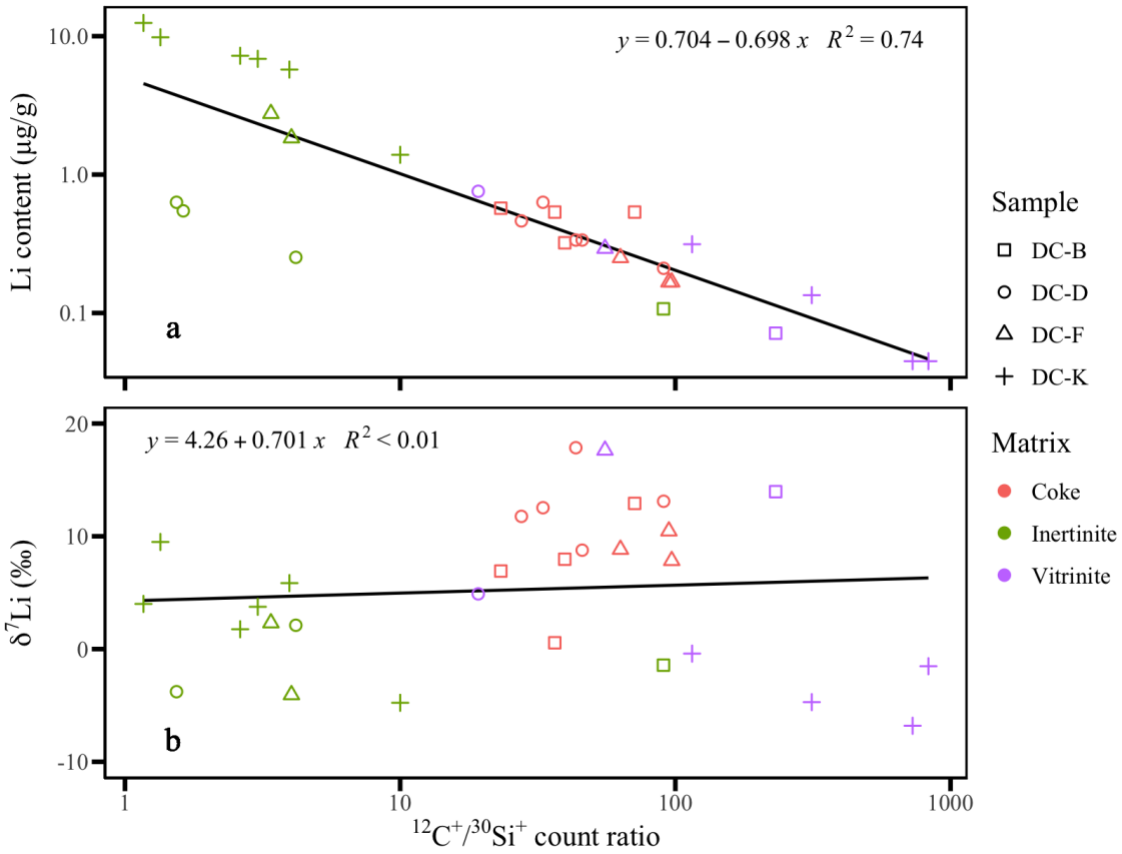

Figure 4.12. Scatter plot of Dutch Creek coal (a) Li-contents and (b) δ^7Li against $^{12}C^+/^{30}Si^+$ count ratio with the point shape indicating the sample and color indicating maceral type or coke. Linear regression trendlines, equations and R^2 values are shown. There is negative correlation (R^2 = 0.74) between the Li-content and $^{12}C^+/^{30}Si^+$ and no correlation between δ^7Li and $^{12}C^+/^{30}Si$.

Discussion

Contact Aureole Temperature Modeling

The width of a contact aureole is directly related to several physical properties of the country rock and the intrusion (e.g., thermal diffusivity, temperature, and intrusion width) (Annen, 2017). In addition to the compositional differences between lamprophyre dike intruding the Vermejo coals and the felsic porphyry dike intruding the Dutch Creek coal samples, the major difference was the emplacement temperature. Mafic intrusions are commonly in the temperature range of 900 °C to 1200 °C (Galushkin, 1997;

Newcombe et al., 2020; Wang and Manga, 2015), while felsic porphyry intrusions are typically emplaced at temperatures ranging from 650 °C to 800 °C (Dilles et al., 2015; Meng et al., 2018; Olson et al., 2017; Schöpa et al., 2017). The higher emplacement temperature for the mafic lamprophyre dike compared to the felsic porphyry dike resulted in a wider contact aureole according to the heat flow modeling (Fig. 4.6). The modeled contact aureole width for the Dutch Creek coal (~0.5 X/D) is consistent with the findings of Finkelman et al., (1998), who found that coal at 0.6 X/D had similar proximate, ultimate and VR_o % results as samples much farther from the dike. For the Vermejo coal contact aureole the visible contact aureole was ~1 X/D. Sample V-E, which was sampled at 0.95 X/D, had a VR_o of 1.02% in comparison to 0.68% for the sample V-UM (sampled at 2.1 X/D). While no samples were collected between V-UM and V-E based on modeling results coal at just above 1 X/D also has elevated VR_o % values relative to sample V-UM, more closely matching the modeled contact aureole width of 1.5 X/D.

Barker et al., (1998) found that vitrinite reflectance becomes an unreliable paleothermometer at distances within 0.3 X/D or at temperatures >300 °C and suggested this may be due to water vapor and supercritical fluids changing the chemical evolution paths of vitrinite. Here, predicted T_{max} values derived from vitrinite reflectance (Bostick and Pawlewicz 1984) approach the T_{max} heat-flow modeling results for the Dutch Creek coal samples (Fig. 4.6c), but greater deviations are observed for the higher temperature Vermejo coal samples (Fig. 4.6a).

Contact Metamorphic Variations of Li-Contents and Li-Isotopes in Coal

To evaluate chemical changes observed in the contact metamorphic zone within a single coal seam, the assumption is made that the depositional unit was relatively

homogenous prior to contact metamorphism. For the Dutch Creek coal Finkelman et al., (1998) found that sample DC-K (unmetamorphosed coal) yielded similar results for proximate and ultimate analyses to samples collected much farther from the dike, thus representing the coal seam average composition. Additionally, bulk Li-contents were similar in the two samples collected beyond the contact aureole (4.7 and 4.8 μg/g) (Finkelman et al., 1998).

Vermejo Coal contact metamorphism. Coal devolatilization, refractory element concentration, and removal or addition of elements by fluids are mechanisms by which the inorganic elemental composition of a sample may change (Finkelman et al., 1998; Section 3.2, this paper). Because there are several potential mechanisms involved in changing the Li-content of coal during contact metamorphism, examining the Li-isotope composition relative to Li-contents can be useful to determine whether Li-flux occurred. However, the mean Li-contents of Vermejo coal macerals are all ≤1.5 μg/g (Table 4.5) and show insignificant changes in Li-content in the contact aureole. Yet, the δ^7Li values of unmetamorphosed coal (V-UM) vitrinite are 18 to 37‰ lighter than macerals within the contact aureole (Table 4.5; Fig. 4.9), suggesting there was preferential loss of ^{6}Li from macerals during contact metamorphism. Vitrinite is the most isotopically light Li maceral type in the unmetamorphosed coal with a mean δ^7Li value of –28.4‰ ± 1.6 (n = 11), which is lighter than the mean values for liptinite (–15.4‰ ± 3.7; n = 2) and inertinite (–10.5‰ ± 3.6; n = 5) (Table 4.5). Any of these macerals could be a source of isotopically light Li to pore fluids and might release the Li at different thermal maturities. However, it is likely that vitrinite is the most significant here, considering that it is the most abundant organic maceral (67.2% dmmf), liptinite is minor (3.6% dmmf) and

inertinite has a low potential for any hydrocarbon release (Zhou et al., 2021), which is thought to be associated with release of Li from kerogen (Teichert et al., 2020; Williams et al., 2015).

According to measurements from acid leachates of low-rank coals, up to 50% of the Li may be associated with the organics (Finkelman et al., 2018). Similarly, sequential extraction of Li from Marcellus shale source rocks showed that up to 20% of the total Li may be hosted by the organic matter (Phan et al., 2016). For Li-isotopes, Li et al., (2020) measured an organic rich Hawaiian soil and showed that the organic fraction of the soil had δ^7Li values ~ 20‰ lighter than the mineral fractions of the soil (i.e., silicates, oxides and carbonates). The preferential accumulation of ^{6}Li in soil organic matter may be the mechanism that leads to lighter δ^7Li values of low-rank coals compared to mature coals that appear to have preferentially released ^{6}Li (Fig. 4.1; Teichert et al., 2020). While the unmetamorphosed coal (V-UM) is not low-rank based on its VR_o (0.68%), it is a high volatile bituminous coal that has yet to release much of its original volatile matter and hydrocarbons (Table 4.1). Sample V-UM is also comprised of 67.2% vitrinite (Table 4.2) which contains the isotopically light (–28‰) Li. The weak negative correlation between δ^7Li values and $^{12}C^+/^{30}Si^+$ (Fig. 4.11b) and the 18 to 37‰ lighter δ^7Li in the unmetamorphosed coal (V-UM) vitrinite compared to coke and vitrinite macerals within the contact aureole, shows that the original OM is enriched in ^{6}Li, and the metamorphism preferentially released the ^{6}Li. As isotopically light Li is released from the OM it can accumulate in pore fluids where it may eventually be incorporated into authigenic minerals. Additionally, the isotopically light Li in porefluids could become incorporated into marine carbonates which can undergo recrystallization during diagenesis (Dellinger

et al., 2020), complicating paleoclimate interpretations drawn from the δ^7Li of those carbonates. Despite the Li-contents in the unmetamorphosed Vermejo coal macerals being typically <1.5 μg/g, porefluids could become concentrated up to ~10 μg/g with isotopically light Li from OM considering a typical coal porosity of 10% (Gan et al., 1972) leading to a rock: porefluid mass ratio in coal of ~12.

Because lithium is an incompatible element, it will remain in magma becoming increasingly concentrated as the magma composition evolves (Best, 2002). The mafic Morley Dike is a lamprophyre which contains phenocrysts of micas which are a likely host of Li (Woolley et al., 1996). The Li-contents of mafic magmas are ~10 μg/g on average and have δ^7Li values typically ranging from –4 to +8‰ (Ryan and Langmuir, 1987; Tomascak et al., 2016). Of course, as igneous intrusions ascend through country rock the Li-content of the magma and magmatic fluids can be enhanced by the assimilation of Li-rich country rock (e.g., Li-rich clays; evaporites). The Morley Dike traveled through ~1500 m of primarily Mesozoic and Paleozoic sandstone, shale, limestone, and conglomerate (Johnson and Finn, 2001) prior to reaching the Vermejo formation. If the dike was enriched in Li either from primary magma or by assimilation, it might enrich pore fluids in Li, but this is not observed in the samples studied that all show low Li-concentrations (~1 μg/g) in the coke and coal within the contact aureole (Fig. 4.7).

Dutch Creek Coal contact metamorphism. The Dutch Creek felsic porphyry intrusion, being from a more evolved magma than the mafic intrusion, was selected for comparison as it might contain higher Li-contents. At the Dutch Creek locality, macerals in sample DC-K (unmetamorphosed coal) have mean δ^7Li values of ranging from –3.3‰

(vitrinite) to +3.3‰ (inertinite) which is consistent with the general trend for U.S. coals (Teichert et al., 2020) showing δ^7Li as a function of VR_o% (1.15%; Fig. 4.1). In this case, isotopically light Li may have been mostly released during burial leaving residual coal enriched in ^{7}Li prior to dike emplacement. Vitrinite in the unmetamorphosed coal (DC-K) is isotopically lighter (–3.3‰ ± 0.1, n = 4) than coke (+10.0‰ ± 2.5, n = 12) and vitrinite (+12.2‰ ± 7.6, n = 3) measured in the contact aureole samples, which suggests that some isotopically light organically bound Li was released upon dike emplacement.

The measured Li-contents vary widely in the unmetamorphosed coal sample (DC-K), and inertinite spot analyses with higher Li-contents (1.4 - 12.5 µg/g) are correlated with lower $^{12}C^+/^{30}Si^+$ (Fig. 4.12a) while vitrinite spots had an average Li-content of only 0.2 µg/g and higher $^{12}C^+/^{30}Si^+$ values. It is likely that the during inertinite spot analyses the primary ion beam overlapped on Li-bearing clay minerals (e.g., illite, kaolinite) (Table 4.2) known to fill the pores of the inertinite maceral fusinite (Dai et al., 2012). Given that inertinite is oxidized organic material and has little potential for further chemical reactivity (Killops and Killops, 2004), it is an unlikely host of significant Li. Similar Li-rich spots were not measured in the samples within the contact aureole, which is likely because diagenetic silicates are in low abundance due to metamorphic recrystallization (Table 4.2; Finkelman et al., 1998). Notably, the bulk Li-contents (reported by Finkelman et al., 1998) are ~10 times higher for the metamorphic samples than Li-content values determined here by SIMS (Table 4.5). The discrepancy is likely because silicate phases containing Li were intentionally avoided in our SIMS analyses that focused on macerals, however silicate phases were included in the bulk analyses. Bulk Li-contents (Table 4.5; Finkelman et al., 1998) show a small increase in Li in the

contact aureole of 2-3 μg/g suggesting that metamorphic silicates might have taken up Li from magmatic and/or hydrothermal fluids. Our SIMS measurements show no increase in the Li-content of the macerals measured (Table 4.5). If during contact metamorphism there was an overall addition of Li from dike-related fluids, the precipitation of authigenic silicate phases would take up Li from dike-related fluids, while organic-Li was being released from the macerals.

Similarities between both contact metamorphosed coals. At both the Vermejo and Dutch Creek sampling localities vitrinite macerals in the un-metamorphosed coal samples were isotopically lighter than inertinite and liptinite macerals (Figs. 4.9 and 4.10). Inertinite and liptinite macerals tended to be more intimately associated with silicates, which may have led to overlap of the analytical crater on silicate phases, supported by the trends of δ^{7}Li with $^{12}C^{+}/^{30}Si$ (Figs. 4.11 & 4.12). Among all samples from the two metamorphosed coal seams, the negative correlation observed between Li-content and $^{12}C^{+}/^{30}Si^{+}$ (Figs. 4.11a, 4.12a) suggests that Li is primarily concentrated in silicates. The question is then, what is the source of Li? Finkelman et al., (2018) found that on average concentrated hydrofluoric acid leached 80% of the total Li from high rank coals and 60% of the Li from low-rank coals, which contain fewer authigenic silicates. They interpreted these results to indicate that the Li in leachates was derived solely from the silicate material. However, other studies have shown that HF digests soil OM by removing O-alkyl functional groups (Dai and Johnson, 1999) and by causing general carbon loss from OM (Rumpel et al., 2006, 2002; Schmidt et al., 1997; Zegouagh et al., 2004). In kerogen, hydrolysis, addition, and condensation reactions can occur with several organic functional groups during HF treatments (Saxby, 1976). Therefore, some

organo-lithium compounds are likely digested by or react with acids such as HF and HCl (Williams and Bose, 2018).

Through electron microprobe studies of low-rank coals, Li et al., (2010; 2007) found that several inorganic elements are concentrated in vitrinite (up to 0.5% Al, 1.5% Ca, 0.1% Mg, 0.7% Fe, 0.2% Ti) that are not associated with sub-micron clay minerals based on the low Si abundances of (0.01 to 0.11%). It is probable that Li is organically bound in immature vitrinite macerals, given that Li readily substitutes for Mg, for example. Thus, the trends between Li-content and $^{12}C^{+}/^{30}Si^{+}$ observed (Figs. 4.11a and 4.12a) may not be solely related to Li in silicates but also may include Li and Si associated with organic compounds, especially in low-rank coals.

Conclusions

Thermal alteration of macerals (vitrinite, liptinite, inertinite) in coal by contact metamorphism was studied to evaluate changes in the Li-content and Li-isotopic composition with temperature. One high volatile bituminous coal seam (Vermejo Fm.) was transected by a mafic dike and another medium volatile bituminous coal seam was transected by a felsic dike (Dutch Creek Mine No.2). In addition to $\delta^{7}Li$ changes as a function of temperature across the contact aureole, Li-contents of bulk analyses show a slight increase in Li near the Dutch Creek dike which is not observed by *in situ* measurements of macerals by SIMS. This may reflect uptake of Li from the felsic dike fluids by silicates in the metamorphosed coals, that was not observed in the mafic dike metamorphosed coals.

An increase in the $\delta^{7}Li$ values was observed in the high volatile bituminous Vermejo coal with proximity to the dike as temperatures increased (Fig. 4.9), which

mirrors the trend observed for coals of different ranks from sedimentary basins across the USA (Fig. 4.1; Teichert et al., 2020). Isotopically light (^{6}Li-enriched), organically bound Li in the unmetamorphosed coal vitrinite (– 28.4±1.6‰) is released into sedimentary pore fluids with increasing thermal maturity. The Dutch Creek coal had been heated by burial to ~ 150 ºC (VR_o = 1.15%) before felsic dike emplacement and had likely released most of the organically bound Li during diagenesis, so there was a smaller range of δ^{7}Li values among the macerals during metamorphism. However, SIMS spot analyses of vitrinite on the Dutch Creek unmetamorphosed coal (DC-K) had lighter δ^{7}Li values than vitrinite and coke measured in the contact zone by 8 to 21‰ suggesting that the isotopically light organo-lithium was not entirely released during burial to 150˚C (Table 4.5).

The most important conclusion from this study is that isotopically light, organically bound Li released from immature kerogen during diagenesis should be considered in studies using Li-isotopes of buried sediments (e.g., marine carbonates) to reconstruct global weathering and paleoclimate. The Li-isotopic composition of pore fluids can be altered by release of ^{6}Li during organic maceral decomposition at temperatures of hydrocarbon generation and higher. The isotopically light Li in pore fluids may be incorporated into authigenic silicates and recrystallized carbonates as well, leading to possible misinterpretations of global weathering and climate in earth's past.

CHAPTER 5

LITHIUM CONTENT AND ISOTOPIC COMPOSITION OF MACERALS AND MINERALS FROM THE GUANBANWUSU COAL (CHINA)

Abstract

The macerals and silicate minerals of two coal samples from the low rank (VR_o = 0.5%) hydrothermally altered Guanbanwusu deposit (Northern China), where ~80 °C hydrothermal fluids enriched the bulk Li-contents (>200 μg/g) were analyzed for Li-content and Li-isotopes using new Li calibrations developed for SIMS. Lithium was concentrated in silicates (mean = 1436 μg/g) while all macerals were more Li depleted (mean < 40 μg/g). Even though δ^7Li values ranged from –6‰ to +17‰, the range of δ^7Li among maceral groups and silicates overlapped considering the standard error ($2\sigma_x$) values, possibly reflecting the influence of post-depositional hydrothermal alteration.

Introduction

Conventionally, Lithium (Li) has been mined from continental brines and pegmatite deposits (Kesler et al., 2012). More recently there have been developments in the mining and exploitation of unconventional Li-resources such as lacustrine clay deposits formed within rhyolitic calderas (Benson et al., 2017), oilfield brines (Li et al., 2021) as well as coal and coal combustion residues (Seredin et al., 2013; Sun et al., 2012a; Xu et al., 2021). Sun et al., (2012a) recommended 80 μg/g as the minimum mining grade for coal and most coals do not contain economic concentrations of Li. Finkelman et al., (1993) found that 7848 U.S. coals had a mean Li-content of 16 ± 20 μg/g, in agreement with the 12 μg/g estimated for worldwide coals (Ketris and Yudovich, 2009). However, coals in China (mean = 29 μg/g; Sun et al., 2010) and South Africa (45–

81 μg/g; Pougnet et al., 1990) have higher Li contents. Several Li-rich (mean >100 μg/g) coal deposits have been identified in the Carboniferous-Permian Jungar and Ningwu coalfields in Northern China (see Qin et al., 2015 for review).

Trace elements in coals can be added through detrital input (e.g., volcanic ash, fluvial detritus), biological input (e.g., plant nutrients, phytoliths), adsorption from Li-rich water and authigenic mineralization (Finkelman, 1993). These elements can vary as much over the micrometer scale as they can over the basin scale (Finkelman, 1993). Within the Li-rich coal deposits from Northern China authors have argued for input of Li from detrital sources such as bauxite from the Benxi Fm. and moyite (quartz-ortho granites) and peraluminous granites from the Yinshan Oldland (Dai et al., 2008; Sun et al., 2016, 2013, 2012, 2010) as well as an authigenic origin with high-Li chlorite precipitating from epigenetic hydrothermal fluids into fusinite cell fillings (Dai et al., 2012). To effectively extract Li from coal and understand its origin, it is necessary to identify which phases are enriched in Li and how the Li-isotopes vary among phases. Here I assess the Li-contents and isotopic compositions of coal macerals and aluminosilicate minerals in two hydrothermally altered coal samples from the Guanbanwusu mine of the Jungar Coalfield, where the mean bulk Li-contents are 175 μg/g (Dai et al., 2012).

Methods

Two sub-bituminous coal samples (G11 and G41) from the No. 6 Guanbanwusu mine in the Jungar coalfield (Northern China) (courtesy of Shifeng Dai; Dai et al., 2012) were selected for detailed study. These samples are enriched in a host of trace elements, including Li, with bulk Li-concentrations of 240 μg/g (G11) and 505 μg/g (G41) (Dai et

al., 2012). Sample G41 was selected because it had the highest Li-concentration of all samples available. Sample G11 was chosen because of its lower mineral matter (15.9 wt.%) compared to many coals from the No. 6 mine which made it easier to measure macerals with minimal silicate contribution. Because of the high Li concentrations, the Li-isotopic compositions of various coal macerals and minerals were precisely measured showing significant isotopic heterogeneity of Li-hosts and whether they were sources or sinks of Li. Samples were prepared as small (10-20 mm diameter) thick sections and polished to a final grit size of 0.05 μm using colloidal silica. Samples were sonified in 0.1 M mannitol to remove surface adsorbed Li, then rinsed in DI water and dried at 60 ºC.

Secondary Ion Mass Spectrometry (SIMS) measurements were carried out at Arizona State University using a Cameca (Ametek Inc.) IMS-6f instrument to evaluate the Li-content and isotopic composition of different macerals and silicates. The SIMS analytical setup and procedures used here are described in Chapter 4, (p.77-79). Because silicate clasts and pore fillings were measured here in addition to macerals a previously published calibration for measuring the Li-content of silicates by SIMS was used (Williams et al., 2012) for the determination of Li-contents in silicates using $^{7}Li^{+}/^{30}Si^{+}$ ion ratios for secondary ions with an excess energy of 75 eV.

$$^{7}Li^{+}/^{30}Si^{+} \times SiO_2\ (wt.\%) = 2.83\times10^{-4} \times Li\ (\mu g/g) \quad (1)$$

Results

Dai et al., (2012) previously published proximate (moisture, ash, fixed-C content) and ultimate (bulk chemical composition) analyses, organic petrology, vitrinite reflectance measurements, mineralogy, and major and trace element determinations for the Guanbanwusu coal samples. Proximate analyses are shown in Table 5.1. Sample G41

is nearly a black shale with significantly more mineral matter (41.6 wt.%) than sample G11 (15.9 wt.%). Both samples have similar thermal maturities with comparable VR_o values and volatile matter abundances.

Table 5.1

Some Values From Proximate Analyses of Guanbanwusu Coals

Sample	Residual Moisture (wt.%, ar)	Volatile Matter (wt.%, dry)	Ash yield (wt.%, dry)	Mineral Matter (wt.%, dry)	Total carbon (wt.%, dry)	Total sulfur (wt.%, dry)	Avg. VR_o random (%)
G11	5.6	33.3	14.5	15.9	68.7	0.43	0.56
G41	4.3	28.3	38.1	41.6	45.8	0.75	0.53

VR_o- vitrinite reflectance in oil; ar stands for "as recieved". Data from Dai et al., (2012)

The minerals present in order of abundance, the mineral matter vol.%, and the abundance of major maceral groups are shown in Table 5.2. More details on the organic petrology and mineralogy can be found in Dai et al., (2012). In previous studies of Guanbanwusu coals (Dai et al., 2012; Sun et al., 2012b), chlorite and kaolinite were thought to be the primary Li-bearing minerals. Notably, inertinite is the dominant organic maceral in these coal samples, which is not uncommon for coal from the Jungar coalfield, while other Paleozoic coals from Northern China typically have <25% inertinite (Dai et al., 2012) on a mineral free basis.

Reflected light microscope images showing several SIMS analytical craters for both samples are presented in Fig. 5.1. Data from all spot analyses are shown in Table 5.3 with organic maceral or silicate indicated, the δ^7Li values and associated errors, Li-contents and $^{12}C^+/^{30}Si^+$ ratios. The Li contents of different macerals and silicates in Guanbanwusu coals ranged from 0.04 μg/g to 3519 μg/g and the δ^7Li values ranged from –6‰ to +17‰. In Table 5.4 the mean values of Li-content and δ^7Li are shown for different maceral types and silicates. For sample G41, silicate spot measurements had Li-

contents greater than the bulk Li values reported (Dai et al., 2012) while macerals had much lower Li-contents (Table 5.4). Among macerals, vitrinite and liptinite have the lowest mean Li-contents (0.5-11.2 μg/g), while inertinite and the mixed groundmass (organic and silicate contribution) had higher Li-contents (19.9-38.6 μg/g).

Table 5.2

Minerals Present and Major Maceral Groups of Guanbanwusu Coals

Sample	Minerals present	Mineral Matter (vol.%, dry)	Vitrinite (wt.%, dmmf)	Inertinite (wt.%, dmmf)	Liptinite (wt.%, dmmf)
G11	kao, boe, chl, sd, qtz, py	*7.9	28.2	65.0	6.6
G41	kao, chl, boe, qtz	*20.8	35.4	56.7	7.9

*Mineral matter vol.% approximated from mineral matter wt.% for some samples by dividing by 2 following Matjie et al., (2016). dmmf indicates " dry mineral matter free"; nm = not measured; NA = not applicable. Qtz = Quartz; Kao = Kaolinite; Chl = Chlorite; Sd = Siderite; Py = Pyrite; Boe = Boehmite

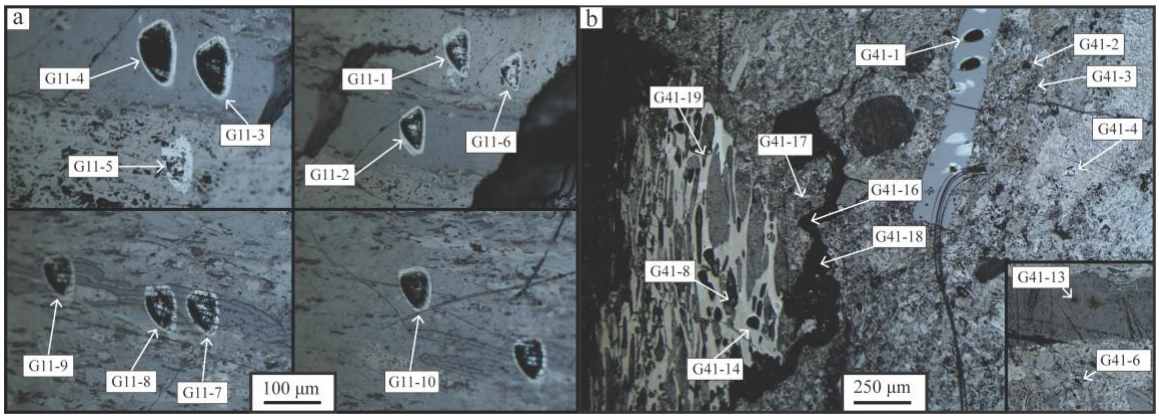

Figure 5.1. Reflected light microscope images of (a) G11 and (b) G41 samples with analytical craters labeled. Analytical craters vary in size according to the primary current used.

For δ^7Li the standard error of the mean values ($2\sigma_x$) overlap for all maceral types and silicates. The large $2\sigma_x$ values for both Li-content and Li-isotopes show the significant heterogeneity within the maceral groups measured (Table 5.3).

Table 5.3

SIMS Results for Guanbanwusu Coal Spot Measurements

Measurement	Coal component	δ^7Li (‰)	S.E. (‰)	P.E. (‰)	Li (μg/g)	$^{12}C^+/^{30}Si^+$
G11-1	Inertinite	-1.9	0.8	0.6	9.69	25.80
G11-5	Inertinite	7.7	0.5	0.4	38.01	3.00
G11-6	Inertinite	11.8	0.6	0.5	12.05	11.60
G11-2	Vitrinite	-5.9	1.2	1.5	0.65	97.40
G11-3	Vitrinite	5.1	1.5	1.2	0.13	249.20
G11-4	Vitrinite	-4.4	0.6	0.5	1.42	46.40
G11-10	Vitrinite	1.8	0.7	0.7	2.88	11.40
G11-7	Liptinite	1.9	1.9	1.7	0.13	199.20
G11-8	Liptinite	10.4	1.0	1.0	0.56	91.30
G11-9	Liptinite	1.8	1.1	0.8	0.90	37.10
G41-8	Inertinite	2.3	1.6	1.2	41.40	4.44
G41-9	Inertinite	5.0	5.0	4.0	0.04	6142.06
G41-4	Inertinite	15.6	0.5	0.5	55.23	1.50
G41-14	Inertinite	16.3	1.4	0.7	16.50	2.88
G41-2	Mixed	13.1	0.5	0.5	28.12	1.10
G41-3	Mixed	16.6	0.5	0.5	17.99	1.60
G41-6	Mixed	-5.2	0.7	0.4	108.50	1.19
G41-10	Mixed	7.1	0.6	0.5	75.20	1.37
G41-11	Mixed	8.2	0.4	0.4	37.80	3.61
G41-12	Mixed	-1.5	0.5	0.5	31.70	2.12
G41-15	Mixed	2.8	1.0	0.8	8.50	2.69
G41-16	Mixed	3.9	0.8	0.5	53.80	2.21
G41-17	Mixed	3.7	0.7	0.6	10.20	2.69
G41-18	Mixed	5.8	2.7	2.3	13.70	27.08
G41-1	Vitrinite	0.2	3.0	2.3	0.09	2594.40
G41-5	Vitrinite	17.4	0.6	0.7	22.30	4.20
G41-7	Silicate	7.5	0.8	0.3	493.00	0.02
G41-13	Silicate	4.4	0.6	0.5	657.00	0.02
G41-19	Silicate	10.3	0.8	0.5	1874.00	0.21
G41-20	Silicate	13.2	0.7	0.4	3518.57	0.02
G41-21	Silicate	14.4	0.7	0.5	638.88	0.05

Mixed spots were within the groundmass with significant contributuions of both silicates and organics. G41 and G11 are Li-rich coal samples from the Guanbanwusu mine (China) (Dai et al., 2012).

Table 5.4.

Average Li Contents and Isotope Ratios of Guanbanwusu Coals

Sample	Bulk Li contents (μg/g)	Avg. Li contents from SIMS (μg/g)	$2\sigma_x$ (μg/g)	δ^7Li (‰)	$2\sigma_x$ (‰)	n
G11	**240**					
Vitrinite		1.3	1.1	-0.9	5.2	4
Inertinite		19.9	18.1	5.9	8.1	3
Liptinite		0.5	0.4	4.7	5.7	3
G41	**505**					
Vitrinite		11.2	22.2	8.8	17.2	2
Inertinite		28.3	24.7	9.8	7.2	4
Mixed		38.6	20.4	5.4	4.0	10
Silicate		1436.3	1154.2	10.0	3.7	5

Mixed matrix spot measurements contained significant silicate and organic material. Bulk Li contents from Dai et al., (2012).

Because $^{12}C^+$ counts per second (cps) from spot to spot vary up to a factor of 10 while the $^{30}Si^+$ cps commonly range over 4 orders of magnitude from spot to spot, the change in the $^{12}C^+/^{30}Si^+$ is typically more indicative of changes in the $^{30}Si^+$cps than $^{12}C^+$ cps (Fig. 5.2). Given that the $^{30}Si^+$ cps are higher in silicates than $^{12}C^+$ cps in predominantly carbonaceous material, the $^{12}C^+/^{30}Si^+ < 0.5$ is defined here as a silicate matrix (Fig. 5.2) and this was confirmed by microscopy and photographically documented. The Li-contents and δ^7Li of spot measurements plotted against the $^{12}C^+/^{30}Si^+$ count ratio for Guanbanwusu coal samples (Fig. 5.3) show a strong negative correlation between Li-content and $^{12}C^+/^{30}Si^+$ ($R^2 = 0.89$; Fig. 5.3a) but no correlation between δ^7Li and $^{12}C^+/^{30}Si^+$ (Fig. 5.3b).

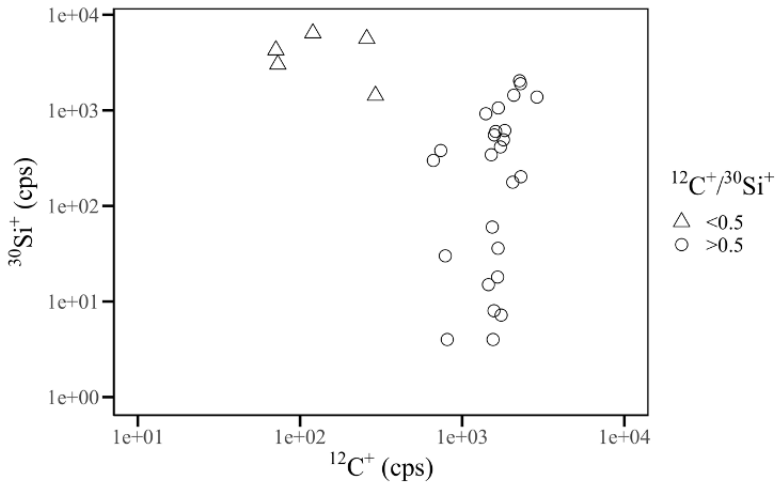

Figure 5.2. Plot showing the $^{12}C^+$ and $^{30}Si^+$ counts per second for spot measurements. Counts were normalized for the current used in each measurement. Silicates that were identified microscopically are the only group that show a marked decrease in $^{12}C^+$ signal and had a $^{12}C^+/^{30}Si^+$ ratio less than 0.5.

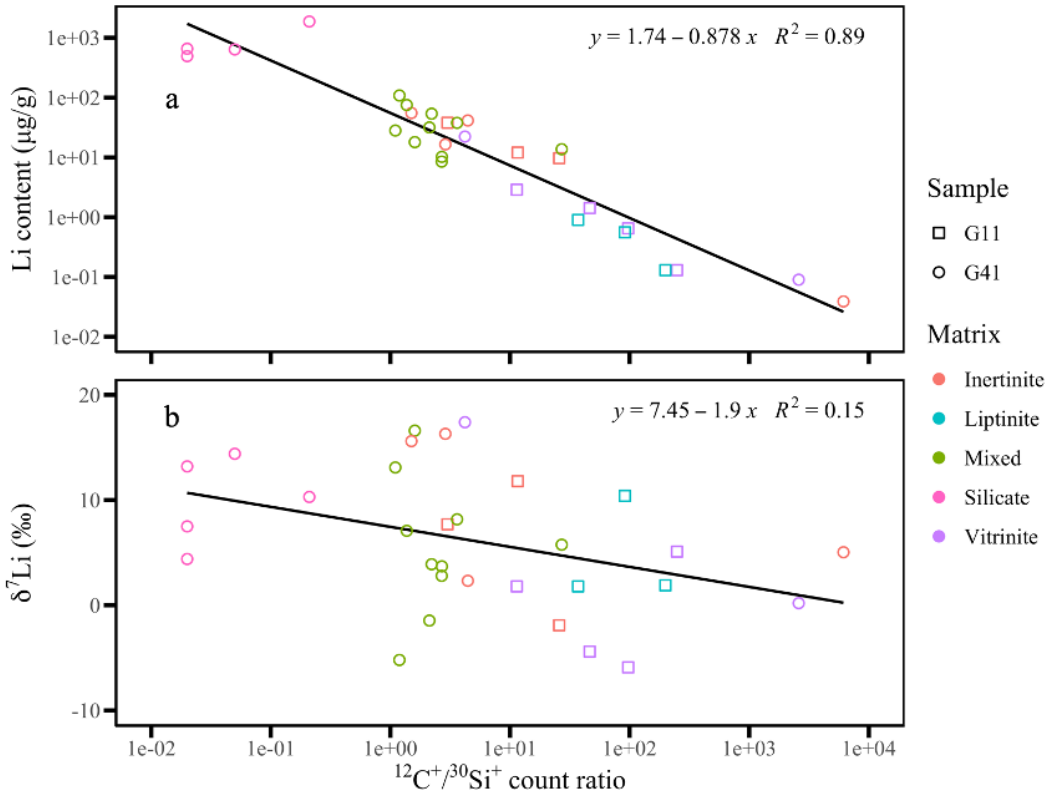

Figure 5.3. Scatter plots of Guanbanwusu coal (a) Li-contents and (b) δ^7Li against $^{12}C^+/^{30}Si^+$ count ratio with the point shape indicating the sample and color indicating maceral type, mixed (organic and silicate overlap) and silicate. Linear regression trendlines, equations and R^2 values are shown. There is a negative correlation (0.86) between Li-content and $^{12}C^+/^{30}Si^+$ and no correlation between δ^7Li and $^{12}C^+/^{30}Si$.

Discussion

Li-Content and Isotope Measurements of Guanbanwusu Coal Macerals

The average bulk Li-content of the Guanbanwusu mine No. 6 coal is 175 μg/g (Dai et al., 2012) which is significantly higher than the reported values of typical immature coals (6 to 11 μg/g) (Finkelman et al., 2018; Ketris and Yudovich, 2009). The strong correlation between Li-content and $^{12}C^{+}/^{30}Si^{+}$ (R^2 = 0.89; Fig. 5.3a) confirms that in this case Li is almost entirely hosted in silicate minerals and not organics as noted by others (Dai et al., 2012; Sun et al., 2012b). Li-contents determined from SIMS spot analyses of macerals were significantly lower than bulk Li-content measurements (Table 5.3; Fig. 5.3a). The inertinite and mixed matrix spot analyses typically had higher Li-contents and lower $^{12}C^{+}/^{30}Si^{+}$ values than vitrinite and liptinite analyses (Fig. 5.3a), likely because of overlapping silicates in inertinite cell fillings (e.g., Fig 5.1b; G41-8, G41-19) and mixed matrix spot analyses. Meanwhile the Li-contents of spot analyses on silicate grains were on average 1436 μg/g (Table 5.4) which is much higher than the Li-contents from bulk values (505 μg/g; Dai et al., 2012), that were diluted by the low Li in the organic fraction of the bulk coal.

Despite being a low rank coal (VR_o ~ 0.5%) the δ^7Li values of coal macerals for the samples G11 and G41 are 10‰ to 20‰ higher than US coals of similar rank (Teichert et al., 2020). While spots measured with high Li-contents are likely due to detrital silicates or the addition of hydrothermal Li incorporated into authigenic silicates, even spots with lower Li contents (<1 μg/g) comprised of almost entirely organics matter have an average δ^7Li value of +2.6 ± 3.8‰; within error of the bulk measurements of these coals (+6‰ to +8‰; He et al., 2019). Thus, it may be that Li chelated with macerals in

addition to precipitating authigenic silicates during a post depositional hydrothermal event. In addition to having high Al, Li, Ga and REE concentrations (Dai et al., 2012) the Guanbanwusu coals are different from typical coals because the primary maceral group is inertinite instead of vitrinite (Table 5.2). Inertinite as the primary maceral group could be derived from charring, oxidation, moldering, fungal attack or desiccation of primary organic material during deposition or early peatification (Taylor et al., 1998). Thus, the higher δ^7Li values in spot measurements on macerals with low Li-content may be due to the unique organic petrology and/or release of organically bound Li during hydrothermal alteration. Alternatively, considering a hydrothermal origin for the Li, the very high Li-content of hydrothermal fluid may have left some isotopically heavy Li adsorbed to the macerals measured in these coals. He et al., (2019) measured the bulk Li-isotope composition for several coals from the No. 6 Guanbanwusu mine by MC-ICP-MS and found that all the samples had bulk δ^7Li values ranging from +6‰ to +8‰. The mean values of the silicates measured in sample G41 here by SIMS are within error of bulk measurements (+10.0 ‰ ± 3.7; Table 5.4).

Results from Li-isotope measurements could support the ideas of both detrital as well as low temperature hydrothermal origins for the high Li-content of the Guanbanwusu No.6 coal. The δ^7Li range of coals measured are comparable to granitic rocks as well as their metamorphic equivalents (–5‰ to +15‰; Tomascak et al., 2016) making it plausible that detrital quartz-ortho and peraluminous granites from the Yinshan Oldland could be source of Li in these coals (Dai et al., 2008; Sun et al., 2016, 2013, 2012, 2010). The alternate hypothesis for Li-enrichment is that low-temperature (80 ºC) hydrothermal fluids, laden with Li (in addition to Al, Ga and REE) enriched the

Guanbanwusu coal by precipitating authigenic Li-enriched chlorite group minerals into coal cell fillings, cleats and fractures (Dai et al., 2012). It has been reported that chlorite can form as a secondary mineral in sedimentary rocks at temperatures as low as 20 ºC (Milliken, 2003) while others have reported that chloritization begins at 50 ºC (Haldar, 2020) or 80 ºC (Bourdelle et al., 2013). If chlorite precipitated in equilibrium with the hydrothermal fluids at 80˚C (Barker and Pawlewicz, 1994; Dai et al., 2012) the +10‰ δ^7Li silicate value (Table 5.4) can be used to calculate the δ^7Li composition of the hydrothermal fluid. Using the isotopic fractionation factor equation $1000 \ln(\alpha) = 6.15 – 9.07(1000/T\ (K))$ (Williams et al., 2012; Williams and Hervig, 2005) appropriate for these clays (Hindshaw et al., 2019), the hydrothermal fluid would have a δ^7Li composition of +29.5‰, which is only slightly lighter than seawater (+31‰; Chan and Edmond, 1988; Misra and Froelich, 2012) and indicates that the Li did not come from an isotopically light organic source.

Conclusions

Low rank coals (VR_o ~ 0.5%) from the Guanbanwusu No. 6 coal mine (China), which were enriched in Li by either detrital or authigenic processes contain aluminosilicates with mean Li-contents of 1436 μg/g (Table 5.4). The high Li-contents in aluminosilicates and a negative correlation between $^{12}C^+/^{30}Si^+$ indicate that Li is predominantly hosted in aluminosilicate phases. Furthermore, the Guanbanwusu coal macerals had much higher δ^7Li values (–1‰ to +10‰) than US coals of the same rank (< –10‰) (Teichert et al., 2020) perhaps due to the inertinite dominant composition of these coals or Li-rich hydrothermal fluid leaving isotopically heavy Li chelated to the macerals. In light of these results both the detrital inputs and hydrothermal origins of the high Li-

contents found in these coals are possible. Assuming the precipitation of authigenic clays in the coal deposit at equilibrium allowed calculation of the Li-isotopic composition of the hydrothermal fluids at +29.5‰.

CHAPTER 6

LITHIUM RELEASE AND ISOTOPE FRACTIONATION DURING COAL HYDROUS PYROLYSIS EXPERIMENTS: INSIGHTS INTO THE LITHIUM CONTRIBUTIONS OF KEROGEN TO SEDIMENTARY POREFLUIDS

Abstract

To understand the significance of Li derived from kerogen in diagenetic settings, several 72-hour hydrous pyrolysis experiments of two separate coal powders (DECS-22 & Four Corners coal) were carried out at temperatures of 250 ºC, 300 ºC and 350 ºC. Additionally, long-term Au-capsule experiments were carried out at 300 ºC for a 1-month on Four Corners and DECS-25 coal powders. Li-contents of experimental fluids after hydrothermal treatments were determined by ICP-MS. Reacted and unreacted coal powders δ^7Li values and mineralogy were determined by SIMS and XRD, respectively.

For two of the samples (DECS-25 & Four Corners) hydrous pyrolysis caused the δ^7Li values of coal powders to become isotopically heavier by 3 to 10‰, indicating ^{6}Li was predominantly released to the water and the Li-content in the fluids increased with temperature. However, sample DECS-22 released Li to the fluid with Li-content being highest in the water at 250 ºC and decreasing at 300 ºC and 350 ºC. The Li-isotope composition of DECS-22 became 14‰ lighter with increasing temperature. This contrasting result may be due to authigenic illite or chlorite incorporating Li, which had been released from kerogen into the water, preferentially taking up ^{6}Li.

Calculations estimate that kerogen could increase the Li-content of diagenetic porefluids by up to 100 mg/L which is significant considering that seawater contains ~0.17 mg/L Li. Furthermore, the isotopically light composition of Li released from

kerogen can change the δ^7Li composition of porefluids. These results are important to consider when reconstructing global weathering and paleoclimates using marine carbonates.

Introduction

Thus far all chapters have been focused on determining the Li-contents and δ^7Li of kerogen from different geologic environments and making inferences about the role of kerogen in the Li geochemical cycle based on those results and considering the findings of other investigators. It has been established that the lithium isotope composition of immature kerogen in coal is typically lighter than mature kerogen (Teichert et al., 2020; Chapter 4). The release of isotopically light organo-lithium during kerogen maturation (i.e., hydrocarbon generation) is the proposed mechanism used to explain the change in the δ^7Li of kerogen with thermal maturation. If isotopically light organo-lithium is being released from kerogen into the porefluids, the δ^7Li of porefluids would become significantly lighter and influence the δ^7Li of authigenic minerals forming from those fluids. Indeed, measurements of authigenic minerals formed within oil and gas fields have lighter δ^7Li than other authigenic minerals in the same basin (Williams et al., 2015, 2013) and oilfield brines tend to have lighter δ^7Li than other terrestrial fluids (see Chapter 2, p.35 and Appendix A Table A.2). However, because this process takes place over geologic time scales and likely at depths of hydrocarbon generation (>1 km; Tissot and Welte, 1984) it is difficult to observe and confirm.

Because of the ubiquity of water on earth, hydrothermal experiments have been carried out as proxies for a wide range of geologic processes. Hydrous pyrolysis experiments refer specifically to hydrothermal experiments where organic matter is

heated to temperatures of hydrocarbon generation in the presence of liquid water. The first hydrous pyrolysis experiments were performed by Brooks and Smith, (1969) who reacted coal and water at temperatures from 210 ºC to 330 ºC to determine changes in the organic chemistry related to hydrocarbon generation. That work has been followed by numerous publications worldwide of hydrous pyrolysis experiments, most of which are concerned with understanding the generation of hydrocarbons from source rocks.

However, Clauer et al., (2022) recently measured the δ^7Li in the illite-smectite clays of the oil-prone Kreyenhagen Shale before and after hydrous pyrolysis and found that the δ^7Li of samples that underwent hydrous pyrolysis were 6 to 11‰ lighter than the untreated sample. They noted that the decrease in δ^7Li in the clays correlated with the decrease in the sample total organic carbon (TOC), suggesting that the organic matter played a role in changing the δ^7Li of clays during hydrous pyrolysis. No studies, known to the author, have measured the Li contents released from kerogen into water during hydrous pyrolysis. In this dissertation research I used hydrous pyrolysis on three separate coal samples to address the following questions. How much Li is released from coal/kerogen during hydrous pyrolysis? Is the amount of Li released from kerogen significant in the Li-geochemical cycle? How do Li-isotopes fractionate between kerogen and water? Lastly, how does the Li-isotope composition added to fluids from kerogen alter the existing isotopic composition of pore-fluids?

Methods

Experimental Coal Samples

Several coal samples studied previously (Teichert et al., 2020) were selected for hydrothermal experiments. Those selected had $^7Li^+/^{12}C^+ > 0.015$ and the $^7Li^+$ signals

were not clearly correlated with $^{30}Si^{+}$ indicating an organic association of Li. Two U.S. Department of Energy Coal Samples from the Pennsylvania State University (PSU) coal repository (DECS-22 & DECS-25) as well as a coal sample from the Navajo Mine in the Four Corners region of New Mexico were selected for hydrothermal experiments (Table 6.1). DECS-22 was chosen because it is a liptinite rich coal (31.8% Liptinite; dry mineral matter free (dmmf)) containing 37.9% dmmf volatile matter. In contrast, DECS-25 is a more typical vitrinite dominant lignite (VR_o = 0.23%) sample with high volatile matter (46.9% dmmf). Lastly, the Four Corners coal sample comes from the San Juan basin (NM, USA) and has high volatile matter (46.2% dmmf) despite its higher thermal maturity (VR_o = 0.50%) in comparison to DECS-25.

Table 6.1

Proximate Analyses and Organic Petrology of Coal Samples

Sample	DECS-22	DECS-25	FC
Proximate analyses			
Residual Moisture (wt.%, ar)	0.9	34.9	9.8
Volatile Matter (wt.%, dry)	30.5	42.0	38.1
Ash yield (wt.%, dry)	23.3	11.9	15.8
Mineral Matter (wt.%, dry)	26.9	13.6	17.5
Total carbon (wt.%, dry)	64.9	65.8	70.3
Total sulfur (wt.%, dry)	1.7	0.7	0.8
Avg. VR_o random (%)	0.8	0.2	0.5
Organic Petrology			
Vitrinite (%)	30.0	74.0	75.2
Inertinite (%)	38.7	22.1	17.6
Liptinite (%)	31.8	3.6	7.2

VR_o- vitrinite reflectance in oil; ar stands for "as recieved".

Sample Preparation for Hydrous Pyrolysis Experiments

Coal samples were powdered to <20 μm using a McCrone micronizing mill for gold capsule experimental powders (Środoń, 2001). Larger volumes of coal were used in René 41 (Ni-Cr alloy) vessels for hydrous pyrolysis and coal powders were ground (<40 μm) using a BICO Ring and Puck mill. Samples were shaken for 24 hours in 1 M NaCl solution to exchange surface adsorbed and clay interlayer Li^+ ions with the preferred Na^+ cations (Jackson and Barak, 2005; Teppen and Miller, 2006). Subsequently, solutions were centrifuged to settle the powders before decanting and rinsing powders in triplicate in DI water (filtered through resin to reduced Li to <1 ng/g Li). Thereafter, samples were rinsed in 0.1 M mannitol solutions which complexes with surface adsorbed Li contaminants (Teichert et al., 2020) and removes them during subsequent washing in triplicate. Preliminary experimental work on the effectiveness of mannitol for the desorption of Li from negatively charged surfaces is described in Appendix D.

Small volume gold capsule hydrous pyrolysis experimental setup. Gold tubing purchased from Depths of the Earth LLC (https://depthsoftheearth.com/) with a 5 mm outer diameter, wall thickness of 0.125 mm and 99.98% purity was used for small volume hydrothermal experiments. The Au-tubing was cut into 40 to 50 mm lengths for hydrothermal experiments, cleaned with ethanol and DI water then annealed using a butane burner and quenched in DI water. One side of each cut Au-tube was crimped, cut and welded together using an arc welder prior to loading coal powders and DI water. Equal parts (150 mg or 200 mg) coal sample and DI water were added to the Au-capsules. For these experiments duplicate Au-capsules containing DECS-25 and the Four Corners coal samples were prepared. To minimize oxidation reactions, Ar gas was blown

over the remaining headspace prior to crimping and cutting the top end of the filled tubing. Au-capsules were welded shut and weighed before and after welding to ensure no water evaporated. To confirm a complete seal Au-capsules were placed in a 150 ºC oven overnight and then weighed again. Successfully sealed capsules are shown in Fig. 6.1.

Figure 6.1. Sealed Au-capsules used for hydrous pyrolysis experiments.

Duplicate sealed Au-capsules containing the DECS-25 and Four Corners samples were added to a cold seal pressure vessel along with water as the pressurizing medium, and the vessel was placed inside a Lindberg-59744-A furnace. The cold seal vessel was heated to 300 ºC and pressurized to 1 kbar (100 MPa) to prevent Au-capsules from bursting. A thermocouple inside the cold seal vessel adjacent to the Au-capsules monitored the temperature. Temperature and pressure conditions were monitored regularly for 1 month after which the vessel containing the Au-capsules was quenched in ice and the Au-capsules were removed and weighed to test for leakage.

The Au-capsules were opened, and powders and fluids were collected into new polypropylene test tubes by rinsing the Au-capsules with 5 to 15 ml of 0.1 M mannitol to extract surface adsorbed-Li. The fluids and coal powders were sonified in a Branson 3510 sonic bath for 2.5 hours and were shaken on a wrist-action shaker for 24 hours before centrifugation to separate solids and fluids. Powders were rinsed three times in DI water, dried at 60 ºC and pressed into round flat pellets using an IR-die cast and Carver Press in preparation for SIMS measurements as described in Teichert et al., (2020), while fluids were retained for measurements by ICP-MS.

Large volume René 41 hydrous pyrolysis experimental setup. A René 41 (Nickel-Chromium alloy) pressure reactor with a volume of 30 ml was used for larger volume experiments (Fig. 6.2). Lewan (1993) found that the composition of the reactor walls does not significantly change the molecular compositions of released hydrocarbons but can significantly change the yields. More recently it has been shown that Ni and Cr in steel catalyzes reductive reactions in organics (Porcheddu et al., 2020) however our goal was not to study the organic compounds but rather the amount of Li (a non-redox sensitive element) released at temperatures of oil generation. On fresh metal reactor surfaces, hydrocarbons react with and form a graphitic carbon layer on reactor walls (carburization) after successive hydrous pyrolysis runs, reducing hydrocarbon yields (Lewan, 1993). Therefore, the René 41 reactor used here underwent several trial runs with coal to carburize the reactor wall and reduce reactions between hydrocarbons and the reactor wall. The reactor was cleaned thoroughly prior to and between each analysis with soap, DI water and a wire brush.

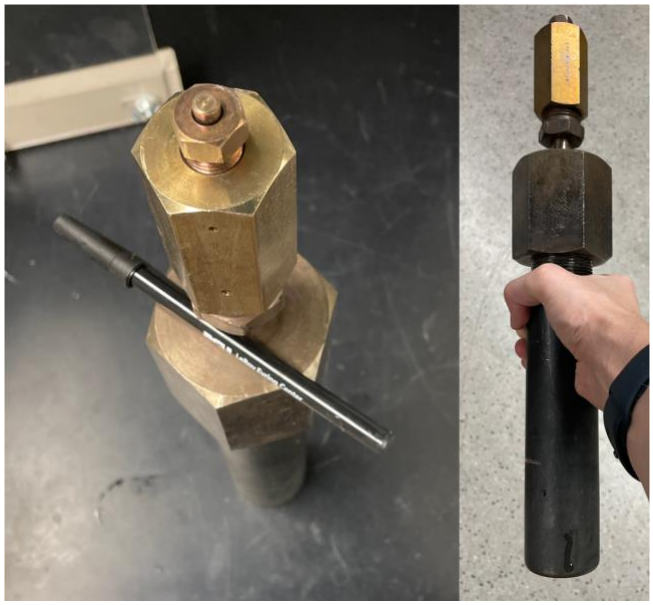

Figure 6.2. René 41 reactor vessel used for hydrous pyrolysis experiments.
The hydrothermal reactor was loaded with 2 g of coal powder and 10 g of DI water.

Argon gas was blown over the headspace for several minutes prior to sealing the vessel. Four Corners and DECS-22 coal samples were each reacted at temperatures of 250 ºC, 300 ºC and 350 ºC (Psat, saturation pressure of water vapor at the given T) for 72-hour durations in a Cress FX-23 electric kiln. A 72-hour heating duration allows for bitumen extraction from kerogen starting at ~300 ºC and breakdown of bitumen into oil starting at 330 ºC in black shale samples (Lewan et al., 1993). A thermocouple next to the reactor was used to monitor experimental temperatures. Next, the reactor was removed from the kiln, cooled and hydrothermal fluids were poured directly from the reactor into new polypropylene test tubes. Particulates were separated from hydrothermal fluids using 0.45 μm polypropylene syringe filters in preparation for ICP-MS measurements. Additional DI water was used to remove powders from the hydrothermal reactor. Powders were rinsed, dried and pressed into pellets for SIMS measurements as described above.

Because water is typically present in the liquid form during diagenesis, hydrous pyrolysis requires that the sample is primarily in contact with liquid water not water vapor or supercritical water fluid (Lewan et al., 1979). To calculate the volume of liquid water (V_l; cm^3) for a given reactor volume (V_r; cm^3) at an experimental temperature (T; ºC), the following expression can be used (ASME, 1979):

$$V_l = \frac{(M_W \gamma_v^T - V_r)\gamma_l^T}{\gamma_v^T - \gamma_l^T} \quad (1)$$

where;

M_W = Mass of liquid water added to the reactor (g)

γ_v^T = Specific volume of liquid water at a given T (cm^3/g)

γ_l^T =Specific volume of water vapor at a given T (cm^3/g)

Each of the hydrothermal experiments described above (Au-capsule and René reactor) meet the requirements for hydrous pyrolysis with liquid water accounting for ≥ 33% of reactor volume at experimental temperatures.

Analytical Techniques

Determination of the Li-contents of hydrothermal fluids was performed at the Arizona State University Metals, Environmental and Terrestrial Analytical Laboratory (METAL) with the Thermo Scientific Quadrupole ICP-MS (iCap™-Q). The hydrothermal fluids were diluted by a factor of 10 with DI water.

Li-isotope measurements of coal powders before and after hydrothermal experiments were performed at Arizona State University *in-situ* by Secondary Ion Mass Spectrometry (SIMS) using a Cameca (Ametek Inc.) IMS-6f. The SIMS instrumental settings and Li-isotope determinations used here are described in detail in Chapter 4. Because of the high mineral content of coal samples (>10%) the Li-contents of coal

powders were not determined by SIMS due to uncertainty in the calibration on a mixed matrix. Multiple spot measurements (30 μm to 50 μm size) were performed on each sample. Briefly, lithium isotope ratios are reported as the per mille deviation from the LSVEC standard (Flesch et al., 1973).

$$\delta^7\text{Li}\ ‰ = \left(\frac{R_{Sample} - R_{Standard}}{R_{Standard}}\right) \times 1000 \quad (2)$$

where;

R = ^{7}Li/^{6}Li and the standard is NIST SRM 612 (R=12.0192)

Qualitative mineral identification was performed on reacted and unreacted coal samples using a Malvern PANalytical Aeris powder X-Ray Diffractometer with Cu kα radiation. Samples were not mounted on a randomly oriented and thus differentiation of several clay minerals was not possible. For the unreacted samples the organic matter was oxidized in 35% H_2O_2 at ~85 °C for 3-6 days prior to XRD measurements, following Ward, (1974) to remove organics and make XRD peaks easier to measure. The reacted powders were also measured by XRD but did not undergo organic oxidation because of the limited material.

Results

Table 6.2 contains the Li-contents of experimental fluids (calculated for a 1:1 solid: liquid mass ratio) from ICP-MS measurements and the mineralogy and mean δ^7Li of coal powders from XRD and SIMS measurements. XRD spectra are shown in Appendix D. Kaolinite/chlorite, quartz and mixed layer illite-smectite (I-S) were present in all samples while detrital muscovite was present only in DECS-22.

The δ^7Li values of individual spot measurements and mean δ^7Li values for the reacted and unreacted coal samples used in the Au-capsule experiments are shown in Fig.

6.3. The mean δ^7Li of coal samples became 10‰ heavier for DECS-25 and 3‰ heavier for Four Corners after Au-capsule hydrous pyrolysis; however, the $2\sigma_x$ (standard error) error bars overlap for the Four Corners samples. The Li-contents released into the water are shown for each of the duplicate Au-capsules in Fig. 6.4.

Table 6.2

XRD, ICP-MS and SIMS Results of Reacted and Unreacted Coal Powders

Sample/Run	Minerals Present	Li-content in water (mg/L)	$2\sigma_x$	δ^7Li in powder (‰)	$2\sigma_x$ (‰)	n
DECS-22	Kao or Chl, Msc, Qtz, Mixed I-S	NA	NA	–0.5	2.4	5
René 41- 250 ºC	Kao or Chl, Msc, Qtz, Mixed I-S	3.7	0.2	–9.0	4.3	5
René 41- 300 ºC	Kao or Chl, Msc, Qtz, Mixed I-S	2.1	0.1	–6.8	3.9	5
René 41- 350 ºC	Kao or Chl, Msc, Qtz,, Mixed I-S	2.5	0.2	–15.3	6.6	5
DECS-25	Kao or Chl, Qtz, , Mixed I-S	NA	NA	–23.3	4.1	4
Au-Capsule 1 Au-Capsule 2	nm	0.064 0.128	0.002 0.004	–11.3	2.1	8
FC	Kao or Chl, Qtz, , Mixed I-S			–8.9	2.2	5
Au-Capsule 1 Au-Capsule 2	nm	4.1 8.0	0.1 0.2	–6.1	1.5	5
René 41- 250 ºC	Kao or Chl, Qtz, , Mixed I-S	0.8	0.1	-9.7	5.3	5
René 41- 300 ºC	Kao or Chl, Qtz, , Mixed I-S	1.7	0.1	-9.3	4.4	5
René 41- 350 ºC	Kao or Chl, Qtz, , Mixed I-S	3.9	0.2	-6.1	4.7	5

Minerals are listed in order of abundance. The coal powders from Au capsules were combined and measured together by SIMS. Kao = Kaolinite; Chl = Chlorite; Msc = Muscovite; Qtz = Quartz; Mixed I-S = Mixed illite-smectite; nm = not measured.

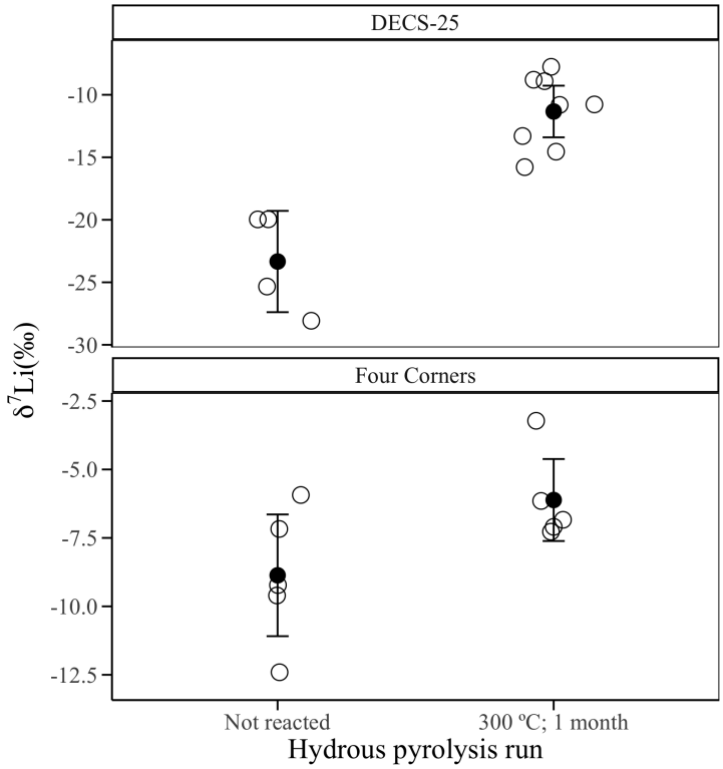

Figure 6.3. The individual spot measurements of δ^7Li values (open circles) and the mean δ^7Li values (black circles) are plotted for unreacted samples and Au-capsule experimental powders. The $2\sigma_x$ values are shown.

The δ^7Li values of individual spot measurements and mean δ^7Li values for the reacted and unreacted coal samples used in the René 41 experiments are shown in Fig. 6.5. For DECS-22 the δ^7Li values show a trend of decreasing δ^7Li with increasing temperature. For the Four Corners sample the $2\sigma_x$ of the δ^7Li values overlap at each temperature; however, the mean value does shift to 3‰ lighter for the sample heated to 350 ºC like the Four Corners Au-capsule that was heated to 300 ºC for a longer duration. The Li-contents released into the water during René 41 experiments are shown in Fig. 6.6. The Li-content from the Four Corners sample increases in the water with increasing temperature. For DECS-22 the Li-content in the water is highest at 250 ºC and decreases progressively at the higher temperatures.

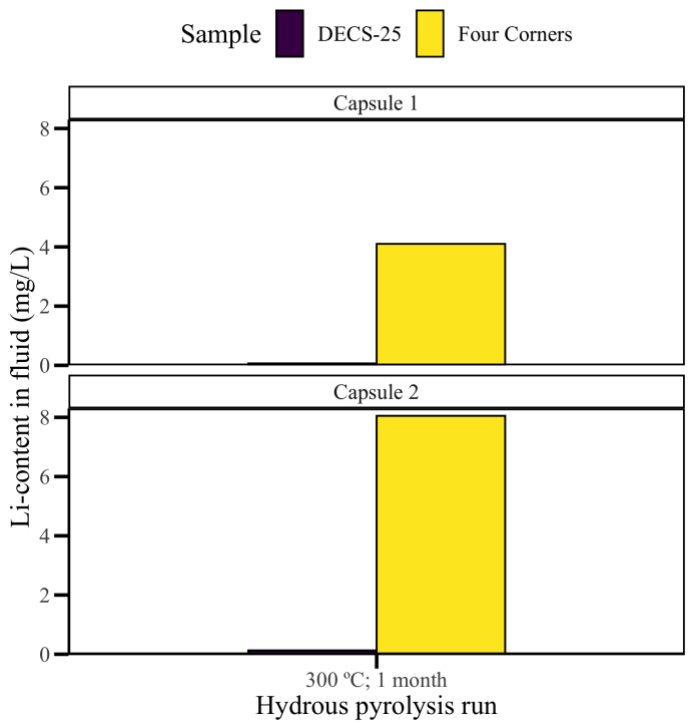

Figure 6.4. The Li contents in duplicate Au-capsule experimental fluids measured by ICP-MS. The values are calculated at a 1:1 coal to water mass ratio.

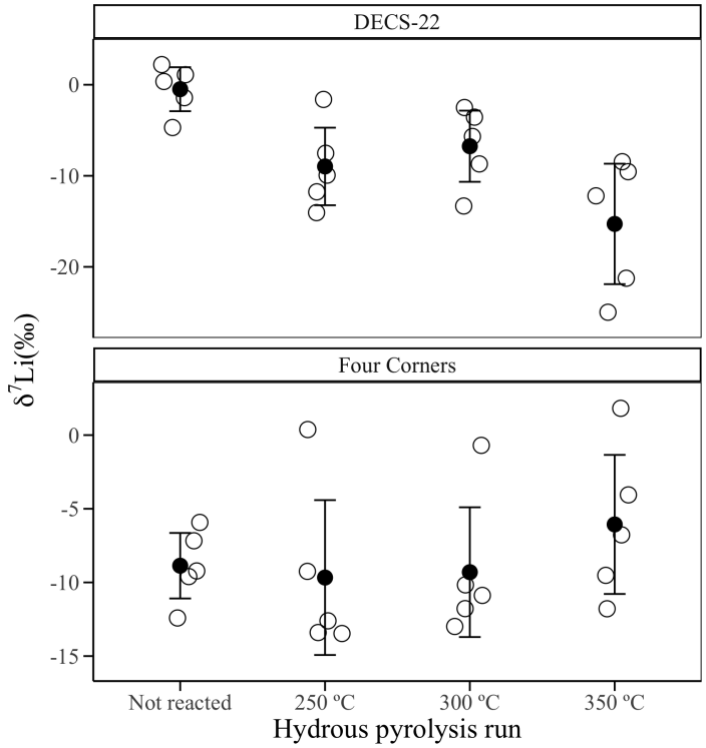

Figure 6.5. The individual spot measurements δ^7Li values (open circles) and the mean δ^7Li values (black circles) are plotted for unreacted samples and René 41 experimental powders. The $2\sigma_x$ values are shown.

Discussion

It is assumed that any Li released from coal powders into the water at the experimental temperatures used here (250 ºC to 350 ºC) is derived from kerogen because the minerals are stable at these temperatures. Surface adsorbed and clay interlayer Li was removed from powders by cation exchange during the sample preparation. Thus, the remaining Li in the coal powder is structurally bound to minerals and organics. Kaolinite and appears to be the most abundant mineral in these coal samples, and it does not undergo phase changes in the presence of water until ≥400 ºC and furthermore dehydroxylation does not occur until ≥520 ºC (Yeskis et al., 1985). Similarly, the dehydroxylation of chlorite and illite in air does not occur until ≥550 ºC and ≥470 ºC, respectively (Araújo et al., 2004; Sánchez-Ramos et al., 2008) and experiments like those performed here show illite is being formed authigenically, taking up Li rather than releasing it as these temperatures (Clauer et al., 2022; Williams and Hervig, 2005). Finally, smectite interlayers collapse and form illite at temperatures of kerogen maturation; however, if Li is removed from smectite interlayers via cation exchange this process should not contribute any Li to the fluid (Williams and Hervig, 2005).

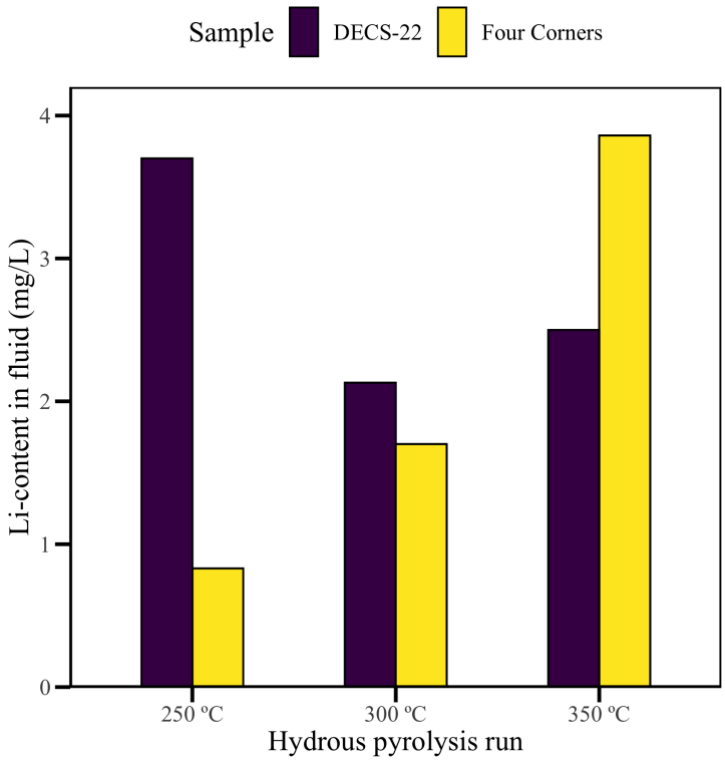

Figure 6.6. The Li contents measured in water by ICP-MS are shown for each temperature in hydrous pyrolysis experiments using René 41 reactor vessel are shown. The values are calculated at a 1:1 coal to water mass ratio.

Au-Capsule Experiments

The δ^7Li values became heavier for both samples (Four Corners and DECS-25) used in Au-capsules experiments after hydrous pyrolysis, consistent with the general trend for Li-isotopes in coal (Teichert et al., 2020) and the study of the Vermejo and Dutch Creek Coal samples (Chapter 4) which show Li becoming isotopically heavier in coal samples with increasing thermal maturity. This indicates that isotopically light Li was preferentially released from kerogen into the water. Interestingly the change in the DECS-25 was greater (10‰) despite the low Li-content (<0.2 mg/L) released into the water, while 4-8 mg/L Li was released from the Four Corners kerogen that only changed by 3‰. The DECS-25 coal is a very immature lignite which accounts for its isotopically

light starting composition (see Chapter 2); however, it must also have contained a very low starting Li-content or undergone extreme Li-isotope fractionation to change the isotope composition by 10‰ while releasing <0.2 mg/L Li.

René 41 Large Volume Experiments

Contrasting with the other samples studied in this suite, the DECS-22 Li-isotope composition becomes lighter with increasing temperature. The mean δ^7Li values of the powders reacted at 250 ºC and 300 ºC were 6 to 8‰ lighter than the unreacted sample. At 350 ºC the mean δ^7Li values were 14‰ lighter than the unreacted DECS-22 sample (Fig. 6.4). Given that the Li content in the water was higher at 250 ºC than at 300 ºC and 350 ºC it is clear that Li is not only being released from the kerogen but is also taken up by another phase at those higher temperatures. Williams and Hervig (2005) conducted hydrothermal experiments at 300 ºC with illite-smecite and showed that the concentration of Li bound in the octahedral layers of illite increased with time during illitization under those conditions. While XRD measurements performed here were not quantitative and cannot determine if illite or chlorite became more prevalent with increasing temperature, if authigenic illite or chlorite formed during hydrous pyrolysis experiments those minerals could incorporate Li into their crystal structures. Additionally, illite prefers ^{6}Li over ^{7}Li which leaves the water isotopically heavier and the bulk coal (containing illite) isotopically lighter as observed (Fig. 6.5). This observation was also reported by Clauer et al., (2022) who found that after hydrous pyrolysis of the Woodford Shale the Li-isotope composition in the illite-smectite clay fraction was 8‰ to 11‰ lighter than the unreacted sample and that this shift in δ^7Li corresponded to a decrease in total organic carbon. A plausible explanation is that isotopically light Li released from kerogen in the

Woodford Shale was then taken up during illite formation, like the proposed mechanism for sample DECS-22. However, it is not clear in these experiments why these authigenic minerals may only be forming in the DECS-22 experiments and not the other coal samples studied.

Using the Li-isotope fractionation equation for authigenic illite in DECS-22 at 350 ºC: $1000 \ln\alpha = 6.15 – 9.07(1000/T\ (K))$ (Williams and Hervig, 2005), the δ^7Li of the water in equilibrium with the illite (assuming bulk coal δ^7Li in the reacted DECS-22 was all in the silicate) would be – 6.9‰. This suggests that the kerogen was releasing isotopically light Li relative to bulk Li in the unreacted coal. Considering that these were only 72-hour experiments equilibrium between the fluid and authigenic illite may not have been reached even though the time required for hydrocarbon generation was reached (Lewan, 1993). Further complicating the use of the isotope fractionation equation to determine the water δ^7Li, kerogen was likely releasing Li to the water as Li was simultaneously being taken up by illite.

For the Four Corners sample the δ^7Li of the powders remained relatively unchanged from the unreacted sample apart from the 350 ºC sample which had a mean δ^7Li value 3‰ heavier than the unreacted sample in agreement with the Four Corners sample from the Au-capsule experiment, indicating that ^{6}Li was being preferentially released into the water. The Li-content released into the water increased with increasing temperature. Lewan (1993) conducted several 72-hour hydrothermal experiments with the Woodford Shale at temperatures ranging from 300 ºC to 365 ºC and found that the breakdown of kerogen to bitumen was highest at 330 ºC and the breakdown of bitumen to

oil peaked at ~350 ºC. Thus, the increase in Li-content released from kerogen to water appears to correspond with an increasing hydrocarbon release.

Knowing the starting bulk Li-content of the coal samples is necessary to accurately determine the Li-isotope composition of the experimental fluid using mass balance calculations (see Appendix D for mass balance calculation details). The bulk content of the Four Corners coal can be approximated using the average Li-content of coals from the Four Corners mine from the CoalQual (Bregg et al., 1998) database (20.5 ± 3.3 μg/g). The concentration of Li in the water for the Four Corners sample was up to 4 mg/L (~20% of the estimated total Li). Using the estimated bulk Li-content, the Li-contents released into the water and the mean δ^7Li values for the coal samples the Li-isotope composition of the experimental fluids can be estimated using mass balance calculations. Mass balance calculations of the Four Corners sample predict the Li-isotope composition of the fluid becomes lighter with increasing temperature (+4.5‰ at 250 ºC; –9.9‰ at 300ºC; – 26.6‰ at 350 ºC). Because the starting Li-content is much greater than the Li-content released to the water these calculations are strongly influenced by small changes in the δ^7Li values. Considering the large $2\sigma_x$ standard error values of mean δ^7Li values more measurements of the δ^7Li are necessary to improve the accuracy of these mass balance calculations.

Application to Natural Porefluids

In applying these results to natural settings, there are constraints that must be noted. First, DI water used in these experiments lacks the dissolved ions contained in pore fluids from a burial diagenesis setting, resulting in different ionic strengths. The DI-water experiments serve as a reference point for future experiments using fluids closer to

those found in nature. Second, substituting geologic timescales for higher temperatures may result in different chemical reaction pathways and mechanisms. Lastly, the experiments take place in a closed system while burial diagenesis occurs in an open system allowing for migration of porefluids.

Because the experimental rock:water mass ratio is known and the natural rock:porefluid mass ratio can be approximated by taking the porosity and the density of coal into account, the amount of Li released from kerogen to porefluids can be calculated. The porosity of the average coal is ~10% (Gan et al., 1972) which yields a rock:porefluid volume ratio of 9. Considering that coal has an average density of 1.35 g/cm^3 (Waples and Waples, 2004) and the density of the DI water used in these experiments is 1 g/cm^3, the rock:porefluid mass ratio would be 12.15. The rock:porefluid mass ratio can then be multiplied by the Li-content from the 1:1 experimental rock:water mass ratio (Table 6.2) to predict how much Li would be added from kerogen to the porefluids as shown in Fig. 6.7. The Four Corners and DECS-22 samples would both increase the porefluids Li-content by up to ~45 mg/L based on the René 41 large volume experiments: up to 100 mg/L according to the Au-capsule experiments. Even the relatively small amount of Li released from DECS-25 kerogen during Au-capsule experiments would increase the Li-content of porefluids by at least 4X the Li concentration of seawater. These calculated Li contents all fall well within the range of Li-contents measured in oilfield brines (0.17 to 500 mg/L; commonly 10's of mg/L) (Bottomley et al., 2003; Chan et al., 2002; Collins, 1975; Eccles and Berhane, 2011; Macpherson et al., 2014; Millot et al., 2011; Phan et al., 2016).

Experiment	Li content (1:1 Coal:Water mass ratio) (mg/L)
Au-Capsule-DECS-25-Capsule 1	0.06
Au-Capsule-DECS-25-Capsule 2	0.13
Au-Capsule-FC-Capsule 1	4.1
Au-Capsule-FC-Capsule 2	8.0
René 41 FC-250	0.8
René 41 FC-300	1.7
René 41 FC-350	3.9
René 41 DECS-22-250	3.7
René 41 DECS-22-300	2.1
René 41 DECS-22-350	2.5

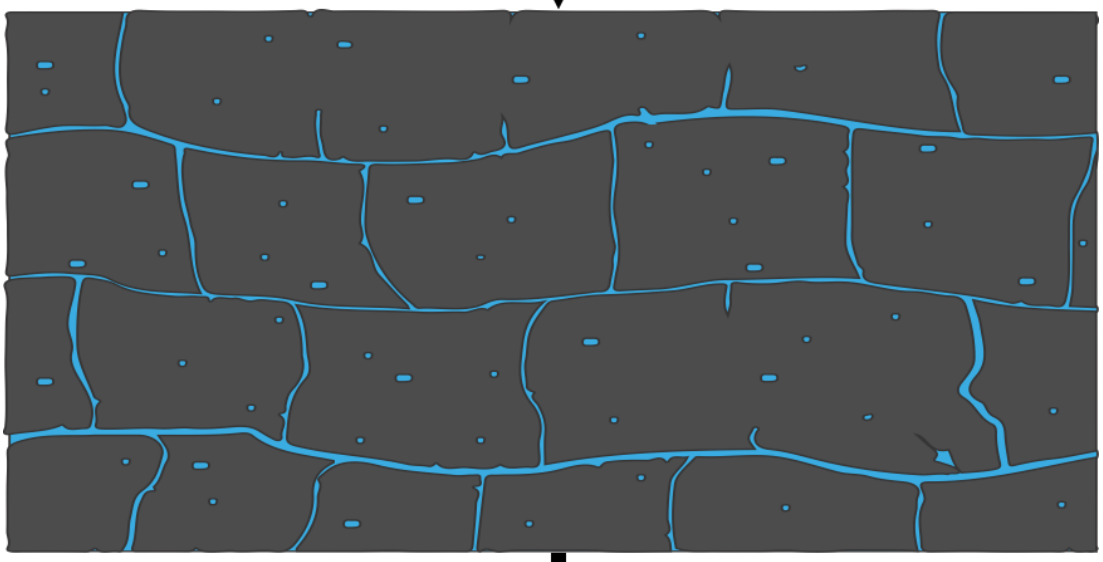

Experiment	Li content (12:1 Coal:Porefluid mass ratio) (mg/L)
Au-Capsule-DECS-25-Capsule 1	0.8
Au-Capsule-DECS-25-Capsule 2	1.6
Au-Capsule-FC-Capsule 1	49.8
Au-Capsule-FC-Capsule 2	97.8
René 41 FC-250	10.1
René 41 FC-300	20.7
René 41 FC-350	46.9
René 41 DECS-22-250	45.0
René 41 DECS-22-300	25.9
René 41 DECS-22-350	30.4

Figure 6.7. Scaling Li-content in experimental fluids up to porefluid concentrations.

Furthermore, because the Li released from kerogen is isotopically lighter than other terrestrial fluids (Teichert et al., 2020) 45 mg/L Li released from kerogen could cause porefluid δ^7Li to become significantly lighter. Using the mass balance calculations from the Four Corners sample as an example, and assuming seawater as a starting fluid composition (0.17 mg/L Li; δ^7Li = +31‰), the δ^7Li of the porefluids after Li release from kerogen would be nearly the same as the calculated values during the experiment (+5.0‰ at 250 ºC; –9.6‰ at 300ºC; – 26.4‰ at 350 ºC). Even considering porefluids that are more concentrated in Li the Li released from organics still shifts the δ^7Li composition of the porefluids significantly. Bottomley et al., (1999) studied the porefluids a of a hypersaline shield brine of marine origin which concentrated Li through evaporative or freezing processes up to ~4 mg/L with a δ^7Li value of +35.1‰. Applying the same mass balance calculations to porefluids with a Li-content and δ^7Li of these shield brines also causes the porefluids to become much isotopically lighter (+13.2‰ at 250 ºC; –2.6‰ at 300ºC; – 21.8‰ at 350 ºC).

Conclusions

Results from the hydrous pyrolysis experiments of three coal samples show that Li is released from kerogen at the temperatures of oil and gas generation. The Li released from kerogen could increase porefluid Li-contents up to ~100 mg/L. Sample DECS-22 became isotopically lighter with increasing rank likely due to the uptake of Li by authigenic illite or chlorite in the bulk coal. In the absence of authigenic minerals that incorporate Li from fluid, the δ^7Li of DECS-25 and Four Corners coals became isotopically heavier with increased temperature, and the water became isotopically lighter, consistent with previous studies. Thus, kerogen is a significant source of

isotopically light Li to diagenetic fluids and must be considered when studying minerals in sedimentary basins that are diagenetically altered.

CHAPTER 7

SUMMARY AND FUTURE EXPLORATION

Summary

This dissertation presents the first measurements of Li-content and δ^7Li of kerogen using new SIMS calibrations determined for carbon matrices and investigates the importance of kerogen in the Li-geochemical cycle. A wide-ranging survey of U.S. coals and shales led to the discovery that the δ^7Li of coal becomes progressively heavier with increasing thermal alteration from lignite up through medium volatile bituminous coal (Chapter 2; Teichert et al., 2020) signifying the preferential release of ^{6}Li during the maturation of hydrocarbons. The results in Chapter 2 necessitated investigation of matrix effects related to SIMS measurements. Homogeneous organic polymer reference materials for SIMS measurements of natural kerogen were made and methodologies for measuring the Li-content and Li-isotope composition of carbonaceous materials were developed (Chapter 3; Teichert et al., 2022). Calibrations derived from these reference materials were applied to measure changes in Li-content and δ^7Li across coal seams which were contact metamorphosed by igneous dikes (Chapter 4; Teichert et al., submitted for publication in Chemical Geology). Results from a high volatile bituminous coal (VR_o = 0.68%) that was contact metamorphosed showed that vitrinite macerals and coke within the contact zone were 18 to 37‰ heavier than vitrinite macerals in the unmetamorphosed coal. While the vitrinite and coke in the contact zone of a medium volatile coal (1.15% VR_o) was 8 to 21‰ heavier than vitrinite macerals in the unmetamorphosed coal because it had already released its isotopically light Li during burial diagenesis.

Departing from typical vitrinite-rich coals, the Li-content and Li-isotope composition was measured for two inertinite dominant Chinese coals, which were enriched in Li (1436 μg/g in silicates) through either detrital or hydrothermal processes. In these unique coals, it was determined that silicates hosted the bulk of the Li and there was little variation in δ^7Li between silicates and coal macerals (Chapter 5). Finally, multiple hydrous pyrolysis experiments of powdered coal samples were carried out (Chapter 6) to determine how much Li is released from kerogen during hydrocarbon generation under hydrous pyrolysis conditions and how the Li-isotopes fractionate between kerogen and DI water. Results from these experiments show that kerogen releases isotopically light Li into water at the temperatures of oil and gas generation. The amount of Li released from kerogen varied significantly among samples but could become concentrated in porefluids up to 100 mg/L, which is significant in diagenetic settings. The isotopically light Li released from kerogen into sedimentary porefluids may influence the Li-isotope composition of authigenic minerals forming in sedimentary basins during diagenesis. Therefore, studies that depend on δ^7Li of buried marine carbonates which have been used to reconstruct global weathering patterns and paleoclimate must consider the potential incorporation of isotopically light Li from organics into those minerals.

Future Explorations

While the work here has led to important observations which aid in understanding the role of kerogen in the Li-geochemical cycle, there are still many questions to be answered. For instance, in the general trend for US coals (Chapter 2; Teichert et al., 2020) the two highest rank coals ($\geq$ 1.68% VR_o) have δ^7Li values as low as the immature

coals and thus do not follow the trend shown from 0.2% to 1.4% VR_o (Fig. 4.1). Why are these high rank coals isotopically light while the similarly high rank coals that were contact metamorphosed are isotopically heavy (Chapter 4)? One idea is that the high rank coals from the general survey reached temperatures at which authigenic clay mineral formation (e.g., illite) became dominant taking up the isotopically light Li released from kerogen, similar to the hydrous pyrolysis results of DECS-22. It is necessary to study the mineralogy of the higher rank coals to test this hypothesis.

In addition to looking at higher rank coals it would be useful to study the Li-content and δ^7Li of coals, source rocks and carbonates across an entire sedimentary basin in detail. First, this would be another test of the validity of the general survey trend between δ^7Li and VR_o. Second, it would be useful to see if carbonates found near mature source rocks or coal are isotopically lighter than carbonates found elsewhere in the basin. Such a result might indicate that the carbonates incorporated Li from an organic source during diagenesis and are not useful indicators of paleoclimate.

Further work can also be done to confirm the δ^7Li variations among different macerals that were observed in Chapter 4. A detailed study of the δ^7Li values of different organic maceral groups would be useful to confirm differences between maceral groups. It would also be beneficial to determine if there are differences in the Li-contents and δ^7Li values of macerals within the vitrinite, liptinite and inertinite groups. Understanding which macerals concentrate isotopically light Li may lead to further insights into how kerogen takes up Li and to which molecules it is bound in the organic structure. Additionally, further study of Li-isotope variations among plants, peat and soil organic

matter is merited considering the results here and other recent studies (Li et al., 2020) of Li-isotope fractionation among organic materials.

More measurements on additional samples from the Guanbanwusu No. 6 coal mine should be performed to verify the results of Chapter 5 which did not show values as isotopically light δ^7Li in the immature macerals corresponding to the US coal survey (Chapter 2). Further SIMS measurements of the Li-contents and δ^7Li of silicates in those samples can also be performed to sort out whether the Li enrichment was primarily depositional or authigenic. Furthermore, it could be useful to study the feasibility of mining Li-fly ash derived from Li-rich coals such as the Guanbanwusu coals or coal from the Black Warrior Coalfield (Alabama, USA; up to 340 μg/g) (Goldhaber et al., 2000).

Several hydrous pyrolysis experiments could be conducted to learn more about how Li is released from kerogen and confirm the results of Chapter 6. Performing multiple hydrous pyrolysis experiments of the same coal sample for different time periods (e.g., 3-hour; 12-hour; 24-hour; 72-hour; etc.) to determine the kerogen-water equilibrium isotope fractionation would be valuable for predicting the Li-isotope composition of porefluids influenced by organics. These experiments could be repeated at multiple temperatures as well. Moreover, conducting hydrous pyrolysis experiments with a range of coal and source rock samples would be useful to determine what coal properties (e.g., organic petrology, rank) determine the amount and isotopic composition of Li released to porefluids. Ideally these would be larger volume experiments so there would be no shortage of sample for proximate and ultimate analyses, XRD and SIMS measurements on reacted powders. Ultimately, final experiments should use water with a similar chemical composition to seawater and compare those results to the pure water

experiments. Ideally these experiments should be conducted using gold vessels to minimize catalytic reactions of organic materials.

While Li from organics may not be significant during weathering of the continental crust, the work here demonstrates that it is important to consider in diagenetic settings. By researching the above questions, the role of kerogen in the Li geochemical cycle may become more fully understood.

REFERENCES

Aarnes, I., Svensen, H., Connolly, J. A. D., & Podladchikov, Y. Y. (2010). How contact metamorphism can trigger global climate changes: Modeling gas generation around igneous sills in sedimentary basins. *Geochimica et Cosmochimica Acta*, *74*(24), 7179–7195. https://doi.org/10.1016/j.gca.2010.09.011

Akar, C. (2014). *Maturity and hydrocarbon potential of the New Albany Shale and Maquoketa Shale in the Illinois Basin, USA* [M.S., Indiana University]. http://search.proquest.com/docview/1651235218/abstract/8E740D210BE34095PQ/1

Albert, S. (2014). *Sedimentology, facies architecture and sequence stratigraphy of the lower Bakken shale member in the Williston Basin, North Dakota, United States of America* [M.S., Colorado State University]. http://search.proquest.com/docview/1614528746/abstract/106EE268C02E41B9PQ/1

Andersen, C. A., & Hinthorne, J. R. (1972). Ion microprobe mass analyzer. *Science*, *175*(4024), 853–860. https://doi.org/10.1126/science.175.4024.853

Annen, C. (2017). Factors affecting the thickness of thermal aureoles. *Frontiers in Earth Science*, *5*, 82. https://doi.org/10.3389/feart.2017.00082

Araújo, J. H. de, de Araújo, J. H., da Silva, N. F., Acchar, W., & Gomes, U. U. (2004). Thermal decomposition of illite. *Materials Research*, *7*(2), 359–361.

ASME, (1979). *ASME steam tables – Thermodynamic and transport properties of steam*, American Society of Mechanical Engineers, New York.

ASTM International, (2011). *Standard test method for microscopical determination of the vitrinite reflectance of coal*. (ASTM D2798-11a). ASTM International, West Conshohocken, PA, www.astm.org.

ASTM International, (2013). *Standard test method for microscopical determination of the maceral composition of coal.* (ASTM D2799-13). ASTM International, West Conshohocken, PA, www.astm.org.

ASTM International, (2015). *Standard test methods for proximate analysis of the analysis sample of coal and coke by instrumental procedures*. (ASTM D7582-15). ASTM International, West Conshohocken, PA, www.astm.org.

ASTM International, (2018). *Standard practice for preparing coal samples for analysis.* (ASTM D2013/D2013M-18). ASTM International, West Conshohocken, PA, www.astm.org.

ASTM International, (2018b). *Standard test method for sulfur in the analysis sample of coal and coke using high-temperature tube furnace combustion*, (ASTM D4239-18e1). ASTM International, West Conshohocken, PA, www.astm.org.

ASTM International. (2019). *Classification of coals by rank*. (ASTM D388-19). ASTM International, West Conshohocken, PA, www.astm.org.

Balter, V., & Vigier, N. (2014). Natural variations of lithium isotopes in a mammalian model. *Metallomics*, *6*(3), 582–586. https://doi.org/10.1039/c3mt00295k

Barker, C. E., Bone, Y., & Lewan, M. D. (1998). Fluid inclusion and vitrinite-reflectance geothermometry compared to heat-flow models of maximum paleotemperature next to dikes, western onshore Gippsland Basin, Australia. *International Journal of Coal Geology*, *37*(1–2), 73–111. https://doi.org/10.1016/S0166-5162(98)00018-4

Barker, C. E., & Goldstein, R. H. (1990). Fluid-inclusion technique for determining maximum temperature in calcite and its comparison to the vitrinite reflectance geothermometer. *Geology*, *18*(10), 1003–1006. https://doi.org/10.1130/0091-7613(1990)018<1003:FITFDM>2.3.CO;2

Barker, C. E., & Pawlewicz, M. J. (1994). Calculation of vitrinite reflectance from thermal histories and peak temperatures. In *Vitrinite reflectance as a maturity parameter* (Vol. 570, pp. 216–229). American Chemical Society. https://doi.org/10.1021/bk-1994-0570.ch014

Bastian, L., Vigier, N., Reynaud, S., Kerros, M.-E., Revel, M., & Bayon, G. (2018). Lithium isotope composition of marine biogenic carbonates and related Reference materials. *Geostandards and Geoanalytical Research*, *42*(3), 403–415. https://doi.org/10.1111/ggr.12218

Basu, A. (2017). Chapter 2 - Evolution of siliciclastic provenance inquiries: A critical appraisal. In R. Mazumder (Ed.), *Sediment provenance* (pp. 5–23). Elsevier. https://doi.org/10.1016/B978-0-12-803386-9.00002-2

Befus, K. S., Walowski, K. J., Hervig, R. L., & Cullen, J. T. (2020). Hydrogen isotope composition of a large silicic magma reservoir preserved in quartz-hosted glass inclusions of the bishop tuff plinian eruption. *Geochemistry, Geophysics, Geosystems*, *21*(12), Article 12. https://doi.org/10.1029/2020GC009358

Bell, D. R., Hervig, R. L., Buseck, P. R., & Aulbach, S. (2009). Lithium isotope analysis of olivine by SIMS: Calibration of a matrix effect and application to magmatic phenocrysts. *Chemical Geology*, *258*(1–2), 5–16. https://doi.org/10.1016/j.chemgeo.2008.10.008

Benson, T. R., Coble, M. A., Rytuba, J. J., & Mahood, G. A. (2017). Lithium enrichment in intracontinental rhyolite magmas leads to Li deposits in caldera basins. *Nature Communications*, *8*(1), 270. https://doi.org/10.1038/s41467-017-00234-y

Berner, R. A., Lasaga, A. C., & Garrels, R. M. (1983). The carbonate-silicate geochemical cycle and its effect on atmospheric carbon dioxide over the past 100 million years. *American Journal of Science*, *283*(7), 641–683. https://doi.org/10.2475/ajs.283.7.641

Best, M. G. (2002). *Igneous and Metamorphic Petrology* (2nd ed.). Wiley-Blackwell. https://www.wiley.com/en-us/Igneous+and+Metamorphic+Petrology%2C+2nd+Edition-p-9781405105880

Bibienne, T., Magnan, J.-F., Rupp, A., & Laroche, N. (2020). From mine to mind and mobiles: Society's increasing dependence on lithium. *Elements*, *16*(4), 265–270. https://doi.org/10.2138/gselements.16.4.265

Bluztajn, J., Rosner, M., Ball, L., & 4. 2 Inorganic and isotope geochemistry, 4 0 Chemistry and material cycles. (2004). *Lithium isotope compositions of silicate reference materials*. *68*. https://gfzpublic.gfz-potsdam.de/pubman/faces/ViewItemFullPage.jsp?itemId=item_232132_1

Boschetti, T., Etiope, G., Pennisi, M., Romain, M., & Toscani, L. (2013). Boron, lithium and methane isotope composition of hyperalkaline waters (Northern Apennines, Italy): Terrestrial serpentinization or mixing with brine? *Applied Geochemistry*, *32*, 17–25. https://doi.org/10.1016/j.apgeochem.2012.08.018

Bostick, N.H., (1973). Time as a factor in thermal metamorphism of phytoclasts (coaly particles). *International Congress of Carboniferous Stratigraphy and Geology*. 7 (1973), pp. 183-193

Bostick, N. H. (1979). Microscopic measurement of the level of catagenesis of solid organic matter in sedimentary rocks to aid exploration for petroleum and to determine former burial temperatures—A Review. In *Aspects of diagenesis*. Society for Sedimentary Geology. https://pubs.geoscienceworld.org/books/book/1079/chapter/10546624/Microscopic-Measurement-of-the-Level-of

Bostick, N. H., & Collins, B. A. (1987). *ABSTRACT: Petrography and programmed pyrolysis of coal and natural coke intruded by an igneous dike, coal basin, Pitkin County, Colorado* (No. 5). *19*, 1. http://archives.datapages.com/data/tsop/TSOPv4_1987/bostick02.htm

Bostick, N. H., & Pawlewicz, M. J. (1984). Paleotemperatures based on vitrinite reflectance of shales and limestone in igneous dike aureoles in the upper cretaceous Pierre Shale, Walsenburg, Colorado. In *Hydrocarbon source rocks of the Greater Rocky Mountain Region* (p. 557). Rocky Mountain Association of Geologists. http://archives.datapages.com/data/rmag/SourceRocks84/bostick.htm

Bottomley, D. J., Chan, L. H., Katz, A., Starinsky, A., & Clark, I. D. (2003). Lithium isotope geochemistry and origin of Canadian shield brines. *Groundwater*, *41*(6), 847–856. https://doi.org/10.1111/j.1745-6584.2003.tb02426.x

Bottomley, D. J., Katz, A., Chan, L. H., Starinsky, A., Douglas, M., Clark, I. D., & Raven, K. G. (1999). The origin and evolution of Canadian shield brines: Evaporation or freezing of seawater? New lithium isotope and geochemical evidence from the Slave craton. *Chemical Geology*, *155*(3–4), 295–320. https://doi.org/10.1016/S0009-2541(98)00166-1

Bourdelle, F., Parra, T., Beyssac, O., Chopin, C., & Vidal, O. (2013). Clay minerals as geo-thermometer: A comparative study based on high spatial resolution analyses of illite and chlorite in Gulf Coast sandstones (Texas, U.S.A.). *American Mineralogist*, *98*(5–6), 914–926. https://doi.org/10.2138/am.2013.4238

Bowell, R. J., Lagos, L., de los Hoyos, C. R., & Declercq, J. (2020). Classification and characteristics of natural lithium resources. *Elements*, *16*(4), 259–264. https://doi.org/10.2138/gselements.16.4.259

Bradley, W. H. (1931). *Origin and microfossils of the oil shale of the Green River formation of Colorado and Utah*. *168*, 57.

Bregg, L. J., Oman, J. K., Tewalt, S. J., Oman, C. L., Rega, N. H., Washington, P. M., & Finkelman, R. B. (1998). *U.S. Geological Survey coal quality (COALQUAL) database: Version 2.0* (Open-File Report OF-97-134; Issue OF-97-134). U.S. Geological Survey. https://ncrdspublic.er.usgs.gov/coalqual/

Brooks, J. D., & Smith, J. W. (1969). The diagenesis of plant lipids during the formation of coal, petroleum and natural gas—II. Coalification and the formation of oil and gas in the Gippsland Basin. *Geochimica et Cosmochimica Acta*, *33*(10), 1183–1194. https://doi.org/10.1016/0016-7037(69)90040-4

Bullock, J., Cathcart, J., & Betterton, W. (2002). *Analytical methods utilized by the United State Geological Sruvey for the analysis of coal and coal combustion by-products.* (Open-File Report No. 02–389; Open-File Report, p. 15). United States Geological Survey. https://citeseerx.ist.psu.edu/viewdoc/download?doi=10.1.1.370.9277&rep=rep1&type=pdf

Burnett, D. S., Jurewicz, A. J. G., Woolum, D. S., Wang, J., Paque, J. M., Nittler, L. R., McKeegan, K. D., Humayun, M., Hervig, R., Heber, V. S., & Guan, Y. (2015). Ion implants as matrix-appropriate calibrators for geochemical ion probe analyses. *Geostandards and Geoanalytical Research*, *39*(3), 265–276. https://doi.org/10.1111/j.1751-908X.2014.00318.x

Burnham, A. K., & Sweeney, J. J. (1989). A chemical kinetic model of vitrinite maturation and reflectance. *Geochimica et Cosmochimica Acta*, *53*(10), 2649–2657. https://doi.org/10.1016/0016-7037(89)90136-1

Canter, L., Zhang, S., Sonnenfeld, M., Bugge, C., Guisinger, M., & Jones, K. (2016). *Chapter 2: Primary and secondary organic matter habit in unconventional reservoirs*. 9–23. https://doi.org/10.1306/13592014M1123691

Carr, A. D., & Williamson, J. E. (1990). The relationship between aromaticity, vitrinite reflectance and maceral composition of coals: Implications for the use of vitrinite reflectance as a maturation parameter. *Organic Geochemistry*, *16*(1), 313–323. https://doi.org/10.1016/0146-6380(90)90051-Z

Castor, S. B., & Henry, C. D. (2020). Lithium-rich claystone in the McDermitt Caldera, Nevada, USA: Geologic, mineralogical, and geochemical characteristics and possible origin. *Minerals*, *10*(1), 68. https://doi.org/10.3390/min10010068

Chan, L. H., & Edmond, J. M. (1988). Variation of lithium isotope composition in the marine environment: A preliminary report. *Geochimica et Cosmochimica Acta*, *52*(6), 1711–1717. https://doi.org/10.1016/0016-7037(88)90239-6

Chan, L.-H., Starinsky, A., & Katz, A. (2002). The behavior of lithium and its isotopes in oilfield brines: Evidence from the Heletz-Kokhav field, Israel. *Geochimica et Cosmochimica Acta*, *66*(4), 615–623. https://doi.org/10.1016/S0016-7037(01)00800-6

Chester, R. (2000). *Marine Geochemistry* (2nd ed.). John Wiley & Sons.

Cho, W. J., Kwon, S., & Choi, J. W. (2009). The thermal conductivity for granite with various water contents. *Engineering Geology*, *107*(3), 167–171. https://doi.org/10.1016/j.enggeo.2009.05.012

Clauer, N., Williams, L. B., & Fallick, A. E. (2022). Tracing organic-inorganic interactions by light stable isotopes (H, Li, B, O) of an oil-bearing shale and its clay fraction during hydrous pyrolysis. *Clays and Clay Minerals*. https://doi.org/10.1007/s42860-021-00163-4

Clergue, C., Dellinger, M., Buss, H. L., Gaillardet, J., Benedetti, M. F., & Dessert, C. (2015). Influence of atmospheric deposits and secondary minerals on Li isotopes budget in a highly weathered catchment, Guadeloupe (Lesser Antilles). *Chemical Geology*, *414*, 28–41. https://doi.org/10.1016/j.chemgeo.2015.08.015

Collins, A. G. (1975a). Chapter 5. Significance of some inorganic constituents and physical properties of oilfield waters. In *Developments in Petroleum Science* (Vol. 1, pp. 133–176). Elsevier. https://doi.org/10.1016/S0376-7361(08)70198-5

Collins, A. G. (1975b). *Geochemistry of oilfield waters*. Elsevier Scientific Pub. Co.

Coombs, D. S., (1961). Some recent work on the lower grades of metamorphism, *Aust. J. Sci. 24*, 203–215.

Cooper, J. R., Crelling, J. C., Rimmer, S. M., & Whittington, A. G. (2007). Coal metamorphism by igneous intrusion in the Raton Basin, CO and NM: Implications for generation of volatiles. *International Journal of Coal Geology*, *71*(1), 15–27. https://doi.org/10.1016/j.coal.2006.05.007

Cronin, J. R., Pizzarello, S., & Frye, J. S. (1987). 13C NMR spectroscopy of the insoluble carbon of carbonaceous chondrites. *Geochimica et Cosmochimica Acta*, *51*(2), 299–303. https://doi.org/10.1016/0016-7037(87)90242-0

Dai, K. H., & Johnson, C. E. (1999). Applicability of solid-state 13C CP/MAS NMR analysis in spodosols: Chemical removal of magnetic materials. *Geoderma*, *93*(3), 289–310. https://doi.org/10.1016/S0016-7061(99)00072-5

Dai, S., Jiang, Y., Ward, C. R., Gu, L., Seredin, V. V., Liu, H., Zhou, D., Wang, X., Sun, Y., Zou, J., & Ren, D. (2012). Mineralogical and geochemical compositions of the coal in the Guanbanwusu mine, Inner Mongolia, China: Further evidence for the existence of an Al (Ga and REE) ore deposit in the Jungar Coalfield. *International Journal of Coal Geology*, *98*, 10–40. https://doi.org/10.1016/j.coal.2012.03.003

Dai, S., Li, D., Chou, C.-L., Zhao, L., Zhang, Y., Ren, D., Ma, Y., & Sun, Y. (2008). Mineralogy and geochemistry of boehmite-rich coals: New insights from the Haerwusu surface mine, Jungar Coalfield, Inner Mongolia, China. *International Journal of Coal Geology*, *74*(3), 185–202. https://doi.org/10.1016/j.coal.2008.01.001

Deline, V. R., Evans, C. A., & Williams, P. (1978b). A unified explanation for secondary ion yields. *Applied Physics Letters*, *33*(7), 578–580. https://doi.org/10.1063/1.90466

Deline , V. R., Katz, W., Evans, C. A., & Williams, P. (1978a). Mechanism of the SIMS matrix effect. *Applied Physics Letters*, *33*(9), 832–835. https://doi.org/10.1063/1.90546

Dellinger, M., Hardisty, D. S., Planavsky, N. J., Gill, B. C., Kalderon-Asael, B., Asael, D., Croissant, T., Swart, P. K., & West, A. J. (2020). The effects of diagenesis on lithium isotope ratios of shallow marine carbonates. *American Journal of Science*, *320*(2), 150–184. https://doi.org/10.2475/02.2020.03

Dellinger, M., West, A. J., Paris, G., Adkins, J. F., Pogge von Strandmann, P. A. E., Ullmann, C. V., Eagle, R. A., Freitas, P., Bagard, M.-L., Ries, J. B., Corsetti, F. A., Perez-Huerta, A., & Kampf, A. R. (2018). The Li isotope composition of marine biogenic carbonates: Patterns and mechanisms. *Geochimica et Cosmochimica Acta*, *236*, 315–335. https://doi.org/10.1016/j.gca.2018.03.014

Deng, R. Chern., & Williams, Peter. (1989). Factors affecting precision and accuracy in quantitative analysis by secondary ion mass spectrometry. *Analytical Chemistry*, *61*(17), 1946–1948. https://doi.org/10.1021/ac00192a035

Dilles, J. H., & John, D. A. (2021). Porphyry and epithermal mineral deposits. In D. Alderton & S. A. Elias (Eds.), *Encyclopedia of Geology (Second Edition)* (pp. 847–866). Academic Press. https://doi.org/10.1016/B978-0-08-102908-4.00005-9

Dilles, J. H., Kent, A. J. R., Wooden, J. L., Tosdal, R. M., Koleszar, A., Lee, R. G., & Farmer, L. P. (2015). Zircon compositional evidence for sulfur-degassing from ore-forming arc magmas. *Economic Geology*, *110*(1), 241–251. https://doi.org/10.2113/econgeo.110.1.241

Dow, W. G. (1977). Kerogen studies and geological interpretations. *Journal of Geochemical Exploration*, *7*, 79–99. https://doi.org/10.1016/0375-6742(77)90078-4

Durand, B. (1980). *Kerogen: Insoluble Organic Matter from Sedimentary Rocks*. Editions Technip.

East, J., Swezey, C., Repetski, J., & Hayba, D. (2012). *Thermal Maturity Map of Devonian Shale in the Illinois, Michigan, and Appalachian Basins of North America* (3214th ed.) [Open-File Report]. U.S. Geological Survey. https://pubs.usgs.gov/sim/3214/pdf/sim3214.pdf

Eccles, D. R., & Berhane, H. (2011). *Geological Introduction to Lithium-Rich Formation Water with Emphasis on the Fox Creek Area of West-Central Alberta (NTS 83F and 83K)* (p. 28) [Open-File Report]. Energy resources Conservation Board. https://ags.aer.ca/document/OFR/OFR_2011_10.pdf

Farquhar, J., Hauri, E., & Wang, J. (1999). New insights into carbon fluid chemistry and graphite precipitation: SIMS analysis of granulite facies graphite from Ponmudi, South India. *Earth and Planetary Science Letters*, *171*(4), 607–621. https://doi.org/10.1016/S0012-821X(99)00177-6

Filby, R. H., & Branthaver, J. F. (Eds.). (1987). *Metal complexes in fossil fuels: Geochemistry, characterization, and processing*. American Chemical Society.

Finkelman, R. B. (1980). *Modes of occurrence of trace elements in coal* [Dissertation]. University of Maryland.

Finkelman, R. B. (1993). Trace and minor elements in coal. In M. H. Engel & S. A. Macko (Eds.), *Organic Geochemistry: Principles and Applications* (pp. 593–607). Springer US. https://doi.org/10.1007/978-1-4615-2890-6_28

Finkelman, R. B., Bostick, N. H., Dulong, F. T., Senftle, F. E., & Thorpe, A. N. (1998). Influence of an igneous intrusion on the inorganic geochemistry of a bituminous coal from Pitkin County, Colorado. *International Journal of Coal Geology*, *36*(3), 223–241. https://doi.org/10.1016/S0166-5162(98)00005-6

Finkelman, R. B., Palmer, C. A., & Wang, P. (2018). Quantification of the modes of occurrence of 42 elements in coal. *International Journal of Coal Geology, 185*, 138–160. https://doi.org/10.1016/j.coal.2017.09.005

Flesch, G. D., Anderson, A. R., & Svec, H. J. (1973). A secondary isotopic standard for 6Li/7Li determinations. *International Journal of Mass Spectrometry and Ion Physics*, *12*(3), 265–272. https://doi.org/10.1016/0020-7381(73)80043-9

Fletcher, I. R., Kilburn, M. R., & Rasmussen, B. (2008). NanoSIMS μm-scale in situ measurement of 13C/12C in early Precambrian organic matter, with permil precision. *International Journal of Mass Spectrometry*, *278*(1), 59–68. https://doi.org/10.1016/j.ijms.2008.08.010

Frank, L. A., Henderson, N. K., & Swisher, R. L. (1969). Degradation of continuous-channel electron multipliers in a laboratory operating environment. *Review of Scientific Instruments*, *40*(5), 685–689. https://doi.org/10.1063/1.1684037

Franzreb, K., Lörinčík, J., & Williams, P. (2004). Quantitative study of oxygen enhancement of sputtered ion yields. I. Argon ion bombardment of a silicon surface with O2 flood. *Surface Science*, *573*(2), 291–309. https://doi.org/10.1016/j.susc.2004.10.001

Gallois, R. W. (1976). Coccolith blooms in the Kimmeridge Clay and origin of North Sea oil. *Nature*, *259*(5543), 473–475. https://doi.org/10.1038/259473b0

Galushkin, Yu. I. (1997). Thermal effects of igneous intrusions on maturity of organic matter: A possible mechanism of intrusion. *Organic Geochemistry*, *26*(11), 645–658. https://doi.org/10.1016/S0146-6380(97)00030-2

Gan, H., Nandi, S. P., & Walker, P. L. (1972). Nature of the porosity in american coals. *Fuel*, *51*(4), 272–277. https://doi.org/10.1016/0016-2361(72)90003-8

Goldhaber, M. G., Bigelow, R. C., Hatch, J. R., & Pashin, J. C. (2000). *Distribution of a suite of elements including arsenic and mercury in Alabama coal* (Miscellaneous Field Studies Map MF-2333). U.S. Geological Survey. https://pubs.usgs.gov/mf/2000/mf-2333/mf2333so.pdf

Gough, L., Shacklette, H., & Case, A. (1977). Element concentrations toxic to plants, animals, and man. *US Geological Survey Bulletin*, *1466*, 78.

Haldar, S. K. (2020). Chapter 3—Basic mineralogy. In S. K. Haldar (Ed.), *Introduction to mineralogy and petrology (Second Edition)* (pp. 109–143). Elsevier. https://doi.org/10.1016/B978-0-12-820585-3.00003-X

Harkness, J. S., Ruhl, L. S., Millot, R., Kloppman, W., Hower, J. C., Hsu-Kim, H., & Vengosh, A. (2015). Lithium isotope fingerprints in coal and coal combustion residuals from the United States. *Procedia Earth and Planetary Science*, *13*, 134–137. https://doi.org/10.1016/j.proeps.2015.07.032

Hartlieb, P., Toifl, M., Kuchar, F., Meisels, R., & Antretter, T. (2016). Thermo-physical properties of selected hard rocks and their relation to microwave-assisted comminution. *Minerals Engineering*, *91*, 34–41. https://doi.org/10.1016/j.mineng.2015.11.008

Hathorne, E., & James, R. (2006). Temporal record of lithium in seawater: A tracer for silicate weathering? *Earth and Planetary Science Letters*, *246*(3–4), 393–406. https://doi.org/10.1016/j.epsl.2006.04.020

Hauri, E. H., Shaw, A. M., Wang, J., Dixon, J. E., King, P. L., & Mandeville, C. (2006). Matrix effects in hydrogen isotope analysis of silicate glasses by SIMS. *Chemical Geology*, *235*(3), 352–365. https://doi.org/10.1016/j.chemgeo.2006.08.010

Hauri, E., Wang, J., Dixon, J. E., King, P. L., Mandeville, C., & Newman, S. (2002). SIMS analysis of volatiles in silicate glasses: 1. Calibration, matrix effects and comparisons with FTIR. *Chemical Geology*, *183*(1), 99–114. https://doi.org/10.1016/S0009-2541(01)00375-8

He, M.-Y., Luo, C., Lu, H., Jin, Z. dong, & Deng, L. (2019). Measurements of lithium isotopic compositions in coal using MC-ICP-MS. *Journal of Analytical Atomic Spectrometry*, *34*(9), 1773–1778. https://doi.org/10.1039/C9JA00204A

Heber, V. S., McKeegan, K. D., Burnett, D. S., Duprat, J., Guan, Y., Jurewicz, A. J. G., Olinger, C. T., & Smith, S. P. (2014). Accurate analysis of shallowly implanted solar wind ions by SIMS backside depth profiling. *Chemical Geology*, *390*, 61–73. https://doi.org/10.1016/j.chemgeo.2014.10.003

Herrin, J. M., & Deming, D. (1996). Thermal conductivity of U.S. coals. *Journal of Geophysical Research: Solid Earth*, *101*(B11), 25381–25386. https://doi.org/10.1029/96JB01884

Hervig, R. L. (1996). Analyses of geological materials for boron by secondary ion mass spectrometry. *Reviews in Mineralogy and Geochemistry*, *33*(1), 789–802.

Hervig, R. L., Bell, D. R., Moore, G., Williams, L. B., Yamamoto, J., & Buseck, P. R. (2004). SIMS Analyses for Li Isotope Ratios: From olivine to clay minerals. *AGU Fall Meeting Abstracts*, *51*, 593. http://adsabs.harvard.edu/abs/2004AGUFM.V51C0593H

Hervig, R. L., Mazdab, F. K., Moore, G., & McMillan, P. F. (2003). Analyzing hydrogen (H2O) in silicate glass by secondary ion mass spectrometry and reflectance Fourier transform infrared spectroscopy. In *Developments in Volcanology* (Vol. 5, pp. 83–103). Elsevier. https://doi.org/10.1016/S1871-644X(03)80025-6

Hervig, R. L., Mazdab, F. K., Williams, P., Guan, Y., Huss, G. R., & Leshin, L. A. (2006). Useful ion yields for Cameca IMS 3f and 6f SIMS: Limits on quantitative analysis. *Chemical Geology*, *227*(1), 83–99. https://doi.org/10.1016/j.chemgeo.2005.09.008

Hettinger, R. D., Roberts, L. N. R., & Gognat, T. A. (2000). Investigations of the distribution and resources of coal in the southern part of the Piceance Basin, Colorado. *U.S. Geological Survey Professional Paper*, *1625-B**. https://pubs.usgs.gov/pp/p1625b/Reports/Chapters/Chapter_O.pdf

Hindshaw, R. S., Tosca, R., Goût, T. L., Farnan, I., Tosca, N. J., & Tipper, E. T. (2019). Experimental constraints on Li isotope fractionation during clay formation. *Geochimica et Cosmochimica Acta*, *250*, 219–237. https://doi.org/10.1016/j.gca.2019.02.015

Hingston, F. J. (1964). Reactions between boron and clays. *Soil Research*, *2*(1), 83–95. https://doi.org/10.1071/sr9640083

Hofker, W. K. (1975). *Implantation of boron in silicon* (INIS-MF--2044; Issue INIS-MF--2044). Amsterdam Univ. (Netherlands). http://inis.iaea.org/Search/search.aspx?orig_q=RN:7234550

Hogan, J. F., & Blum, J. D. (2003). Boron and lithium isotopes as groundwater tracers: A study at the Fresh Kills Landfill, Staten Island, New York, USA. *Applied Geochemistry*, *18*(4), 615–627. https://doi.org/10.1016/S0883-2927(02)00153-1

Hollocher, K., & Ruiz, J. (1995). Major and trace element determinations on NIST glass standard reference materials 611, 612, 614 and 1834 by inductively coupled plasma-mass spectrometry. *Geostandards and Geoanalytical Research*, *19*(1), 27–34. https://doi.org/10.1111/j.1751-908X.1995.tb00149.x

Hong, H.-J., Ryu, T., Park, I.-S., Kim, M., Shin, J., Kim, B.-G., & Chung, K.-S. (2018). Highly porous and surface-expanded spinel hydrogen manganese oxide (HMO)/Al2O3 composite for effective lithium (Li) recovery from seawater. *Chemical Engineering Journal*, *337*, 455–461. https://doi.org/10.1016/j.cej.2017.12.130

Horstman, E. L. (1957). The distribution of lithium, rubidium and caesium in igneous and sedimentary rocks. *Geochimica et Cosmochimica Acta*, *12*(1), 1–28. https://doi.org/10.1016/0016-7037(57)90014-5

Hosterman, J. (1990). Chemistry and mineralogy of natural bitumens and heavy oils and Their Reservoir rocks from the United States, Canada, Trinidad and Tobago, and Venezuela. *1047*, 19.

House, C. H., Schopf, J. W., McKeegan, K. D., Coath, C. D., Harrison, T. M., & Stetter, K. O. (2000). Carbon isotopic composition of individual Precambrian microfossils. *Geology*, *28*(8), 707–710. https://doi.org/10.1130/0091-7613(2000)28<707:CICOIP>2.0.CO;2

Hu, P., Hou, X., Zhang, J., Li, S., Wu, H., Damø, A. J., Li, H., Wu, Q., & Xi, X. (2018). Distribution and occurrence of lithium in high-alumina-coal fly ash. *International Journal of Coal Geology*, *189*, 27–34. https://doi.org/10.1016/j.coal.2018.02.011

Huber, M. L., Perkins, R. A., Friend, D. G., Sengers, J. V., Assael, M. J., Metaxa, I. N., Miyagawa, K., Hellmann, R., & Vogel, E. (2012). New international formulation for the thermal conductivity of H2O. *Journal of Physical and Chemical Reference Data*, *41*(3), 033102. https://doi.org/10.1063/1.4738955

Hunt, J. M. (1996). *Petroleum geochemistry and geology*. W.H. Freeman and Company.

Hutton, A. C., & Hower, J. C. (1999). Cannel coals: Implications for classification and terminology. *International Journal of Coal Geology*, *41*(1), 157–188. https://doi.org/10.1016/S0166-5162(99)00015-4

IEA (2021), *The role of critical minerals in clean energy transitions*, IEA, Paris https://www.iea.org/reports/the-role-of-critical-minerals-in-clean-energy-transitions

International Committee for Coal and Organic Petrology (ICCP), (1998). The new vitrinite classification (ICCP System, 1994). *Fuel* 77: 349–358.

International Committee for Coal and Organic Petrology (ICCP), (2001). The new inertinite classification (ICCP System, 1994). *Fuel* 80: 459–471.

Isa, J., Kohl, I. E., Liu, M.-C., Wasson, J. T., Young, E. D., & McKeegan, K. D. (2017). Quantification of oxygen isotope SIMS matrix effects in olivine samples: Correlation with sputter rate. *Chemical Geology*, *458*, 14–21. https://doi.org/10.1016/j.chemgeo.2017.03.020

Ishida, A., Kitajima, K., Williford, K. H., Tuite, M. L., Kakegawa, T., & Valley, J. W. (2018). Simultaneous in situ analysis of carbon and nitrogen isotope ratios in organic matter by secondary ion mass spectrometry. *Geostandards and Geoanalytical Research*, *42*(2), 189–203. https://doi.org/10.1111/ggr.12209

Iyer, K., Svensen, H., & Schmid, D. W. (2018). SILLi 1.0: A 1-D numerical tool quantifying the thermal effects of sill intrusions. *Geoscientific Model Development*, *11*(1), 43–60. https://doi.org/10.5194/gmd-11-43-2018

Jackson, M. L., & Barak, P. W. (2005). *Soil chemical analysis: Advanced course : a manual of methods useful for instruction and research in soil chemistry, physical chemistry of soils, soil fertility, and soil genesis*. Parallel Press, University of Wisconsin-Madison Libraries.

Jeffcoate, A. B., Elliott, T., Kasemann, S. A., Ionov, D., Cooper, K., & Brooker, R. (2007). Li isotope fractionation in peridotites and mafic melts. *Geochimica et Cosmochimica Acta*, *71*(1), 202–218. https://doi.org/10.1016/j.gca.2006.06.1611

Jin, H. (2014). *Source rock potential of the Bakken shales in the Williston Basin, North Dakota and Montana* [Ph.D., Colorado School of Mines]. http://search.proquest.com/docview/1498479642/abstract/65C61C592D1E45EAPQ/1

Jin, H., & Sonnenberg, S. A. (2013, August 12). *Characterization for Source Rock Potential of the Bakken Shales in the Williston Basin, North Dakota and Montana*. SPE/AAPG/SEG Unconventional Resources Technology Conference. https://doi.org/10.1190/urtec2013-013

Johnson, R. B. (1969). *Geologic map of the Trinidad quadrangle, south-central Colorado* [Geologic Map]. U.S. Geological Survey. https://ngmdb.usgs.gov/Prodesc/proddesc_9346.htm

Johnson, R., & Finn, T. (2001). *Potential for a basin-centered gas accumulation in the Raton Basin, Colorado and New Mexico*. https://doi.org/10.3133/b2184B

Jones, R. W. (1981). *Some mass balance and geological constraints on migration mechanisms* (No. 1). *65*(1), 20. https://doi.org/10.1306/2F91977E-16CE-11D7-8645000102C1865D

Kaminsky, F. V., Shilobreeva, S. N., Ber, B. Ya., & Kazantsev, D. Yu. (2020). Quantification of hydrogen in natural diamond by secondary ion mass spectrometry (SIMS). *Doklady Earth Sciences*, *494*(1), 699–703. https://doi.org/10.1134/S1028334X20090093

Kasemann, S. A., Jeffcoate, A. B., & Elliott, T. (2005). Lithium isotope composition of basalt glass reference material. *Analytical Chemistry*, *77*(16), 5251–5257. https://doi.org/10.1021/ac048178h

Kaufman, A. J., & Xiao, S. (2003). High CO2 levels in the Proterozoic atmosphere estimated from analyses of individual microfossils. *Nature*, *425*(6955), 279–282. https://doi.org/10.1038/nature01902

Kavanagh, L., Keohane, J., Cabellos, G., Lloyd, A., & Cleary, J. (2018). Induced plant accumulation of lithium. *Geosciences*, *8*(2), 56. https://doi.org/10.3390/geosciences8020056

Kennedy, M. J., & Wagner, T. (2011). Clay mineral continental amplifier for marine carbon sequestration in a greenhouse ocean. *Proceedings of the National Academy of Sciences*, *108*(24), 9776–9781. https://doi.org/10.1073/pnas.1018670108

Kesler, S. E., Gruber, P. W., Medina, P. A., Keoleian, G. A., Everson, M. P., & Wallington, T. J. (2012). Global lithium resources: Relative importance of pegmatite, brine and other deposits. *Ore Geology Reviews*, *48*, 55–69. https://doi.org/10.1016/j.oregeorev.2012.05.006

Ketris, M. P., & Yudovich, Ya. E. (2009). Estimations of clarkes for Carbonaceous biolithes: World averages for trace element contents in black shales and coals. *International Journal of Coal Geology*, *78*(2), 135–148. https://doi.org/10.1016/j.coal.2009.01.002

Killops, S., & Killops, V. (2004). *Introduction to Organic Geochemistry*. John Wiley & Sons, Ltd. https://doi.org/10.1002/9781118697214.ch4

Kolka, R., Bridgham, S. D., & Ping, C.-L. (2016). *Soils of peatlands: Histosols and gelisols*. https://www.nrs.fs.fed.us/pubs/49906

Kump, L. R., Brantley, S. L., & Arthur, M. A. (2000). Chemical weathering, atmospheric CO2, and climate. *Annual Review of Earth and Planetary Sciences*, *28*(1), 611–667. https://doi.org/10.1146/annurev.earth.28.1.611

Lechler, M., Pogge von Strandmann, P. A. E., Jenkyns, H. C., Prosser, G., & Parente, M. (2015). Lithium-isotope evidence for enhanced silicate weathering during OAE 1a (Early Aptian Selli event). *Earth and Planetary Science Letters*, *432*, 210–222. https://doi.org/10.1016/j.epsl.2015.09.052

Lemarchand, E., Chabaux, F., Vigier, N., Millot, R., & Pierret, M.-C. (2010). Lithium isotope systematics in a forested granitic catchment (Strengbach, Vosges Mountains, France). *Geochimica et Cosmochimica Acta*, *74*(16), 4612–4628. https://doi.org/10.1016/j.gca.2010.04.057

Lesher, C. E., & Spera, F. J. (2015). Thermodynamic and transport properties of silicate melts and magma. In *The encyclopedia of volcanoes* (pp. 113–141). Elsevier. https://doi.org/10.1016/B978-0-12-385938-9.00005-5

Leta, D. P., & Morrison, G. H. (1980). Ion implantation for in-situ quantitative ion microprobe analysis. *Analytical Chemistry*, *52*(2), 277–280. https://doi.org/10.1021/ac50052a015

Lewan, M. D. (1993). Laboratory simulation of petroleum formation. In M. H. Engel & S. A. Macko (Eds.), *Organic Geochemistry: Principles and Applications* (pp. 419–442). Springer US. https://doi.org/10.1007/978-1-4615-2890-6_18

Lewan, M. D., Comer, J. B., Hamilton Smith, T., Hasenmueller, N. R., Guthrie, J. M., Hatch, J. R., Gautier, D. L., & Franki, W. T. (1995). *Feasibility Study of Material-Balance Assessment of Petroleum from the New Albany Shale in the Illinois Basin*. *2137*, 40.

Lewan, M. D., & Ruble, T. E. (2002). Comparison of petroleum generation kinetics by isothermal hydrous and nonisothermal open-system pyrolysis. *Organic Geochemistry*, *33*(12), 1457–1475. https://doi.org/10.1016/S0146-6380(02)00182-1

Lewan, M. D., Winters, J. C., & McDonald, J. H. (1979). Generation of oil-like pyrolyzates from organic-rich shales. *Science*, *203*(4383), 897–899. https://doi.org/10.1126/science.203.4383.897

Li, J., Chen, F., Ling, Z., & Li, T. (2021). Lithium sources in oilfield waters from the Qaidam Basin, Tibetan Plateau: Geochemical and Li isotopic evidence. *Ore Geology Reviews*, *139*, 104481. https://doi.org/10.1016/j.oregeorev.2021.104481

Li, W., Liu, X.-M., & Chadwick, O. A. (2020). Lithium isotope behavior in Hawaiian regoliths: Soil-atmosphere-biosphere exchanges. *Geochimica et Cosmochimica Acta*, *285*, 175–192. https://doi.org/10.1016/j.gca.2020.07.012

Li, Y., Wiedenbeck, M., Shcheka, S., & Keppler, H. (2013). Nitrogen solubility in upper mantle minerals. *Earth and Planetary Science Letters*, *377–378*, 311–323. https://doi.org/10.1016/j.epsl.2013.07.013

Li, Z., Ward, C. R., & Gurba, L. W. (2007). Occurrence of non-mineral inorganic elements in low-rank coal macerals as shown by electron microprobe element mapping techniques. *International Journal of Coal Geology*, *70*(1), 137–149. https://doi.org/10.1016/j.coal.2006.04.009

Li, Z., Ward, C. R., & Gurba, L. W. (2010). Occurrence of non-mineral inorganic elements in macerals of low-rank coals. *International Journal of Coal Geology*, *81*(4), 242–250. https://doi.org/10.1016/j.coal.2009.02.004

Liebl, H. (1975). Secondary−ion mass spectrometry and its use in depth profiling. *Journal of Vacuum Science and Technology*, *12*(1), 385–391. https://doi.org/10.1116/1.568798

Littke, R., & Leythaeuser, D. (1993). Migration of oil and gas in coals: Chapter 10. In *Hydrocarbons from coal* (Vol. 180, pp. 219–236). American Association of Petroleum Geologists. http://archives.datapages.com/data/specpubs/mineral1/data/a180/a180/0001/0200/0219.htm

Liu, C., & Wang, P. (2013). The role of algal blooms in the formation of lacustrine petroleum source rocks—Evidence from Jiyang depression, Bohai Gulf Rift Basin, eastern China. *Palaeogeography, Palaeoclimatology, Palaeoecology*, *388*, 15–22. https://doi.org/10.1016/j.palaeo.2013.07.024

Lobus, N. V. (2016). Elemental composition of zooplankton in the Kara Sea and the bays on the eastern side of Novaya Zemlya. *Oceanology*, *56*(6), 809–818. https://doi.org/10.1134/S0001437016050088

Loftus, G. W. F., & Greensmith, J. T. (1988). The lacustrine Burdiehouse Limestone Formation—A key to the deposition of the Dinantian oil shales of Scotland. *Geological Society, London, Special Publications*, *40*(1), 219–234. https://doi.org/10.1144/GSL.SP.1988.040.01.19

Macpherson, G. L. (2015). Lithium in fluids from Paleozoic-aged reservoirs, Appalachian plateau region, USA. *Applied Geochemistry*, *60*, 72–77. https://doi.org/10.1016/j.apgeochem.2015.04.013

Macpherson, G. L., Capo, R. C., Stewart, B. W., Phan, T. T., Schroeder, K., & Hammack, R. W. (2014). Temperature-dependent Li isotope ratios in Appalachian plateau and Gulf Coast sedimentary basin saline water. *Geofluids*, *14*(4), 419–429. https://doi.org/10.1111/gfl.12084

Marriott, C. S., Henderson, G. M., Crompton, R., Staubwasser, M., & Shaw, S. (2004). Effect of mineralogy, salinity, and temperature on Li/Ca and Li isotope composition of calcium carbonate. *Chemical Geology*, *212*(1), 5–15. https://doi.org/10.1016/j.chemgeo.2004.08.002

Mathews, J. P., & Pisupati, S. (2018). Penn State and Argonne Premium Coal Sample Bank and database. *Penn State and Argonne Premium Coal Sample Bank and Database*. http://www.energy.psu.edu/cst/index.html

Matjie, R. H., Li, Z., Ward, C. R., Bunt, J. R., & Strydom, C. A. (2016). Determination of mineral matter and elemental composition of individual macerals in coals from Highveld mines. *Journal of the Southern African Institute of Mining and Metallurgy*, *116*(2), 169–180. https://doi.org/10.17159/2411-9717/2016/v116n2a8

McCabe. (1991). Tectonic controls on coal accumulation. *Societe Geologique de France*, *162*(2), 277–282.

McCarthy, K., Niemann, M., Palmowski, D., Peters, K., & Stankiewicz, A. (2011). Basic petroleum geochemistry for source rock evaluation. *Oilfield Review*, *23*, 32–43.

Meija, J., Coplen, T. B., Berglund, M., Brand, W. A., Bièvre, P. D., Gröning, M., Holden, N. E., Irrgeher, J., Loss, R. D., Walczyk, T., & Prohaska, T. (2016). Atomic weights of the elements 2013 (IUPAC Technical Report). *Pure and Applied Chemistry*, *88*(3), 265–291. https://doi.org/10.1515/pac-2015-0305

Meng, X., Mao, J., Zhang, C., Zhang, D., & Liu, H. (2018). Melt recharge, f O2-T conditions, and metal fertility of felsic magmas: Zircon trace element chemistry of Cu-Au porphyries in the Sanjiang orogenic belt, southwest China. *Mineralium Deposita*, *53*(5), 649–663. https://doi.org/10.1007/s00126-017-0768-y

Milliken, K. L. (2003). 7.07—Late diagenesis and mass transfer in sandstone–shale sequences. In H. D. Holland & K. K. Turekian (Eds.), *Treatise on Geochemistry* (pp. 159–190). Pergamon. https://doi.org/10.1016/B0-08-043751-6/07091-2

Millot, R., Guerrot, C., Innocent, C., Négrel, Ph., & Sanjuan, B. (2011). Chemical, multi-isotopic (Li–B–Sr–U–H–O) and thermal characterization of Triassic formation waters from the Paris Basin. *Chemical Geology*, *283*(3), 226–241. https://doi.org/10.1016/j.chemgeo.2011.01.020

Millot, R., Scaillet, B., & Sanjuan, B. (2010). Lithium isotopes in island arc geothermal systems: Guadeloupe, Martinique (French West Indies) and experimental approach. *Geochimica et Cosmochimica Acta*, *74*(6), 1852–1871. https://doi.org/10.1016/j.gca.2009.12.007

Misra, S., & Froelich, P. N. (2012). Lithium isotope history of Cenozoic seawater: changes in silicate weathering and reverse weathering. *Science*, *335*(6070), 818–823. https://doi.org/10.1126/science.1214697

Mojzsis, S. J., Arrhenius, G., McKeegan, K. D., Harrison, T. M., Nutman, A. P., & Friend, C. R. L. (1996). Evidence for life on earth before 3,800 million years ago. *Nature*, *384*(6604), 55–59. https://doi.org/10.1038/384055a0

Moore, D. M., & Reynolds Jr., R. C. (1997). *X-Ray Diffraction and the Identification and Analysis of Clay Minerals* (2nd ed.). Oxford University Press.

Mukhopadhyay, P. K. (1994). Vitrinite reflectance as a maturity parameter: Petrographic and molecular characterization and its applications to basin modeling. In P. K. Mukhopadhyay & W. G. Dow (Eds.), *Vitrinite Reflectance as a Maturity Parameter* (Vol. 570, pp. 1–24). American Chemical Society. https://doi.org/10.1021/bk-1994-0570.ch001

Négrel, P., Millot, R., Brenot, A., & Bertin, C. (2010). Lithium isotopes as tracers of groundwater circulation in a peat land. *Chemical Geology*, *276*(1–2), 119–127. https://doi.org/10.1016/j.chemgeo.2010.06.008

Newcombe, M. E., Plank, T., Zhang, Y., Holycross, M., Barth, A., Lloyd, A. S., Ferguson, D., Houghton, B. F., & Hauri, E. (2020). Magma pressure-temperature-time paths during mafic explosive eruptions. *Frontiers in Earth Science*, *8*, 378. https://doi.org/10.3389/feart.2020.531911

Nichols, D. J., & Traverse, A. (1971). *Palynology, petrology, and depositional environments of some early Tertiary lignites in Texas*. *2*, 37–48. JSTOR. https://doi.org/10.2307/3687276

Nuccio, V. F., & Hatch, J. R. (1996). *Vitrinite reflectance suppression in the New Alabany shale, Illinois Basin—Vitrinite reflectance and rock-eval data* (Open-File Report* No. 96–665; Issues 96–665, p. 38). U.S. Geological Survey. https://pubs.usgs.gov/of/1996/0665/report.pdf

Nuñez, J., Renslow, R., Cliff, J. B., & Anderton, C. R. (2017). NanoSIMS for biological applications: Current practices and analyses. *Biointerphases*, *13*(3), 03B301. https://doi.org/10.1116/1.4993628

Olson, N. H., Dilles, J. H., Kent, A. J. R., & Lang, J. R. (2017). Geochemistry of the Cretaceous Kaskanak batholith and genesis of the Pebble porphyry Cu-Au-Mo deposit, Southwest Alaska. *American Mineralogist*, *102*(8), 1597–1621. https://doi.org/10.2138/am-2017-6053

Orem, W. H., & Finkelman, R. B. (2003). Coal formation and geochemistry. In H. D. Holland & K. K. Turekian (Eds.), *Treatise on Geochemistry* (pp. 191–222). Pergamon. https://doi.org/10.1016/B0-08-043751-6/07097-3

Orphan, V. J., House, C. H., Hinrichs, K.-U., McKeegan, K. D., & DeLong, E. F. (2001). Methane-consuming archaea revealed by directly coupled isotopic and phylogenetic analysis. *Science*, *293*(5529), 484–487.

Othmane, G., Hull, S., Fayek, M., Rouxel, O., Lahd Geagea, M., & Kyser, T. K. (2015). Hydrogen and copper isotope analysis of turquoise by SIMS: Calibration and matrix effects. *Chemical Geology*, *395*, 41–49. https://doi.org/10.1016/j.chemgeo.2014.11.024

Palmer, C. A. (1997). *The chemical analysis of Argonne Premium Coal Samples*. *2144*, 106.

Parr, S.W., (1922). The classification of coal. *Journal of Industrial and Engineering Chemistry*. *14 (10)*, 919–922.

Parr, S.W., (1928). The classification of coal. *University of Illinois Engineering Experiment Station Bulletin* 180, 62 p.

Pawlewicz, M., & Finn, T. (2002). *Vitrinite reflectance data for the Greater Green River Basin, southwestern Wyoming, northwestern Colorado, and northeastern Utah*. *02–339*, 16.

Pendias, H., & Kabata-Pendias, A. (2000). *Trace elements in soils and plants, Third Edition*. CRC Press. https://doi.org/10.1201/9781420039900

Penniston-Dorland, S., Liu, X.-M., & Rudnick, R. L. (2017). Lithium isotope geochemistry. *Reviews in Mineralogy and Geochemistry*, *82*(1), 165–217. https://doi.org/10.2138/rmg.2017.82.6

Peters, K. E., & Cassa, M. (2007). Applied source rock geochemistry. In L. B. Magoon & W. G. Dow (Eds.), *The Petroleum System – from Source to Trap* (pp. 93–120). American Association of Petroleum Geologists.

Peters, K. E., Xia, X., Pomerantz, A. E., & Mullins, O. C. (2016). Chapter 3—Geochemistry applied to evaluation of unconventional resources. In Y. Z. Ma & S. A. Holditch (Eds.), *Unconventional Oil and Gas Resources Handbook* (pp. 71–126). Gulf Professional Publishing. https://doi.org/10.1016/B978-0-12-802238-2.00003-1

Petersen, H. I. (2006). The petroleum generation potential and effective oil window of humic coals related to coal composition and age. *International Journal of Coal Geology*, *67*(4), 221–248. https://doi.org/10.1016/j.coal.2006.01.005

Phan, T. T., Capo, R. C., Stewart, B. W., Macpherson, G. L., Rowan, E. L., & Hammack, R. W. (2016). Factors controlling Li concentration and isotopic composition in formation waters and host rocks of Marcellus Shale, Appalachian Basin. *Chemical Geology*, *420*, 162–179. https://doi.org/10.1016/j.chemgeo.2015.11.003

Pickel, W., Kus, J., Flores, D., Kalaitzidis, S., Christanis, K., Cardott, B. J., Misz-Kennan, M., Rodrigues, S., Hentschel, A., Hamor-Vido, M., Crosdale, P., & Wagner, N. (2017). Classification of liptinite – ICCP System 1994. *International Journal of Coal Geology*, *169*, 40–61. https://doi.org/10.1016/j.coal.2016.11.004

Pistiner, J. S., & Henderson, G. M. (2003). Lithium-isotope fractionation during continental weathering processes. *Earth and Planetary Science Letters*, *214*(1), 327–339. https://doi.org/10.1016/S0012-821X(03)00348-0

Pittion, J. L., & Gouadain, J. (1985). Maturity studies of the Jurassic 'Coal Unit' in three wells from the Haltenbanken area. In B. M. Thomas (Ed.), *Petroleum geochemistry in exploration of the Norwegian Shelf* (pp. 205–211). Springer Netherlands. https://doi.org/10.1007/978-94-009-4199-1_17

Pogge von Strandmann, P. A. E., Burton, K. W., Opfergelt, S., Genson, B., Guicharnaud, R. A., & Gislason, S. R. (2021). The lithium isotope response to the variable weathering of soils in Iceland. *Geochimica et Cosmochimica Acta*, *313*, 55–73. https://doi.org/10.1016/j.gca.2021.08.020

Pogge von Strandmann, P. A. E., Desrochers, A., Murphy, M. J., Finlay, A. J., Selby, D., & Lenton, T. M. (2017). Global climate stabilisation by chemical weathering during the Hirnantian glaciation. *Geochemical Perspectives Letters*, 230–237. https://doi.org/10.7185/geochemlet.1726

Pogge von Strandmann, P. A. E., Fraser, W. T., Hammond, S. J., Tarbuck, G., Wood, I. G., Oelkers, E. H., & Murphy, M. J. (2019). Experimental determination of Li isotope behaviour during basalt weathering. *Chemical Geology*, *517*, 34–43. https://doi.org/10.1016/j.chemgeo.2019.04.020

Pogge von Strandmann, P. A. E., Jenkyns, H. C., & Woodfine, R. G. (2013). Lithium isotope evidence for enhanced weathering during Oceanic Anoxic Event 2. *Nature Geoscience*, *6*(8), 668–672. https://doi.org/10.1038/ngeo1875

Pogge von Strandmann, P. A. E. P., Kasemann, S. A., & Wimpenny, J. B. (2020). Lithium and lithium isotopes in earth's surface cycles. *Elements*, *16*(4), 253–258. https://doi.org/10.2138/gselements.16.4.253

Pogge von Strandmann, P. A. E., Porcelli, D., James, R. H., van Calsteren, P., Schaefer, B., Cartwright, I., Reynolds, B. C., & Burton, K. W. (2014). Chemical weathering processes in the Great Artesian Basin: Evidence from lithium and silicon isotopes. *Earth and Planetary Science Letters*, *406*, 24–36. https://doi.org/10.1016/j.epsl.2014.09.014

Porcheddu, A., Colacino, E., De Luca, L., & Delogu, F. (2020). Metal-Mediated and Metal-Catalyzed Reactions Under Mechanochemical Conditions. *ACS Catalysis*, *10(15)*, 8344–8394. https://doi.org/10.1021/acscatal.0c00142

Pougnet, M. A. B., Wyrley-birch, J. M., & Orren, M. J. (1990). The boron and lithium content of South African coals and coal ashes. *International Journal of Environmental Analytical Chemistry*, *38*(4), 539–549. https://doi.org/10.1080/03067319008026956

Qin, S., Zhao, C., Li, Y., & Zhang, Y. (2015). Review of coal as a promising source of lithium. *International Journal of Oil, Gas and Coal Technology*, *9*(2), 215. https://doi.org/10.1504/IJOGCT.2015.067490

Regier, M. E., Hervig, R. L., Myers, M. L., Roggensack, K., & Wilson, C. J. N. (2016). Analyzing nitrogen in natural and synthetic silicate glasses by secondary ion mass spectrometry. *Chemical Geology*, *447*, 27–39. https://doi.org/10.1016/j.chemgeo.2016.10.019

Romer, R. L., & Meixner, A. (2014). Lithium and boron isotopic fractionation in sedimentary rocks during metamorphism – The role of rock composition and protolith mineralogy. *Geochimica et Cosmochimica Acta*, *128*, 158–177. https://doi.org/10.1016/j.gca.2013.11.032

Rumpel, C., Kögel-Knabner, I., & Bruhn, F. (2002). Vertical distribution, age, and chemical composition of organic carbon in two forest soils of different pedogenesis. *Organic Geochemistry*, *33*(10), 1131–1142. https://doi.org/10.1016/S0146-6380(02)00088-8

Rumpel, C., Rabia, N., Derenne, S., Quenea, K., Eusterhues, K., Kögel-Knabner, I., & Mariotti, A. (2006). Alteration of soil organic matter following treatment with hydrofluoric acid (HF). *Organic Geochemistry*, *37*(11), 1437–1451. https://doi.org/10.1016/j.orggeochem.2006.07.001

Russell, W. L. (1951). *Principles of petroleum geology* (1st ed.). McGraw-Hill.

Ryan, J. G., & Langmuir, C. H. (1987). The systematics of lithium abundances in young volcanic rocks. *Geochimica et Cosmochimica Acta*, *51*(6), 1727–1741. https://doi.org/10.1016/0016-7037(87)90351-6

Sánchez-Ramos, S., Doménech-Carbó, A., Gimeno-Adelantado, J. V., Peris-Vicente, J., & Valle-Algarra, F. M. (2008). Thermal decomposition of chromite spinel with chlorite admixture. *Thermochimica Acta, 476(1),* 11–19. https://doi.org/10.1016/j.tca.2008.07.003

Sangély, L., Chaussidon, M., Michels, R., & Huault, V. (2005). Microanalysis of carbon isotope composition in organic matter by secondary ion mass spectrometry. *Chemical Geology*, *223*(4), 179–195. https://doi.org/10.1016/j.chemgeo.2005.06.001

Saxby, J. D. (1976). Chapter 6 Chemical separation and characterization of kerogen from oil shale. In *Developments in petroleum science* (Vol. 5, pp. 103–128). Elsevier. https://doi.org/10.1016/S0376-7361(08)70046-3

Schmidt, M. W. I., Knicker, H., Hatcher, P. G., & Kogel-Knabner, I. (1997). Improvement of 13C and 15N CPMAS NMR spectra of bulk soils, particle size fractions and organic material by treatment with 10% hydrofluoric acid. *European Journal of Soil Science*, *48*(2), 319–328. https://doi.org/10.1111/j.1365-2389.1997.tb00552.x

Schöpa, A., Annen, C., Dilles, J. H., Sparks, R. S. J., & Blundy, J. D. (2017). Magma emplacement rates and porphyry copper deposits: Thermal modeling of the Yerington Batholith, Nevada. *Economic Geology*, *112*(7), 1653–1672. https://doi.org/10.5382/econgeo.2017.4525

Seah, M. P., & Shard, A. G. (2018). The matrix effect in secondary ion mass spectrometry. *Applied Surface Science*, *439*, 605–611. https://doi.org/10.1016/j.apsusc.2018.01.065

Selley, R. C., & Sonnenberg, S. A. (2015). Chapter 6—The Reservoir. In R. C. Selley & S. A. Sonnenberg (Eds.), *Elements of petroleum geology (Third Edition)* (pp. 255–320). Academic Press. https://doi.org/10.1016/B978-0-12-386031-6.00006-0

Seredin, V. V., Dai, S., Sun, Y., & Chekryzhov, I. Yu. (2013). Coal deposits as promising sources of rare metals for alternative power and energy-efficient technologies. *Applied Geochemistry*, *31*, 1–11. https://doi.org/10.1016/j.apgeochem.2013.01.009

Shahzad, B., Tanveer, M., Hassan, W., Shah, A. N., Anjum, S. A., Cheema, S. A., & Ali, I. (2016). Lithium toxicity in plants: Reasons, mechanisms and remediation possibilities – A review. *Plant Physiology and Biochemistry*, *107*, 104–115. https://doi.org/10.1016/j.plaphy.2016.05.034

Shimizu, N. (1979). Energy filtering and quantitative SIMS Analysis of silicates for major and trace elements. In A. Benninghoven, C. A. Evans, R. A. Powell, R. Shimizu, & H. A. Storms (Eds.), *Secondary ion mass spectrometry SIMS II* (pp. 62–63). Springer. https://doi.org/10.1007/978-3-642-61871-0_18

Sigmund, P. (1969). Theory of sputtering. I. Sputtering yield of amorphous and polycrystalline targets. *Physical Review*, *187*(2), 768–768. https://doi.org/10.1103/PhysRev.187.768

Simons, D. S., Chi, P. H., & Kim, K. J. (2005). Quantitative measurement of arsenic implant dose by SIMS. *Journal of Surface Analysis*, *12*, 157–160.

Sposito, G., Skipper, N. T., Sutton, R., Park, S., Soper, A. K., & Greathouse, J. A. (1999). Surface geochemistry of the clay minerals. *Proceedings of the National Academy of Sciences*, *96*(7), 3358–3364. https://doi.org/10.1073/pnas.96.7.3358

SRM 612, (2012). *Trace elements in glass*; National Institute of Standards and Technology; U.S. Department of Commerce: Gaithersburg, MD.

Środoń, J. (2001). Quantitative X-Ray Diffraction Analysis of Clay-Bearing Rocks from Random Preparations. Clays and Clay Minerals, 49(6), 514–528. https://doi.org/10.1346/CCMN.2001.0490604

Steele, R. C. J., Heber, V. S., & McKeegan, K. D. (2017). Matrix effects on the relative sensitivity factors for manganese and chromium during ion microprobe analysis of carbonate: Implications for early Solar System chronology. *Geochimica et Cosmochimica Acta*, *201*, 245–259. https://doi.org/10.1016/j.gca.2016.10.046

Steinhoefel, G., Brantley, S. L., & Fantle, M. S. (2021). Lithium isotopic fractionation during weathering and erosion of shale. *Geochimica et Cosmochimica Acta*, *295*, 155–177. https://doi.org/10.1016/j.gca.2020.12.006

Sun, H., Xiao, Y., Gao, Y., Zhang, G., Casey, J. F., & Shen, Y. (2018). Rapid enhancement of chemical weathering recorded by extremely light seawater lithium isotopes at the Permian–Triassic boundary. *Proceedings of the National Academy of Sciences*, *115*(15), 3782–3787. https://doi.org/10.1073/pnas.1711862115

Sun, L.-C., & Lee, H.-T. (2016). Evaluation of changes in macerals and geochemical properties during hydrocarbon generation based on pyrolysis of lignite from Mainland China. *Carbonates and Evaporites*, *31*(1), 61–68. https://doi.org/10.1007/s13146-015-0240-y

Sun, Y., Li, Y., Zhao, C., Lin, M., Wang, J., & Qin, S. (2010). Concentrations of Lithium in Chinese Coals. *Energy Exploration & Exploitation*, *28*(2), 97–104. https://doi.org/10.1260/0144-5987.28.2.97

Sun, Y., Yang, J., & Zhao, C. (2012a). Minimum mining grade of associated Li deposits in coal seams. *Energy Exploration & Exploitation*, *30*(2), 167–170. https://doi.org/10.1260/0144-5987.30.2.167

Sun, Y., Zhao, C., Li, Y., Wang, J., & Liu, S. (2012b). Li distribution and mode of occurrences in Li-bearing coal seam# 6 from the Guanbanwusu Mine, Inner Mongolia, Northern China. *Energy Exploration & Exploitation*, *30*(1), 109–130. https://doi.org/10.1260/0144-5987.30.1.109

Sun, Y., Zhao, C., Zhang, J., Yang, J., Zhang, Y., Yuan, Y., Xu, J., & Duan, D. (2013). Concentrations of valuable elements of the coals from the Pingshuo mining district, Ningwu Coalfield, Northern China. *Energy Exploration & Exploitation*, *31*(5), 727–744. https://doi.org/10.1260/0144-5987.31.5.727

Swaine, D. J. (1990). Mode of occurrence of trace elements in coal. In *Trace Elements in Coal* (pp. 27–49). Elsevier. https://doi.org/10.1016/B978-0-408-03309-1.50008-3

Swanson, V. (1975). *Collection, chemical analysis, and evaluation of coal samples in 1975*. *76–468*, 503. https://doi.org/10.3133/ofr76468

Sweeney, J. J., & Burnham, A. K. (1990). Evaluation of a simple model of vitrinite reflectance based on chemical kinetics (1). *AAPG Bulletin, 74*. https://doi.org/10.1306/0C9B251F-1710-11D7-8645000102C1865D

Taylor, G. H., Teichmüller, M., Davis, A., Diessel, C. F. K., Littke, R., & Robert, P. (1998). *Organic petrology* (1st ed.). Gebrüder Borntraeger Verlagsbuchhandlung. https://www.schweizerbart.de/publications/detail/isbn/9783443010362/Organic_Petrology

Teichert, Z., Bose, M., & Williams, L. B. (2020). Lithium isotope compositions of U.S. coals and source rocks: Potential tracer of hydrocarbons. *Chemical Geology, 549*, 119694. https://doi.org/10.1016/j.chemgeo.2020.119694

Teichert, Z., Bose, M., Williams, P., Hervig, R. L., & Williams, L. B. (2022). Secondary ion mass spectrometry reference materials for lithium in carbonaceous matrices. *Geostandards and Geoanalytical Research*, ggr.12415. https://doi.org/10.1111/ggr.12415

Teng, F.-Z., McDonough, W. F., Rudnick, R. L., Dalpé, C., Tomascak, P. B., Chappell, B. W., & Gao, S. (2004). Lithium isotopic composition and concentration of the upper continental crust. *Geochimica et Cosmochimica Acta*, *68*(20), 4167–4178. https://doi.org/10.1016/j.gca.2004.03.031

Teppen, B. J., & Miller, D. M. (2006). Hydration energy determines isovalent cation exchange selectivity by clay minerals. *Soil Science Society of America Journal*, *70*(1), 31–40. https://doi.org/10.2136/sssaj2004.0212

Thébault, J., Jolivet, A., Waeles, M., Tabouret, H., Sabarot, S., Pécheyran, C., Leynaert, A., Jochum, K. P., Schöne, B. R., Fröhlich, L., Siebert, V., Amice, E., & Chauvaud, L. (2022). Scallop shells as geochemical archives of phytoplankton-related ecological processes in a temperate coastal ecosystem. *Limnology and Oceanography*, *67*(1), 187–202. https://doi.org/10.1002/lno.11985

Thibon, F., Weppe, L., Vigier, N., Churlaud, C., Lacoue-Labarthe, T., Metian, M., Cherel, Y., & Bustamante, P. (2021). Large-scale survey of lithium concentrations in marine organisms. *Science of The Total Environment*, *751*, 141453. https://doi.org/10.1016/j.scitotenv.2020.141453

Tissot, B. P., Pelet, R., & Ungerer, P. (1987). Thermal history of sedimentary basins, maturation indices, and kinetics of oil and gas generation. *AAPG Bulletin*, *71*(12), 1445–1466. https://doi.org/10.1306/703C80E7-1707-11D7-8645000102C1865D

Tissot, B. P., & Welte, D. H. (1984). *Petroleum formation and occurrence. A New approach to oil and gas exploration*. Springer-Verlag.

Tomascak, P. B., Hemming, N. G., & Hemming, S. R. (2003). The lithium isotopic composition of waters of the Mono Basin, California. *Geochimica et Cosmochimica Acta, 67*(4), 601–611. https://doi.org/10.1016/S0016-7037(02)01132-8

Tomascak, P. B., Magna, T., & Dohmen, R. (2016). *Advances in lithium isotope geochemistry*. Springer International Publishing. https://doi.org/10.1007/978-3-319-01430-2

Tonarini, S., Pennisi, M., & Leeman, W. P. (1997). Precise boron isotopic analysis of complex silicate (rock) samples using alkali carbonate fusion and ion-exchange separation. *Chemical Geology*, *142*(1), 129–137. https://doi.org/10.1016/S0009-2541(97)00087-9

Ullmann, C. V., Campbell, H. J., Frei, R., Hesselbo, S. P., Pogge von Strandmann, P. A. E., & Korte, C. (2013). Partial diagenetic overprint of Late Jurassic belemnites from New Zealand: Implications for the preservation potential of δ^7Li values in calcite fossils. *Geochimica et Cosmochimica Acta*, *120*, 80–96. https://doi.org/10.1016/j.gca.2013.06.029

U.S. Geological Survey, 2021, *Mineral commodity summaries 2021*: U.S. Geological Survey, 200 p., https://doi.org/10.3133/mcs2021.

Van Krevelen, D. W. (1950). Graphical-statistical method for the study of structure and reaction processes of coal. *Fuel*, *29*, 269–284.

Van Krevelen, D. W. (1961). *Coal* (1st ed.). Elsevier.

Van Krevelen, D. W., & Schuyer, J. (1957). *Coal science* (1st ed.). Elsevier.

Vandenbroucke, M., & Largeau, C. (2007). Kerogen origin, evolution and structure. *Organic Geochemistry*, *38*(5), 719–833. https://doi.org/10.1016/j.orggeochem.2007.01.001

Vigier, N., Decarreau, A., Millot, R., Carignan, J., Petit, S., & France-Lanord, C. (2008). Quantifying Li isotope fractionation during smectite formation and implications for the Li cycle. *Geochimica et Cosmochimica Acta, 72*(3), 780–792. https://doi.org/10.1016/j.gca.2007.11.011

Vorres, K. S. (1990). The Argonne Premium Coal Sample Program. *Energy & Fuels*, *4*(5), 420–426. https://doi.org/10.1021/ef00023a001

Wagner, W., & Pruß, A. (2002). The IAPWS Formulation 1995 for the thermodynamic properties of ordinary water substance for general and scientific use. *Journal of Physical and Chemical Reference Data*, *31*(2), 387–535. https://doi.org/10.1063/1.1461829

Wang, D., & Manga, M. (2015). Organic matter maturation in the contact aureole of an igneous sill as a tracer of hydrothermal convection: A tracer of hydrothermal convection. *Journal of Geophysical Research: Solid Earth*, *120*(6), 4102–4112. https://doi.org/10.1002/2015JB011877

Waples, D. W., & Waples, J. S. (2004). A review and evaluation of specific heat capacities of rocks, minerals, and subsurface fluids. Part 1: Minerals and nonporous rocks. *Natural Resources Research*, *13*(2), 97–122. https://doi.org/10.1023/B:NARR.0000032647.41046.e7

Ward, C. R. (1974). Isolation of mineral matter from Australian bituminous coals using hydrogen peroxide. *Fuel*, *53*(3), 220–221. https://doi.org/10.1016/0016-2361(74)90015-5

Williams, L. B., & Bose, M. (2018, June). *Measurements of the lithium isotope heterogeneity in coals and kerogen indicate an unrecognized lithium contribution to the global geochemical cycles*. CMS 55th Annual Conference.

Williams, L. B., Clauer, N., & Hervig, R. L. (2012). CHAPTER 4: Light stable isotope microanalysis of clays in sedimentary rocks. In *Quantitative mineralogy and microanalysis of sediments and sedimentary rocks* (Vol. 42, p. 20).

Williams, L. B., Crawford Elliott, W., & Hervig, R. L. (2015). Tracing hydrocarbons in gas shale using lithium and boron isotopes: Denver Basin USA, Wattenberg Gas Field. *Chemical Geology*, *417*, 404–413. https://doi.org/10.1016/j.chemgeo.2015.10.027

Williams, L. B., & Hervig, R. L. (2004). Boron isotope composition of coals: A potential tracer of organic contaminated fluids. *Applied Geochemistry*, *19*(10), 1625–1636. https://doi.org/10.1016/j.apgeochem.2004.02.007

Williams, L. B., & Hervig, R. L. (2005). Lithium and boron isotopes in illite-smectite: The importance of crystal size. *Geochimica et Cosmochimica Acta*, *69*(24), 5705–5716. https://doi.org/10.1016/j.gca.2005.08.005

Williams, L. B., Środoń, J., Huff, W. D., Clauer, N., & Hervig, R. L. (2013). Light element distributions (N, B, Li) in Baltic Basin bentonites record organic sources. *Geochimica et Cosmochimica Acta*, *120*(Supplement C), 582–599. https://doi.org/10.1016/j.gca.2013.07.004

Williams, P. (1979a). Current problems in low energy ion beam materials analysis with SIMS. *IEEE Transactions on Nuclear Science*, *26*(1), 1807–1811. https://doi.org/10.1109/TNS.1979.4330489

Williams, P. (1979b). The sputtering process and sputtered ion emission. *Surface Science*, *90*(2), 588–634. https://doi.org/10.1016/0039-6028(79)90363-7

Williams, P. (1985). Secondary ion mass spectrometry. *Annual Review of Materials Science*, 34.

Williams, P., Stika, K. M., Davies, J. A., & Jackman, T. E. (1983). Quantitative SIMS analysis of hydrogenated amorphous silicon using superimposed deuterium implant standards. *Nuclear Instruments and Methods in Physics Research*, *218*(1–3), 299–302. https://doi.org/10.1016/0167-5087(83)90994-8

Wilson, G. C., & Long, J. V. P. (1982). SIMS analysis of lithium: Ion implantation and matrix effects. *International Journal of Mass Spectrometry and Ion Physics*, *42*(1), 63–75. https://doi.org/10.1016/0020-7381(82)80053-3

Wilson, R. G., Stevie, F. A., & Magee, C. W. (1989). *Secondary ion mass spectrometry: A practical handbook for depth profiling and bulk impurity analysis*. Wiley.

Wimpenny, J., Gíslason, S. R., James, R. H., Gannoun, A., Pogge Von Strandmann, P. A. E., & Burton, K. W. (2010). The behaviour of Li and Mg isotopes during primary phase dissolution and secondary mineral formation in basalt. *Geochimica et Cosmochimica Acta*, *74*(18), 5259–5279. https://doi.org/10.1016/j.gca.2010.06.028

Witherow, R. A., Lyons, W. B., & Henderson, G. M. (2010). Lithium isotopic composition of the McMurdo Dry Valleys aquatic systems. *Chemical Geology*, *275*(3), 139–147. https://doi.org/10.1016/j.chemgeo.2010.04.017

Woolley, A. R., Bergman, S. C., Edgar, A. D., Le Bas, M. J., Mitchell, R. H., Rock, N. M. S., & Scott Smith, B. H. (1996). Classification of lamprophyres, lamproites, kimberlites, and the kalsilitc, mellitic and leucitic rocks. *The Canadian Mineralogist*, *34*, 175–186.

Wunder, B., Meixner, A., Romer, R. L., Feenstra, A., Schettler, G., & Heinrich, W. (2007). Lithium isotope fractionation between Li-bearing staurolite, Li-mica and aqueous fluids: An experimental study. *Chemical Geology*, *238*(3), 277–290. https://doi.org/10.1016/j.chemgeo.2006.12.001

Xu, H., Liu, C., Mi, X., Wang, Z., Han, J., Zeng, G., Liu, P., Guan, Q., Ji, H., & Huang, S. (2021). Extraction of lithium from coal fly ash by low-temperature ammonium fluoride activation-assisted leaching. *Separation and Purification Technology*, *279*, 119757. https://doi.org/10.1016/j.seppur.2021.119757

Yeskis, D., Koster van Groos, A. F., & Guggenheim, S. (1985). The dehydroxylation of kaolinite. *American Mineralogist*, *70*(1–2), 159–164.

Zegouagh, Y., Derenne, S., Dignac, M. F., Baruiso, E., Mariotti, A., & Largeau, C. (2004). Demineralisation of a crop soil by mild hydrofluoric acid treatment: Influence on organic matter composition and pyrolysis. *Journal of Analytical and Applied Pyrolysis*, *71*(1), 119–135. https://doi.org/10.1016/S0165-2370(03)00059-7

Zhou, H., Wu, C., Pan, J., Wang, Z., Niu, Q., & Du, M. (2021). Research on molecular structure characteristics of vitrinite and inertinite from bituminous coal with FTIR, Micro-Raman, and XRD spectroscopy. *Energy & Fuels*, *35*(2), 1322–1335. https://doi.org/10.1021/acs.energyfuels.0c03586

Ziegler, J. F., Ziegler, M. D., & Biersack, J. P. (2010). SRIM – The stopping and range of ions in matter (2010). *Nuclear Instruments and Methods in Physics Research Section B: Beam Interactions with Materials and Atoms*, *268*(11), 1818–1823. https://doi.org/10.1016/j.nimb.2010.02.091

Zinner, E., Fahey, A. J., & McKeegan, K. D. (1986). Characterization of electron multipliers by charge distributions. In A. Benninghoven, R. J. Colton, D. S. Simons, & H. W. Werner (Eds.), *Secondary ion mass spectrometry SIMS V* (pp. 170–172). Springer. https://doi.org/10.1007/978-3-642-82724-2_42

Zinner, E., & Walker, R. M. (1975). Ion-probe studies of artificially implanted ions in lunar samples. *Proc. Lunar Sci Conf. 6th*, 17. https://hdl.handle.net/20.500.11753/1620

Zinner, E., Walker, R. M., Chaumont, J., & Dran, J. C. (1976). Ion probe analysis of artificially implanted ions in terrestrial samples and surface enhanced ions in lunar sample 76215,77. *Proc. Lunar Sci Conf. 7th*, 32. https://hdl.handle.net/20.500.11753/1626

APPENDIX A

SUPPLEMENTARY INFORMATION FOR CHAPTER 2

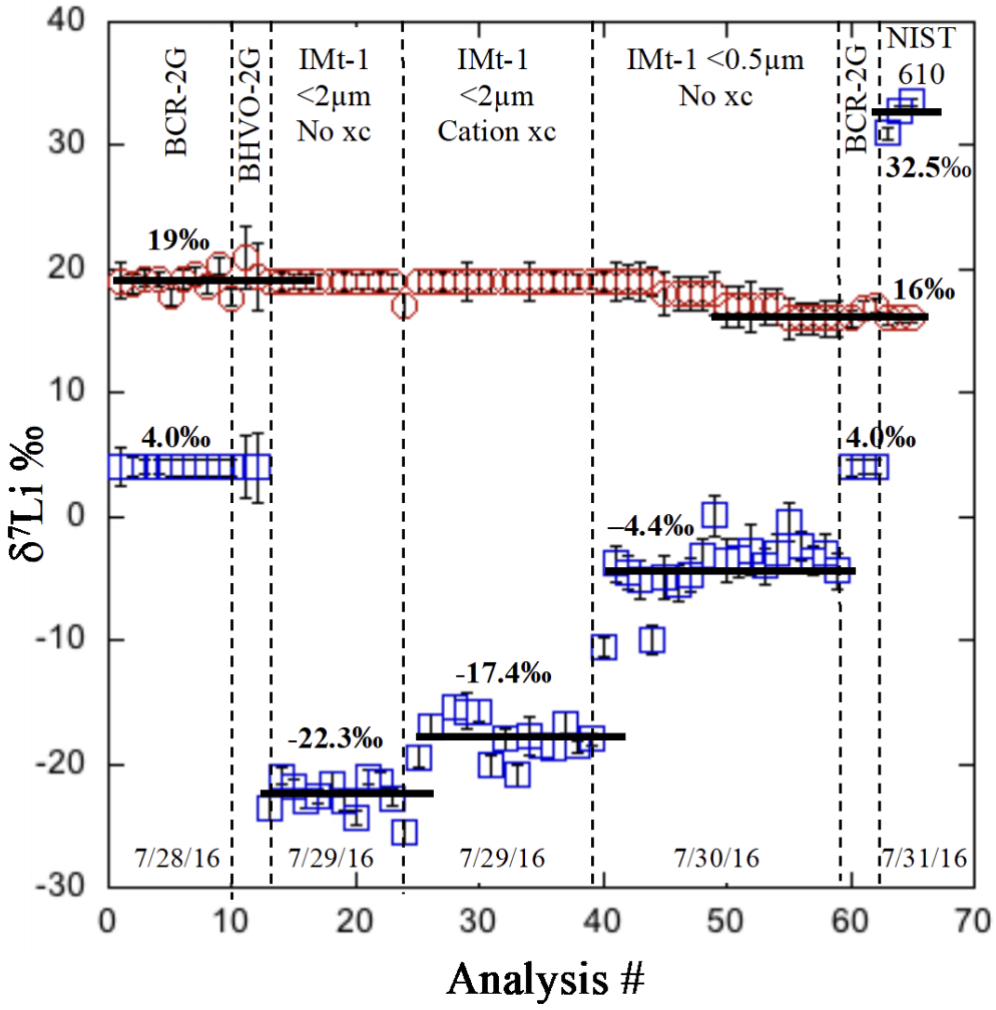

Figure A.1. Plot showing instrumental mass fractionation (red circles) and standard reference material (blue squares) δ^7Li measurements over a four-day session (2016); 1σ error bars shown. The IMF drift was 3‰ over the session, verified by standards BCR-2G (4 ± 1‰; le Roux et al., 2010); BHVO-2G (3.5 ± 1‰; Kasemann et al., 2005); IMt-1 illite (-3.7 ± 1‰; ICP-MS analysis, Rudnick Lab., Univ. Maryland) and NIST 610 (+32.5 ± 2‰; Brand et al., 2014). Black bars through data sets indicate the unknown average ‰, relative to published δ^7Li values of standards verified by ICP-MS or TIMS analyses. The illite IMt-1 reference material δ^7Li was determined by ICP-MS on a <0.5 µm size fraction. That value (–3.4 ± 1.0 ‰) gave IMF values consistent with other standards tested (BCR-2G, BHVO-2G and NIST SRM 610). However, the δ^7Li measured on cation exchanged (xc) IMt-1 shows a lower δ^7Li value (–17.4 ± 0.6 ‰). This demonstrates the importance of removing interlayer species from clay minerals so that the δ^7Li value reflects only the octahedral Li in equilibrium with the fluid. This revised δ^7Li value for IMt-1 (cation exchanged) was verified relative to other silicate δ^7Li standards measured in the same session.

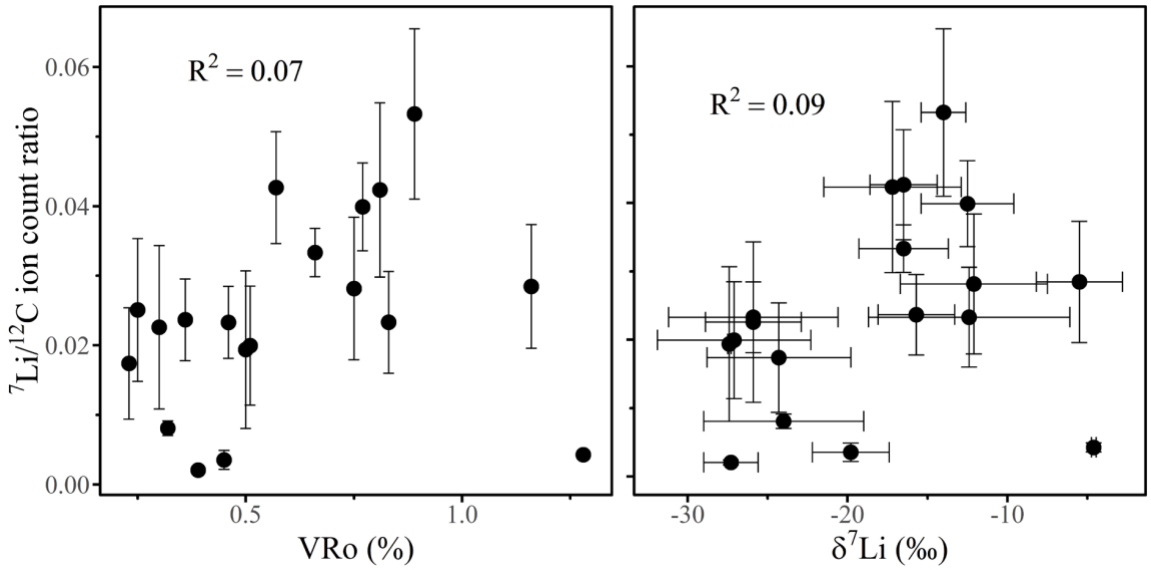

Figure A.2. $^{7}Li/^{12}C$ ion ratios on multiple spots on the coal samples from IMS-6f measurements plotted against VR_o and $\delta^{7}Li$ (1σ standard error bars are shown). No significant correlation between $^{7}Li/^{12}C$ and VR_o or $\delta^{7}Li$ is observed. Likely, this is because these samples come from different deposits with differing initial Li contents.

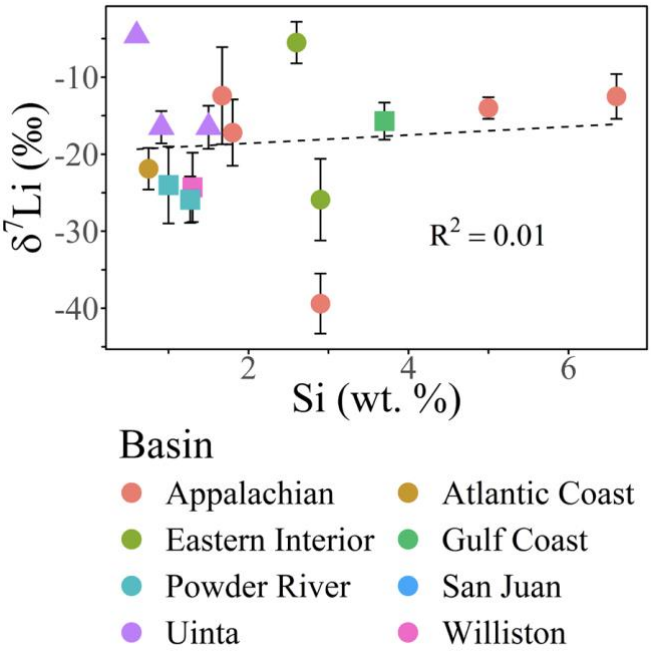

Figure A.3. Si wt.% is plotted against $\delta^{7}Li$ of coals and shows no correlation, indicating that $\delta^{7}Li$ is not related to silicate ash content. Symbols in A.3-A.8 indicate age; Tertiary (squares), Cretaceous (triangles) and Carboniferous (circles).

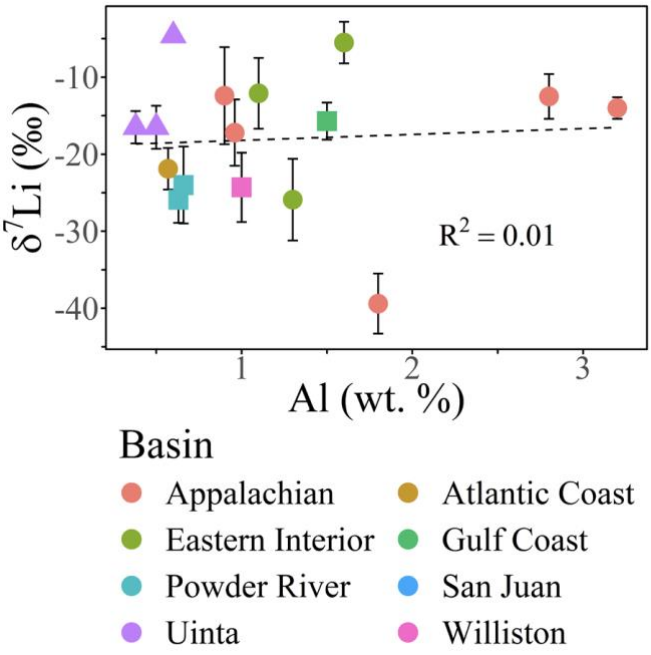

Figure A.4. Al wt.% is plotted against δ^7Li of coals and shows no correlation indicating that δ^7Li is not related to aluminosilicate ash content.

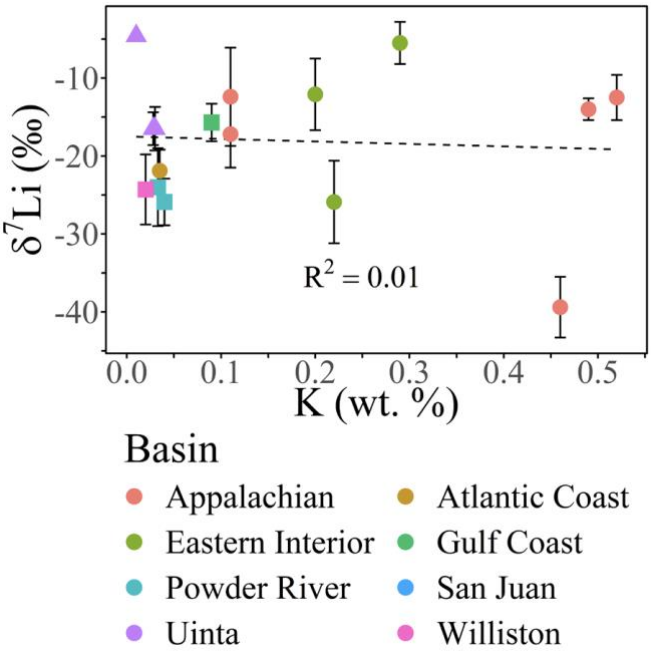

Figure A.5. K wt.% is plotted against δ^7Li of coals and shows no correlation, indicating that δ^7Li is not related to K-bearing minerals.

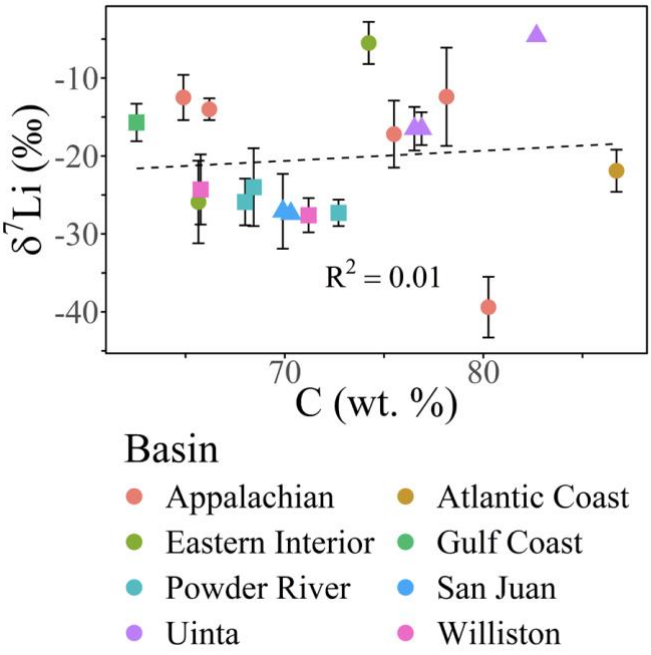

Figure A.6. C wt.% is plotted against δ^7Li and shows no correlation, indicating that δ^7Li values are not related to C content of the coals.

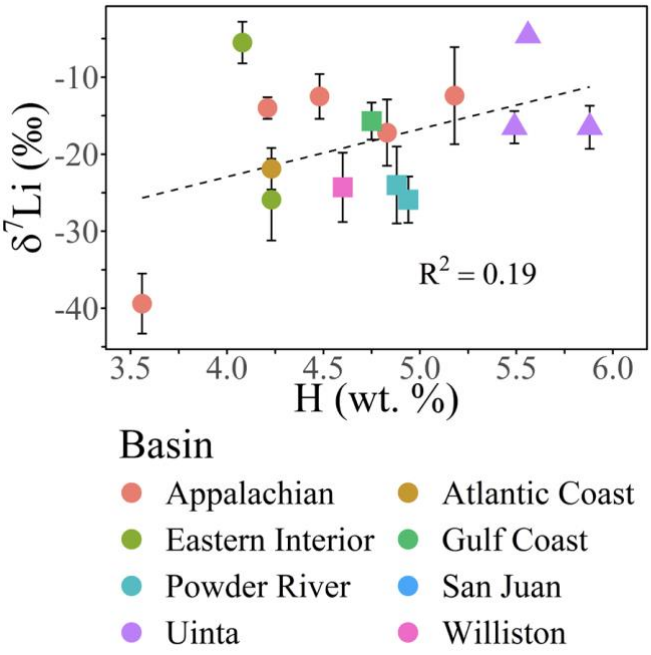

Figure A.7. H wt.% is plotted against δ^7Li and shows showing no correlation, indicating that δ^7Li is not related to H content of the coals.

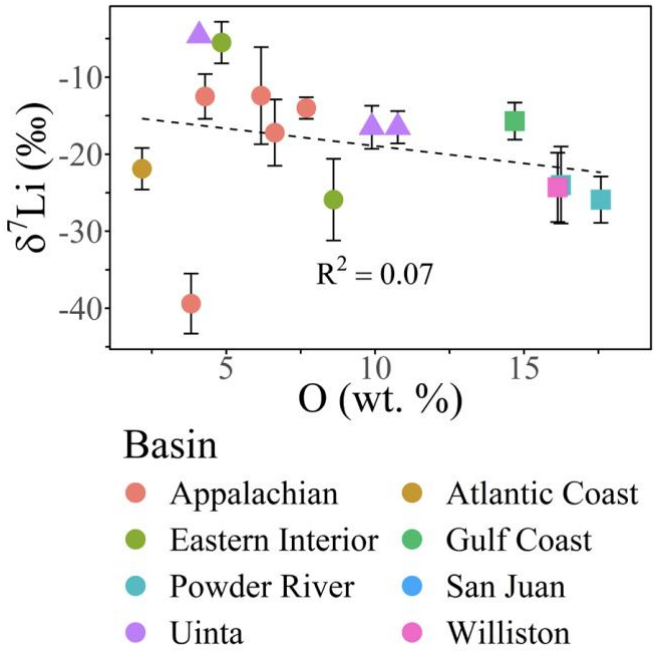

Figure A.8. O wt.% is plotted against δ^7Li and shows no correlation, indicating that δ^7Li is not related to O content of the coals.

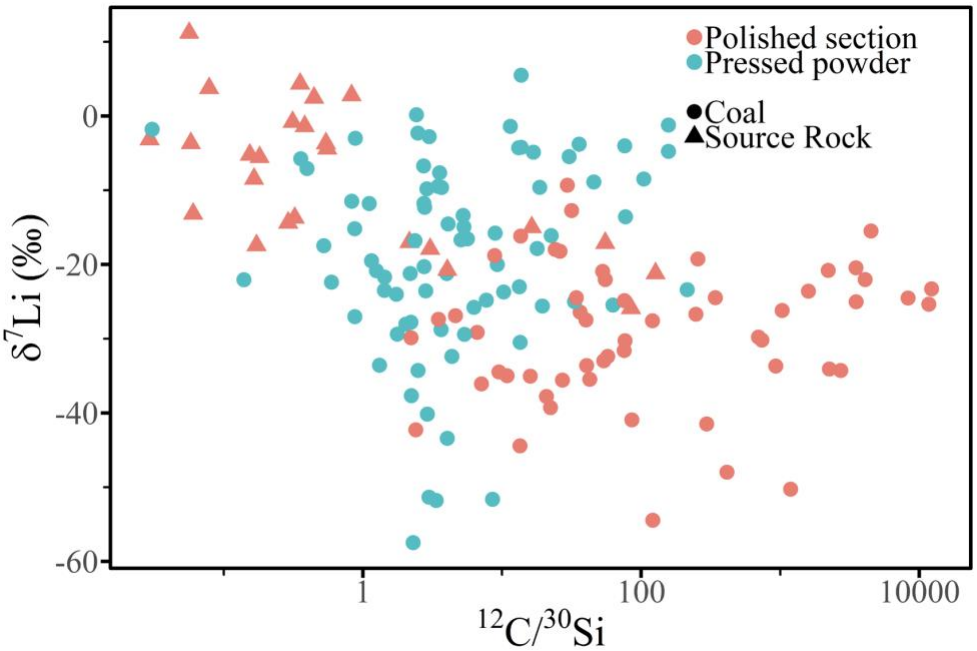

Figure A.9. Plot showing δ^7Li versus the $^{12}C/^{30}Si$ ratios for 158 spot analyses (Table A1). These data were used to define Si-rich areas where $^{12}C/^{30}Si$ ratios are <1.0. Their average δ^7Li value is –7.3 ± 1.7‰ (n=28). C-rich areas were defined where $^{12}C/^{30}Si \geq 1$, and their average δ^7Li is –23.6 ± 1.1‰ (n=130).

Table A.1

Li-isotope compositions and analytical errors for all samples reported in Chapter 2.

Sample	δ^7Li (‰)	S.E. ‰	P.E. ‰	n
APCS 1	-9.7	0.8	0.6	
APCS 1	-4.9	0.7	0.6	
APCS 1	-16.1	0.6	0.5	
APCS 1	0.2	0.3	0.3	
APCS 1	-9.6	0.5	0.3	
APCS 1	-3.8	0.3	0.2	
APCS 1	5.5	0.6	0.6	
AVG ± S.E. (n)	**-5.5**	**2.7**		7
APCS 2	-30.5	1.5	0.8	
APCS 2	-13.6	1.2	1.0	
APCS 2	-8.9	1.3	0.9	
APCS 2	-22.1	0.7	0.5	
APCS 2	-43.4	0.9	0.8	
APCS 2	-25.6	1.0	0.9	
AVG ± S.E. (n)	**-24.0**	**5.0**		6
APCS 3	-1.4	0.7	0.4	
APCS 3	-29.4	0.8	0.6	
APCS 3	-37.8	0.9	0.4	
APCS 3	-36.2	2.1	1.6	
APCS 3	-46.5	1.0	0.6	
APCS 3	-36.6	1.3	0.9	
APCS 3	-25.7	1.2	0.9	
APCS 3	-15.0	1.5	1.2	
APCS 3	-4.2	1.0	0.6	
AVG ± S.E. (n)	**-25.9**	**5.3**		9
APCS 4	-21.2	0.7	0.6	
APCS 4	-20.3	0.6	0.4	
APCS 4	-23.0	0.6	0.4	
APCS 4	-4.3	1.1	0.7	
AVG ± S.E. (n)	**-17.2**	**4.3**		**4**
APCS 5	-16.7	1.0	0.5	
APCS 5	-23.4	0.7	0.4	
APCS 5	-25.5	0.9	0.7	
AVG ± S.E. (n)	**-21.9**	**2.7**		**3**
APCS 6	-18.6	0.8	0.5	
APCS 6	-14.4	1.4	0.9	
AVG ± S.E. (n)	**-16.5**	**2.1**		**2**
APCS 7	-7.8	0.3	0.3	
APCS 7	-15.0	0.4	0.3	
APCS 7	-17.5	0.7	0.6	
APCS 7	-15.7	1.2	1.0	
APCS 7	-15.4	5.6	5.9	
APCS 7	-12.3	0.5	0.4	
AVG ± S.E. (n)	**-14.0**	**1.4**		**6**

Sample	δ^7Li (‰)	S.E. ‰	P.E. ‰	n
Bakken Shale NS	-5.2	0.7	0.7	
Bakken Shale NS	11.2	1.3	0.9	
Bakken Shale NS	-13.2	0.6	0.8	
Bakken Shale NS	-3.7	1.4	0.8	
Bakken Shale NS	-3.2	1.1	0.9	
Bakken Shale NS	-13.7	1.5	1.0	
Bakken Shale NS	-17.4	0.7	0.5	
Bakken Shale NS	-5.5	1.5	0.8	
Bakken Shale NS	-8.5	1.5	1.2	
AVG ± S.E. (n)	**-8.8**	**1.9**		**9**
Black Thunder	-25.0	1.1	1.0	
Black Thunder	-22.1	1.0	0.9	
Black Thunder	-20.5	0.8	0.9	
Black Thunder	-19.3	1.4	1.0	
Black Thunder	-15.5	0.9	0.8	
Black Thunder	-26.4	1.2	0.9	
Black Thunder	-22.1	1.3	0.7	
Black Thunder	-35.5	1.6	1.2	
Black Thunder	-29.2	2.6	2.4	
Black Thunder	-24.5	1.3	1.2	
Black Thunder	-23.6	1.1	1.1	
Black Thunder	-26.2	1.1	1.2	
Black Thunder	-33.6	1.4	1.1	
Black Thunder	-26.7	1.3	1.2	
Black Thunder	-26.9	1.5	1.3	
Black Thunder	-20.8	1.2	1.0	
Black Thunder	-23.3	1.3	1.3	
Black Thunder	-34.1	2	1.8	
Black Thunder	-34.3	1.6	1.6	
Black Thunder	-50.3	2	1.4	
Black Thunder	-33.7	1.7	1.8	
AVG ± S.E. (n)	**-27.3**	**1.7**		**21**
Four Corners	-16.2	1.6	1.2	
Four Corners	-35.1	1.0	0.8	
Four Corners	-18.8	1.2	0.6	
Four Corners	-18.2	1.9	1.0	
Four Corners	-20.9	1.4	0.8	
Four Corners	-48.0	1.7	1.3	
Four Corners	-27.5	1.1	0.7	
Four Corners	-33.0	1.1	0.6	
Four Corners	-24.9	1.4	1.0	
Four Corners	-24.5	1.4	1.0	
Four Corners	-18.0	1.1	0.6	
Four Corners	-54.5	1.2	0.8	

Table A.1 Continued

DECS 1	-14.6	0.6	0.4		Four Corners	-44.5	0.9	0.5	
DECS 1	-2.8	0.8	0.5		Four Corners	-11.8	0.5	0.4	
DECS 1	-15.8	0.9	0.8		Four Corners	-1.8	0.5	0.3	
DECS 1	-2.3	0.9	0.5		Four Corners	-7.1	0.4	0.2	
DECS 1	-24.0	0.6	0.4		Four Corners	-11.5	0.6	0.5	
DECS 1	-5.8	0.7	0.4		Four Corners	-23.5	0.8	0.4	
DECS 1	-21.2	1.0	0.8		Four Corners	-22.4	0.6	0.3	
DECS 1	-9.5	1.1	1.0		Four Corners	-17.5	0.7	0.4	
DECS 1 NS	-28.1	0.9	0.8		Four Corners	-15.2	0.6	0.3	
DECS 1 NS	-21.7	1.2	0.9		Four Corners	-37.8	0.6	0.6	
DECS 1 NS	-19.5	1.4	1.4		Four Corners	-34.5	0.8	0.4	
DECS 1 NS	-13.4	1.3	1.3		Four Corners	-41.5	1.5	0.8	
DECS 1 NS	-25.8	2.3	2.1		Four Corners	-36.1	0.7	0.5	
AVG ± S.E. (n)	**-15.7**	**2.4**		**13**	Four Corners	-39.3	0.7	0.5	
DECS 21	-32.4	1.5	0.8		Four Corners	-35.6	1.3	1.1	
DECS 21	-23.6	0.9	0.5		Four Corners	-29.9	0.3	0.2	
DECS 21	-27.8	0.7	0.4		Four Corners	-31.6	1.4	1.2	
DECS 21	-37.7	0.5	0.3		Four Corners	-35.0	0.4	0.3	
DECS 21	-51.8	0.8	0.4		Four Corners	-30.3	1.2	0.9	
DECS 21 NS	-51.4	0.8	0.6		Four Corners	-30.2	1.1	1.1	
DECS 21 NS	-27.0	0.8	0.8		Four Corners	-27.6	1.3	1.5	
DECS 21 NS	-57.5	1.2	0.9		**AVG ± S.E. (n)**	**-27.4**	**0.1**		**33**
DECS 21 NS	-33.6	0.7	0.6		Green River	-20.7	0.4	0.3	
DECS 21 NS	-51.6	1.2	0.9		Green River	-4.4	0.9	0.5	
AVG ± S.E. (n)	**-39.4**	**3.9**		**10**	Green River *	-17.0	0.8	0.3	
DECS 22	-11.8	0.7	0.5		Green River *	-17.9	1.9	0.5	
DECS 22	-20.9	0.6	0.3		**AVG ± S.E. (n)**	**-15.0**	**3.6**		**4**
DECS 22	-7.7	0.5	0.4		New Albany	2.8	0.8	0.4	
DECS 22	-9.8	0.4	0.4		New Albany	-0.8	0.5	0.3	
AVG ± S.E. (n)	**-12.5**	**2.9**		**4**	New Albany	-3.7	0.4	0.3	
DECS 25 *	-23.7	0.8	0.3		New Albany	3.7	0.4	0.3	
DECS 25	-34.6	0.6	0.3		New Albany	-1.4	0.4	0.3	
DECS 25	-34.0	0.8	0.5		New Albany	-14.4	0.6	0.6	
DECS 25	-16.1	1.4	1.2		New Albany	2.5	0.3	0.3	
DECS 25	-12.9	2.9	2.5		New Albany	4.3	0.4	0.4	
AVG ± S.E. (n)	**-24.3**	**4.5**		**5**	**AVG ± S.E. (n)**	**-0.9**	**2.2**		**8**
DECS 3	-8.5	1.4	1.0		NIST 1632cr	-24.8	2.1	1.3	
DECS 3	-4.0	0.8	0.6		NIST 1632cr	-40.2	1.4	1.3	
DECS 3	-4.8	1.4	1.1		**AVG ± S.E. (n)**	-32.5	7.7		**2**
DECS 3	-1.2	1.4	1.2		NIST 2684b	-16.6	1.4	1.1	
AVG ± S.E. (n)	**-4.6**	**0.15**		**4**	NIST 2684b	-3.0	0.6	0.4	
DECS 34	-6.7	0.6	0.3		NIST 2684b	-16.8	1.3	0.8	
DECS 34	-5.5	0.9	0.6		**AVG ± S.E. (n)**	-12.1	4.6		3

Table A.1 Continued

DECS 34	-25.0	0.7	0.5		San Juan	-12.7	0.8	0.5	
AVG ± S.E. (n)	**-12.4**	**6.3**		**3**	San Juan	-9.3	1.0	0.5	
DECS 39	-34.3	1.4	0.7		San Juan	-27.4	1.2	0.6	
DECS 39	-28.8	0.7	0.4		San Juan	-41.0	1.0	0.5	
DECS 39	-20.0	1.5	1.1		San Juan	-42.3	1.7	1.1	
DECS 39	-17.9	1.6	1.4		San Juan	-24.5	2.3	1.4	
DECS 39	-28.4	1.2	0.6		San Juan	-32.4	2.5	1.3	
AVG ± S.E. (n)	**-25.9**	**3.0**		**5**	**AVG ± S.E. (n)**	**-27.1**	**4.8**		**7**
DECS 6	-15.5	1.2	0.6		Savage Lignite	-29.8	2.4	2.7	
DECS 6	-9.8	1.2	0.8		Savage Lignite	-25.4	1.2	1.1	
DECS 6	-17.6	0.6	0.6		**AVG ± S.E. (n)**	**-27.6**	**2.2**		**2**
DECS 6	-23.2	0.9	0.6		Wilcox	-15.0	2.8	1.7	
AVG ± S.E. (n)	**-16.5**	**2.8**		**4**	Wilcox	-17.1	2.6	1.7	
S.E. = standard error of the mean;					Wilcox	-25.9	2.7	1.4	
P.E. = predicted error; n = # of analyses					Wilcox	-21.2	3	1.5	
NS = Spot measurements done by NanoSIMS.					**AVG ± S.E. (n)**	**-19.8**	**2.4**		**4**
Note: analyses were discarded if SE > 2PE with the exception of measurements with * where PE < 0.5.									

Table A.2

δ^7Li values of deep groundwaters and oilfield brines from several studies.

Author	Sampling Locations	Fluid Type	Basinal details (i.e.rock type associated with fluids; oilfield associated)	δ^7Li ranges or mean values
Boschetti et al., 2013	Northern Apennines, Italy	Springwater (groundwater)	Issued from mafic/ultramafic ophiolite	+24.3 ‰ mean value for peridotite associated water & +29 to 35 ‰ for hyperalkaline spring waters.
Bottomley et al., 2003	Manitoba, Ontario, Saskatchewan 2600-2800 m deep wells	Hypersaline Ca/Cl rich shield brines. Oilfield brine sample from Williston Basin.	Metavolcanic and metasedimentary rocks. Williston fluids from carbonate red river fm. in oilfield.	+24 to 45 ‰ for shield brines +15‰ for a single Williston basin fluid sample.
Bottomley et al.,1999	Northwest Terrotories 700-1600 m deep wells	Hypersaline Ca/Cl rich shield brines.	Metavolcanic and metasedimentary rocks	Mean value +35.1 ‰
Chan et al., 2002	Heletz–Kokhav oilfield, Israel	Oilfield produced fluid. Brine was separated from oil and then measured.	Sampled from sandstone and dolomite units	+17.9 to +26.3 ‰
Eccles DR, Berhane H (2011)	Alberta Basin	Oilfield produced waters.	Devonian fm. waters	+6 to +16 ‰
Hogan and Blum, 2003	Staten Island, New York Shallow wells 3-40 m deep	Groundwater from seawater, freshwater and landfill leachate	Glacial and glaciolacustrine sediments underlain by schist	Freshwater +21.5 to +26.0 ‰ Seawater +30 to +51 ‰ Transition +24.7 to +30.6 ‰
Macpherson, 2014 (Geofluids) "Temperature-dependent Li isotope ratios in Appalachian Plateau and Gulf Coast Sedimentary Basin saline water"	(i) Pennsylvania (ii) Pennsylvania (iii) Gulf Basin	Oilfield produced waters.	(i)Appalachian Plateau Middle Devonian Marcellus Group (ii) Appalachian Plateau Upper Devonian Bradford and Venango Groups (iii) (Plio-Pleisto to Jurassic-aged reservoirs	(i) +12.49 to +15.23 (ii) +8.15 to +9.54 (iii) +4.21 to +16.27
Millot et al., 2011	Paris Basin	Oilfield produced waters.	Taken from sandstone reservoirs.	+6.7 to +10.9 ‰
Phan et al., 2016	(i)Southwest Pennsylvania (ii) South central New York	Oilfield produced waters.	(i) Upper Devonian sandstone fm. waters (ii)Marcellus Group.	(i) +14.6 ‰ (ii) +10.0 ‰

Table A.2 Continued

Pogge von Strandmann et al., 2014	Artesian Basin, Australia 427-827 m depth	Deep Groundwater	Sandstone, siltstone and mudstone aquifer	+9 to +16 ‰ Lighter than river water (~+23 ‰) and seawater +31 ‰.
Williams et al., 2015	Denver Basin, USA	Paleo fluids calculated from illite-water α	Cretaceous bentonites collected from shale	-3 to +5 ‰ paleo fluid from coarse illite in the Wattenburg Gas Field (WGF) and +14 to +17 in coarse illite outside the WGF
Williams et al., 2013	Baltic Basin	Paleo fluids calculated from illite-water α	Ordovician-Silurian Bentonites	The δ7Li values in I-S from bentonites near oilfields was -10‰, indicating fluid δ7Li values ~+8‰ (at 100˚C)
The studies shown here indicate that deep fluids associated with oil and gas generation tend to be lighter than other deep groundwaters and brine fluids.				

Table A.3

Li-contents and δ^7Li values of macerals on polished samples.

Measurement	Maceral	Maceral Group	δ^7Li (‰)	S.E. (‰)	P.E. (‰)	$^7Li^+/^{30}Si^+$	$^7Li^+/^{12}C^+$	$^{12}C^+/^{30}Si^+$	Li content (µg/g)
BT_1	Ulminite	Huminite	-26.4	1.2	0.9	0.2	0.0055	36.5	0.33
BT_2	Ulminite	Huminite	-22.1	1.3	0.7	0.3	0.0048	55.3	0.29
BT_3	Ulminite	Huminite	-35.5	1.6	1.2	0.1	0.0033	42.8	0.20
BT_4	Ulminite	Huminite	-29.2	2.6	2.4	0.0	0.0012	6.6	0.07
BT_5	Textinite	Huminite	-24.5	1.3	1.2	7.5	0.0009	8309.9	0.05
BT_6	Textinite	Huminite	-23.6	1.1	1.1	2.3	0.0014	1596.5	0.09
BT_7	Ulminite	Huminite	-26.2	1.1	1.2	1.0	0.0010	1032.9	0.06
BT_8	Ulminite	Huminite	-33.6	1.4	1.1	0.1	0.0014	40.6	0.08
BT_9	Ulminite	Huminite	-26.7	1.3	1.2	0.2	0.0009	248.2	0.05
BT_10	Ulminite	Huminite	-26.9	1.5	1.3	0.0	0.0036	4.6	0.21
BT_11	Ulminite	Huminite	-20.8	1.2	1	2.7	0.0012	2217.2	0.07
BT_12	Semifusinite	Inertinite	-23.3	1.3	1.3	20.5	0.0017	12267.2	0.10
BT_13	Semifusinite	Inertinite	-34.1	2	1.8	1.5	0.0007	2257.1	0.04
BT_14	Corpohuminite	Huminite	-50.3	2	1.6	0.8	0.0007	1190.5	0.04
BT_16	Secretinite	Inertinite	-113.9	1.2	0.9	0.8	0.0014	551.4	0.09
BT_17	Corpohuminite	Huminite	-52.1	0.9	0.4	0.2	0.0003	554.7	0.02
BT_18	Secretinite	Inertinite	-33.7	1.7	1.8	0.7	0.0008	929.5	0.05
BT_19	Semifusinite	Inertinite	-34.3	1.6	1.6	2.0	0.0007	2729.9	0.04
FC_1	Collotelinite	Vitrinite	-49.0	1.7	1.3	0.5	0.0012	414.4	0.20
FC_2	Collotelinite	Vitrinite	-28.5	1.1	0.7	0.1	0.0023	40.2	0.38
FC_3	Collotelinite	Vitrinite	-34.0	1.1	0.6	0.2	0.0037	54.0	0.60
FC_4	Collotelinite	Vitrinite	-22.9	1.4	1	0.1	0.0014	75.9	0.24
FC_5	Collotelinite	Vitrinite	-22.5	1.4	1	0.4	0.0012	342.1	0.20
FC_6	Intertodetrinite	Inertinite	-3.4	0.7	0.3	0.1	0.1825	0.6	29.84
FC_8	Collodetrinite	Vitrinite	-17.9	3.2	1.9	0.0	0.0089	1.9	1.46
FC_12	Collotelinite	Vitrinite	-33.4	1	0.4	0.2	0.0035	49.9	0.58
FC_13	Collotelinite	Vitrinite	-44.5	0.9	0.5	1.5	0.1112	13.5	18.19
FC_14	Collotelinite	Vitrinite	-37.8	0.6	0.6	0.5	0.0245	20.9	4.00
FC_16	Collotelinite	Vitrinite	-32.1	0.7	0.3	0.2	0.0292	8.4	4.77
FC_17	Collotelinite	Vitrinite	-34.5	0.8	0.4	0.6	0.0596	9.5	9.75
FC_18	Collotelinite	Vitrinite	-40.7	1.4	0.4	0.5	0.0795	6.0	13.00
FC_19	Collotelinite	Vitrinite	-88.2	1.3	0.5	1.0	0.0106	95.4	1.73
FC_20	Collotelinite	Vitrinite	-54.3	1	0.4	0.8	0.0147	53.8	2.40
FC_23	Gelinite	Vitrinite	-45.5	1.5	0.8	1.8	0.0061	296.5	0.99
FC_26	Collotelinite	Vitrinite	-47.3	1.1	0.4	0.8	0.0219	36.1	3.58
SJ_2	Collotelinite	Vitrinite	-30.3	1	0.4	0.3	0.0726	3.5	11.87
SJ_3	Collotelinite	Vitrinite	-41.0	1	0.5	0.1	0.0015	85.9	0.25
SJ_5	Resinite	Liptinite	-42.3	1.7	1.1	0.2	0.0890	2.4	14.55
SJ_6	Fusinite	Inertinite	-30.9	0.3	0.3	1.3	0.0489	27.3	7.99
SJ_7	Collodetrinite	Vitrinite	-75.1	1.1	0.4	0.7	0.0306	22.5	5.00
SJ_9	Resinite	Liptinite	-29.9	3.5	1.9	0.3	0.0065	52.1	1.06
SJ_10	Fusinite	Inertinite	-24.5	2.3	1.4	0.2	0.0056	34.2	0.91
SJ_11	Collodetrinite	Vitrinite	-32.4	2.5	1.3	0.2	0.0039	57.5	0.64

BT = Black Thunder; FC = Four Corners; SJ = San Juan. Errors are 1σ.

APPENDIX B

SUPPLEMENTARY INFORMATION FOR CHAPTER 3

Appendix B1: Absolute Calibration of Implant Fluences

Because the implant fluence is one of the values that is used in calculating K*, it is important that it is known accurately. Owing to the fact that actual implant fluences may be different than the fluence which was specified for implantation (Heber et al.,

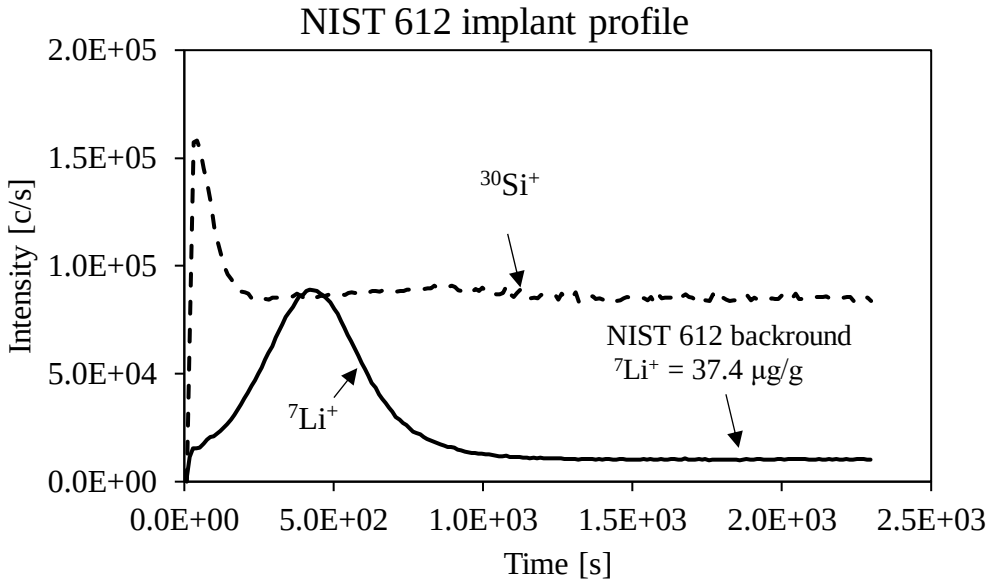

Figure B.1. Depth profile of NIST 612 using setup 3 (Table 3) and no energy offset. The RSF is determined from the background $^{7}Li^{+}$ concentration and used to calculate the fluence of the implant.

2014) it is necessary to determine the actual implant fluence. In order to do this a sample with a known concentration of the implant species must be implanted along with other samples. Here the NIST SRM 612 standard is known to have an intrinsic ^{7}Li concentration of 37.4 µg/g (Fig. B.1).

This corresponds to an atomic density of $7.39*10^{18}$ atoms/cm^3. By measuring the background count rates of $^{7}Li^{+}$ and $^{30}Si^{+}$ one can calculate a Relative Sensitivity Factor from the background with the following expression.

$$RSF = \frac{^{7}Li\ atomic\ density}{^{7}Li^{+}\ count\ rate \Big/ ^{30}Si^{+} count\ rate} \quad \text{(B.1.1)}$$

The background calculated RSF can be used to calculate the absolute fluence of the implant with the following relationship.

$$\phi = \frac{RSF\ \mathrm{z}\ \gamma_{\mathrm{s}}}{\gamma_{\mathrm{m}}\ \mathrm{t}} \quad \text{(B.1.2)}$$

where;

ϕ = Fluence of implant species (implant atoms/cm^2)

RSF = Relative sensitivity factor (implant atoms/cm^3)/(^{7}Li count rate/^{12}C count rate)

γ_m =Mean matrix reference ion intensity (counts/second; $^{12}C^+$)

t = Time spent measuring the implant species (seconds)

z = Crater depth (cm)

γ_s = Integrated secondary ion counts of implant species (counts; $^7Li^+$)

Correcting for background, the instantaneous count rate and backscattered ions (TRIM simulations calculate 1.4% of Li ions directed at the sample during implantation were backscattered) we determined the absolute fluence of $^7Li^+$ is 9.96*10^{14}, which is within 0.5% error of the nominal dose of 1.0*10^{15}.

The NIST 612 sample was implanted for the isotope experiment batch of samples. In order to determine the absolute fluence of the content calibration batch of samples it was necessary to compare implant profiles of the isotope calibration batch (absolute fluence known from NIST 612 calibration) with the content calibration batch (absolute fluence unknown). We measured the glassy carbon samples from each of the different batches with the exact same conditions. Because the fluence of the glassy carbon implanted with the isotope batch (experiment 2) is known, we calculated an RSF for glassy carbon by

rearranging Eq. B.1.2. The RSF in the glassy carbon was used to calibrate to absolute implant fluence in the glassy carbon that was implanted in the content calibration batch. From this calibration we calculated a dose of $1.55*10^{15}$ which is within 1% of the nominal dose of $1.56*10^{15}$.

Appendix B2: Calculation of Sputter Yield and Useful Secondary Ion Yield

Sputter yield: The sputter yield (S) is defined as the total number of atoms sputtered (n_{sp}) per impinging primary atom (n_p).

$$S = \frac{n_{sp}}{n_p} \tag{B.2.1}$$

The numerator n_{sp} can be calculated as follows

$$n_{sp} = \frac{V\,\rho}{u_{avg}\,NA} \tag{B.2.2}$$

where;

V = sputtered volume (cm^3), determined from crater depth measurement and rastered area

ρ = Material density (g/cm^3)

u_{avg} = The molar mass of the average atom in the material (g/mole), determined by taking a weighted average of the major elements present.

$NA =$ Avogadro's number (6.023E23 atoms/mole)

The denominator n_p is determined with the following expression

$$n_p = \frac{I\,n_{ion}\,t}{e} \tag{B.2.3}$$

where;

$I =$ Primary current (Ampere, i.e., coulombs/s)

$n_{ion} =$ Number of atoms per primary ion (e.g., 2 for O_2^- and 1 for O^-)

$e =$ Magnitude of elementary charge (1.602E-19 coulombs (C))

$t =$ Total analysis time (s)

Useful secondary ion yield: The useful ion yield (UY) is the mass selected ions of a given species detected (γ) per atom of that species sputtered (n_{sp}).

$$UY = \frac{\gamma}{n_{sp}} \tag{B.2.4}$$

We note that γ should represent the total number of ions that would be detected assuming the instrument is measuring only that species for the entire analysis. Therefore, when peak switching this value must be corrected by determining the duty cycle (i.e., the amount of time spent measuring the ion of interest out of the entire cycle time) and dividing the intensity at each cycle by the duty cycle. After this correction (if necessary) γ is calculated by integrating the counts over all of the cycles. If there is a background this must be subtracted prior to integrating.

Different approaches are required when calculating n_{sp} of an implanted ion compared to a matrix ion and calculations for both are given below.

Matrix ion species

$$n_{sp} = N_{ref}\ V\ FA \tag{B.2.5}$$

where;

$N_{ref} =$ The atomic density of the reference ion (atoms/cm^3). See equation 3 in paper for calculation details.

$FA =$ The ratio of the analyzed area (i.e., the area being allowed through the field aperture) to the rastered area.

Implant ion species

$$n_{sp} = \left(\frac{\phi}{z}\right) V \text{ FA} \qquad \text{(B.2.6)}$$

where;

ϕ = Fluence of implant species (atoms/cm^2)

z = Crater depth (cm)

APPENDIX C

SUPPLEMENTARY INFORMATION FOR CHAPTER 4

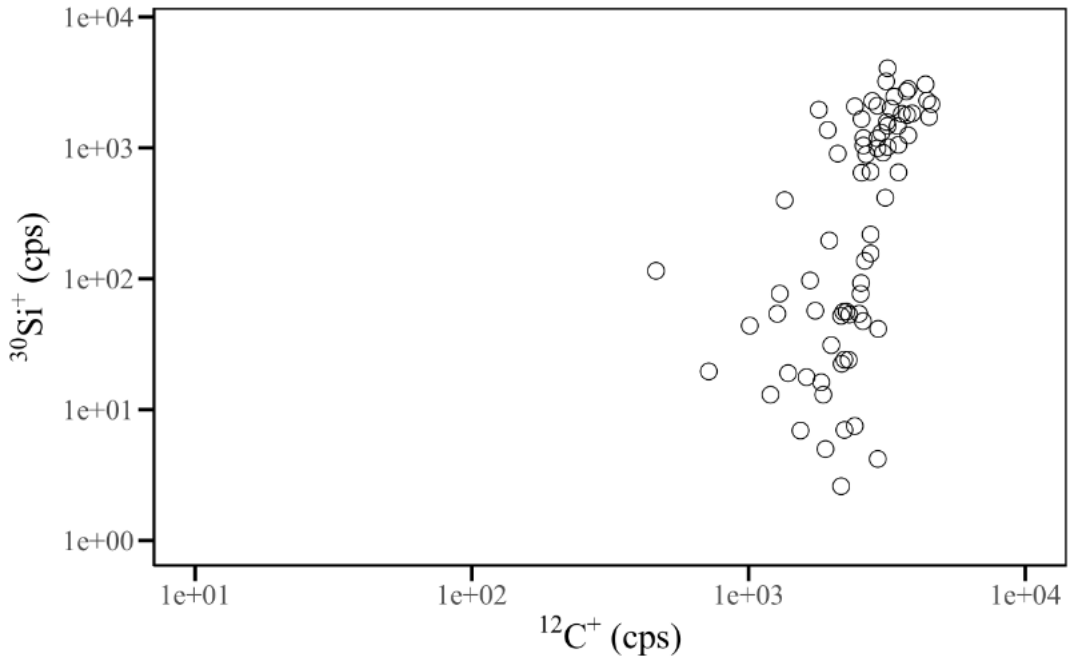

Figure C.1. Plot showing the $^{12}C^{+}$ and $^{30}Si^{+}$ counts per second for spot measurements. Counts were normalized for the current used in each measurement. The $^{12}C^{+}$ counts span a much smaller range than the $^{30}Si^{+}$ counts indicating that $^{30}Si^{+}$ counts typically control on the $^{12}C^{+}/^{30}Si^{+}$ ratio for organics. Silicates that were identified microscopically are the only group that show a marked decrease in $^{12}C^{+}$ signal and had a $^{12}C^{+}/^{30}Si^{+}$ ratio less than 0.5.

Table C.1

SILLi 1.0 Model Input Parameters

Variable Name	Vermejo	Dutch Creek	Units	References
Pore water density	1050	1050	(kg/m3)	Approximated from brine waters densities
Pore water heat capacity	3000	3000	(J/kg/C)	(Wagner and Pruss, 2002)
Pore water thermal conductivity	0.6	0.6	(W/m/K)	(Huber et al., 2012)
Coal Density	1350	1350	(kg/m3)	(Waples and Waples, 2004)
Coal heat capacity	1300	1300	(J/kg/C)	(Waples and Waples, 2004)
Coal Porosity	0.1	0.1	(Pore vol./Rock vol.)	(Gan et al., 1972)
Coal thermal conductivity	0.33	0.33	(W/m/K)	(Herrin and Deming, 1996)
Total organic carbon (TOC)	74	84	(wt. %)	Used total C wt.% (Table 2)
Latent heat of dehydration	170	170	(kJ/kg)	(Wang and Manga, 2015)
Latent heat of organic maturation	375	375	(kJ/kg)	(Aarnes et al., 2010)
Dike thickness	1.6	1.53	(m)	(Bostick and Collins, 1987)
Dike emplacement temperature	1100	750	(°C)	(Dilles et al., 2015; Dilles and John, 2021; Galushkin, 1997; Meng et al., 2018; Olson et al., 2017; Schöpa et al., 2017)
Melt density	2700	2200	(kg/m3)	(Best, 2002)
Melt heat capacity	1484	1375	(J/kg/C)	(Lesher and Spera, 2015)
Solid dike density	2900	2700	(kg/m3)	(Best, 2002)
Solid dike heat capacity	1150	1150	(J/kg/C)	(Hartlieb et al., 2016)
Solid dike thermal conductivity	2.1	2.7	(W/m/K)	(Cho et al., 2009; Galushkin, 1997)
Solidus temperature	950	650	(°C)	(Dilles et al., 2015; Dilles and John, 2021; Galushkin, 1997; Meng et al., 2018; Olson et al., 2017; Schöpa et al., 2017)
Liquidus temperature	1150	1050	(°C)	(Dilles et al., 2015; Dilles and John, 2021; Galushkin, 1997; Meng et al., 2018; Olson et al., 2017; Schöpa et al., 2017)
Latent heat of crystallization	376	376	(kJ/kg)	(Wang and Manga, 2015)

Table C.2

Maceral Contents Determined for Vermejo Fm. Coals (Vol.%; on Mineral-Free Basis).

Sample	V-A	V-B	V-C	V-D	V-E	V-CR
CD	0.0	0.0	0.0	0.0	7.6	14.8
CT	0.0	0.0	0.0	0.0	40.4	47.6
T	0.0	0.0	0.0	0.0	0.0	0.0
CG	0.0	0.0	0.0	0.0	0.0	0.8
VD	0.0	0.0	0.0	0.0	0.0	0.0
G	0.0	0.0	0.0	0.0	0.0	4.0
Total-V	**0.0**	**0.0**	**0.0**	**0.0**	**48.0**	**67.2**
SF	0.0	0.0	0.0	0.0	2.0	6.0
F	24.0	20.8	17.6	16.0	10.0	19.6
Ma	0.0	0.0	0.0	0.0	0.0	1.2
Mi	0.0	0.0	0.0	0.0	0.0	0.0
Sec	0.0	1.6	0.8	1.6	0.0	0.0
ID	0.8	0.8	4.8	0.0	1.2	2.0
Fg	0.0	0.0	0.0	0.0	0.0	0.4
Total-I	**24.8**	**23.2**	**23.2**	**17.6**	**13.2**	**29.2**
Sp	0.0	0.0	0.0	0.0	1.6	2.8
Cut	0.0	0.0	0.0	0.0	0.0	0.0
Re	0.0	0.0	0.0	0.0	0.0	0.8
Sub	0.0	0.0	0.0	0.0	0.0	0.0
Total-L	**0.0**	**0.0**	**0.0**	**0.0**	**1.6**	**3.6**
Coke	**75.2**	**76.8**	**76.8**	**82.4**	**37.2**	**0.0**

Point counts of organic matter (macerals) were performed for each sample using a Zeiss epiplan 40X oil immersion objective, in conjunction with a 1.6X magnification changer (final magnification of 640X). A Zeiss 02 fluorescence filter set, with a 450-490 nm excitation filter, a 510 nm beam-splitter, and a 520 nm emission filter, was used in conjunction with a high-intensity metal halide light source for fluorescent light microscopy to confirm the identification of liptinite macerals. Coal maceral terminology follows nomenclature outlined by the International Commission for Coal and Organic Petrology (ICCP, 1994, 2000; Pickel et al., 2017). CD, collodetrinite; CT, collotelinite; T, telinite; CG, corpogelinite; VD, vitrodetrinite; G, Gelinite; Total-V, total vitrinites; SF, semifusinite; F, fusinite; Ma, macrinite; Mi, micrinite; Sec, Secretinite; ID, inertodetrinite; Fg, funginite; Total-I, total inertinites; Sp, sporinite; Cut, cutinite; Re, resinite, Sub, Suberinite; Total-L, total liptinites

Table C.3

Spot analyses of Vermejo and Dutch Creek macerals

Measurement	Primary maceral or coke	δ^7Li (‰)	S.E. (‰)	P.E. (‰)	Li (μg/g)	$^{12}C^+/^{30}Si^+$
V-A-1	Coke	-7.6	1.4	0.9	0.70	2.5
V-A-2	Coke	-11.7	1.1	0.7	0.93	1.0
V-A-3	Coke	-1.9	1.9	0.9	0.68	2.3
V-A-4	Coke	-1.8	1.1	0.5	1.00	1.4
V-A-5	Coke	-1.8	1.6	0.5	0.95	1.5
V-B-1	Coke	14.3	1.3	1.0	0.55	3.0
V-B-2	Coke	10.2	1.2	1.1	0.57	2.5
V-B-3	Coke	2.8	1.4	1.3	0.37	4.2
V-B-4	Inertinite	-0.3	1.2	1	0.41	12.7
V-B-5	Coke	9.0	0.9	0.9	0.55	3.0
V-B-6	Coke	11.8	1.0	1	0.82	2.0
V-B-7	Coke	10.3	0.9	1	0.46	2.2
V-B-8	Coke	7.3	0.7	0.8	1.05	1.4
V-C-1	Coke	2.2	1.0	1.1	0.77	1.9
V-C-2	Coke	2.7	0.7	0.8	0.62	2.1
V-C-3	Coke	1.8	1.0	0.8	0.66	2.1
V-C-4	Inertinite	-3.0	1.1	0.9	0.53	1.3
V-C-5	Coke	5.2	1.0	1.1	0.61	2.5
V-D-1	Coke	3.8	0.9	0.8	0.52	3.1
V-D-2	Coke	3.0	1.1	1.0	0.59	2.3
V-D-3	Inertinite	5.5	0.6	0.6	2.58	0.3
V-D-4	Inertinite	17.7	0.8	0.7	0.43	0.8
V-D-5	Coke	7.7	0.7	0.7	0.72	1.6
V-E-1	Vitrinite	-14.9	0.9	0.9	1.58	2.0
V-E-2	Vitrinite	-11.4	0.7	0.8	1.38	2.2
V-E-3	Vitrinite	-5.8	2.9	2.1	0.21	19.9
V-E-4	Coke	-9.3	0.8	0.9	0.55	5.4
V-E-5	Coke	-12.3	1.3	0.8	0.96	4.8
V-E-6	Vitrinite	-12.2	1.8	1.7	0.26	18.3
V-E-7	Liptinite	-8.3	0.9	0.8	0.93	2.2
V-E-8	Vitrinite	-3.0	1.1	1.0	0.82	3.3

Table C.3 Continued

V-CR-1	Vitrinite	-21.1	1.0	1.0	0.68	11.4
V-CR-2	Vitrinite	-25.3	1.8	1.8	0.28	87.2
V-CR-3	Inertinite	-6.0	1.6	0.8	0.17	10.7
V-CR-4	Vitrinite	-30.5	1.8	1.7	0.22	21.6
V-CR-5	Vitrinite	-27.9	1.8	1.6	0.25	115.1
V-CR-6	Liptinite	-11.7	1.7	1.5	0.16	4.4
V-CR-7	Vitrinite	-37.8	1.9	2.2	0.23	9.4
V-CR-8	Inertinite	-22.9	2.2	2	0.14	147.7
V-CR-9	Vitrinite	-30.0	1.9	2.1	0.20	32.0
V-CR-10	Vitrinite	-21.0	2.3	2.4	0.21	23.5
V-CR-11	Inertinite	-14.0	1.1	1	0.78	1.4
V-CR-12	Inertinite	-7.1	0.7	0.8	1.67	0.9
V-CR-13	Vitrinite	-26.8	1.9	2.1	0.33	7.3
V-CR-14	Liptinite	-19.2	2.0	2.4	0.26	16.9
V-CR-15	Vitrinite	-32.6	1.4	1.8	0.46	351.6
V-CR-16	Vitrinite	-34.0	1.5	1.6	0.36	326.3
V-CR-17	Vitrinite	-25.1	2.0	2.3	0.32	40.3
V-CR-18	Inertinite	-2.6	0.5	0.4	0.56	1.2
DC-B-1	Coke	8.0	2.6	2.4	0.32	39.6
DC-B-2	Coke	6.9	0.8	0.9	0.57	23.2
DC-B-3	Coke	0.6	1.0	1.1	0.54	36.5
DC-B-4	Vitrinite	14.0	2.9	3.1	0.07	231.4
DC-B-5	Inertinite	-1.4	1.3	1.5	0.11	90.5
DC-B-6	Coke	12.9	0.9	0.9	0.54	71.1
DC-D-1	Coke	8.8	1.1	1.1	0.34	45.9
DC-D-2	Coke	11.8	1.0	1	0.46	27.6
DC-D-3	Inertinite	-3.8	1.0	0.6	0.63	1.5
DC-D-4	Coke	12.5	0.7	0.6	0.63	33.0
DC-D-5	Coke	17.9	1.3	1.3	0.34	43.5
DC-D-6	Coke	13.1	1.1	1.1	0.21	90.7
DC-D-7	Vitrinite	4.9	0.8	0.9	0.76	19.2
DC-D-8	Inertinite	2.1	1.3	1.3	0.25	4.2

Table C.3 Continued

DC-F-1	Inertinite	-4.1	1.1	1.3	1.84	4.0
DC-F-2	Inertinite	2.3	0.6	0.6	2.76	3.4
DC-F-3	Coke	7.8	1.3	1.5	0.17	97.0
DC-F-4	Coke	10.5	1.3	1.2	0.17	94.7
DC-F-5	Vitrinite	17.6	1.1	1.1	0.29	55.5
DC-F-6	Coke	8.8	1.0	1.0	0.25	63.2
DC-K-1	Vitrinite	-4.7	1.2	0.9	0.13	313.1
DC-K-2	Vitrinite	-1.5	1.6	1.6	0.04	831.0
DC-K-3	Vitrinite	-0.4	1.5	1.3	0.31	115.0
DC-K-4	Inertinite	9.5	0.4	0.5	9.82	1.3
DC-K-5	Inertinite	4.0	0.5	0.5	12.46	1.2
DC-K-6	Inertinite	-4.8	1.0	1.1	1.39	10.0
DC-K-7	Inertinite	1.8	0.5	0.4	7.22	2.6
DC-K-8	Inertinite	3.7	0.4	0.4	6.86	3.0
DC-K-9	Vitrinite	-6.8	1.6	1.3	0.04	728.0
DC-K-10	Inertinite	5.8	0.6	0.4	5.74	4.0

APPENDIX D

SUPPLEMENTARY INFORMATION FOR CHAPTER 6

Appendix D1: Effectiveness of Mannitol for Li Ion Desorption

Background

To measure the Li that is structurally bound to either kerogen or minerals it was imperative to remove any Li contaminants as well as exchangeable surface adsorbed Li ions. Clay minerals commonly have negatively charged surfaces due to deficiencies in charge resulting from ion substitution in crystal structures (Jackson and Barak, 2005; Moore and Reynolds, 1997) resulting in a high cation exchange capacity (CEC; commonly >100 meq/100g). The CEC defines the quantity of cations a given sediment can hold. Soil organic matter, rich in carboxyl groups can also have large CEC values (Derkowski and Marynowski, 2016). Yuan et al., (1967) found that soil organic matter accounted for 66.4% to 96.5% of the CEC in four different Florida soil types. Some oxygen rich functional groups, important to the CEC of organics, are retained in kerogen during diagenesis and can become reactivated by the oxidation of kerogen during weathering (Derkowski and Marynowski, 2016).

Cation exchange solutions that contain an abundance (1M or more) of a preferred cation with similar ionic radius and charge, preferentially exchange cations that are not bound to the mineral. For example, NH_4^+, K^+ or Na^+ are preferred over adsorbed Li because Li has a higher hydration energy (Teppen and Miller, 2006). Alternatively, chemicals in solution may complex with the adsorbed Li because they form stronger bonds with the Li ion than the adsorption bond. Hingston, (1964) used the alcohol mannitol ($C_6H_{14}O_6$) to complex with and remove B atoms from the surfaces of clay minerals and the optimal concentration (0.1 M) for B-Mannitol complexation was determined by Tonarini et al., (1997). Medical professionals use mannitol as a diuretic to

remove excess Li from human kidneys (Noormohamed and Lant, 1995). In preparation for SIMS measurements, Williams et al., (2015) rinsed clay samples for 24 hours in 0.1 M Mannitol solution followed by triplicate rinses in DI water, to remove adsorbed Li and B from clay minerals. This procedure was followed during sample preparation of coal powders, polished coal sections and implant standards as outlined in each Chapter. No studies were found which have attempted to quantify the effectiveness of Mannitol as a desorbing agent of adsorbed Li ions, therefore the effectiveness of mannitol at removing Li from charged surfaces was studied. Ammonium chloride (NH_4Cl) is preferred for cation exchange in clay minerals treatments because of the affinity of NH_4^+ for clay interlayers (Williams et al., 2012; Zhang et al., 1998). In the following experiment Li was adsorbed to kaolinite and then desorbed using 0.1 M Mannitol and 1 M NH_4Cl for comparison, in order to determine the usefulness of Mannitol in removing surface exchangeable Li^+ from negatively charged surfaces.

Methods

One gram of KGa-1 kaolinite standard reference clay (www.clays.org/sourceclays) was added to four separate test tubes and each was rinsed in 40 ml of de-ionized (DI) water for one hour to remove Li contaminants that were not surface adsorbed. Post rinsing, samples were centrifuged, fluids were collected, and powders dried overnight at 60 °C. After drying, two samples of KGa-1 were sonified with an ultrasonicator in 40 ml of 0.1 M Mannitol and the other two samples were sonified in 40 ml of 1 M NH_4Cl. Next samples shook for 24 hours in the 0.1 M Mannitol and 1 M NH_4Cl solutions. The solutions were collected by centrifugation, and the KGa-1 samples were rinsed three times in DI water and then dried overnight. Lithium was

adsorbed to KGa-1 by shaking it in 1 M LiCl solution for 48 hours. LiCl solutions were collected, the samples were rinsed three times in DI water (to remove Li that was not surface adsorbed) and dried. Once again, two KGa-1 samples were rinsed in 0.1 M Mannitol and the other two samples were rinsed in 1 M NH_4Cl for 24 hours. Finally, samples were rinsed three times in DI water and dried. The pH of the solutions was recorded at every major step of the process and solutions, rinses and blanks were retained for analysis of Li-contents by ICP-MS (METALS Lab, Arizona State University). Finally, the samples were filtered through 0.45 µm Polypropylene syringe filters to purify the solutes.

Determination of Li-contents in fluids was performed at the Arizona State University Metals, Environmental and Terrestrial Analytical Laboratory (METAL) with the Thermo Scientific Quadrupole ICP-MS (iCap™-Q). The 1 M LiCl solutions were diluted by a factor of 10,000 and all other samples were undiluted. Triplicate rinses in DI water were combined for ICP-MS analyses. The Li-content results of fluids from duplicate test tubes were averaged (i.e., fluids from the two test tubes rinsed in 0.1 M Mannitol were averaged and fluids from the test tubes rinsed in 1 M NH_4Cl were averaged).

Results

Fig. D.1 shows the Li-contents of the 0.1 M Mannitol and 1 M NH_4Cl initial and second treatments after shaking overnight with KGa-1. The initial treatment took place prior to the adsorption of Li onto KGa-1 using the 1 M LiCl solution and therefore the adsorbed Li-content was unknown. For the second treatment an approximate adsorbed Li-content was calculated via mass balance calculations by subtracting the Li concentrations

of the 1 M LiCl after shaking overnight with KGa-1 and the triplicate rinsings in DI water from the original Li concentration of the 1 M LiCl solution.

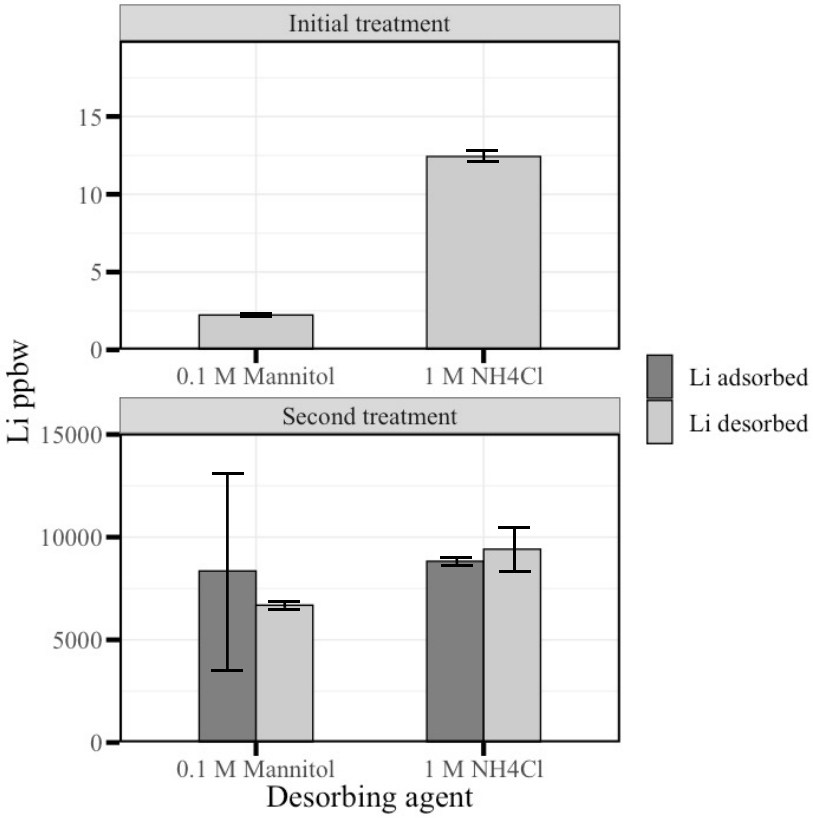

Figure D.1. The mean desorbed Li contents measured by ICP-MS are plotted for the initial (untreated) clay and after addition of 1M LiCl in the second treatment and removal of exchangeable Li using of 0.1 M Mannitol and 1 M NH_4Cl solutions. Additionally, the mean adsorbed Li-contents from 1 M LiCl treatments are shown. The error bars represent the standard error of the mean from duplicate treatments.

The Li desorbed by the 0.1 M Mannitol in the initial experiment (2.2 ± 0.1 μg/L) amounted to 18% of the Li that was removed by the 1 M NH_4Cl (12.4 ± 0.6 μg/L) during the initial treatment. For the second rinsing, after addition of 1M LiCl, the 0.1 M Mannitol desorbed an average concentration of 6690 ± 240 μg/L which amounted to 71% of the Li removed by the 1 M NH_4Cl (9400 ± 2100 μg/L). In the second treatment the Li

removed by both 0.1 M Mannitol and 1 M NH_4Cl was within error of the calculated adsorbed Li.

Discussion

The 0.1 M Mannitol was almost as effective as the 1 M NH_4Cl when there were high amounts of Li adsorbed to the KGa-1 kaolinite. The cause for this may be that when the kaolinite surfaces are Li saturated more of the Li atoms are held in low energy adsorption sites that are easily desorbed or exchanged. Thus, the percentage of the total Li ions that are desorbed from a given mineral is likely a function of the negative charge on the mineral surface as well as how saturated the surface is with adsorbed ions.

One major limitation of this preliminary work was the lack of access to a high speed (>10k rpm) centrifuge. While decanting, the last portion of the fluid being decanted had to be left in the test tube so that significant amounts of clay were not removed. This fact likely led to the large standard errors shown in Fig. D.1. Future experiments testing the effectiveness of Mannitol solutions as a desorbing agent should consider adsorbing different concentrations of Li to kaolinite to determine how that affects the percentage of Li removed by Mannitol.

Appendix D2: XRD Spectra of Hydrous Pyrolysis Samples

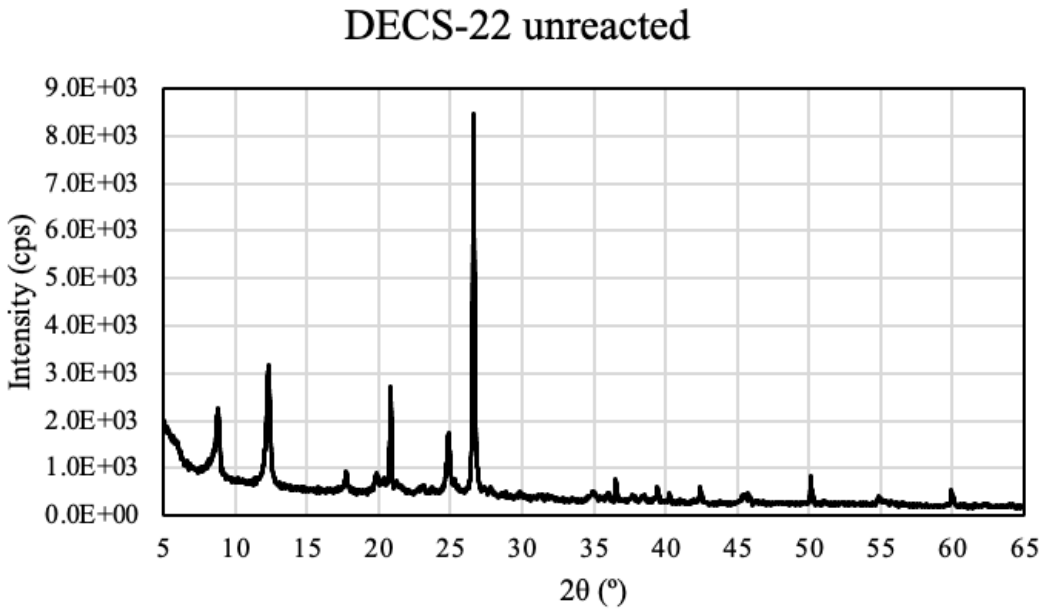

Figure D.2. X-ray diffraction spectrum of the unreacted DECS-22 coal after digestion in H_2O_2.

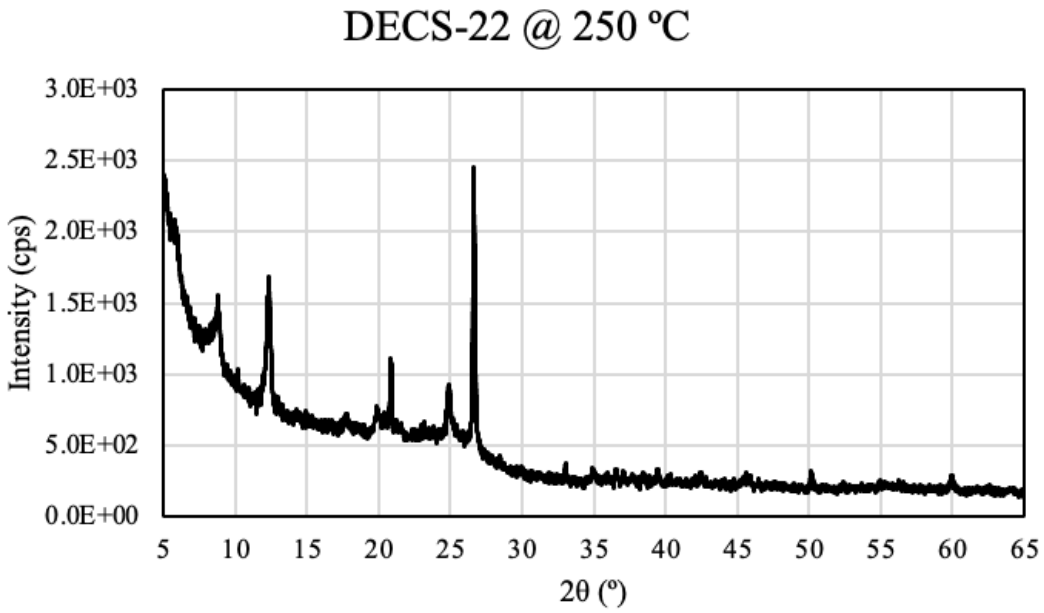

Figure D.3. X-ray diffraction spectrum of the DECS-22 coal powder after undergoing hydrous pyrolysis at 250 ºC for 72 hours.

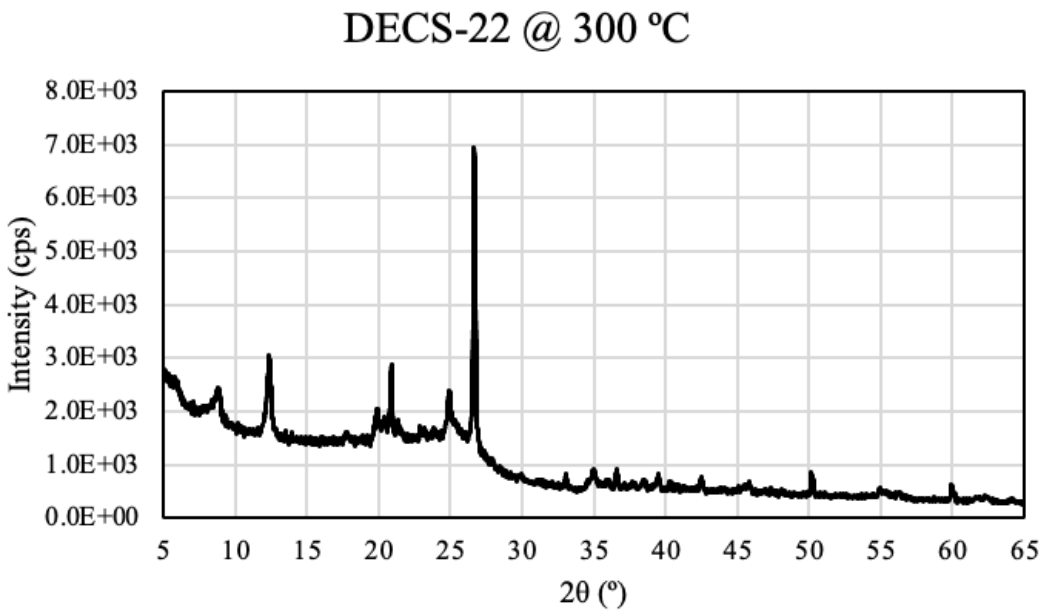

Figure D.4. X-ray diffraction spectrum of the DECS-22 coal powder after undergoing hydrous pyrolysis at 300 ºC for 72 hours.

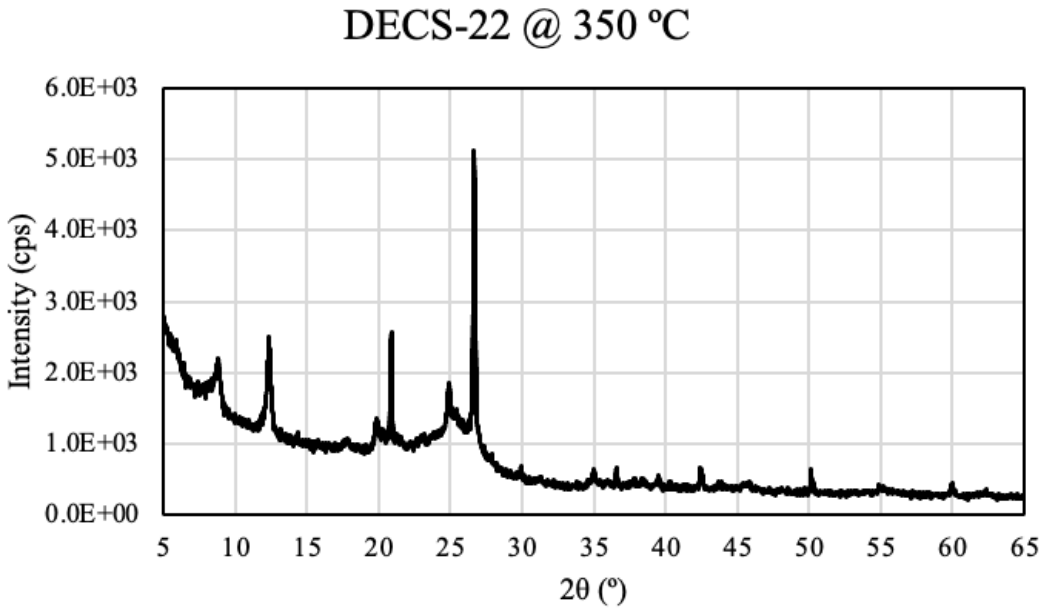

Figure D.5. X-ray diffraction spectrum of the DECS-22 coal powder after undergoing hydrous pyrolysis at 350 ºC for 72 hours.

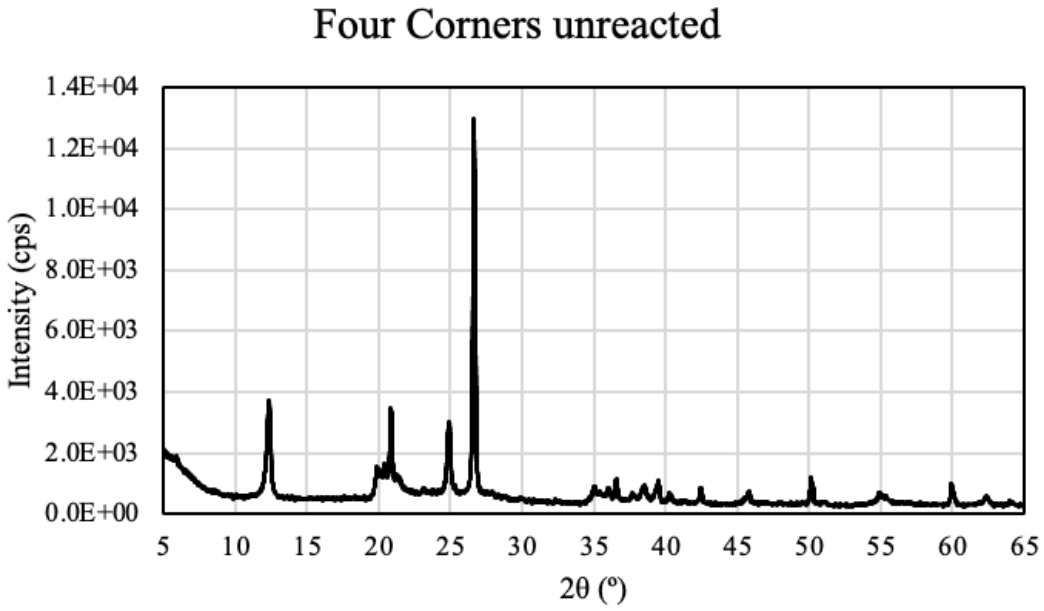

Figure D.6. X-ray diffraction spectrum of the unreacted Four Corners coal after digestion in H_2O_2.

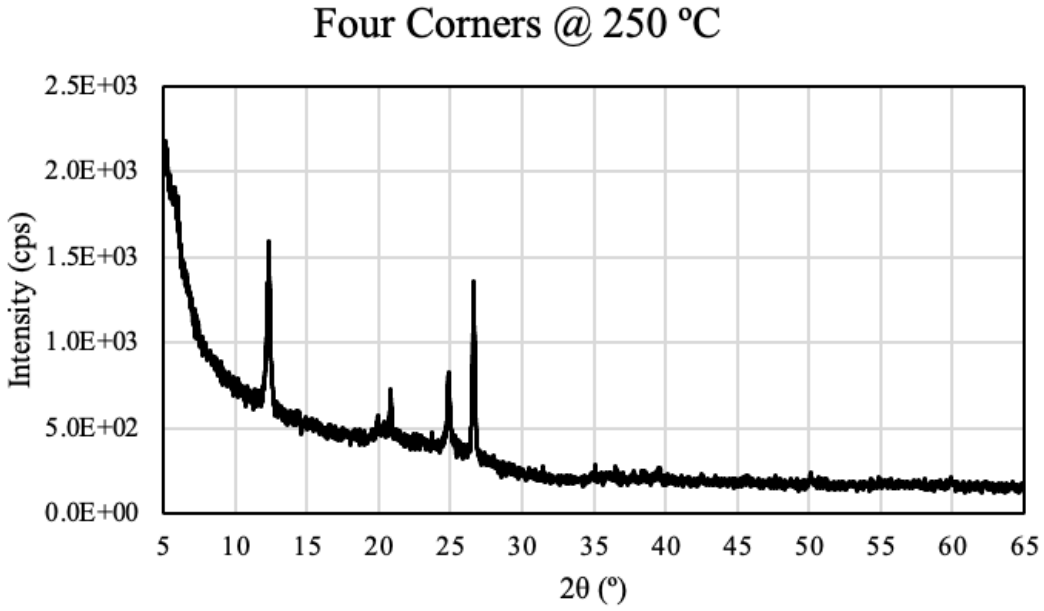

Figure D.5. X-ray diffraction spectrum of the Four Corners coal powder after undergoing hydrous pyrolysis at 250 ºC for 72 hours.

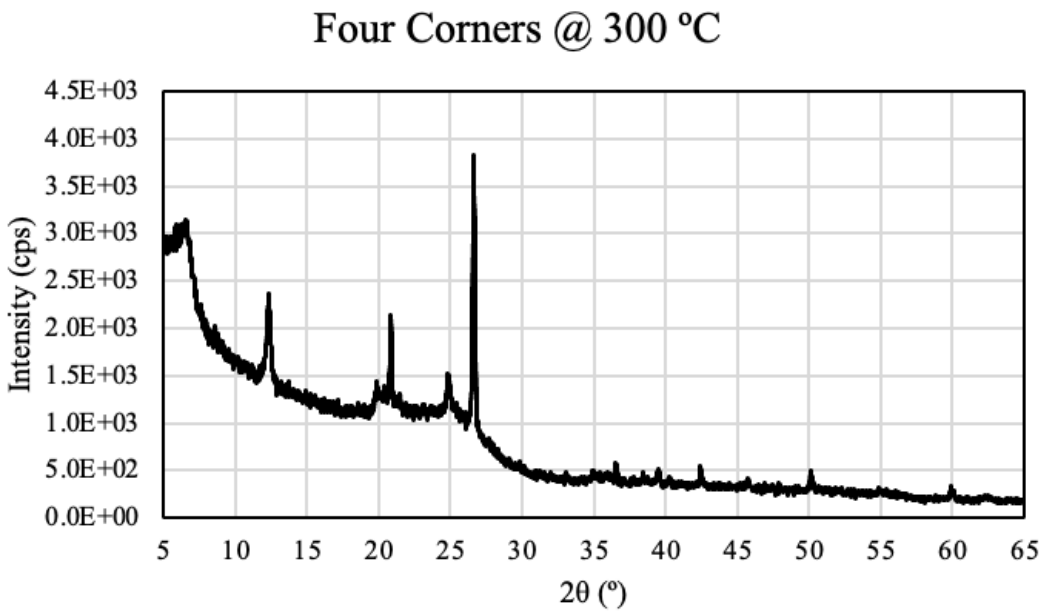

Figure D.6. X-ray diffraction spectrum of the Four Corners coal powder after undergoing hydrous pyrolysis at 300 ºC for 72 hours.

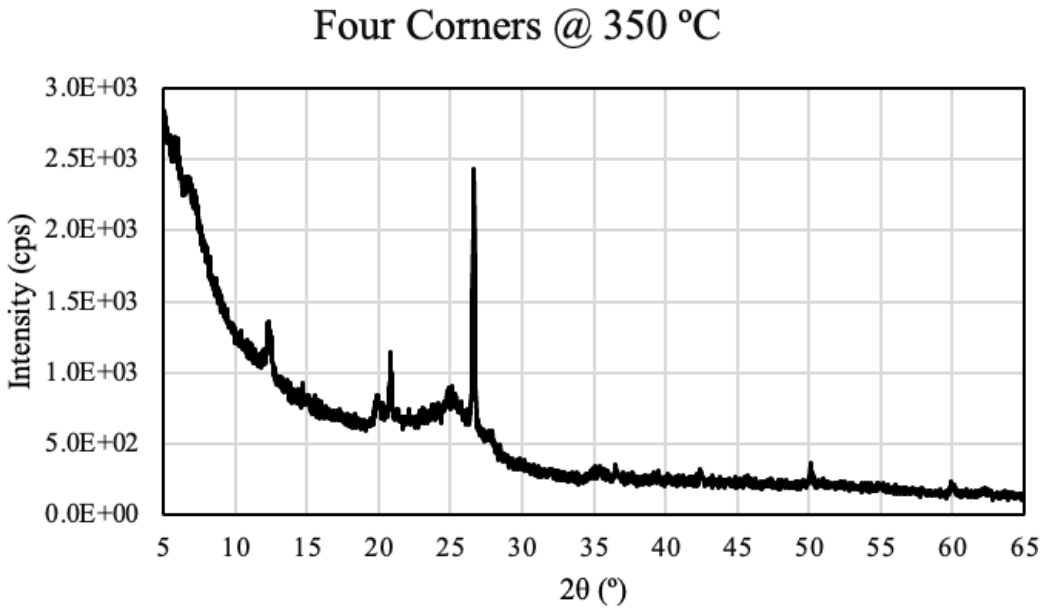

Figure D.7. X-ray diffraction spectrum of the Four Corners coal powder after undergoing hydrous pyrolysis at 350 ºC for 72 hours.

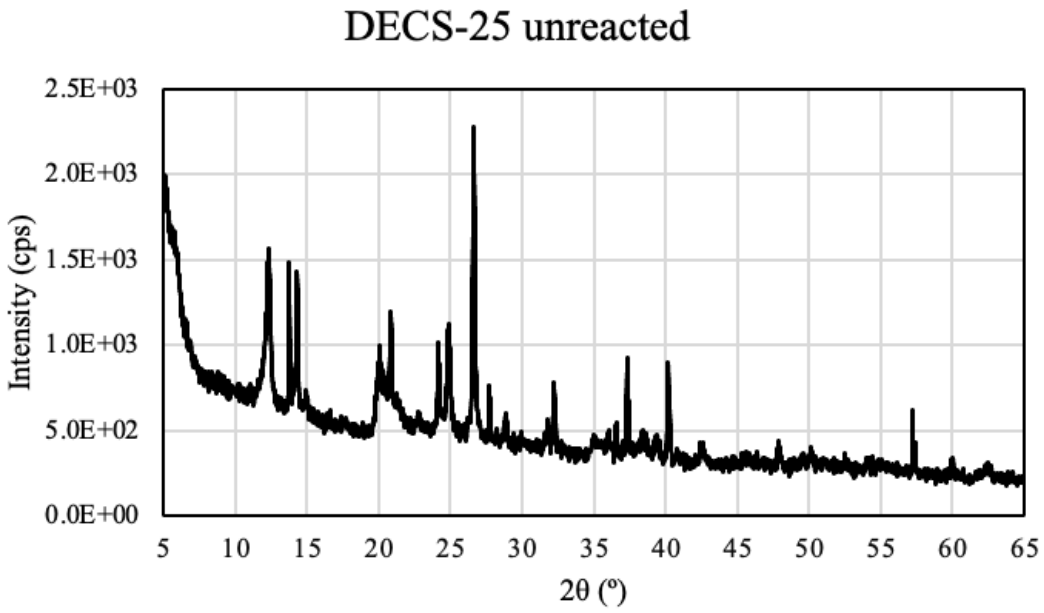

Figure D.8. X-ray diffraction spectrum of the unreacted DECS-25 coal after digestion in H_2O_2.

Appendix D3: Mass balance calculations

Step 1: Determine how much the Li-contents of porefluids would increase for each experimental case. The first step is to determine the porosity (Φ) of the rock of interest. The porosity gives the volumetric ratio of porefluid:rock which can be converted to a mass ratio (M) using the densities of the rock (ρ_{rock}) and the experimental water (ρ_{water}) using the following expression.

$$MR = (\Phi * \rho_{water}) / (\Phi * (1 - \rho_{rock})) \quad (D.3.1)$$

From there, one can take the Li-content measured in experimental water at a 1:1 water:rock mass ratio and divide that value by MR to scale the concentration up to what would be present in the porefluids (Li_{w1}).

Step 2: Predict the Li-isotope composition of the water based on changes in the rock Li-isotope composition before and after each experiment. First, it is ideal if the Li-content of the rock prior to hydrous pyrolysis (Li_{r1}) is known. The amount of Li measured in the water after the experiment (Li_{w1}) can be subtracted from Li_{r1} to determine the amount of Li remaining in the rock after hydrous pyrolysis (Li_{r2}) assuming the same units (e.g, μg/g) are used for both the rock and water. From there one must take the measured atomic Li-isotope ratio in the powder prior to hydrous pyrolysis (R_{r1at}) and after hydrous pyrolysis (R_{r2at}) and convert those ratios to the Li-isotope weight ratios for before (R_{r1wt}) and after (R_{r2at}) the experiment using the differences in mass between ^{7}Li and ^{6}Li. Then the total mass of each Li-isotope in the rock before and after can be determined using the following expressions.

^{7}Li mass in the rock prior to experiment (M_{7Li1}):

$$M_{7Li1} = (R_{r1wt} / (R_{r1wt} + 1)) * Li_{r1} \quad (D.3.2)$$

^{6}Li mass in the rock prior to experiment (M_{6Li1}):

$$M_{6Li1} = (1 / (R_{r1wt} + 1)) * Li_{r1} \quad \text{(D.3.3)}$$

^{7}Li mass in the rock after the experiment (M_{7Li2}):

$$M_{7Li2} = (R_{r2wt} / (R_{r2wt} + 1)) * Li_{r2} \quad \text{(D.3.4)}$$

^{6}Li mass in the rock after the experiment (M_{6Li2}):

$$M_{6Li2} = (1 / (R_{r2wt} + 1)) * Li_{r2} \quad \text{(D.3.5)}$$

The Li-isotope mass ratio in the water ($R_{w.wt}$) can then be determined as follows:

$$R_{w.wt} = (M_{7Li1} - M_{7Li2}) / (M_{6Li1} - M_{6Li2}) \quad \text{(D.3.5)}$$

The isotope mass ratio in the water can then be converted into an atomic mass ratio ($R_{w.at}$) and then into $\delta^{7}Li$ notation if desired ($\delta^{7}Li_{w}$).

Step 3: Predict how the Li-isotope composition of porefluids with seawater (or other) composition would change when Li is released from kerogen. In natural settings Li is already present in the porefluids with a distinct concentration (Li_{sw}) and Li-isotope composition ($\delta^{7}Li_{sw}$). The new Li-isotope composition of the fluids after addition of Li from kerogen ($\delta^{7}Li_{new}$) can be predicted with the following expression:

$$\delta^{7}Li_{new} = (\delta^{7}Li_{w} * (Li_{w1} / (Li_{w1} + Li_{sw}))) + (\delta^{7}Li_{sw} * (Li_{sw} / (\delta^{7}Li_{w} + Li_{sw}) \quad \text{(D.3.6)}$$